INFORMATION TO USERS

This manuscript has been reproduced from the microfilm master. UMI films the text directly from the original or copy submitted. Thus, some thesis and dissertation copies are in typewriter face, while others may be from any type of computer printer.

The quality of this reproduction is dependent upon the quality of the copy submitted. Broken or indistinct print, colored or poor quality illustrations and photographs, print bleedthrough, substandard margins, and improper alignment can adversely affect reproduction.

In the unlikely event that the author did not send UMI a complete manuscript and there are missing pages, these will be noted. Also, if unauthorized copyright material had to be removed, a note will indicate the deletion.

Oversize materials (e.g., maps, drawings, charts) are reproduced by sectioning the original, beginning at the upper left-hand corner and continuing from left to right in equal sections with small overlaps.

Photographs included in the original manuscript have been reproduced xerographically in this copy. Higher quality 6" x 9" black and white photographic prints are available for any photographs or illustrations appearing in this copy for an additional charge. Contact UMI directly to order.

Bell & Howell Information and Learning
300 North Zeeb Road, Ann Arbor, MI 48106-1346 USA

UMI®
800-521-0600

Multi-Variable Optimal Numerical Control Using Adaptive Model for identification of Thermally Induced Deformation in High-Speed Machine Tools

Steven Fraser

A Thesis
in
The Department
of Mechanical Engineering

Presented in Partial Fulfilment of the Requirements
for the Degree of Doctor of Philosophy
Concordia University
Montreal, Quebec, Canada

August 8, 1997

ABSTRACT

Multi-Variable Optimal Numerical Control Using Adaptive Model for identification of Thermally Induced Deformation in High-Speed Machine Tools

Steven Fraser, Ph.D.
Concordia University, 1997

Thermally induced deformation in machining has been accorded an equal place with other sources of error, namely tool wear and mechanical deflection. The demand of the manufacturing sector to control the residual thermal errors below ±10 μm in the whole working range of the machine tool has not yet been achieved. Since it is impossible to design machine tools that are thermally stable within this range, a feedback control system emerges as a logical and practical solution.

The major problem in implementing real-time control systems for thermal deflection is that it is not possible to directly measure the relative thermal displacement between the tool and the workpiece during machining, prohibiting the use of true feedback control. Process models relating the thermal deformation to the temperature rise at some points on the structure are frequently used, but since complicated models are not practical in a real-time control environment, simplified empirical models of the structure are employed. Based on the results reported in the literature, one can conclude that this will lead to poor predictions.

In order to improve the accuracy and reliability of thermal deflection estimation, a new concept of *generalized modelling* is expanded in this thesis to develop accurate real-time process models relating practical measured temperature points to the net thermal deflection of a machine tool structure. The first of these models deals with the identification of the generation of heat sources from the delayed temperature time response of measured points on the structure. The second model deals with the identification of the nonlinear effects that are introduced by contact interfaces within the machine tool structure. It has been shown that the accuracy of these models is within ±4 microns for typical configurations of a multi-component machine tool.

The estimated thermal deflection error is compensated by means of a feedback/ feedforward control system, using NC position control and electronically-controlled resistance heating pads as a micro-positioning actuation mechanism. The feedforward controller was designed using the method of model inversion, and the feedback controller was optimized using the LQR error minimization technique. The procedure was validated on linear and nonlinear machine tool models. It has been shown that the estimation and control system reduces the thermal deflection error to within ±10 microns, a reduction of 96%, for multi-component machine tool structures of typical geometry, using economical hardware and data acquisition techniques.

ACKNOWLEDGEMENTS

The author would like to express his sincere gratitude to co-supervisors Dr. M.O.M. Osman and Dr. M.H. Attia for their valuable insight and tireless attention to detail. It is by their standard of excellence that I would always hope to be judged.

Thanks also to George Seeger and the rest of the Concordia machine shop for excellent support.

The financial support of the Natural Sciences and Engineering Research Council is also acknowledged and appreciated.

Special thanks to my parents and to my fiancé Tara Vatcher for their patience and constant encouragement.

TABLE OF CONTENTS

LIST OF FIGURES

LIST OF SYMBOLS

δ	Thermal Deflection
u	Control Signal
Q_d	Disturbance Heat Generation
q_c	Control Heat Generation
δ^e	Estimated Thermal Deflection
T	Temperature
ΔT	Temperature Difference
T_a	Temperature Ambient
r	Radial Distance
r_0	Radius of Circular Heat Source
Q	Heat Generation
α	Thermal Diffusivity
h	Convection Co-Efficient of Heat Transfer
k	Thermal Conductivity
w	Thickness of Plate
g(r,t)	Internal Heat Generation Rate per Unit Volume
β	Variable of Integration
J_0	Bessel Function Type Zero
τ	Time Variable for Integration
a	Constant
α	Constant
K	Constant
t	Time
λ_n	Approach of Contacting Surface Asperities
p_n	Normal Pressure
c_n	Interface Normal Compliance
m	Constant
k_n	Normal Stiffness
λ_s	Elastic Shear Deflection
p_s	Tangential Stress
c_s	Interface Shear Compliance
k_s	Shear Stiffness
$p_{s,limit}$	Limiting Shear Stress
R	Constant
s	Constant
s	Laplacian Variable
ψ	Probability Density Function of Asperity Heights
p_m	Flow Stress
A	Surface Area
R_{MAC}	Macroscopic Constriction Resistance

R_G Gap Resistance
R_{mic} Microscopic Constriction Resistance
R_f Interstitial Fluid Resistance
$R_{t,mic}$ Total Microscopic Constriction Resistances
C Constant
K_h Harmonic Thermal Conductivity
H_B Brinell Hardness
L Length of Joint
ϕ Angle of Vector with z-axis
θ Angle of xy projection with x-axis
d Displacement Vector
f_n Normal Force
μ Co-Efficient of Friction
f_t Tangential Force
f_n Normal Force
R_{th} Thermal Resistance of Interface Element
$K_{e,th}$ Equivalent Conductivity of the Thermal Brick Contact Element
[k] Stiffness Matrix
E Modulus of Elasticity
G(r,s) Inverse Thermal Transfer Function
$H_T(r,s)$ Direct Thermal Transfer Function
I Imaginary Component of Complex Variable
$D(\beta)$ Oscillatory Part of Integrand
$D_a(\beta)$ Limit of Oscillatory Part of Integrand
$\bar{D}(\beta)$ Modified Oscillatory Part of Integrand
T Time Interval
S_k Cumulative Sum
S^a_k Euler Transform
G^p Proper Part of Transfer Function
A_j Magnitude of j^{th} Order Singularity
$u_s(t)$ Unit Step Function
$u_i(t)$ Unit Impulse Function
f_R Regularization Function
$T_R(r,t)$ Regularized Temperature Step Response
$H_R(r,t)$ Regularized Thermal Transfer Function
FF(s) Butterworth Filter Transfer Function
z Discrete Time Delay Operator
H_x Thermal Deflection x-deflection Transfer Function
H_y Thermal Deflection y-deflection Transfer Function
E_e^x Ratio Effective x-Deflection Delay and Thermal Time Constant
E_e^y Ratio Effective y-Deflection Delay and Thermal Time Constant
δT Temperature Deviation
q_t Heat Conduction Through Element

ΔT_{ss}	Steady-State Temperature Difference
T1	Temperature of Node 1
T2	Temperature of Node 2
q1	Heat Generation of Source 1
q2	Heat Generation of Source 2
N_x	Reference State-Variable Matrix
N_u	Reference Control Signal Matrix
Υ	Cost Function
Φ	Discrete Input State Matrix
Γ	Discrete System State Matrix
x	State Vector
H	Hamiltonian Matrix
δ^d	Disturbance Thermal Deflection
K_0	Controller Gain
V_s	Set Point Voltage
V_a	Feedback Voltage
V_c	Control Voltage
P_a	Actual Power Generation
u_{ff}	Feedforward Control Signal
u_{fb}	Feedback Control Signal

CHAPTER 1: INTRODUCTION

1.1 Objectives

A review of the research pertaining to thermally induced error in machine tools reveals that at the present time thermal deformation may contribute more than 50% of the machining error in high speed, high precision applications [1]. Since residual errors cannot be fully avoided at the design stage, compensation of the thermal deformation of machine tool structures emerges as a viable and practical solution. An industrial on-line correcting system for the thermal deformation of machine tools, guaranteeing residual errors of $< \pm 10$ μm is urgently needed but it does not exist today [2].

The objective of this thesis is to develop an on-line deflection control system that is capable of maintaining the structural thermal deflection of a machine tool within a range of 10 μm. The system must estimate the state of thermal deflection indirectly, using a small number of measured temperature points, and it must be able to accommodate the situation where the measured temperature points cannot be located on or very near to the sources of heat generation. In order to meet the 10 μm range objective on all machine tools, the system must also be able to predict and compensate for nonlinear joint effects, which have been shown to exist in a machine tool structure [3].

Although the nonlinear joint interaction problem has been studied by Attia [3], the quantitative effects are not as yet well understood. The second objective of this thesis is to study the problem of joint interaction by means of accurate finite-element modelling of the contact interface and how it interrelates with the temperature and stress distributions in the machine tool structure. A good understanding of the nature and of the effects of the contact problem is essential, particularly with regard to the conditions which would create and accentuate contact induced nonlinearity, and the effect that electric heater actuators might have on this. The second

part of this objective is to develop a generalized model which can be used in real-time to accurately predict joint induced deflection in a machine tool so that it may be compensated by the control system.

In order to gain a realistic impression of the measurement and power actuation problems that would be encountered on a real machine tool, the validation of the compensation system must be performed on a physical model of a machine tool structure. The measurement and actuation systems that will be used on the model should be identical to those which would be used on a real machine tool. The measurement and actuation hardware should be standard off the shelf equipment that will be chosen with economy as well as performance in mind.

1.2 The Control System Method of Compensating for Thermal Deflection

The method for dealing with thermal deflection that will be implemented in this thesis entails the identification and compensation of the thermal deflection by means of a control system. The simplest representation of a feedback control system is shown in figure 1.1. Apart from the physical system, there are three important operations involved in a feedback control system: (1) the measurement of the controlled variable δ, (2) the generation of a control signal u_c, and (3) the actuation of the compensation by means of a physical element. The choice of the best actuation element depends on the type of machine tool which is being considered. The position control system of an NC machine tool presents an attractive option to effect the desired compensation [4], but it may not be adequate to compensate for the bending mode of deformation, depending on the configuration of the machine. For non-NC machines there is no position controller to effect compensation so another actuation method must be employed. In this investigation, control systems based on two different types of actuation element shall be developed, using (1) the position controller of an NC machine tool, and (2) an array of artificial electric heaters that shall be attached to the surface of the structure to produce a controlled thermal deflection. The first actuation method is the most convenient and effective method for

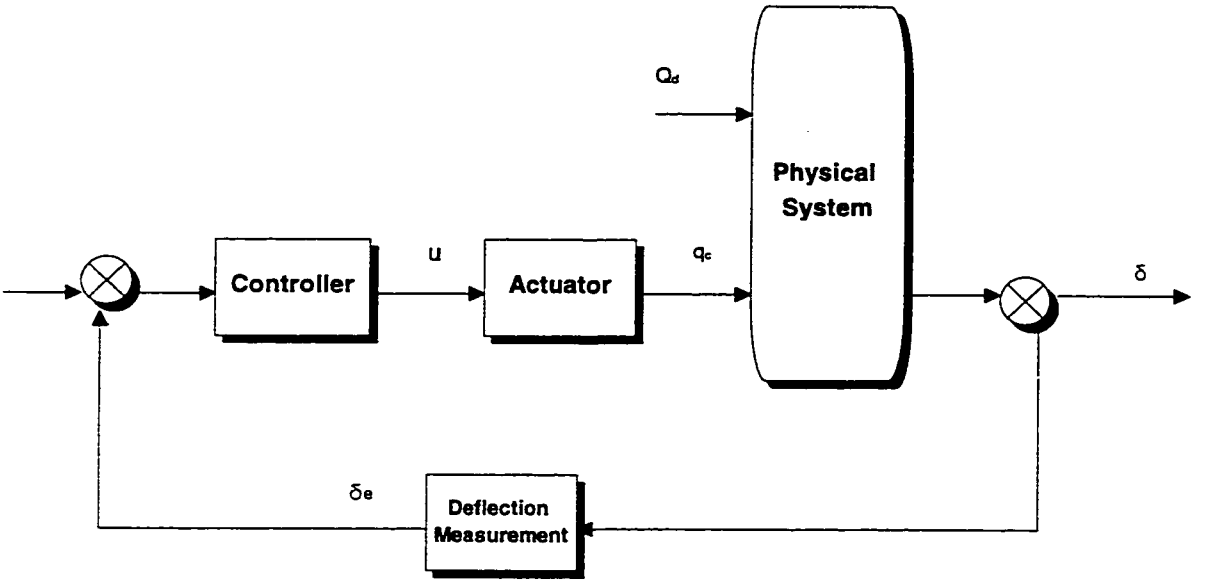

Figure 1.1: Block Diagram of Feedback Control System

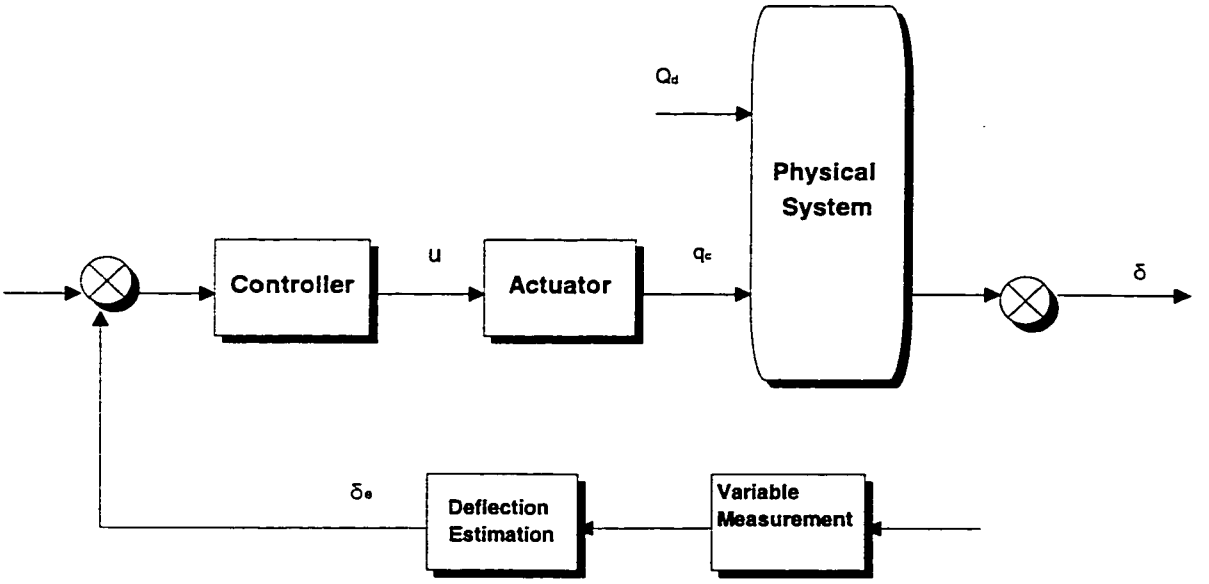

Figure 1.2: Block Diagram of Control System with Controlled Variable Estimation

NC machines with three axis position control. The second actuation method can be used to retrofit existing conventional machine tools and has been used by others [5] [6]. In general, an appropriate combination of these two actuation methods is adequate for most machine tools. This thesis will demonstrate both NC position control, and the possibility of using artificial heating elements as the sole means of effecting compensation, which represents the most severe test to the proposed control system in terms of the response time and dynamic characteristics.

1.3 Estimating the Thermal Deflection

The control system shown in figure 1.1 cannot be implemented in an industrial environment because it is not possible to directly measure the relative thermal displacement between the tool and workpiece $\delta(x,y,z,t)$ while the machine is in operation. Figure 1.2 shows that an additional element is required, which is a variable representing the estimated thermal deflection δ'. The implication of using an estimated controlled variable in the feedback is that the control system does not then form a closed loop. Any deviation in the estimated thermal deflection from the actual thermal deflection translates directly to a control system error, since the control system is not capable of minimizing this type of error. The main difficulty in implementing a successful control system in industrial environment is the process of estimating the thermal deflection accurately. The bulk of this thesis shall be concerned with the problem of estimating the thermal deflection in a real time environment.

The process of estimating the thermal deflection requires a process model relating the thermal deflection to another system variable that is more easily measured. The only variable that is really suitable for this purpose is the temperature distribution in the structure, or some part of it. The inadequacy of conventional process models for estimating the thermal deflection of the structure from discrete temperature measurement $T_j(x,y,z,t)$, $1<j<n$, is due to the fact that the models are either too complex and slow, or too simple and inaccurate. From the principles of thermoelasticity, one can argue that the thermal deformation of a structure is uniquely defined

by the whole temperature field T(x,y,z,t), and therefore, a subset of the information contained in $T_j(x,y,z,t)$ is not adequate. This fact has been emphasized by Spur et al [7]. and Weck et al. [8].

For a given thermal system, the complete temperature field T(x,y,z,t) and the heat input to the system $Q_d(t)$ are equivalent and are thermodynamically interchangeable. Therefore, the main thrust of the proposed approach is not to correlate thermal displacements to discrete temperature measurements, but to use the latter to estimate the heat input to the structure, and then proceed with the solution of the direct thermal and deformation problems. The mathematical sequence, as shown in Figure 1.3, involves the following three processes: First, solving the inverse heat conduction problem IHCP in which the heat input to the structure is determined in real-time from the measurement of temperature at points on the surface of the structure. Once the heat inputs have been identified, the thermal process model will then produce the entire temperature distribution, in effect filling in the gaps of the incomplete temperature measurements. Finally, the thermal deformation process model acts on the temperature distribution to estimate the components of the thermally-induced error vector δ.

The success of this modelling approach depends upon the accuracy and reliability of the process models in figure 1.3. Purely analytical models are not possible in a complicated machine structure, and purely empirical models also must be rejected because they are too inaccurate, even with an unmanageably large number of calibration parameters. Furthermore, it will be shown that for nonlinear machine tool systems the measurable system variables do not contain sufficient information to uniquely define the thermal deflection system, with the implication that the extrapolation of the calibration inputs is extremely unreliable. The approach that will be taken here is to develop a model that takes the approximate mathematical form of the solution and refines it by empirical calibration of the analytical parameters. Such a model is neither empirical nor analytical, but rather a hybrid between the two. The hybrid model is accurate

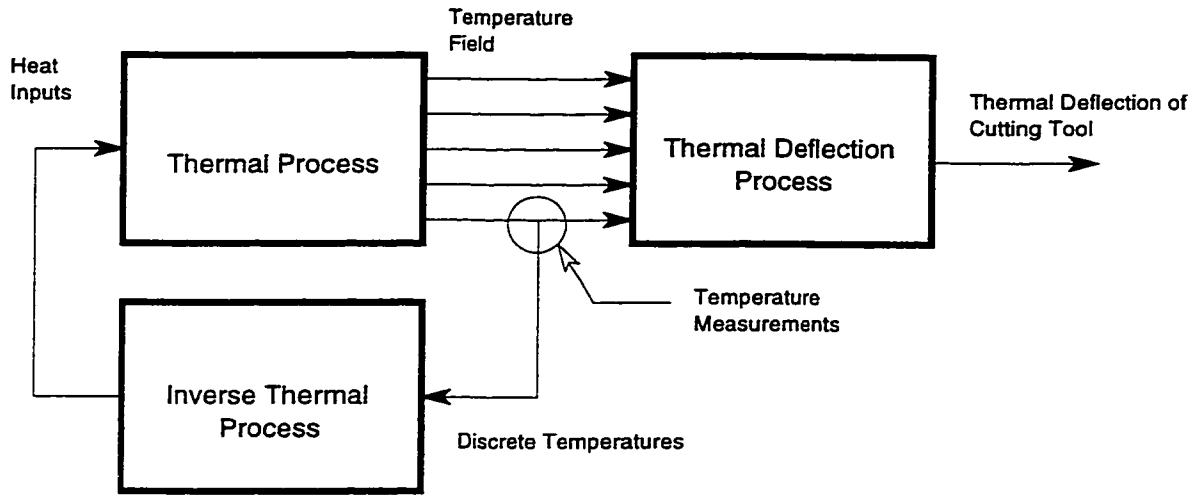

Figure 1.3: Correlation between the thermal loading, temperature field and thermal deformation of the structure

because it is calibrated from empirical data, however since its mathematical form simulates the real system, it is able to extrapolate the calibration inputs in ways not possible with an empirical model.

1.4 The Method of Solution for the Inverse Model

The block in figure 1.3 labelled 'inverse thermal model' defines the relationship between the measured temperatures and the heat generation. This is an inverse problem, as discussed in chapter 2, and so it suffers from three special problems of (1) the difficulty of expressing the solution in explicit form, (2) non-uniqueness of the solution, and (3) instability. The third special problem is inherent to the nature of the system and so it must be dealt with by the regularization of the model. The first two special problems are not inherent to the system, and so can be avoided by the type of solution method. For linear systems, the first two special problems can be avoided by a solution method based on the Laplace transform. The method of deriving the solution is as follows: (1) transform the model of the temperature step response to the Laplace domain, (2) Determine the direct transfer function in the Laplace domain by dividing the transformed step response by the Laplace transform of the step input, (3) determine the inverse transfer function by taking the reciprocal of the direct transfer function, and (4) transform the inverse transfer function to the time domain. The solution is then obtained by a convolution of the measured temperature corresponding to an arbitrary heat input with the inverse transfer function in the time domain. It will be shown that even nonlinear machine tool systems can be dealt with by a variation of this procedure, by taking advantage of the linearity of the thermal aspects of the system.

1.5 Overview of the Thesis

Chapter 2 contains a literature review of the present state of the art in the fields of thermal deflection modelling and estimation, real-time identification of structural heat generation, control of thermal deflection, and small temperature measurement. The methods and

conclusions from each of these reviews will be significant for the development of the thermal deflection control system which will be built upon in subsequent chapters.

The original work of this thesis begins in chapter 3 with a thorough development and evaluation of a hybrid form of modelling which shall be called the *Fundamental Generalized Method*. The objective of the chapter is to introduce the concept, develop the thermal model of a machine tool structure, and demonstrate the capabilities of this form of modelling of a machine structure. Particular attention shall be given to investigating the accuracy of the representation and the ability of the model to extrapolate limited calibration data by emulating the mathematical behaviour of the real system. The physical systems which will be presented in the chapter are for the purpose of verification only and will not be used in the subsequent chapters.

In chapter 4 two models shall be developed for the purpose of verification of the methods that will be developed in subsequent chapters. The first of these models is a physical structure which shall be designed to simulate the thermal deflection behaviour of a real machine tool in operation. This model will not contain any joint nonlinearity, and will be used to verify the method of controlling thermal deflection for a machine tool with negligible joint nonlinearity. The second model that will be developed is a finite-element model of a machine tool structure which exhibits a considerable nonlinear effect due to the nonlinear joint interaction. Considerable attention will be given to the problem of modelling the contact interface from a thermal and mechanical stress perspective.

In chapter 5, the mathematical solution to the inverse problem of estimating heat generation from discrete temperature measurements will be derived, accommodating the situation where the measured points are located relatively far from the source of heat generation. The methods that shall be employed include the analytical transformation of the direct thermal

model to the Laplace domain, the manipulation of the inverse transfer function in the Laplace domain, and the numerical transformation of the inverse transfer function to the time domain. The procedure for using the inverse transfer function to estimate the heat generation in real time will also be developed.

In chapter 6 the complete algorithm for estimating the thermal deflection of a linear machine tool structure will be developed. The algorithm will also be implemented on the linear machine tool model that was derived in chapter 4, and the performance of the system will be investigated.

In chapter 7, a new concept will be developed for estimating the thermal deflection in a machine tool with considerable joint nonlinearity and will be implemented on the nonlinear machine tool model that was derived in chapter 4. The model of the nonlinear contact joint will be derived using the generalized modelling approach.

In chapter 8 a combinational feedforward/feedback control system for minimizing thermal deflection will be developed and tested for both the linear and nonlinear systems. Two methods of control actuation shall be investigated, which are NC position control and artificial electric heater compensation. The possibility of using electric heater compensation alone shall be investigated, which represents the most severe test in terms of response time and dynamic characteristics.

CHAPTER 2: LITERATURE REVIEW

2.1 Introduction

This chapter begins with a brief discussion of the sources of inaccuracy in machine tools, and the relative significance of thermal deflection error. This is followed by a discussion of the design procedures which have been shown to improve the thermal stability of the machine tools, and the residual thermal error that cannot be reduced further at the design stage. The state of the current research into measurement and real-time compensation of thermal deflection error is then reviewed, focusing primarily on the issue of real-time modelling for estimating the thermal deflection error while the machine tool is in operation. The method of *generalized modelling* for maximizing the accuracy and numerical efficiency of the real-time estimation process will be reviewed, followed by a review of the inverse heat conduction problem (IHCP), which forms an integral part of the generalized modelling approach. The chapter will conclude with a review of compensation mechanisms and the control system architecture that is appropriate for the micro-position compensation of thermal error in machine tools.

2.2 Accuracy in Machine Tools

2.2.1 The Sources of Inaccuracy

The accuracy of a machine tool is described by its ability to correctly position a cutting tool relative to the work piece, and maintain the correct position during the cutting operation. The sources of inaccuracy derive from i) structural imperfections, ii) measurement effects, iii) mechanical effects, and iv) thermal effects:

i) Structural imperfections include deviations in the uniformity of guide ways, and the imperfect alignment of the spindles, chucks, and bearings. This is often called kinematic inaccuracy, because it derives from positioning errors that occur in the absence of any thermal or mechanical loading. The accuracy of the machining can be no greater than the accuracy of the machine itself, so much depends on the production capability of the manufacturer.

ii) Measurement effects are the uncertainty in the measured positions of the cutting tool and workpiece. The accuracy of the machine is limited by the ability of the operator to correctly position the cutting tool. This is especially true for numerically controlled machine tools, where the cutting path is programmed from a computer model, and the tool is positioned automatically with respect to a reference point.

iii) Mechanical effects include the static and dynamic compliance of the machine structure and cutting tool, and the wear of the cutting tool. Mechanical effects have received a considerable amount of attention over the past twenty years, as industry has demanded greater and greater accuracy from the machine tools.

iv) Thermal effects are the changes in the relative position between the cutting tool and work piece that derive from the thermal loading of the machine tool. Thermal effects are an inevitable consequence of the machining process because of the thermal loading and large physical dimensions of the structure. The sources of thermal loading include changes in the ambient temperature, and steady and quasi-static temperature gradients due to internal sources of heat generation. In contrast to the problem of mechanical loading, thermal loading has not been extensively studied, for a number of reasons, primarily [8] :

- A general lack of interest due to inadequate understanding of the problem by the general user.
- The need for no load tests.
- The need for a described 'duty cycle' appropriate to each test.
- The requirement for instrumentation not normally found on the shop floor.

Only one part of the inaccuracy problem will be dealt with in this thesis, which is the deformation due to the thermal loading of the machine tool.

2.2.2 The Sources and Nature of the Thermal Deflection Error

There are two principal sources of thermal deflection error: uniform changes in the ambient temperature, and temperature gradients from internal sources of heat generation. There

are three predominant places where the deformation occurs: the structural frame of the machine tool, the cutting tool, and the workpiece. The deformation of the cutting tool and the work piece is due to the high intensity heat generation at the tip of the cutting tool, and from the chips and cutting fluid [9]. The deformation of the structure is primarily due to internal sources of heat generation, such as bearings, motor, and gearbox [10]. Changes in the ambient temperature can also have a strong effect on structural thermal deformation, but environmental conditions are relatively easier to control by air conditioning or air showering, sometimes within a sealed cubicle [11].

2.2.3 The Relative Significance of Thermal Deformation

The significance of thermal deformation as compared to other sources of inaccuracy depends on a number of factors, including the size of the machine tool and the work piece, and the co-efficients of thermal expansion. From an examination of available test data, Attia [12] was unable to find any conventional machine tool with a coefficient of expansion of less than 0.01 mm/m for a temperature change of $\pm 1\,^{\circ}C$. Thus, thermal deformation can be a significant problem even in relatively small machine tools, and it is usually a very serious problem in large machine tools [13].

Opitz (cited in [14]) states that the errors caused by thermal deformations have, in many cases, the same order of magnitude or higher than the errors due to kinematic inaccuracy and the static and dynamic compliance. Mottu [15] states that from his experience, 50 to 60% of the errors in precision parts result from thermal errors. As a rule of thumb, Weck (cited in [14]) stated that thermal effects in steel parts become significant at a tolerance of about 2.5 μm. For pieces over 25 cm long the threshold is about 25 μm, and for aluminum pieces it can be as high as 125 μm. Weck is referring to the problem of thermal deformation of the workpiece, but in most conventional operations the structural deformation of the machine tool is a greater source

of thermal error. For most machine tools of conventional size, thermal deformation is a significant source of error for tolerances below 10 μm [14].

The area of machining where thermal error is a principal concern even for normal tolerances is in automated and NC machine tools. From a historical perspective it has been the human machine tool operator that has been the principal mechanism for controlling thermal deformation [15]. It is common practice for operators to leave a machine running overnight or even for days at a time so that it will be 'warmed up', which has the effect of reducing the thermal error from load-independent heat sources [16]. In an automated machining environment the machine operator is often not as experienced and does not have as much time to devote to any one machine tool. For one normal sized drill press machine, the thermal deflection displacement between the cold start and warmed up condition was found to be in excess of 120 μm, and even more deflection would be expected from a larger machine of the same design.

2.3 Reducing the Thermally Induced Error at the Design Stage

The internal heat sources of a machine tool are the various elements of the drive and power transmission system, including motors, gears, bearings, pumps, hydraulic oil, and the machining process itself. It has been indicated in [16] that 60% of the power input to a machine tool is dissipated in the drive and power transmission system, inducing machining error by the thermal deformation of the structural frame. The remaining 40% finds its way into the cutting tool and work piece, and into the chips and cutting fluid. The local deformation of the cutting tool is higher than the deformation of the frame because of the extremely high temperature of the cutting tool, but the total deformation is usually less because of the small dimensions [9]. Much of the heat from the cutting process flows back into the structural frame of the machine tool, resulting in additional deformation of the structure.

Much of the thermally induced deformation can be eliminated at the design stage, by methods as simple as proper chip disposal, and cooling the cutting fluid [14]. Other techniques include:

-External location of the major heat sources, like the motor and bearings [17].
-The utilization of thermal symmetry, so that the thermal deformation is symmetric about some point or axis, and the net deflection of the point or axis is zero [18].
-The appropriate positioning and attachment of heat sources, so that the deformation in critical directions is minimized [19] [20].
-The use of structural materials which are capable of rapid and uniform distribution of heat to minimize temperature gradients.
-Using insulation to control the flow of heat, and direct it away from critical areas [21].
-Direct temperature control of the structure by a shower or bath of cooling fluid [22] [23].

Although the problem of thermally induced error can be reduced at the design stage, it is inevitable that there will be some residual thermal error because of the sources of heat generation external to the machine structure [12]. Compensation of the thermal deformation of machine tool structures emerges, therefore, as a viable and practical solution. An industrial on-line correcting system for the thermal deformation of machine tools, guaranteeing residual errors of $< \pm 10$ μm is urgently needed but it does not exist today [2].

2.4 Measurement and Compensation in Real Time

2.4.1 Direct Measurement

One of the main problems with implementing real-time control systems to regulate thermal deformation of the machine tools is the difficulty of measuring the relative thermal displacement vector [δ] between the tool and the workpiece during machining [12] [24] [25]. Tonshoff et al. [25] studied the problem of direct deflection measurement. They looked at a

number of displacement sensors with a resolution less than 1 μm, including touching gauge fingers (resolution 0.5 μm), and non-touching optical sensors (resolution 1 μm). The sensors were applied directly to the machine tool, and used to intermittently sample the relative deflection between the cutting tool and work piece.

Direct measurement establishes the real position of the tool. This allows for the compensation of all sources of inaccuracy, whether or not they are thermally induced. It also eliminates the need to model the structure, as is required for indirect measurement. The disadvantage of direct measurement is that the delicate sensors are easily damaged during the operation of the tool. Also, their presence is intrusive, interfering with the smooth operation of the machine tool. Finally, the presence of chips and cutting fluid in the working environment makes the readings unreliable, especially for optical type sensors. After thoroughly studying the problem, Tonshoff concludes that "The direct and continuous detection of thermally induced displacements in most machine tools is not possible, because direct working sensors cannot be used during the machining process". Tonshoff et al. [25] tested another direct measurement technique using integrating expansion sensors. The sensors are placed at strategic locations on the machine tool structure between the machining table and the cutting tool. The sensors are tightly fixed to the machine structure, and directly measure the thermal expansion. The expansion is integrated in a line from the work to the tool, giving a direct estimation of the thermal deflection in the structure. The weakness in this method is the relatively low resolution of the expansion sensors.

2.4.2 Indirect Measurement

Because of the difficulties associated with direct measurement, most compensation schemes utilize an alternate physical property to indirectly measure the thermal deflection, namely, displacement [25] [26] [27] [28] and temperature [8] [29] [30] [31], that are easily measured at some points on the structure. For the case of displacement measured systems, the

displacement measurement was used to drive error maps, that were collected off-line [5] [25][27][28] [32] For temperature measured systems the relationship between the measured temperature and the thermal deflection is not so easily defined. Sartori, Balsamo, and Marques [33] use a thermal deflection model that divides the structure into a number of simpler components, and use a combination of finite-element equations and polynomial curve-fitting to represent the components. The model expresses the structural thermal deformation as a function of the temperature distribution. The measurement scheme requires more than 100 thermocouples, and the thermal model consists of some 1400 equations. The authors believe that the large number of thermocouples is a minor problem, because of the low cost of sensors and data acquisition cards. The results showed that 80 to 85 % of the deformation could be explained by the model. The obvious problem with this method is the large number of thermocouples and the complexity of the deflection model. Many of the thermocouples are located in difficult positions, around internal bearings and spindles, and the positioning must be accurate if the model is to yield good results.

In order to avoid the problems associated with exact modelling of the machine tool structure, some researchers have attempted to define an empirical relationship between the thermal deflection and a smaller number of measured temperature points, using an empirical model in the form of a calibrated polynomial expression [8] [34] [35] [36] Chiappulini et al. [2] use five measured temperatures at five points on the structure, one close to each of the major internal sources of heat in the machine tool. The transfer function relating the measured temperatures to the thermal deformation is based on a polynomial equation, where the empirical parameters are found by optimizing the fit between the empirical model and the response of the test structure for a variety of operating conditions. The displacement response of the structure was measured by three displacement transducers mounted on the mandrill nose of the test milling machine. Ichimya et al. [37] used an empirical transfer function to relate discrete temperatures to the thermal deformation of a milling machine structure. The empirical constants

are determined separately for each input load condition, so the parameters must be changed each time the loading conditions change. With a continuously variable load, the accuracy of the results deteriorates rapidly.

The principal reason why methods of measurement and compensation have not yet led to an acceptable solution to the problem is that the process models which have been developed thus far are not adequate for estimating thermal deflection in a real time environment [2]. The simple polynomial expressions that are most often used to relate discrete temperature measurements to thermal deflection [34][35][37] [38] are not accurate enough, and are unreliable for untested inputs. While the accuracy of the models is essential to the performance of the control system, the effect of a long processing time can be equally detrimental. When the controller cycling period is large, a lot of uncompensated deformation occurs between changes in the controller output, and the control system is always behind the present state of deformation. The complex empirical process models used by Balsamo [33] to compensate for the thermal deformation of the CMM structure introduced a 5-10 minute delay into the control cycle. Despite the accuracy of the model, the low sampling frequency of the control system prevents its use in machine tools.

Recently, an empirically-based modelling approach was used to define a multiple variable thermal error model and to integrate it in a single volumetric error function [29] [39]. To modify the coefficients of the error model periodically, an adaptive methodology [26][32] and artificial neural networks [1][25] are used. The inherent weakness of the indirect measurement approach stems from the fact that the empirical base function bears no physical similarity to the actual phenomena. This makes the solution unreliable outside of the range of tested inputs. In addition, the information contained in the discrete measurements is incomplete [8][19], and therefore the problem is not uniquely defined. To capture the appropriate temperature sensor locations, and thus improving the accuracy of predictions, as many as 100

temperature sensors were used, resulting in a very slow control cycle of the order of 5-10 minutes [33].

Recently, Mou et al. [26][32] [40] developed an adaptive methodology to modify the error model coefficients periodically. Although this technology is being used by the US automotive industry, there are a number of issues that need to be resolved; the economical aspect of applying thermal mapping and compensation algorithms in a shop environment, as well as the generalization of this approach and the resulting software package to all classes of machine tools [41]. Artificial neural network models were also used [42] [43] [44] to identify and to update periodically the coefficients of the process model. Indirect displacement measurements at some locations on the structure have also been used to generate off-line error maps [5][12][25][27][28]. Ferreira, and Liu [27] estimated the parameters in the geometric error model as functions of the thermal state and history of those localized regions. The limited repeatability of the probes and the time needed to collect sufficient data may present a serious challenge for industrial implementation of this system.

2.4.3 Numerical Approaches to Estimating the Thermal Deflection

Finite difference and finite element models have been used for real-time estimation of the temperature field in the structure, and thus to fully describe the state of the system [30] [45] [46]. This approach has a number of drawbacks as well. First, the magnitudes of the internal heat sources were predetermined from off-line calibrations, and thus leading to erroneous predictions. Second, numerical models are either too simple and inaccurate or too complex and slow to be used in real-time control applications. Some efforts were made to compromise between the conflicting requirements of speed and accuracy of predictions. This was achieved either by using the temperature field only as the feedback signal to the control system [30] or by considering the problem to be two-dimensional and analysing the thermoelastic behaviour of a single component of the structure [45]. Obviously, the reliability of these solutions is also

compromised in this process, and the approach cannot be generalized or extended to all machine tool types and structures.

2.4.4 The Generalized Modelling Approach and the IHCP

In response to the problems associated with both the empirical and numerical approaches, the author of this thesis and Attia have recently proposed a new control system [47], which is based on the following two principles. First, the complete temperature field and the heat input $q_d(t)$ to a given system are thermodynamically equivalent and interchangeable. Therefore, instead of correlating [δ] to discrete temperature measurements, the temperature difference between two points located near the heat source $\Delta T(t)$ is used to estimate the heat input to the structure (as an inverse heat conduction problem IHCP), and then proceed with the solution of the direct thermal and deformation problems. This approach solves the problem of non-uniqueness resulting from using incomplete measurement information. Second, by following the generalized modelling method [47], the analytical description of the thermal and deformation processes are established and used to construct simple dynamic models that are calibrated from the step response of the real structure [6]. The generalized modelling method is based on a semi-empirical modelling approach, and has been used to predict the temperature field in a machine tool structure. This method is more accurate and reliable than conventional empirical methods, and preserves the approximate mathematical form of the solution by pre-defining a mathematical base expression through an analytical solution to a simplified model. This method was extensively tested using finite-element computer simulation models of complicated machine tool structures, and it was shown to reproduce the accuracy of a finite-element model but two orders of magnitude faster.

A number of problems are solved by adopting this methodology. First, the empirical calibration is limited to finding the constants in a physically meaningful base function, thus improving the accuracy of the prediction for the full range of operation. Second, the thermal

transfer function can be inversed to determine the heat input to the structure in real time [48]. without resorting to off-line calibration. With the s-domain representation of the dynamic models of the thermal and deformation processes, the design and performance of the control system can be optimized in terms of its transient response, stability and steady state errors. In addition, this approach ensures that the requirements of accuracy, stability, and computational efficiency of the IHCP solution and control algorithms are not in conflict, and can be achieved simultaneously. The other main advantage of this methodology is that the formulation of the problem given in [6][48] is generalized in such a way that it can directly be applied to any machine tool structure without further analytical development or modelling by the end user. The need of the industry to have a generalized approach and software compensation package that can be applied to all classes of machine tools has been recognized for some time [41].

The major potential weakness of this approach is that it is based on the assumption of linear thermal and thermal deformation systems in a machine tool structure. It has been shown that a machine tool structure can exhibit significant nonlinear thermal deformation behaviour because of the contact joint phenomenon [3]. The nonlinearity derives from a variable contact resistance of surface contact joints, where the contact resistance is related to the contact pressure distribution in the joint. Thus, variations in the mechanical loading of the structure create changes in the contact resistance which in turn affect the temperature distribution and the thermal deformation. Since thermal loading can itself produce significant contact stress, the thermal and thermal deformation systems are coupled, and a thermal input by itself can exhibit a nonlinear thermal deformation response. Although the reported accuracy of the deflection estimation using this approach was high, the verification was done on a linear finite-element model of a single component machine structure. No investigation of how the nonlinearity of a real, multi-component machine tool would affect these results has yet been published by the authors.

To obtain acceptable levels of stability, accuracy and dynamic performance, an inverse heat conduction solver is incorporated in the control system in reference [47] to estimate the heat input q(t) to the structure in real time. A critical review of the available inverse heat conduction problem IHCP solutions shall now be presented, with a special emphasis placed on applications involving real-time execution and multi-dimensional structures.

2.5 The Inverse Heat Conduction Problem

2.5.1 The Nature of the IHCP

When the heat input to a system is estimated from the temperature measurement at some points distant from the source, this is known as an inverse heat conduction problem IHCP. The IHCP is an ill-posed problem due to the nature of the input function (the measured temperatures), which is *discrete* in time, *lagged*, and *damped* and contains *random errors*. As a result, the solution of the IHCP is characterized by its *instability* and *non-uniqueness* [49] [50]. To solve practical IHCP's, finite difference, finite element and boundary element methods are used [51] [52] [53] [54]. The techniques used to stabilize inverse analyses can be classified into three main categories; function specifications, regularization, and space marching methods.

2.5.2 Available Solutions

In the *function specification methods FSM*, the final form of the heat flux variation with time, q(t), is assumed. The unknown parameters in the assumed form are estimated by forcing the inverse solution to agree with the measured temperatures in a least square sense. If exact matching between the measured and estimated temperatures is sought, the solver will have no capability to control the inherent instability of the problem [51]. To overcome the instability and non-uniqueness problems, the system of equations is rendered 'over-determined' by either using more sensor locations (spatial smoothing) or incorporating additional future measurements (temporal smoothing). The second approach, which produces better results, was proposed by

Beck in the form of a sequential FS solution [55]. Future time temperatures were also used by others, e.g., [56] [57].

Regularization methods RM developed by Miller et al. [58], Tikhanov et al. [59], and Alifanov et al. [60] were introduced to reduce excursions in the unknown function, q(t), by adding regularization coefficients to the least squares criterion. Another useful regularization method is the iterative regularization *IR* [61], which uses two solutions besides the direct problem; the sensitivity, the adjoint problems. Regularization methods are based on a whole-domain analysis, in which all the heat flux components are simultaneously estimated for all times and positions. The exception to that are the mollification method [62], which is formulated in a sequential form, and Beck et al.'s procedure [63], which combines the sequential features of the FSM and the special function that is minimized in the regularization method. In comparison with sequential algorithms, regularization methods require large storage capacity and computation time, but they are less sensitive to measurement random errors [64]. Unfortunately, in both global and sequential procedures, greater stability is only achieved with a loss of accuracy [65]. Also, the two requirements of unbiased and minimum variance heat flux estimates cannot be satisfied simultaneously, since they are interrelated [49]. The selection of the optimum value of the regularization parameter, or the number of future times in the FSM, presents an area of great difficulty, since it depends on a global bound factor, which is unknown in advance [63].

The *space marching method SMM* is similar to the finite difference method, but instead of solving explicitly for the temperature distribution from known boundary conditions, it works by extrapolating interior temperature data to the boundary. This method is difficult to apply to multi-dimensional problems, and requires a large number of well-positioned temperature sensors in order to be accurate. Various versions of this method include the work published in [55] [66]. Other general procedures for solving the IHCP include Hills et al.'s method [67],

the integral method [68], the neural network and expert system approaches [69], and Monte Carlo method [70].

2.5.3 Solution of the IHCP for Real-time Feedback Control Applications

To integrate an IHCP solution algorithm in a real-time control system, the following requirements must be satisfied: stability of the solution *without future data*, computational efficiency, accuracy, and the possibility of representing the solution in the s-domain for design of the control system.

The stability of the IHCP solution presents a dilemma. On the one hand, the un-regularized method is fast but inherently unstable [51]. On the other hand, methods which provide acceptable level of stability require either partial (as in FSM) or full (as in regularization and Monte Carlo methods) future information, which are not available in real-time control environment. As pointed out by Hensel [50], a real-time state inverse estimator will be noncausal by design if it uses future time data. When a multi-dimensional IHCP is solved, the computation time becomes unacceptably large for real-time applications. The computationally efficient method of Monte Carlo, for example, requires approximately 30 minutes, on a 486-25 PC processor to solve an IHCP involving a simple cylinder with six embedded sensors [70]. The accuracy of the IHCP solution is another important factor, since the prediction will be used to generate the feedback control signal to the controller. Relative errors of more than 50% have been reported in various IHCP solution schemes [71] [72].

From the analysis presented above, it is evident that available IHCP solutions were not motivated by applications involving multi-dimensional structures and real-time execution. These limitations were recognized by Hensel [50], who recommended future work to develop algorithms that can be applied in real-time for feedback control applications. The need for better

techniques and new algorithms to solve effectively complex multi-dimensional IHCP's and to include heuristic information in the type of inverse analyses has also been recognized [50].

2.5.4 The Convolution Integral Approach

In response to these problems, a new method has been developed by the Author and Attia to estimate the transient heat input to machine tool structures in real time [48]. The method is based on the convolution integral approach using the generalized inverse thermal transfer function $G^{-1}(s)$. An expression for $G^{-1}(s)$ has been developed to describe the thermal response behaviour of machine tool structures. The mathematical form of $G^{-1}(s)$ was determined from an analytical solution to the linear heat conduction equation with appropriate boundary conditions. The calibration of the model was done using the temperature time response for a step input in heat generation. The singularity functions in $G^{-1}(s)$ were identified and an analytical solution of its inverse Laplace transformation was derived. The analytical part of the transfer function $G^{-1}(s)$ was transformed using numerical transformation techniques that were developed by the authors specifically for this application. The convolution integral of $G^{-1}(s)$ which defines the solution to the IHCP is computed numerically in real time. Computer-simulated test cases were presented to demonstrate the proposed method, incorporating simulated discontinuities and random errors in the discrete measured temperatures. The results showed that the computational time has been improved by one to two orders of magnitude over available methods to achieve a control cycle of less than 1 second, without compromising the accuracy and stability requirements. The authors concluded that the performance could not have been achieved using any of the other available inverse analysis solutions.

The principal weakness of the convolution approach proposed in [48] is that the mathematical form of the generalized temperature model which defines the inverse transfer function solution cannot accommodate an initial delay to a step response in heat generation,

where such a delay is inherent to all thermal systems. By defining the mathematical form of the generalized model without an initial delay, the inverse transfer function $G^{-1}(s)$ is stable and well-posed in its mathematical form. The authors admit however, that for measured temperatures located relatively far from the heat source, the discrepancy between the mathematical forms of the model and the real system becomes significant. Thus, the reported accuracy of this method may only be achieved if the measured temperatures on the machine structure can be located relatively close to the source of the heat generation.

2.4.5 Measurement of Small temperatures

The method of estimating thermal deflection from temperature measurements requires an accurate temperature measurement probe, and digital acquisition equipment. The accuracy and repeatability that is required of the temperature measurement apparatus depends on such factors as the range of the measured temperature, and the sensitivity of the estimation algorithm to random and systematic temperature measurement error. Since it will become necessary to measure small temperatures for estimating the thermal deflection of the machine tool structure, available methods of temperature measurement shall now be reviewed.

There are three types of temperature measurement device that are suitable for real-time control: Thermocouples, RTDs, and thermistors. Thermocouples are characterized by a very large operating temperature range and good thermal stability over time, however the accuracy and repeatability are normally larger than 1.0 °C unless very special precautions are taken [73]. RTDs are characterized by a generally lower operating temperature range than thermocouples, but with easily obtainable accuracy and repeatability better than 0.01 °C [73]. The obtainable repeatability of RTDs has been reported below 0.001°C without particularly expensive instrumentation, although the accuracy can only approach the repeatability when precision calibration equipment is available [74]. Thermistor type devices are characterized by a very low operating temperature less than 250 °C, and by a highly nonlinear behaviour. The temperature

range is not a negative factor for temperature measurement on a machine tool structure since the surface temperature should never exceed 100 °C. The nonlinear behaviour of the probe is not a disadvantage either when the raw data can be processed in real time by a digital computer that has been programmed with the calibration curve.

For the measurement of temperature below 150 °C, thermistor probes are characterized by extremely high accuracy and repeatability. Thermistor based thermometers with a standard deviation of 14 μ°C accuracy have been reported in the literature [75]. More recently, a thermistor based thermometer with an accuracy of 2 μ°C at room temperature was reported [76]. The main practical considerations for such a precise measurement are the Johnson noise, caused by random activity at the molecular level, and resistance changes in the leads and wires connecting the thermistor probe to the source of data acquisition. For less precise applications, accuracy and repeatability better than 0.01 °C can be achieved easily using standard off the shelf thermistors [77]. Although the standard thermistors have a hysteresis repeatability less than 100 μ°C, there is a tendency for them to drift when operated at elevated temperatures for a period of months or years[73]. For off the shelf thermistors and ordinary applications, the accuracy and repeatability will most often be governed by the accuracy of the data acquisition system, rather than by the thermistor itself.

2.6 Actuation Mechanism for the Compensation of Thermal Deflection

Assuming that an accurate method of estimating the thermal deflection is available, there still remains the problem of actuating compensation in real time. Position control systems of NC machine tools [2][30] [78], micro-positioning piezoelectric actuator attached to the tool post [45], and artificial electric heaters [4][5][7][31] have been used to compensate for the thermal deformation of machine tool structures. Although the NC controller is an attractive option to effect the desired compensation, it may not be adequate to compensate for the bending mode of deformation, especially when the degrees of freedom available to the cutting tool and

workpiece cannot accommodate this effect, e.g., turning processes. The addition of piezoelectric actuators offers micro-position control of the non-NC axes, however the process is expensive, it suffers from a limited stroke, and it introduces additional mechanical compliance into the machine tool structure.

In reference [79], artificial heating elements attached to the surface of the structure were used by the author and Attia as the actuation mechanism of the simulated control system. In the simulated test cases, the authors demonstrated that electric heating elements could be used effectively to compensate for thermal deflection in a multiple-axis coupled environment, as would be expected in a real machine structure. The advantage of this type of actuation is that it provides an economical solution for retrofitting existing conventional machine tools. It can also be combined with numerical position controllers for NC machine tools. The disadvantage is that the dynamics of the actuators introduce additional displacement error. Furthermore, the authors did not deal with the problems of actuator saturation and actuator control in a real time environment on a physical structure. In the simulated test cases the power required and the power delivered were assumed to be equal.

2.7 The Control System Strategy

In general, a machine tool requires a three-axis position control system for the three co-ordinate displacement axes. In the case of NC or piezoelectric position actuation there is no coupling between axes and so the control system may be broken down into three independent controllers. The use of heating elements as an actuation mechanism presents a more difficult control system design problem for the following reasons:

i- It provides a one-directional actuation (only heating, with no cooling capacity).

ii- It has a low speed of response, in comparison with NC controllers, due to large time constant.

iii- Strong coupledness of various control heaters is inevitable.

The axes are coupled because it is generally not possible to position a heater such that it produces deflection along only one co-ordinate axis. The strategy of the authors in reference [79] was to position the heaters such that each one produces positive or negative deflection principally on one co-ordinate axis. The fact that the heaters produce positive heating only means that the control system will be inherently nonlinear. The nonlinearity is aggravated further because there is always a maximum heating capacity which can produce saturation effects. The effect of the large time constant that is associated with heater actuators is to reduce the bandwidth of the closed loop feedback system, which has the effect of reducing the tracking accuracy of the control system.

The control system that was used in reference [79] is based on PID compensation of each axis with constant feedforward elements. Although this system was shown to give acceptable results for the simulated test cases, the control system parameters were not optimized for any particular operating conditions, and the design was done largely by trial and error. Furthermore, there was no provision to minimize actuation error, and the design did not take advantage of the more powerful state feedback architecture.

CHAPTER 3: THE CONCEPT OF GENERALIZED MODELLING

3.1 Introduction

This chapter begins with a discussion of the theoretical foundation of the generalized modelling concept, which combines an analytical model of the system with empirical calibration. An analytical expression which is suitable for modelling the temperature distribution in a three dimensional machine tool structure will be presented, and calibrated for a finite-element model of a large machine structure. The performance of the generalized model for predicting the temperature distribution in the finite-element model will be investigated, using experimental data obtained from various thermal inputs to the system model. The validation procedure will demonstrate the inherent strengths and weaknesses of the generalized modelling concept, as applied to a thermal model of a machine structure.

3.2 The Types of Process Models

The three basic types of process modelling are (a) analytical, (b) numerical, and (c) empirical models. Analytical solutions to the thermal deformation problem of real machine tool structures, which are characterized by their complicated geometry, as well as the position- and time-dependence of thermal loading and boundary conditions, are not readily available. Numerical models such as finite-element and finite-difference are generally too slow for real-time applications. Therefore, dynamic models based on empirical calibration seem to be the most appropriate approach to the problem under consideration. However, because of the stringent requirements of accuracy and speed from the process models, the simple polynomial empirical models which have previously been tested by Spur et al. [37], Ichimaya [34][35] [80] and others are too simple and inaccurate to be effective. Their inherent weaknesses can be attributed to the fact that the empirical base function bears no physical similarity to the actual mathematical form of the solution. This makes the solution unreliable outside of the range of tested inputs, and a large amount of test data is needed to calibrate the model. Moreover, the

solution does not reveal the internal relationship and interactions between the process variables.

3.3 The Fundamental Generalized Solution

It is evident that the accuracy of an empirical model of a real dynamic process can be improved significantly by paying careful attention to the selection of the base function. A complex process that has no analytical description, can adequately be approximated by the analytical solution to a similar, but yet simpler, phenomenon which is physically related. The solution to the latter problem will be referred to as the *fundamental generalized solution FGS,* which was first proposed by the author in {86}. By examining the structure of this analytical solution, *FGS*, it is possible to identify the mathematical features of and attributes of the real process and to construct a physically meaningful empirical model by grouping the analytical parameters into empirical constants. In this process, the analytical parameters will lose their strict physical significance that they held in the analytical model.

With the satisfaction of the mathematical similarity between the real process and the empirical model, one obtains a more accurate solution with less calibration data and fewer empirical parameters. Furthermore, the calibrated model is more reliable with untested inputs and it can even be used reliably to extrapolate data, since it forces the data to conform to the same mathematical form as the real process. For on-line modelling and control of the thermal deformation process in machine tool structures, the identification of the mathematical relationship between the process parameters ensures the stability of the solution of the IHCP and allows the control system to be optimally designed to take advantage of the physical dynamics of the process.

The theoretical foundation for the premise that problems which are physically related tend to be mathematically related as well, on which the *generalized modelling* concept is based, can be established from the observations made by Boussinesq [81], and Kondratiev [82]. They

showed that the solutions of the heat conduction equation for bodies of different geometries and different boundary conditions are mathematically similar in their structure, which takes the form of the sum of infinite series whose terms are rapidly decreasing exponential functions:

$$T-T_a = \sum_{n=1}^{\infty} A_n F(m_n, x_i) \exp^{-m_n(\frac{\alpha t}{l^2})} \tag{3.1}$$

where, T_a is the ambient temperature, A_n is a constant coefficient which depends on the initial conditions, $F(m_n,x_i)$ is the eigenfunction, which depends on the geometric features of the body and the space coordinates x_i, and m_n are the eigenvalues (the roots of the characteristic equation). The symbols α and ℓ represent the material thermal diffusivity and the characteristic length of the body, respectively.

In order to correctly choose the form of the alternate model, i.e., the *FGS*, it is necessary to satisfy the condition of mathematical similarity between the fundamental and the real problems. While there are no definite similarity laws to follow, the two problems should be physically similar in nature, formulation, boundary conditions, and initial conditions. The simplified *fundamental generalized* problem should also be capable of yielding at least a partial analytical solution.

To illustrate the concept of mathematical similarity, Figures 3.1(a) and 3.1(b) show finite-element models of a circular plate (r=127 mm) with a central circular heat source (r_0=8.47 mm, Q=370 W), and a square plate (12.7×12.7 mm) with a central square heat source (8.47×8.47 mm, Q=115 W), respectively. The plates are made of Cast Iron (α=17.19 mm^2/s) and have the same thickness (25.4 mm), but their characteristic dimensions and heat source intensities are quite different. Figure 3.2(a) shows the transient temperature profiles in each plate at a specific nodal point 'A' for a unit step heat input. In the case of the circular plate, node A is located at r=76.2 mm from the centre, and in the case of the square plate, node A is located at 77.82 mm

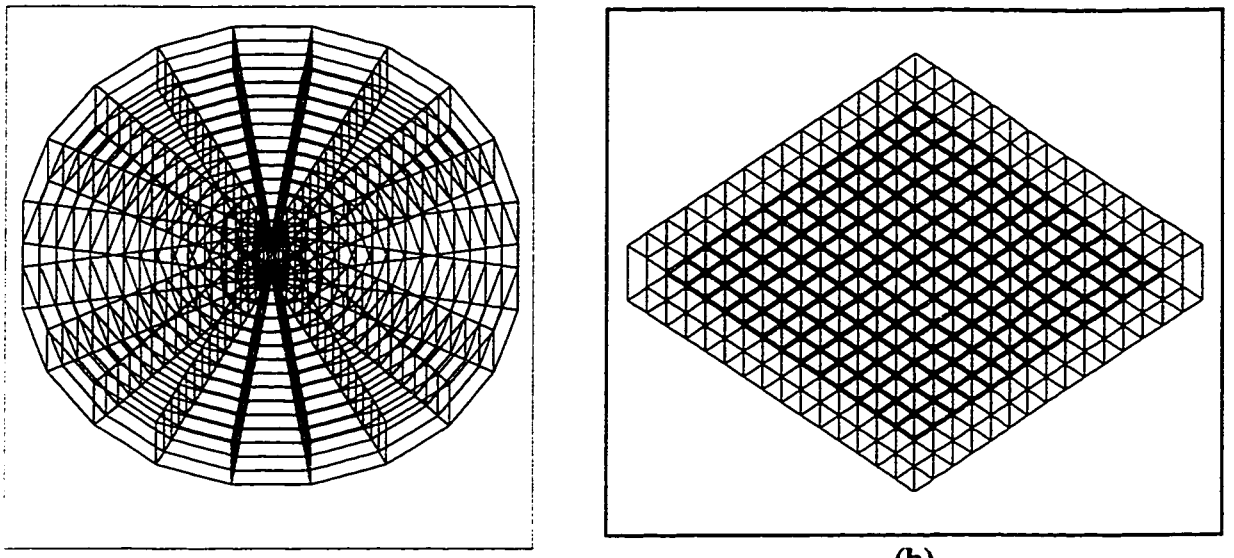

(a) (b)

Fig. 3.1 Finite-Element Models of Plates with Centeral Heat Source

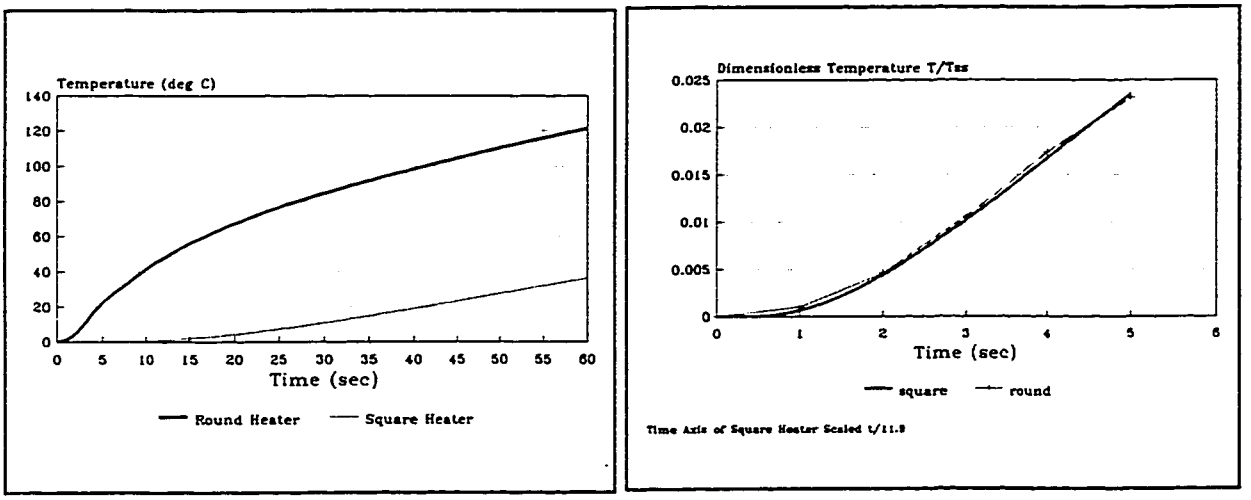

(a) (b)

Fig. 3.2 Thermal response at point 'A' on the circular and square plates: (a) without, and (b) with adjustment of the time scales

from the centre in the diagonal direction. Although the profiles of the temperature rise appear quite different in Figure 3.2(a), the similarity in the mathematical nature of the solutions can be seen when the scale of the temperature and time axes are changed on the square heater profile. Through a trial and error procedure, the two curves were made to have a perfect match (within the accuracy of the FEM), as shown in Figure 3.2(b). The complexity of the mathematical structure of the solution can, however, be judged from the observation that the ratio between the two time scales, which results in a single graph, was neither related to the time constants nor to the duration of the transient stage. In this example, if no analytical representation were available for a plate with a square heat source, the mathematical form could be approximately determined from a consideration of the plate with the circular source, assuming that the solution of that problem is available.

3.4 The Generalized Solution for the Temperature Field in the Machine Tool Structure

The formulation of the proposed *generalized modelling* method consists of three stages: *(a)* the determination of the approximate mathematical form of the general solution to the real process *FGS*, *(b)* the construction of an empirical base expression which is mathematically related to the real process, and (c) calibration of the empirical base expression with experimental data from the real process. The flow chart presented in figure 3.3 shows how the proposed method would be implemented to model a real process. Block 1 represents the selection of the alternate *fundamental generalized* model which is physically similar to the real process but in simplified form. In block 2, the general solution for the simplified model is derived, and in block 5 the step solution is obtained. In blocks 3 and 6 the analytical expressions representing the general and step solutions for the simplified model are transformed into empirical base functions by lumping the analytical parameters into empirical constants. In block 7 the step solution is curve-fit to the step response of the actual process by calibrating the parameters with experimental (or computer simulation) data. The expression derived in block 3, combined with

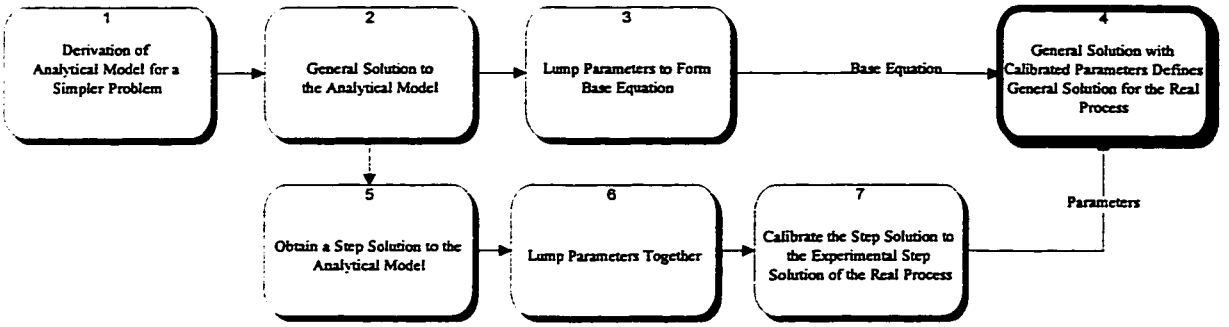

Figure 3.3 Flowchart showing the *generalized modelling* procedure

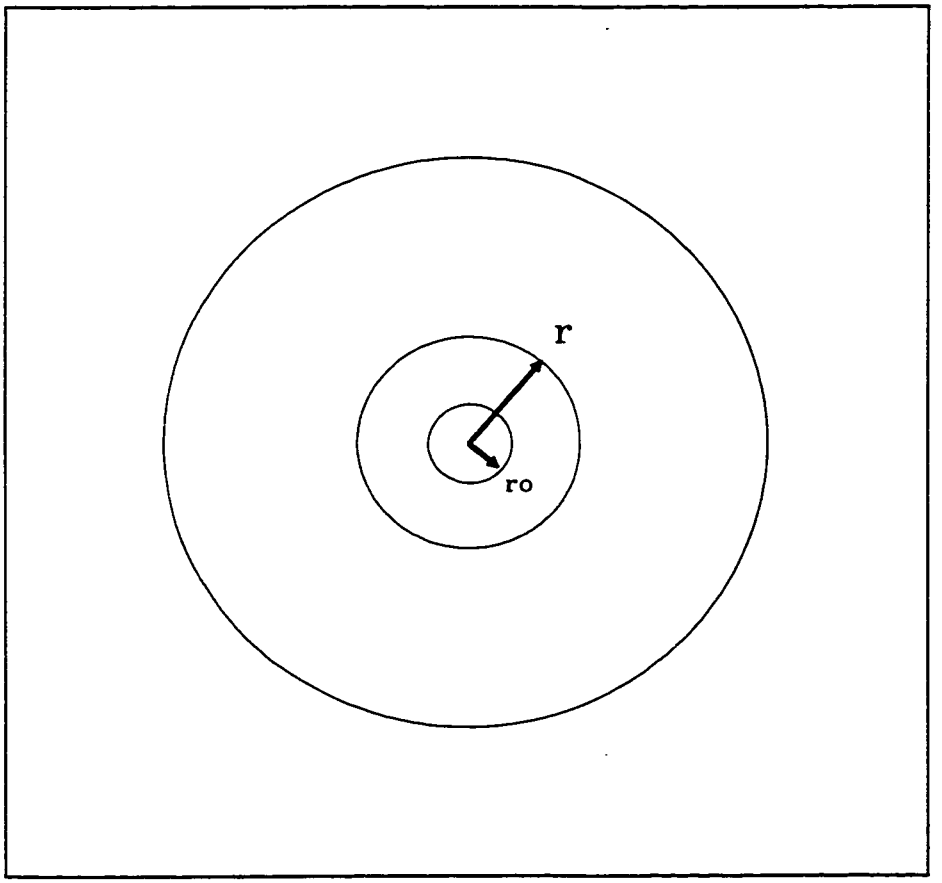

Fig. 3.4: Fundamental Generalized model of an infinite plate

the empirical parameters derived in block 7, define the general solution for the real process (block 4).

For a linear problem, the response of the system to any input is fully defined by the step response. It is therefore possible to calibrate the empirical solution from the measured transient response to a single input, which is usually the step response. If a step input cannot be generated in the real process, one may use a ramp or other known function. For a non-linear model, several responses would be required for calibration, covering the entire useable range of the output variable. This approach is more convenient than conventional empirical methods where a large number of experimental responses are required to calibrate the model. If the parameter variation is small, as is often the case, a non-linear model could also be adequately calibrated from a single input. In what follows, the *generalized modelling* method will be applied to obtain a model for the thermal response behaviour of a machine structure.

3.4.1 Stage 1: Selection of the simplified analytical model describing the thermal response of the machine tool structure

A machine tool structural component is a large hollow shell with external slideways, internal ribs and brackets, and various sources of heat sources. In order to implement the *generalized modelling* concept, the analytical solution to a mathematically related problem is required. Figure 3.4 shows a thin infinite plate with a convective boundary condition on the face and a central ring of heat generation. This simplified model is analogous to the problem of one heat generating source in a machine structure, since the bends and folds in the real structure do not introduce any thermal resistance. In other words, the machine tool structure can be visualized as if its walls are bent out flat into a large thin plate of uniform thickness. The internal ribs and brackets are not included in the simplified model because they do not greatly alter the mathematical structure of the solution. Heat sources take a variety of shapes and sizes, but they can be adequately represented in the simplified model as a circular ring of heat

generation. This statement will be confirmed in section 3.4. Since the problem is assumed to be linear, multiple sources are accommodated by superposition of the individual models.

The plate in figure 3.4 is thin and the source is radially symmetric, so the governing differential equation is the one-dimensional heat conduction equation with convection and internal heat generation:

$$\frac{\partial^2 T}{\partial r^2} + \frac{1}{r}\frac{\partial T}{\partial r} - aT + \frac{g(r,t)}{k} = \frac{1}{\alpha}\frac{\partial T}{\partial t} \tag{3.2}$$

where:

$$\begin{aligned} a &= \frac{h}{kw} \\ h &= \textit{convection co-efficient of heat transfer} \\ k &= \textit{thermal conductivity} \\ w &= \textit{thickness of the plate} \\ \alpha &= \textit{thermal diffusivity} \\ g(r,t) &= \textit{internal heat generation per unit volume} \end{aligned} \tag{3.3}$$

The internal heat generation is zero everywhere in the plate except for the thin ring at $r=r_0$. If the thickness of the heat generating ring approaches zero, $\Delta r \rightarrow 0$, then the internal heat generation per unit volume is expressed as:

$$g(r,t) = \frac{q(t)}{2\pi r_0 w}\delta(r-r_0) \tag{3.4}$$

Where $\delta(r-r_0)$ is the space impulse function. If the plate is at ambient temperature at t=0, then the boundary and initial conditions are: T = 0, when t = 0, and T= 0, when r = ∞. The analytical solution to this problem has previously been derived by the author [83], using the methods of Hankel and Laplace transformations [47]. The general solution is:

$$T(r,t) = \frac{\alpha}{2\pi kw}\int_0^{\infty} \beta\, J_0(\beta r) J_0(\beta r_0)\, e^{-(a+\beta^2)\alpha t} \int_0^{t} q(\tau)\, e^{(\beta^2+a)\alpha t}\, d\tau\, d\beta \tag{3.5}$$

If the heat generation is function q(t) is taken to be a step function of magnitude q at t=0, then the temperature step response simplifies to:

$$T(r,t) = \frac{q}{2\pi kw}\int_0^{\infty}\frac{\beta}{\beta^2+a}J_0(\beta r)J_0(\beta r_0)\left[1-e^{-(a+\beta^2)\alpha t}\right]d\beta \qquad (3.6)$$

3.4.2 Stage 2: Transforming the Analytical Thermal Solution into an Empirical Base Function

There are four groups of analytical parameters in equations (3.5) and (3.6) which are: $1/(2\pi kw)$, r_0, a, α. These parameters are replaced by four empirical constants: K= $1/(2\pi kw)$, r_0, a, α, to yield the following empirical base equation for the step solution:

$$T(r,t) = Kq\int_0^{\infty}\frac{\beta}{\beta^2+a}J_0(\beta r)J_0(\beta r_0)\left[1-e^{-(a+\beta^2)\alpha t}\right]d\beta \qquad (3.7)$$

The two independent variables in the equations are time t, and radial distance from the source r.

3.4.3 Stage 3: Calibrating the Thermal Base Equation

There are a variety of methods to curve-fit the parameters of the base equation but the most common is the least squares method. If the error residual is defined by the equation:

$$S = \sum_{i=1}^{n}(Y(t_i)-T(t_i,a_1,a_2,..a_m))^2 \qquad (3.8)$$

Where $Y(t_i)$ is the measured data and $T(t_i)$ is the analytical base, and a_1, a_2,...a_m are the empirical parameters of the analytical base, the least square solution is found by solving the following system of equations:

$$\sum_{i=1}^{n}\frac{\partial T(t_i,a_1,a_2,..a_m)}{\partial a_1}T(t_i,a_1,a_2,..a_m) - \sum_{i=1}^{n}\frac{\partial T(t_i,a_1,a_2,..a_m)}{\partial a_1}Y(t_i) = 0$$

.... (3.9)

$$\sum_{i=1}^{n}\frac{\partial T(t_i,a_1,a_2,..a_m)}{\partial a_m}T(t_i,a_1,a_2,..a_m) - \sum_{i=1}^{n}\frac{\partial T(t_i,a_1,a_2,..a_m)}{\partial a_m}Y(t_i) = 0$$

There are 'm' empirical parameters and 'm' simultaneous equations in the form of equation (3.9). The equations are non-linear, so the solution requires a method of solving a system of 'm' non-linear equations for 'm' unknown parameters. This was done using a non-linear least-square parameter calibration algorithm, that was developed for this purpose.

3.5. Computer Simulation Test Case

In this section, the concept of *generalized modelling* for the thermal response in a machine tool structure will be validated on a computer simulated model. The purpose of this test is to verify the accuracy of the model and its capability to determine the temperature distribution in real-time. In the test case, the transient temperature field in the whole structure was predicted to verify the capacity of the calibrated model to interpolate data reliably for a range of input functions unrelated to the calibration data.

The test case is a finite element model of a large complex structure (550x1000x1500 mm) with internal ribs, representing a part of a machine tool, as shown in figure 3.5. The square heat source is applied near the centre of the box face. This finite-element model was created using the general purpose finite-element package ALGOR [84]. The procedure for calibrating the model is as follows:

(1) Determine the optimal parameter values by matching the response of equation (3.7) to the temperature step response at different values of radius r, using a non-linear least-square parameter calibration algorithm. The algorithm involves the solution of a system of non-linear simultaneous equations because of the non-linearity of the governing equations (Equation 3.9).

(2) The optimal parameter values have some random variation from point to point because of statistical considerations in the calibration algorithm and errors in the finite-element solution. This random variation is reduced by smoothing the variation of one of the

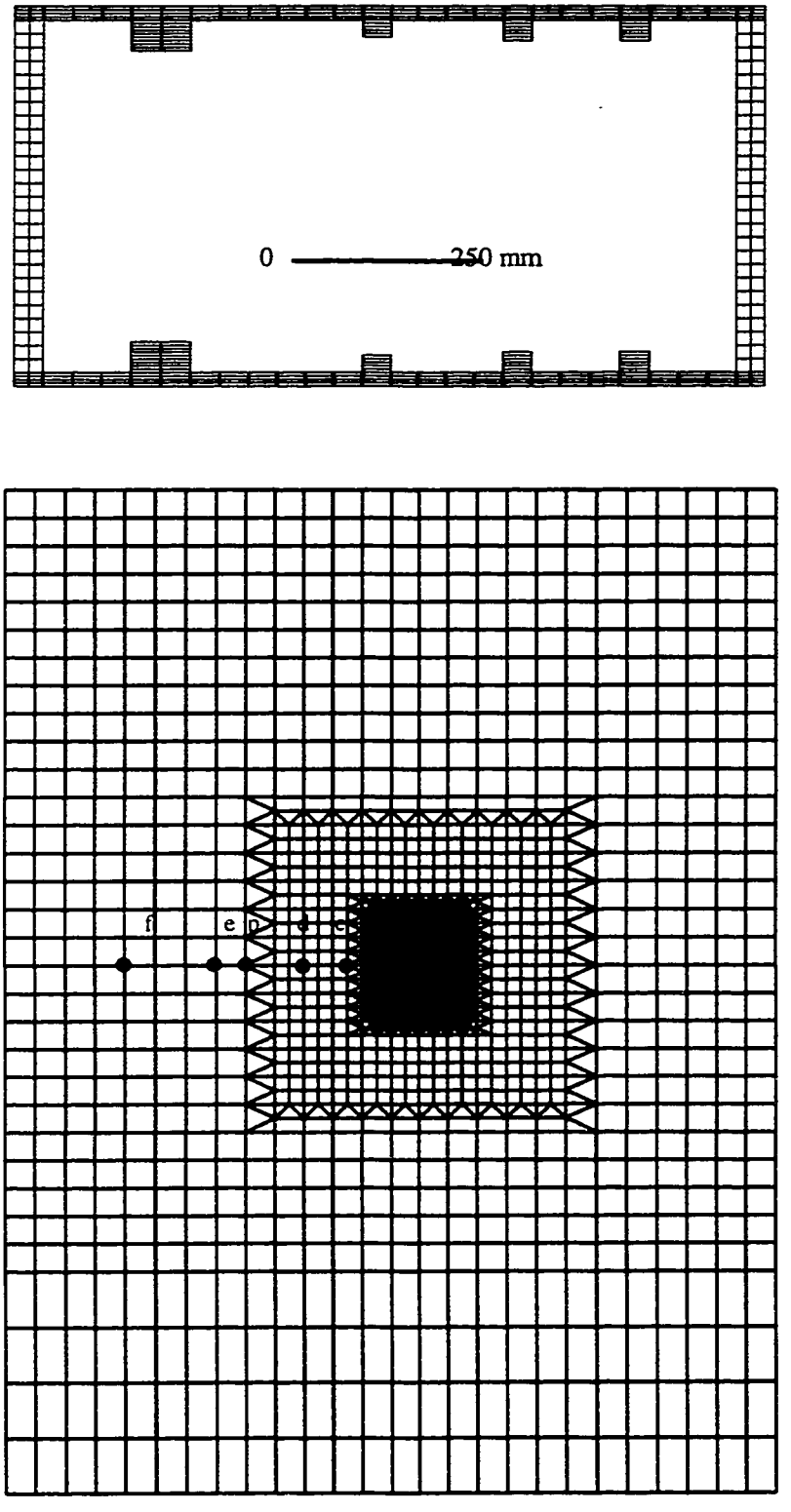

Figure 3.5 Finite Element Model of Test Structure 1

parameters and recalibrating the others. After several iterations a smooth parameter variation curve is determined.

Figure 3.6 shows two temperature profiles at two points on the structure (see inset, figure 3.5), along with the generalized solution, obtained by calibrating the parameters a, α and K. Figure 3.7 is a plot of the parameter values for different radial distances from the source. The parameter variation curves are independent of the angular position with respect to the source because the model is large and, therefore, the end effects do not become a factor. There is significant parameter variation with r in the vicinity of the source, but the curve becomes flat as $r/r_0>10$. The reason for the variation in the vicinity of the source is that there is greater mathematical discrepancy between the forms of the generalized and finite-element models in this region. At larger distances from the source, the difference in the assumed profile of thermal input becomes less significant. In order to accurately represent the temperature distribution in the vicinity of the source it is necessary to vary the parameters with r, as indicated in figure 3.7. The temperature distribution was found to be very insensitive to the parameter r_0 except where $r=r_0$, so the value was held constant at $r_0=15.2$ mm.

Figure 3.8 shows how the generalized model can be used to accurately estimate the temperature profile at an uncalibrated node by interpolating the parameter data in figure 3.7. The calibrated model will determine the temperature at any point on the structure at any instant of time, t, for any input. In this test case, seven measured nodes provided sufficient data to calibrate the generalized model because the dimensions of the box are relatively large.

3.6 Conclusions from the Evaluation of the Generalized Modelling Method

The evaluation of the generalized modelling method on the finite-element test case has demonstrated several important advantages over finite-element models and traditional empirical models. The advantages of the generalized model over a finite-element model are:

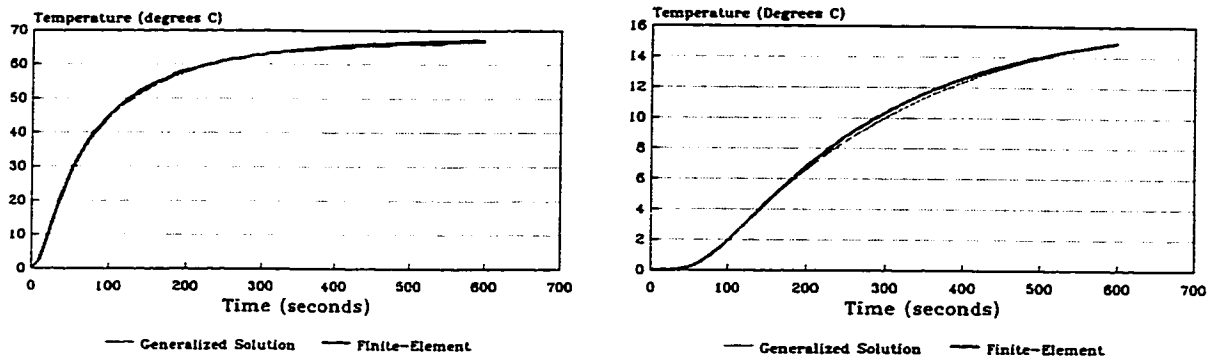

Fig. 3.6: Temperature profiles at two points on the test structure 1: (a) r = 50.8 mm, (b) r= 157 mm

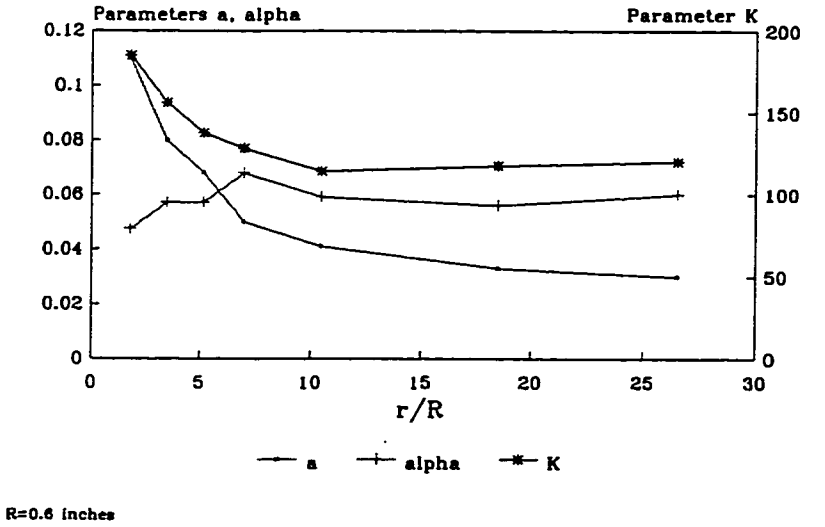

Figure 3.7: Paramater Variation in Structure

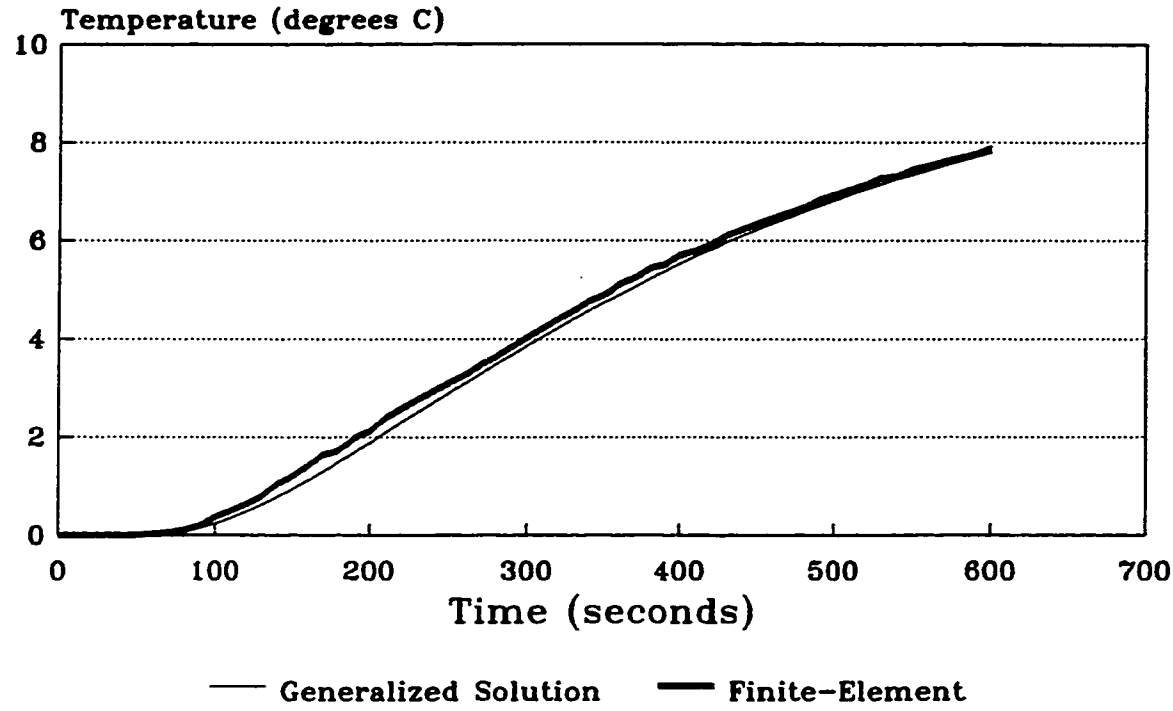

Fig. 3.8: Prediction of the thermal response of uncalibrated point on the test structure 1, using the generalized model

(1) the generalized model is computationally fast enough to be used in an on-line environment (an improvement of two orders of magnitude),

(2) it is possible to determine the temperature profiles of a limited number of points, independently of the other points in the structure, and

(3) the intricate modelling of complicated geometry and boundary conditions is not required.

The advantages over traditional empirical models are:

(1) the generalized model typically contains a much smaller number of parameters than a traditional empirical model to achieve the same level of accuracy,

(2) the generalized model forces the calibration data to conform to the correct mathematical form of the system, and

(3) the generalized model can extrapolate the response of the system well beyond the range of the calibrated inputs, which makes it possible to determine a complete solution from limited measurement data.

Because of these characteristics, the generalized modelling method is the best method of modelling processes in real time where the relationship between the input and output system variables is only partially known. The mathematical basis of the generalized method allows the system model to go beyond the raw calibration data to identify the actual physical relationship between the input and output system variables, even when this relationship is not completely defined by the calibration data. It does all of this with enough speed to be used in a real time environment. All of these characteristics are essential to the development that follows in subsequent chapters.

CHAPTER 4: DESIGN OF PHYSICAL AND COMPUTER SIMULATION MODELS OF LINEAR AND NONLINEAR MACHINE TOOL STRUCTURES

4.1 Introduction

In this chapter, two models of a machine tool structure will be designed and constructed. The first is a physical model with temperature and displacement measurement equipment, and electric heating elements on the surface of the structure. This model is designed so as to be similar to a real machine tool in its thermal and thermal deformation properties. The model will be designed to minimize the nonlinear effects that are produced by fixed and sliding joints. The second model is a finite-element model, representing a thick walled machine tool structure exhibiting significant joint induced nonlinearity in its thermal deformation behaviour. In order to accurately simulate the behaviour of the contact joints within the structure, a new contact element will be developed, which will accurately simulate the contact pressure induced changes in the thermal properties of the element. An iterative solution algorithm will be developed, utilizing a commercial finite-element package to solve the linear system matrix during each iteration. These models will be utilized in later chapters to validate the thermal deflection estimation and control method that will be developed.

4.2 The Requirements of the Models

The method of controlling thermal deflection that will be developed in this thesis is intended for application with real machine tools. The verification of the method will be done however, using models of simulated machine structures rather than operational machine tools. There are several reasons why a custom built model is preferable to a real machine for the validation of the procedure that will be developed:

1. A model can be made to include certain features which are not commonly found in most machine tools, but which pose special problems that will be dealt with in this thesis.

2. A model can be designed so as to exclude additional sources of error which are not dealt with in this procedure, but which may obscure the validation process.
3. A model can be designed so as to accentuate the thermal deflection, and to introduce extreme stimuli which might occur randomly or very infrequently in a real machine tool.
4. A model allows better control over input and environmental variables so as to better identify potential problems and weaknesses with the procedure.

It will be shown that there are two distinct cases which may be encountered in practice. In the first case, the thermal deflection response of the machine tool structure is essentially linear, and in the second case there is a significant non-linearity which arises because of joint interaction. For the first of these cases a physical scale model of a machine structure will be designed. For the second of these cases it was found that a physical model is impractical because of the large dimensions of the structure which would be required. Furthermore, the behaviour of the nonlinear machine structure is less well understood, and a thorough analysis would require the measurement of variables which are not easily accessible in a physical model. For example, it will be shown that an understanding the behaviour of the contact pressure distribution at a joint in the seconds following a thermal input is an important consideration. The contact pressure distribution cannot be easily measured on a physical model, but it can be easily determined on a finite-element model. Thus, the second verification model is a nonlinear thermal deflection finite element model of a machine structure.

In order for the validation of the method for controlling thermal deflection to be convincing, the models that are used must be authentic in the sense that they behave in the same way as would real machine tool systems. This is of particular concern in the case of the nonlinear finite-element model, because of the difficulty associated with accurately representing the contact interface between two components in the form of a finite-element model. Since it will be shown that this contact interface is the source of the system

nonlinearity, particularly careful attention must be paid to the modelling of the interface, so as to simulate the actual nonlinearity that is encountered in real machine tool systems. Several commercial finite-element modelling packages were investigated, including ALGOR, ANSYS, CATIA, and ABACUS, however none of these commercial packages provide a satisfactory combination of elements to simulate the thermal and mechanical properties of the contact for the requirements of the verification model. In this chapter, a custom designed contact element will be developed, along with a nonlinear solution algorithm.

4.3 The Linear Physical Model

4.3.1 Estimating the Requirements for the System Variables

The experimental model to be used for the verification of the method without joint non-linearity is a scale model of a machine tool structure. The model must have thermal and thermal deflection characteristics which are similar to a real vertical milling machine. Figure 4.1 shows the temperature distribution in a real vertical milling machine running at maximum speed with zero load. The image was generated by an infrared thermal imaging camera. The figure shows two major heat sources in the structure, the motor assembly near the rear of the overarm, and the spindle bearing near the front of the overarm. The maximum temperature rise is 58 degrees Celsius near the top of the spindle bearing heat source. The steady state thermal deflection of the cutting tool assembly relative to the table for this machine is 3.5 thou or 89 microns in the horizontal direction and -1.9 thou or -48 microns in the vertical direction. The experimental model should have a general shape and configuration which is consistent with the vertical milling machine. The one aspect where there must be a considerable dissimilarity is in the wall thickness of the structure, which cannot be more than 6.4mm for economic reasons. The average wall thickness of most machine tools exceeds 25mm.

It is an important consideration that the maximum temperature and the temperature distribution in the model be similar to that of the real machine tool. The derivation of the

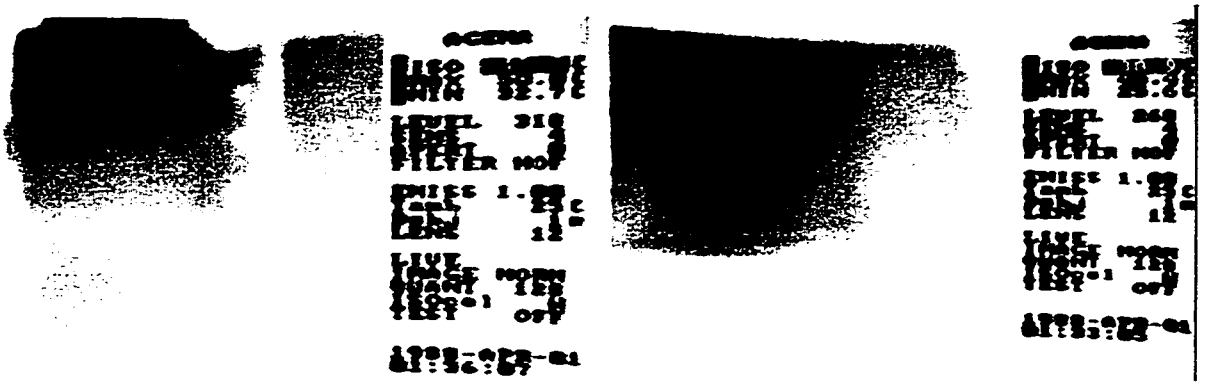

(a) Front of Overarm (b) Rear of Overarm

Figure 4.1 Temperature Distribution in Real Milling Machine Structure

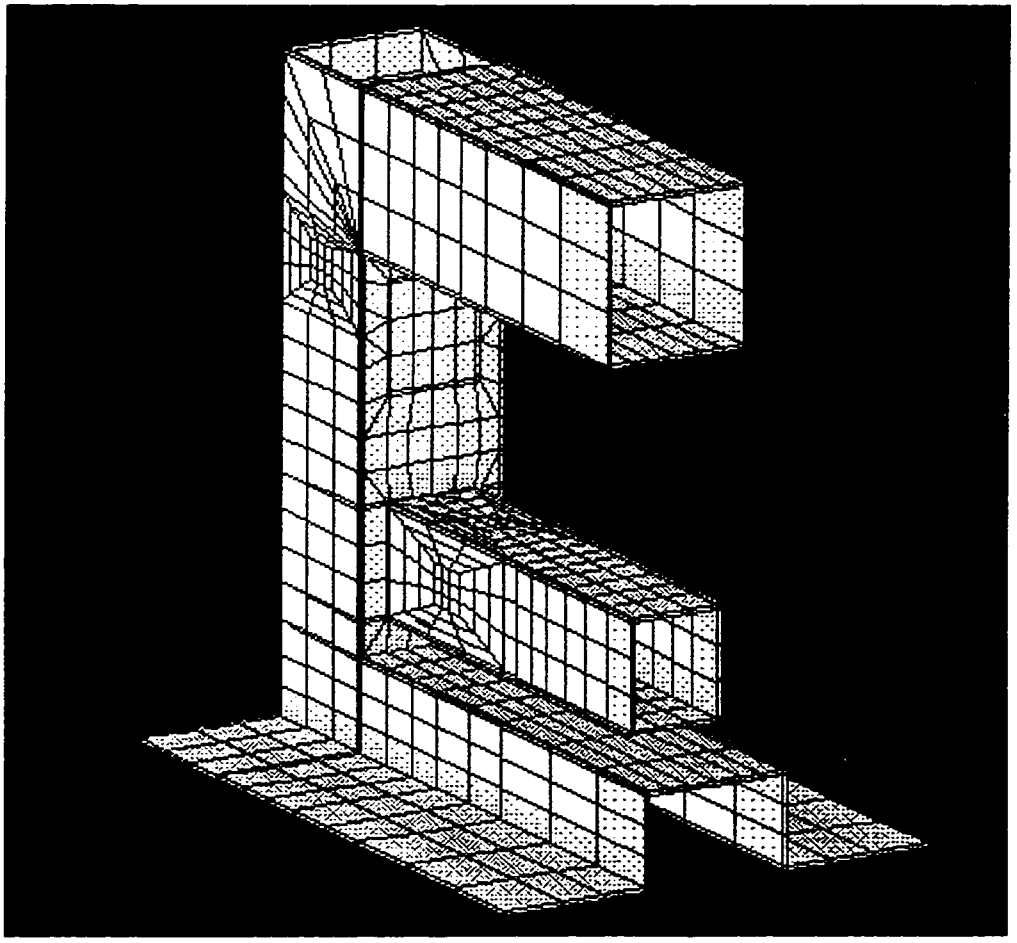

Figure 4.2: Finite Element Model of Linear Test Structure

procedure that follows in later chapters is based on the assumption of a linear thermal model, and the validity of this assumption can only be properly tested if the operating temperature of the experimental model is consistent with the operational temperature of a real machine tool.

Another important consideration is the maximum thermal deflection of the model compared to that of a real machine tool. The real milling machine produced a maximum thermal deflection of 89 microns. This order of deflection is typical for small machine tools, but higher thermal deflection would be expected from larger machines. While the thermal deflection of the experimental model should not be too much greater than 89 microns, it is desirable to obtain a greater maximum deflection from the model so as to accentuate the phenomenon which is being studied. The location of the main heat source in the model will be moved slightly from those shown in figure 4.1, so as to increase the maximum deflection somewhat.

Prior to constructing the experimental model, extensive finite-element modelling was done to ensure that the model, when built, would have the desired characteristics. Figure 4.2 shows a solid model of the finite-element mesh representing the experimental model. Figure 4.3 shows the dimensions of the actual model assembly. The structure is constructed out of a quarter inch (6 mm) square section column which was cut and welded at the edges indicated. All of the joints are seam welded so as to make one continuous thermal structure. The finite-element analysis done prior to the construction of the model revealed that no significant joint non-linearity could be introduced without significantly increasing the wall thickness of the model. Since this is impractical, the experimental model was designed as a mono-component structure without any joint interaction whatsoever.

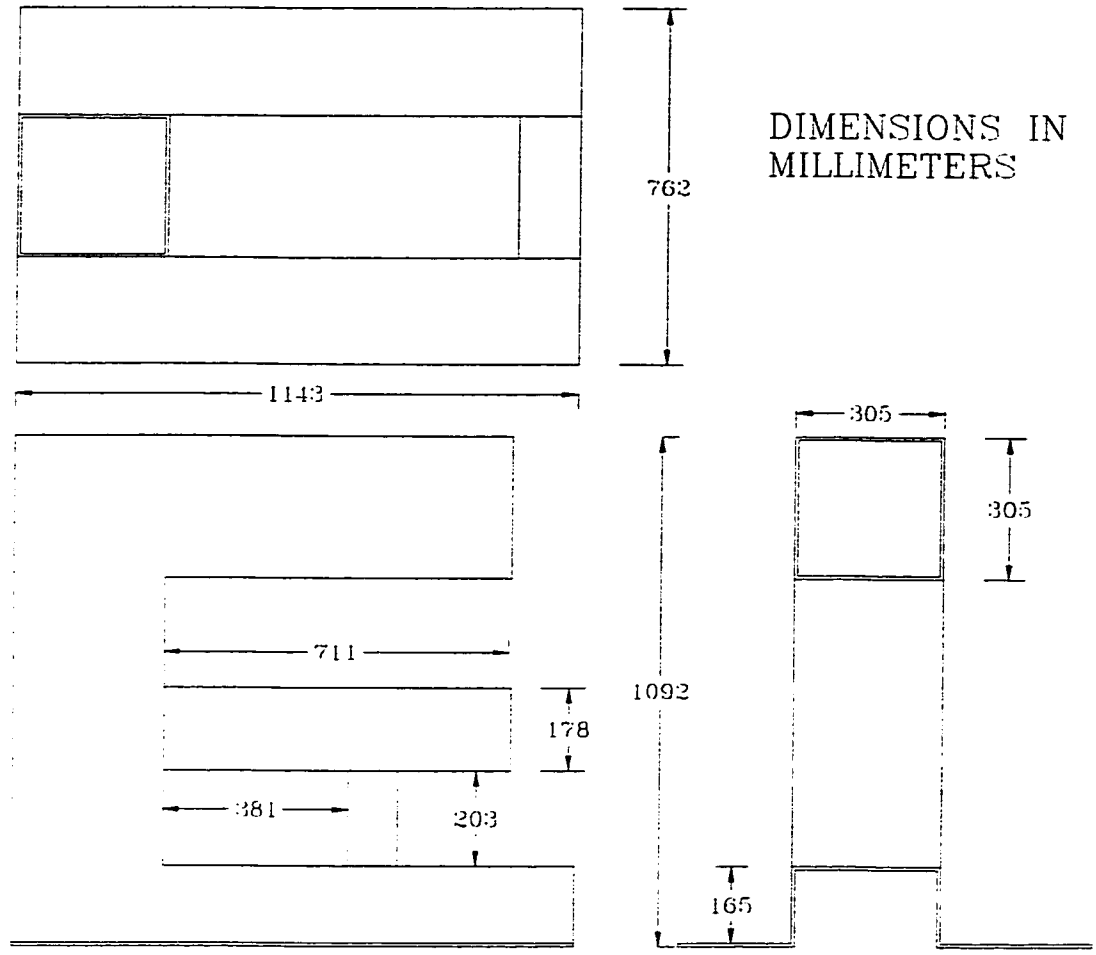

Figure 4.3: Dimensions of Linear Model

4.3.2 Configuration of the Model and Measurement Apparatus

Figure 4.4 shows the machine drawings for the displacement transducer holder, and figure 4.5 shows the machine drawings for the transducer clamping mechanism. The clamps hold the LVDT transducers, as shown in the figure, and attach to the holder by means of the slots shown in figure 4.4. The clamps can be adjusted into position by moving them in the sliding slots, and then fixed into position by the set screws shown in figure 4.5. The LVDT transducers have a hardened ball tip that is spring loaded to maintain contact with the probe. The linear stroke is 1.0 mm, with a repeatability of 0.15 μm and a nominal accuracy of 2.0 μm within a range of 250 μm. The assembly has two LVDT transducers oriented mutually perpendicular to measure the displacement along two co-ordinate axes. The third co-ordinate, which is the direction into the vertical plane in figure 4.3 is not measured. The deflection in this direction will be negligible because of the symmetry of the model and the symmetry of the heat sources.

Temperature on the surface of the structure is measured using thermistors that are glued onto the structure with high conductivity adhesive. Thermistors have a higher resolution than thermocouples, they also have greater repeatability and do not require calibration by the user. However they are nonlinear devices which require a calibrated conversion equation. This is not really a disadvantage in this case because the controller is implemented by a computer which will perform the conversion.

The data acquisition system employs a Microstar Laboratories DAP 2400 data acquisition card. The card includes analog data acquisition hardware and a 16-bit microprocessor. The card operates on a real time multitasking operating system called DAPL. It employs 12 bit analog to digital conversion and has a nominal maximum sampling rate of 50 kHz. Most of the data processing is performed by a Pentium 60 MHZ computer running C++ through DOS, although some input signal processing is done in parallel by the data acquisition processor.

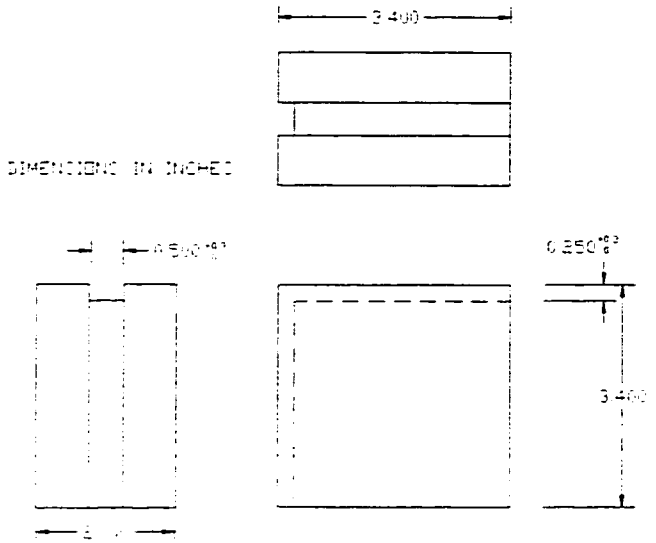

Figure 4.4: Transducer Holder Assembly

Figure 4.5: Displacement Transducer Clamp Assembly

The system has a maximum of 15 single ended inputs and two controlled outputs. The controlled output voltage signals connect to voltage controlled power supplies which drive the resistance heating pads. The heating pads are glued onto the structure with high conductivity adhesive, and are used both to simulate the disturbance heat sources of a real machine tool, and also as artificial heat sources for control.

Figure 4.6 shows a schematic drawing of the structure showing the measured x and y axes, the configuration of the test structure, the location of the heat sources, and the points of measured temperature. Notice that the location of the sources has been moved slightly from the locations shown in the real structure in figure 4.1. The heat source at the base of the overarm was moved about a third of the way down the column. This has the effect of accentuating the thermal deflection resulting from the same heat input. A heat source in that location is fairly common in some milling machine tools, either for a bearing or for the motor assembly. Another difference is that there is only one independent heat source, since both of the sources shown in the figure and the two placed symmetrically on the other side are connected to the same power source. Because the temperature and thermal deflection are completely linear, as will be shown shortly, additional sources can be dealt with by the superposition principle.

4.3.3 Comparison of the Model System Variables with a Real Machine Tool System

Figure 4.7 shows the temperature distribution in the test structure for a dimensionless heat input of Q=1.0. The maximum temperature is 82.5 degrees Celsius, which is a temperature increase of 58 degrees above room temperature. Figure 4.8 shows the temperature distribution on the finite-element model of the structure for the same input Q=1.0. The maximum temperature and the temperature distribution is in agreement with the test structure, which is consistent with the temperature distribution of the real machine tool in figure 4.1. The maximum temperature is somewhat higher in the experimental model than in the real machine,

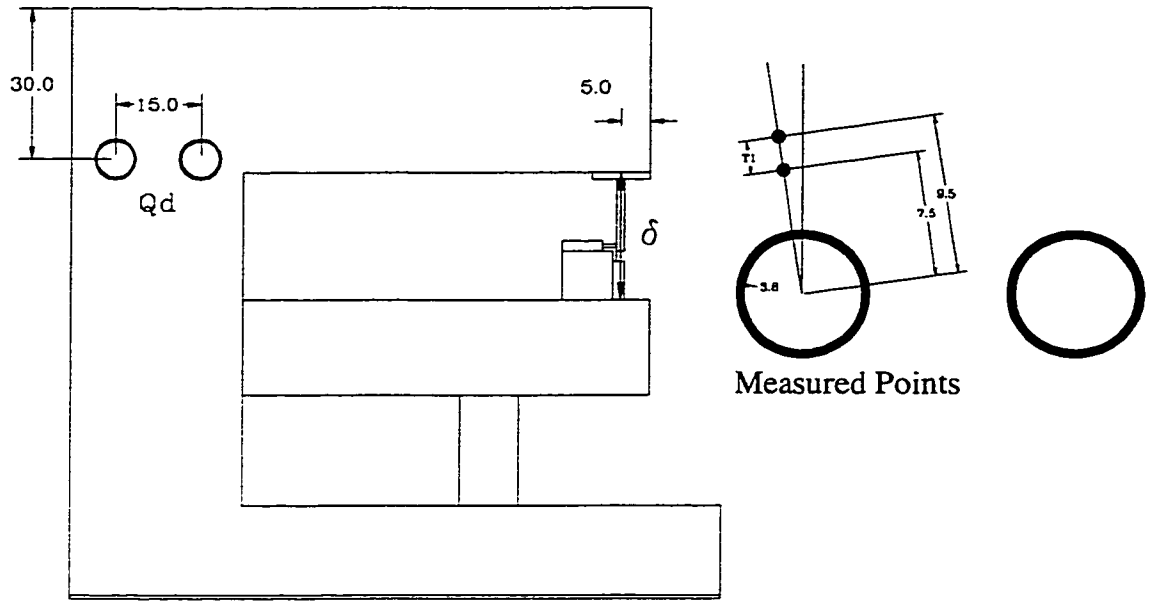

Figure 4.6: Schematic Drawing of Linear Test Model (Dimensions in Centimeters)

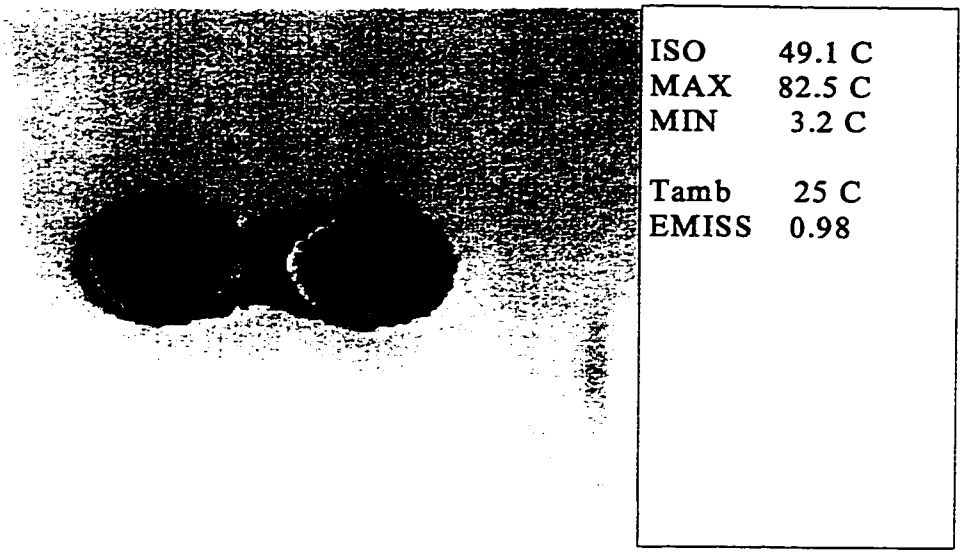

Figure 4.8: Temperature Distribution in Linear Test Structure for Q=1.0

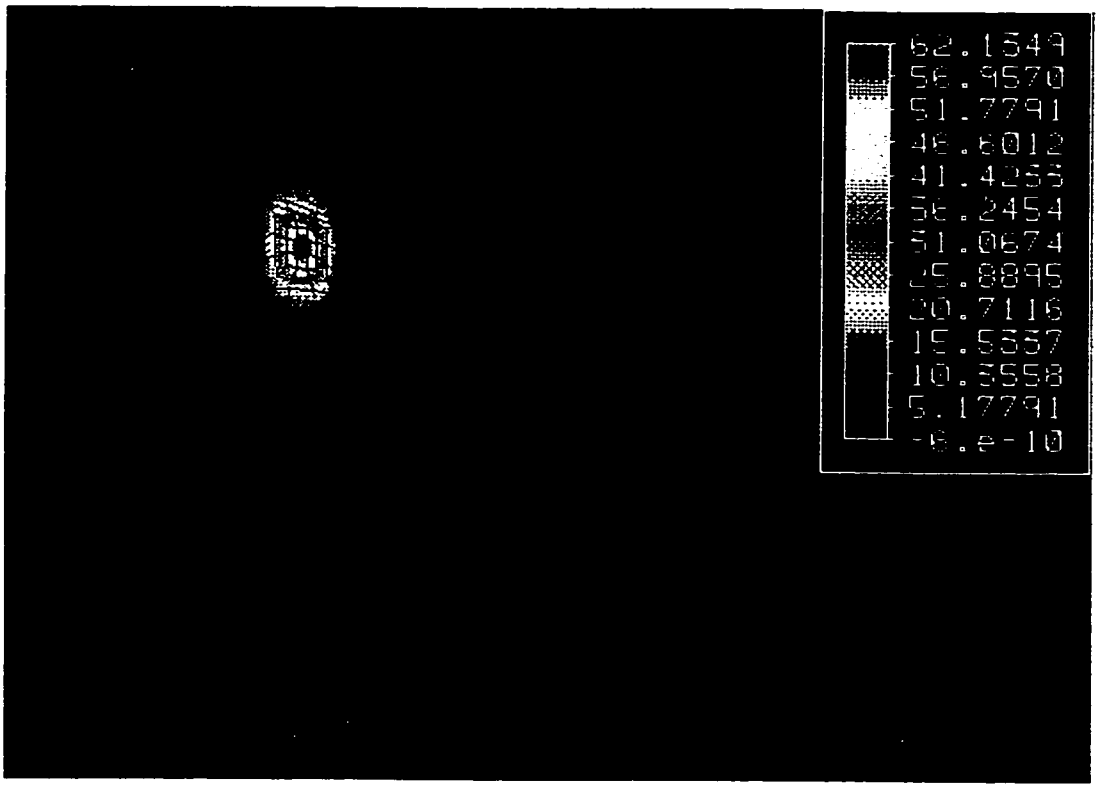

Figure 4.9: Temperature Distribution in Finite-Element Model of Test Structure

but this is due to the fact that the heater in the experimental model is on the surface, while the heat source on the real machine is buried within the structure, producing a more distributed temperature distribution at the surface. The maximum thermal deflection of the structure, which is the steady-state thermal deflection for the maximum heat input Q=1.0, is 78 microns in the x-direction and 242 microns in the y-direction. This is somewhat higher than the maximum thermal deflection for the real structure in figure 4.1, but it is in the same order of magnitude and comparable to the thermal deflection of many machine tools.

4.3.4 The Control Heat Sources

Figure 4.9 shows the temperature distribution of the finite-element model of the structure with three operating heat sources. The additional two sources are used to simulate the effect of the control heat sources in the real test model. The locations shown were found to be suitable locations for generating thermal deflection along the X and Y axes with minimum heating power and temperature rise. An analysis of various finite-element models suggested the design shown in the figures above, with the control heaters placed in the locations indicated by the hot zones in figure 4.9. However, the locations of the heat sources on the real model will differ somewhat from that shown in the figure. A photograph of the complete physical setup is shown in figure 4.10.

4.4 The Non-Linear Computer Simulation Model with Joint Interaction

4.4.1 Nonlinear Thermoelastic Behaviour of Machine Tool Structures due to Contact Joints

The main source of thermal deflection nonlinearity in a machine tool structure is the interaction between thermal stress and thermal resistance at the interface between machine components. The effect of fixed and sliding joints on the static, dynamic and thermal behaviour of machine tools, and consequently machining accuracy, has been well recognized for some time. In recent years, the development of the theory on non-linear thermoelastic behaviour of structural joints [85] revealed the importance of the distribution of the thermal

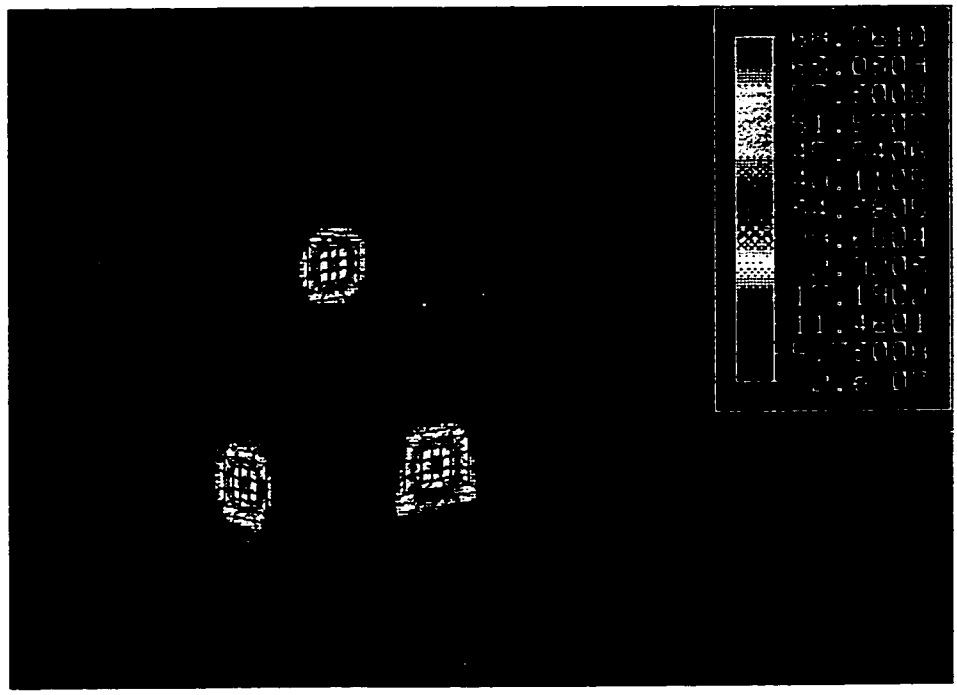

Figure 4.9: Temperature Distribution in Finite-Element Model of Linear Test Structure for three Simulated Heat Sources

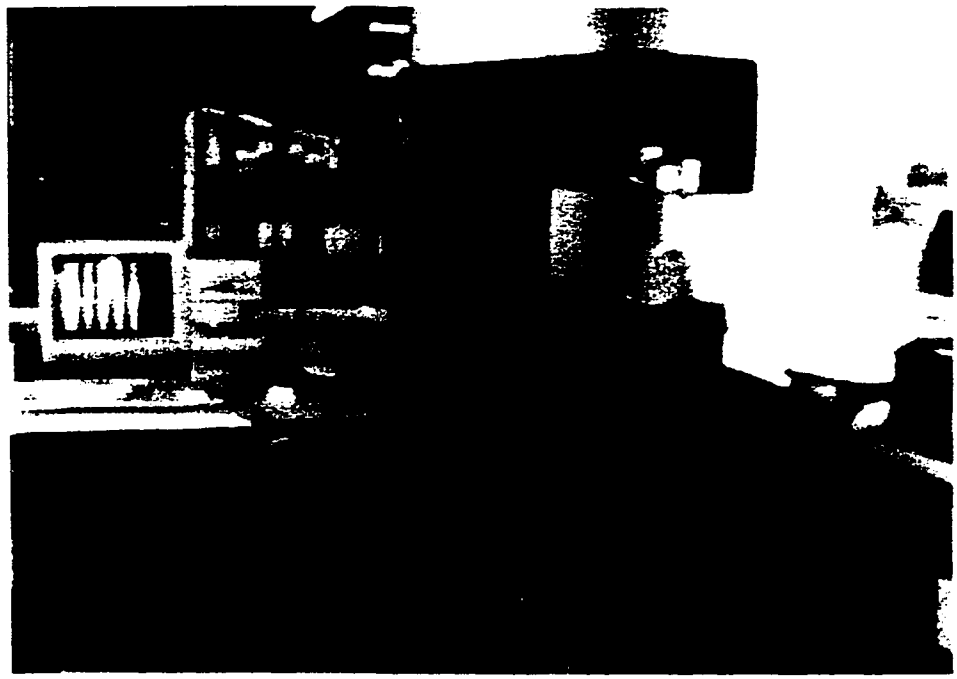

Figure 4.10: Photograph of Physical Model

contact resistance and stresses on the thermal deformation of the whole structure [86]. Proper design of the joint to control the contact pressure presents a conflict of requirements between the static stiffness and the damping capacity [87] [88]. Friction damping is determined by the friction force and the relative slip amplitude. This mechanism is again associated with another conflict of requirement; the increase in contact pressure results in an increase in the friction force and a decrease in the micro-slip amplitude. Micro-slip results also in fretting wear at the joint which may affect the long-term performance of the machine tool [89].

Therefore, a proper modelling of the machine tool structure and its joints requires an understanding of the physical phenomena and interaction that take place at the joint. It also requires accurate description and idealization of the boundary conditions. Specifically, the modelling should recognize the nonlinear nature of the thermoelastic behaviour of the structure and the importance of predicting the distributions of the contact stresses and the thermal contact resistance, as well as micro-slip and separation.

4.4.2 The Nature of the Thermal and Stiffness Characteristics of the Contact Joint

4.4.2.1 Surface compliance in the normal and shear directions

The extensive experimental and theoretical work carried out on the stiffness of flat joints [90] [91] [92] [93] [94] [95] [96] showed that upon normal loading the surface asperities deflect both elastically and plastically. During unloading, however, the normal deflection curve is purely elastic as long as the initial maximum load is not exceeded. The elastic recovery of the deformed asperities was found to be non-linear due to the increase in the bearing area.

The empirical nonlinear compliance of contacting surfaces, which relates the approach of contacting surface asperities λ_n to the applied pressure p_n, was found to follow this form [90][91]:

$$\lambda_n = c_n p_n^m \tag{4.1}$$

The constants c_n and m in Equation (4.1) depend on the material of contacting solids and the roughness and waviness of contacting surfaces. From Equation (4.1), the dependance of the normal stiffness of the interface k_n on the contact pressure is described by the following relation:

$$k_n = \frac{dp_n}{d\lambda_n} = \frac{p_n^{1-m}}{m\,c_n} \tag{4.2}$$

When repeated tangential stress p_s is applied to contacting surfaces, the elastic shear deflection λ_s is governed by the following linear relationship [92][96]:

$$\lambda_s = c_s\, p_s \tag{4.3}$$

where, c_s is the interface shear compliance. Therefore, the shear stiffness of the interface k_s is:

$$k_s = \frac{dp_s}{d\lambda_s} = \frac{1}{c_s} \tag{4.4}$$

When the shear stress p_s reaches a liming value $p_{s,\,limit}$, it overcomes the frictional resistance resulting in a relative micro-slip between contacting bodies. The shear compliance is not only dependent on the materials of the solids and surface finish, but also dependent on the normal pressure p_n [92][96]:

$$c_s = \frac{R}{p_n^{\,s}} \tag{4.5}$$

where, R and s are again parameters dependent on the pair of materials and surface finish. The analysis carried out by Back et al. [93] showed that the relationship between elastic surface deflection and contact pressure p_n takes the form given by equation (4.1), when the probability function of the asperity heights is described by the following relation:

$$\psi(z) = b\,(z)^{(1-\bar{m})/\bar{m}} \tag{4.6}$$

In this case, the constants c_n and m in equation (4.1) are: $m = \bar{m}$ and $c_n = (p_m.n.A_i)\,(b.m)$, where, p_m is the flow stress of the softer material, n is the density of the micro contacts, and A_i is the area of a single micro-contact. Tsukada et al. [94][95] confirmed the validity of the

empirical relationship $\lambda_n\{p_n\}$ described by equation (4.1) when the density probability function $\psi(z)$ of the surface asperity heights is a normal distribution.

4.4.2.2 Thermal contact resistance

Micro-contacts are usually clustered within a smaller number of bounded zones known as the contour areas or the macro-contacts. As the heat flow lines approach the contact zone, they tend to converge towards the least resistance paths, giving rise to the known "thermal constriction resistance". Therefore, the total heat flow will be divided into a number n_1 of separate channels which correspond to the macroscopic constriction resistance $\mathbf{R}_{MAC}$ in the contact region, and the gap resistance $\mathbf{R}_G$ in the non-contact region. Microscopic constriction resistances $\mathbf{R}_{mic}$ and interstitial fluid resistances $\mathbf{R}_f$ are subsequently created as each of the heat flow channels is subdivided again into a number n_2 of microscopic heat flow channels, each correspond to a single micro-contact and its surrounding interstitial fluid. Microscopic and macroscopic constriction resistances can be added together [97] to determine the overall thermal contact resistance $\mathbf{R}_C$:

$$\mathbf{R}_C = \left[\sum_{i=1}^{n_1} \left(\frac{1}{\mathbf{R}_G} + \frac{1}{\mathbf{R}_{MIC} + \mathbf{R}_{MAC}} \right)_i \right]^{-1} \tag{4.7}$$

where the *total microscopic contact resistance* $\mathbf{R}_{MIC}$ within one contour area is defined as follows:

$$\mathbf{R}_{MIC} = \left[\sum_{j=1}^{n_2} \left(\frac{1}{\mathbf{R}_f} + \frac{1}{\mathbf{R}_{mic}} \right)_j \right]^{-1} \tag{4.8}$$

assuming that the n_2 isothermal micro-contact areas are identical (radius = a) and are thermally connected. For normally distributed surface asperities, the total microscopic constriction resistance $\mathbf{R}_{t,mic}$ (without the contribution of the interstitial fluid) can be estimated from the following equation [98]:

$$\mathbf{R}_{t,mic} = \left[C \left(\frac{\dot{m}}{\sigma} \right) k_h \left(\frac{p_n}{H_B} \right)^{0.985} \right]^{-1} \tag{4.9}$$

where, C is a constant, k_h is the harmonic thermal conductivity of the contacting solids; $k_h = 2k_1 k_2 / (k_1 + k_2)$, $\dot{m}$ is the mean of absolute slope of surface asperities, p_n is the normal contact pressure, and H_B is the hardness of the softer material. To account for the contribution of the oxide film to the contact resistance, Schankula et al. [99] developed a model to modify the microscopic thermal constriction. This model was expressed in terms of the thermal conductivity and the thickness of the oxide layer.

To estimate the *macroscopic constriction resistance* component $\mathbf{R}_{MAC}$, the thermal boundary condition over the contour area can be assumed as: isothermal, constant heat flux, or that the heat flux at any point is proportional to the local contact pressure p_n. Mikic [100] followed the third assumption, which represents an upper bound, and obtained the following relation:

$$\mathbf{R}_{MAC} = \frac{4L}{k} \sum_{n=1}^{\infty} \frac{1}{n} \left[\int_0^1 \left(\frac{p_n}{p_o} \right) \cos(n \pi \bar{x}) \, d\bar{x} \right]^2 \tag{4.10}$$

where, p_o is the average contact pressure along the joint, $\bar{x} = x/L$, x is the position of any point along the joint, and L is the length of the joint along which the pressure $p_n(x)$ is distributed.

A statistical model for predicting the *interstitial fluid resistance* $\mathbf{R}_f$ between isotropic conforming rough surfaces was developed by Yovanovich et al. [101]. The model accounts for the change from free molecular to transition, slip and eventually to continuum regimes as the gap thickness increases. The gas conductivity model developed by Turyk and Yovanovich [102] can be used here to estimate the *gap resistance* $\mathbf{R}_G$ between two rough wavy surfaces.

4.4.3 Modelling and Idealization of the Thermoelastic Characteristics of the Joint

4.4.3.1 Stiffness matrix of the three-dimensional interface element

The three-dimensional interface element, which models the normal and shear compliance of the interface, has different properties in each of the three principal directions. It should be noted that in measuring the surface deflections λ_n and λ_s (equations (4.1) and(4.3)), the elasticity of the subsurface layer and the bulk of the material were not included. Therefore, when equations (4.2) and (4.4) are used as the constitutive laws of the interface element, we are able to model the joint at a microscopic level. By connecting the interface element directly onto the nodes of the linear substructure, the non-linear elastic behaviour of the contact interface is physically distinct from the linear substructure.

Definition of the local coordinate system

Figure 4.11 shows how the normal direction for a pair of nodes is defined by the imaginary line in three-dimensional space connecting the designated node pair. The tangential surface is the plane that is perpendicular to the normal line, at the midpoint between the two nodes. The initial locations of the nodes may be chosen so as to create a smooth surface as in figure 4.11(a), or an irregular surface as in figure 4.11(b). In either case, the surface nodes must be placed so as to properly define the normal to the surface at the given point.

Figure 4.12 shows the normal line connecting two nodes, I and j, in the global co-ordinate system, labelled the X, Y, and Z axes. The orientation of the vector $\overline{\mathbf{P_1 P_2}}$ is defined by two angles, ϕ and θ, where ϕ represents the angle between $\overline{\mathbf{P_1 P_2}}$ and the global Z axis and θ represents the angle between the projection of $\overline{\mathbf{P_1 P_2}}$ into the X-Y plane and the global x-axis.

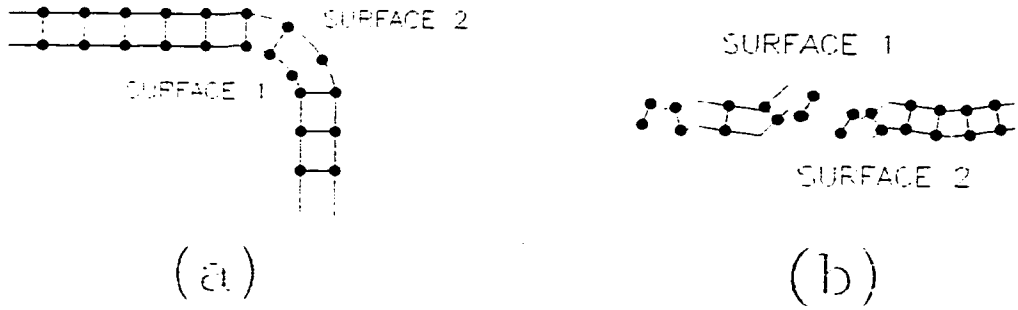

Figure 4.11: Surfaces defining Contact Elements

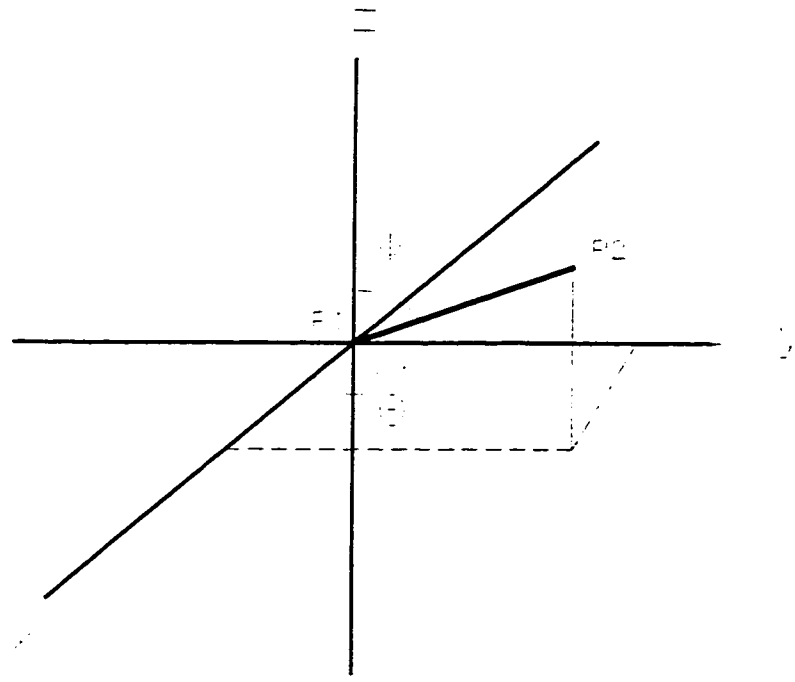

Figure 4.12: Global Co-ordinate System

Transformation of coordinates

Numerical treatment of thermal and mechanical contact problems require the transformation of the displacement vector solution from the global coordinate system to the local system ($\{\bar{\mathbf{d}}\}_{X,Y,Z} \rightarrow \{d\}_{x,y,z}$) to obtain the normal and shear stiffness of the contacting surfaces. To determine whether separation and/or micro-slip take (s) place the calculation of the local normal and shear stresses are required. This will be followed by the transformation of the local nodal force vector to the global coordinates system ($\{f\}_{x,y,z} \rightarrow \{\bar{\mathbf{f}}\}_{X,Y,Z}$), to define the boundary conditions for the linear stress problem. It should be noted that the displacements d_X, d_Y and d_Z represent the differences between the nodal deflection u, v, and w, in the X, Y, and Z directions, respectively:

$$\begin{aligned} d_X &= u_j - u_i \\ d_Y &= v_j - v_i \\ d_Z &= w_j - w_i \end{aligned} \tag{4.11}$$

where I and j are the indices of the two nodes connected by the element.

A vector in the direction of $\overline{\mathbf{P_1}\,\mathbf{P_2}}$ with magnitude f_n transforms to the global co-ordinate system as follows:

$$\begin{aligned} \mathbf{f}_X &= f_n \sin\phi \cos\theta \\ \mathbf{f}_Y &= f_n \sin\phi \sin\theta \\ \mathbf{f}_Z &= f_n \cos\phi \end{aligned} \tag{4.12}$$

If we assume that the contacting surfaces are isotropic, then the local *tx*-axis may be arbitrarily assigned the orientation angles $\theta_{tx} = \theta$ and $\phi_{ty} = \phi + 90$, so that the local *tx* and global X axes coincide when both $\theta_{tx} = 0$ and $\phi_{tx} = 0$. With the *tx*-axis defined in this way, ϕ represents the angle by which the local co-ordinate system is rotated about the local *ty*-axis and θ represents the angle of rotation about the local normal *n*- (or z) axis. Thus, the local *ty*-axis will always be found in the global XY plane, with orientation angles $\theta_{tx} = \theta + 90$ and $\phi_{tx} = 90$. Vectors

f_{tx} and f_{ty} may be expressed in terms of the normal directional angles by substituting into equations (4.12) as follows:

$$\begin{aligned} \mathbf{f}_X &= f_{tx} \cos\phi \cos\theta \\ \mathbf{f}_Y &= f_{tx} \cos\phi \sin\theta \\ \mathbf{f}_Z &= -f_{tx} \sin\phi \end{aligned} \tag{4.13}$$

and

$$\begin{aligned} \mathbf{f}_X &= -f_{ty} \sin\theta \\ \mathbf{f}_Y &= -f_{ty} \cos\phi \\ \mathbf{f}_Z &= 0 \end{aligned} \tag{4.14}$$

The transformation of the nodal force and displacement vectors form the local to the global coordinates systems is given by the following matrix notation:

$$\{\bar{\mathbf{f}}\} = [\mathbf{T}]\ \{f\} \tag{4.15}$$

and

$$\{\bar{\mathbf{d}}\} = [\mathbf{T}]\ \{d\} \tag{4.16}$$

where

$$\{f\}] = \begin{Bmatrix} f_{tx} \\ f_{ty} \\ f_n \end{Bmatrix}, \text{ and } \{\bar{\mathbf{f}}\} = \begin{Bmatrix} \mathrm{f}_X \\ \mathrm{f}_Y \\ \mathrm{f}_Z \end{Bmatrix} \tag{4.17}$$

and

$$\{d\} = \begin{Bmatrix} d_{tx} \\ d_{ty} \\ d_n \end{Bmatrix}, \text{ and } \{\bar{\mathbf{d}}\} = \begin{Bmatrix} \mathrm{d}_X \\ \mathrm{d}_Y \\ \mathrm{d}_Z \end{Bmatrix} \tag{4.18}$$

The transformation matrix [**T**] is defined as:

$$[T] = \begin{bmatrix} \cos(\phi)\cos(\theta) & -\sin(\theta) & \sin(\phi)\cos(\theta) \\ \cos(\phi)\sin(\theta) & -\cos(\theta) & \sin(\phi)\sin(\theta) \\ -\sin(\phi) & 0 & \cos(\phi) \end{bmatrix} \tag{4.19}$$

The inverse transformations are:

$$\{f\} = [T]^{-1}\{\bar{f}\}, \quad \text{and}$$
$$\{d\} = [T]^{-1}\{\bar{d}\} \tag{4.20}$$

Stiffness and force matrices in the global coordinate system

The local stiffness matrix of the three-dimensional contact element $[k]$ defines the relation between the local force and displacement vectors:

$$\{f\} = [k]\{d\} = [k][T]^{-1}[\bar{d}] \tag{4.21}$$

where,

$$[k] = \begin{bmatrix} k_{tx} & 0 & 0 \\ 0 & k_{ty} & 0 \\ 0 & 0 & k_n \end{bmatrix} \tag{4.22}$$

The element k_n, k_{tx} and k_{ty} of the local stiffness matrix $[k]$ are defined by equations (4.2) and (4.4). For isotropic surfaces, $k_{tx} = k_{ty} = k_s$. The local stiffness components $k_{tx} = k_{ty} = k_n = 0$, when separation or micro-slip takes place at a given location. In the case of slipping, opposite nodal friction forces are applied to the corresponding nodes; $f_t = \mu f_n$. From equations (4.15) and (4.21), the force vector in the global coordinate system is:

$$\{\bar{f}\} = [T][k][T]^{-1}\{\bar{d}\} \tag{4.23}$$

Given the 3×3 Thus local stiffness matrix $[k]$ (equation (4.22)), the 6×6 global stiffness matrix $[\mathbf{k}]$ is 4 is the assembled as follows:

$$\begin{Bmatrix} f_X^i \\ f_Y^i \\ f_Z^i \\ f_X^j \\ f_Y^j \\ f_Z^j \end{Bmatrix} = \begin{bmatrix} k & & -k & \\ & & & \\ & & & \\ -k & & -k & \end{bmatrix} \begin{Bmatrix} u^i \\ v^i \\ w^i \\ u^j \\ v^j \\ w^j \end{Bmatrix} \tag{4.24}$$

4.4.3.2 Thermal contact conductivity matrix of the interface element

The thermal interface elements are three dimensional brick elements with variable conductivity that is a function of the contact pressure, material properties and surface topography. Since equation (4.9) was found to produce lower values than those obtained experimentally [98], the coefficient and the exponent in equation (4.9) can be made equal to unity for simplicity and to agree with experimental observations. It can also be argued that the contact spots under higher local contact pressure will experience a higher contribution of the macroscopic constriction resistance as a result of the convergence of the heat flow lines at these locations. Therefore, to obtain the distribution of the macroscopic constriction resistance along the joint, Attia and Kops [85] assumed that the local value of $\mathbf{R}_{mac}$ is directly proportional to the local contact pressure.

Equating the thermal contact resistance of the interface $\mathbf{R}_c$ with the thermal resistance of the interface element $\mathbf{R}_{th}$, $\mathbf{R}_{th} = \Delta\ell/(k_e)$, yields an expression for the equivalent conductivity of the thermal brick contact element, $k_{e,th}$:

$$k_{e,th} = [\Delta\ell]\left[\frac{1}{\mathbf{R}_{e,mic_t} + \mathbf{R}_{e,mac}}\right] \tag{4.25}$$

where:

$$\mathbf{R}_{e,mic_t} = \left(\frac{\sigma}{\dot{m}\, k_h}\right)\left(\frac{H}{p_n}\right)$$

$$\mathbf{R}_{e,mac} = \frac{4L}{k}\sum_{n=1}^{\infty}\frac{1}{n}\left[\int_0^1 \left(\frac{p_n}{p_o}\right)\cos\,(n\pi\bar{x})d\bar{x}\right]^2 \times p_n \sum_{n=1}^{N}\frac{1}{p_{n,i}} \tag{4.26}$$

where $\Delta\ell$ is the thickness of the contact element, and the other parameters are defined as in equation (4.9). The contact pressure in equation (4.25), is the average pressure over the eight nodes of the brick element. It should also be noted that equation (4.25) represents the additional resistance introduced by the interface, excluding the thermal resistance of the subsurface layer and the bulk material.

4.4.4 Algorithm for Predicting the Thermoelastic Response Behaviour of Nonlinear Machine Tool Structures

Figure 4.13 shows the flowchart for the algorithm used to predict the thermal response of machine tool structures. There are three modules and three program utilities that are integrated for automated execution of the analysis. The first *interface element module*, uses the global displacements of the interface nodes and to define the global thermal contact conductivity $[\boldsymbol{C}]$ and stiffness $[\boldsymbol{k}]$ matrices, as well as the nodal force vector $\{\mathbf{f}_s\}$ to be applied to the interface elements if micro-slip was detected. Given the matrix [C], the temperature field in the structure is obtained using the second *thermal processor module*. The thermal deformation $\{\bar{\mathbf{d}}\}$ and thermal contact stresses are determined using the third *stress processor module*. The program modules are connected by the following three utilities:

1. The interface stiffness and contact conductivity matrices utility, which reads the latest $[\boldsymbol{C}]$ and $[\boldsymbol{k}]$ and $\{\mathbf{f}_s\}$ generated by the interface element module and updates the thermal and stress finite element models.
2. The second utility reads the nodal temperatures $\{\mathbf{t}\}$ generated by the thermal processor and writes $\{\mathbf{t}\}$ into the stress model.
3. The third utility reads the output of the stress processor to feed the interface element module with $\{\bar{\mathbf{d}}\}$.

If the difference between the initial and final deflections of the contact elements are greater than a predetermined tolerance then the updated deflections replace the initial deflections and the cycle begins again. A separate routine has also been developed and implemented to accelerate the convergence of the solution to the state of equilibrium.

In what follows, the first module which generates the stiffness and conductivity matrices will be briefly discussed.

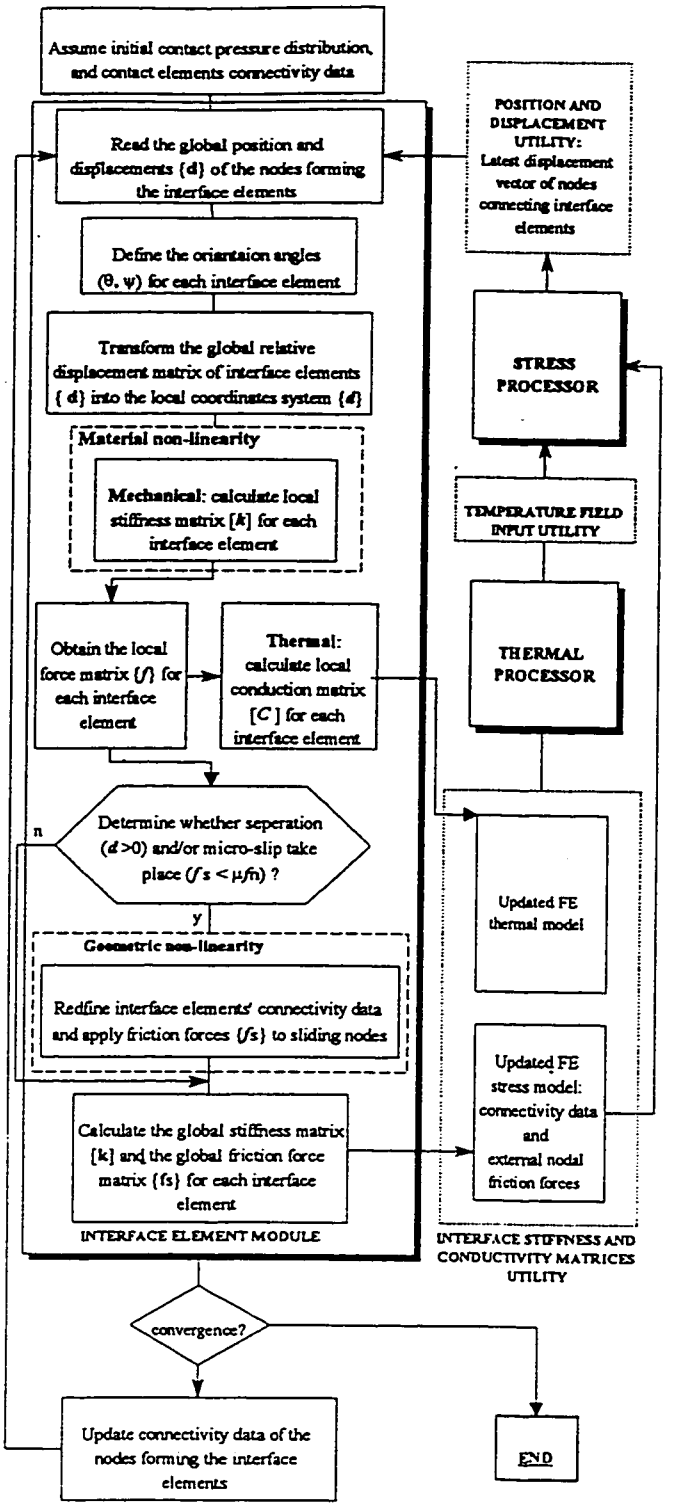

Figure 4.13: Flow Chart of the Contact Element Algorithm

Generation of the stiffness and conductivity matrices module

This program module proceeds in the following sequence:

- Establish the nodes to be connected by interface elements and read nodal positions and deflections from the output of the latest linear stress analysis iteration.
- Define the orientation angles θ and ψ for each interface element.
- Transform the global displacement matrix into the local domain and calculate $[k]$.
- Calculate the local force vector $\{f\}$ in the interface elements and test if the resultant shear nodal force $f_t > \mu f_n$. If this condition is satisfied, then $k_{tx} = k_{ty} = 0$ a force equal to μf_n is applied in the direction of f_t on node I and opposite to f_t on node j.
- Calculate the global stiffness matrix $[\mathbf{k}]$ and the global friction force vector $\{\mathbf{f}_s\}$ applied to the interface nodes as a result of micro-slip.
- Update the interface elements connectivity data.

The information obtained in the last two steps are to be input into the thermal and stress processors through the interface element utility, as discussed earlier.

4.4.5 The Complete Computer Model of the Nonlinear Machine Tool Structure

Figure 4.14 shows a three-dimensional box-shaped model of a horizontal milling machine. There are two heat sources (Q = 90 W) that are symmetrically placed in the column wall to represent bearings. The dimensions of the envelope containing the structure are 145 x 115 x 50 cm. The structure wall thickness of is 5 cm. The contact between the column and the table is assumed to take place over two strips 40 x 7.5 cm. A colour enhanced solid model of the column and contact strips with the table removed is shown in figure 4.15.

The physical and thermal properties of the material are those of gray cast iron: the thermal conductivity k= 40 Kcal/mh°C, the coefficient of thermal expansion α=13.7x10^{-6} mm/mm°C, the modulus of elasticity E= 1.06x10^6 kg/cm^2, and Brinell hardness H_B = 200. All external

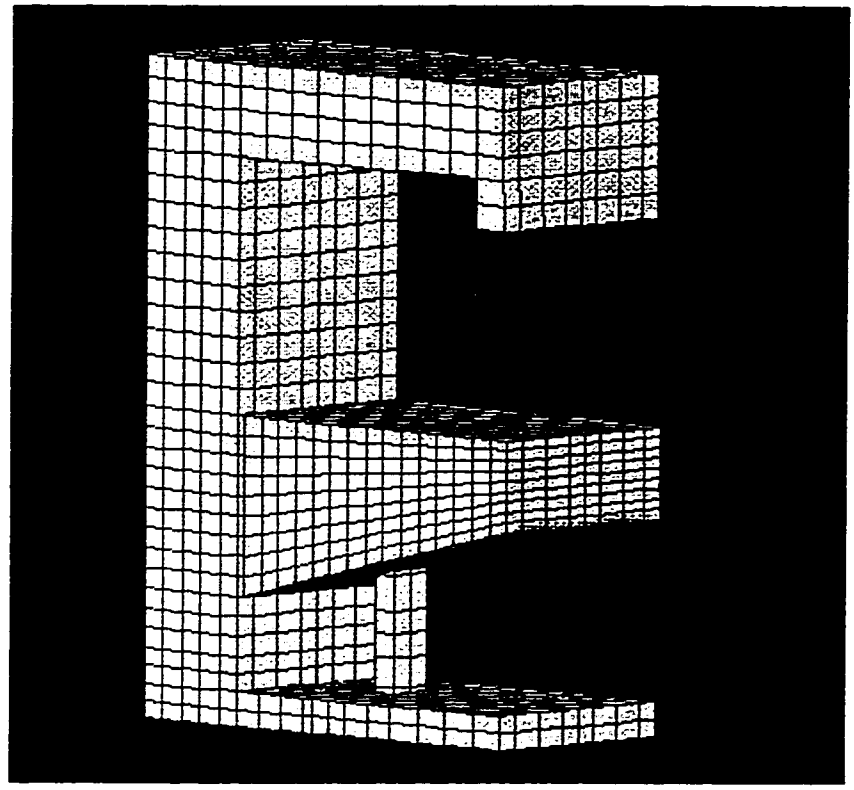

Figure 4.14: Nonlinear Finite Element Test Structure

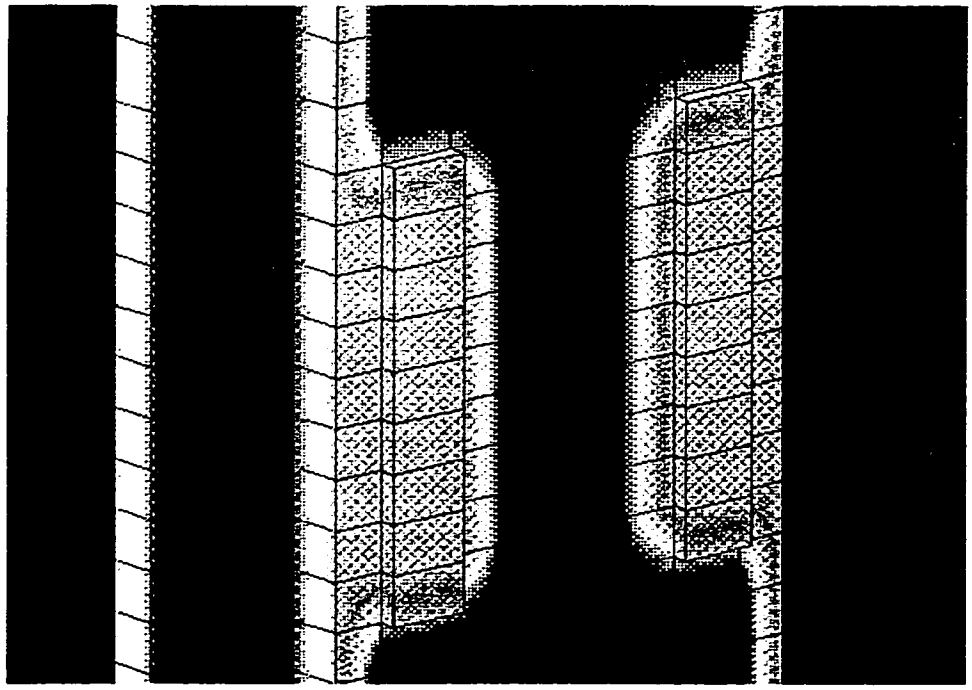

Figure 4.15: Color Enhancement of Contact Guideways

surfaces are exposed to convection, h = 6 kW/cm^2. In this model, the rigidity of the support screw is simulated by using a material of E = 3x10^7 kg/cm^2. The initial mechanical pressure is assumed to be uniformly distributed over the contact interface, $p_{c,mech}$ = 45 kg/cm^2.

The characteristics of the contacting surfaces, which determine their stiffness and thermal contact resistance are: standard deviation of surface roughness = 1.25 μm, and the average of the absolute slope of surface asperities= 0.14. The parameters which define the normal and shear compliance of the contact interface (equations (4.1) and (4.5)), using the kg/cm^2 and μm units are: c_n = 0.65, m = 0.5, s = 0.5 and R= 0.75.

CHAPTER 5: DERIVATION OF THE INVERSE TRANSFER FUNCTION FOR ESTIMATING HEAT GENERATION

5.1 Introduction

In this chapter, a procedure will be developed for calculating the magnitude of heat generation in a machine tool structure in real time, from temperature measurements in the vicinity of the heat sources. The development will begin with the determination of a generalized model of the temperature response to a heat source in the machine tool structure. The analytical form of the generalized model will be derived in such a way that it can accommodate an initial delay in the temperature step response, allowing for an accurate representation of a machine tool system where temperature must be measured relatively far from the source. The generalized model will then be transformed to the Laplace domain in the form of an analytical expression, which shall be inverted to define the Laplace transfer function of the inverse thermal system. Numerical methods will be developed to transform the transfer function to the time domain in the form of a convolution integral transfer function, suitable for real time computation. Stabilization of the inverse transfer function, called regularization, will be dealt with by a systematic approach.

5.2 The Derivation of the Inverse Transfer Function in The Laplace Domain

The general solution for the temperature distribution in a large plate with a circular heat generating ring of radius r_0 was derived in [83] and presented as equation (3.5). The equation is repeated here as follows:

$$T(r,t) = \frac{\alpha}{2\pi kw}\int_0^{\infty} \beta\, J_0(\beta r) J_0(\beta r_0)\, e^{-(a+\beta^2)\alpha t} \int_0^{t} q(\tau)\, e^{(\beta^2+a)\alpha t}\, d\tau\, d\beta \qquad (5.1)$$

If the heat generation is function q(t) is taken to be a step function of magnitude q at t=0, then the temperature step response simplifies to:

$$T(r,t) = \frac{q}{2\pi kw}\int_0^{\infty}\frac{\beta}{\beta^2+a}J_0(\beta r)J_0(\beta r_0)\left[1-e^{-(a+\beta^2)\alpha t}\right]d\beta \qquad (5.2)$$

After lumping the parameters $2\pi kw$ into an empirical parameter K, the generalized equation for a heat source in a large plate is obtained as follows:

$$T(r,t) = Kq\int_0^{\infty}\frac{\beta}{\beta^2+a}J_0(\beta r)J_0(\beta r_0)\left[1-e^{-(a+\beta^2)\alpha t}\right]d\beta \qquad (5.3)$$

The above equation is the generalized step response, presented in chapter 4. The Generalized step response shall now be transformed analytically to the Laplace domain by means of the transformation equation:

$$F(s) = \int_0^{\infty}e^{-st}f(t)\,dt \qquad (5.4)$$

where f(t) is the function in the time domain, F(s) is the transformed function in the Laplace domain, and s is the Laplacian operator. Substituting equation (5.3) into equation (5.4) and reversing the order of integration yields:

$$T(r,s) = Kq\int_0^{\infty}\frac{\beta}{\beta^2+a}J_0(\beta r)J_0(\beta r_0)\left(\int_0^{\infty}e^{-st}\left[1-e^{-(a+\beta^2)\alpha t}\right]dt\right)d\beta \qquad (5.5)$$

The part of the equation inside the brackets evaluates to:

$$\int_0^{\infty}e^{-st}(1-e^{-(a+\beta^2)\alpha t})dt = \frac{\alpha(a+\beta^2)}{s(s+[a+\beta^2]\alpha)} \qquad (5.6)$$

Thus the transformed equation is given by:

$$T(r,s) = K\alpha q\int_0^{\infty}\frac{\beta J_0(\beta r)J_0(\beta r_0)}{s(s+[a+\beta^2]\alpha)}d\beta \qquad (5.7)$$

Since the input corresponding to the step response is Q(s)=q/s, the transfer function $H_T(s)=T(r,s)/Q(s)$ is obtained by multiplying equation (5.7) by s/q, to yield:

$$H_T(r,s) = K\alpha \int_0^{\infty} \frac{\beta\, J_0(\beta r)\, J_0(\beta r_0)}{s+[a+\beta^2]\alpha} d\beta \tag{5.8}$$

In the Laplace domain, finding the inverse transfer function from the direct transfer function is trivial since it is found simply by taking the reciprocal of the direct transfer function. Thus:

$$G(r,s) = \frac{1}{H_T(r,s)} = \frac{1}{K\alpha \int_0^{\infty} \frac{\beta\, J_0(\beta r)\, J_0(\beta r_0)}{s+[a+\beta^2]\alpha} d\beta} \tag{5.9}$$

If the three parameters K, a, α, and r_0 are calibrated from experimental data, equation (5.9) gives the inverse transfer function in the Laplace domain, as a function of the Laplacian variable s.

In a later section of this chapter, the Laplace domain transfer function G(r,s) shall be transformed into the time domain transfer function G(r,t) by means of the inverse Laplace transform equation:

$$G(r,t) = \int_{\sigma-j\infty}^{\sigma+j\infty} e^{st} G(r,s)\, ds \tag{5.10}$$

where σ is a real number that is larger than the largest pole of G(r,s). Taking s=R+Ij, and assuming that R meets the conditions imposed on σ and that G(r,t) is a causal function, equation (5.10) becomes the real integral {46}{86}:

$$G(r,t) = \frac{e^{Rt}}{\pi} \int_0^{\infty} \Re\{G(r,R+Ij)\} \cos(tI) - \Im\{G(r,R+Ij)\} \sin(tI)\, dI \tag{5.11}$$

where from equation (5.9):

$$\Re\{G(r,R+Ij)\} = \frac{\Re\{H_T(r,R+Ij)\}}{\Re\{H_T(r,R+Ij)\}^2+\Im\{H_T(r,R+Ij)\}^2}$$

$$\Im\{G(r,R+Ij)\} = \frac{-\Im\{H_T(r,R+Ij)\}}{\Re\{H_T(r,R+Ij)\}^2+\Im\{H_T(r,R+Ij)\}^2} \tag{5.12}$$

In order to successfully solve equation (5.11) numerically for different values of t, the expression for $H_T(r,s)$ in equation (5.8) will have to be evaluated over a wide range of complex values, extending from s=0+0j to s→∞+∞j. It will be shown that for a given time value t, the real component of s will be constant, and so $H_T(r,s)$ will have to be evaluated incrementally in the range s=R+0j to s→R+∞j.

The improper integral in equation (5.8) has no closed form solution and is difficult to evaluate numerically. The numerical problem arises because the decaying oscillatory integrand is coupled with an infinite limit on the integration. In order to preserve the accuracy of the approximation, the numerical integration must incorporate a certain minimum number of samples for each oscillation, and it must include the contributions from all oscillations with magnitudes above a certain threshold level. For slowly decaying functions with high oscillating frequencies, the number of samples for the numerical integration becomes very large. The number of samples affects the computation time of the numerical integration algorithm, but more importantly there is a practical limit on the number of samples that can be used for a given numerical resolution of the compiler. Since each addition and subtraction performed by the computer in executing the numerical integration algorithm introduces some round off error, the accumulated truncation error becomes larger as the number of samples increases. This implies a practical limit on the number of samples, and hence on the usable range of the numerical solution. The usable range is severely limited for this equation because of the Bessel functions in the integrand. The two numerical estimates for $J_0(x)$ are the bottleneck, both in terms of computation time and truncation error.

In general, the larger the value of s, the greater is the number of samples required for the numerical evaluation of equation (5.8). Equation (5.8) was integrated directly on the VAX 7600 mainframe computer in double precision (12 significant digits) and in quadruple precision (24 significant digits), for various sample point distributions. The conclusion of this

effort was that direct integration of equation (5.8) cannot result in a transfer function which is accurately invertible to the time domain by equations (5.11) (5.12) because of truncation error. The extremely long computation time also makes it impractical to consider using higher numerical precision with greater numbers of sample points.

5.3 The Numerical Calculation of the Inverse Transfer Function in the Laplace Domain

5.3.1 The Convergence Problem

In order to consider the convergence properties of equation (5.8) in more detail the integrand function is considered separately from equation (5.8) as follows:

$$Integrand(r,s) = \alpha\,\beta\,J_0(\beta r)\,J_0(\beta r_0)\frac{\beta}{s+[a+\beta^2]\alpha} \tag{5.13}$$

If s is a complex variable in the form R+Ij, where R is the real component and I is the imaginary component, then the integrand can be expressed by its real and imaginary components:

$$\begin{aligned} \Re\{Integrand(r,s)\} &= J_0(\beta r)\,J_0(\beta r_0)\,\alpha\beta\frac{R+\alpha(a+\beta^2)}{(R+\alpha[a+\beta^2])^2+I^2} \\ \Im\{Integrand(r,s)\} &= -J_0(\beta r)\,J_0(\beta r_0)\,\alpha\beta\frac{I}{(R+\alpha[a+\beta^2])^2+I^2} \end{aligned} \tag{5.14}$$

Each of the above equations will be considered in two parts, with the first part containing the Bessel functions:

$$P_1 = J_0(\beta r)\,J_0(\beta r_0)\,\alpha\beta \tag{5.15}$$

and the second part being the balance of the equation. Now it can be shown that as $x\to\infty$, the Bessel equation converges to a purely harmonic function:

$$\lim_{x\to\infty} J_0(x) = \frac{\cos(x)+\sin(x)}{\sqrt{\pi x}} \tag{5.16}$$

Thus, as $\beta\to\infty$, equation (5.15) approaches the function:

$$P_1 = \frac{(\cos(\beta r)+\sin(\beta r))(\cos(\beta r_0)+\sin(\beta r_0))}{\frac{\pi}{\alpha}\sqrt{rr_0}} \tag{5.17}$$

which is a harmonic function with frequencies defined by r and r_0 that neither decays nor grows as $\beta \to \infty$. Therefore, in order for the integral in equation (5.8) to converge to a finite result, the second part of the real and imaginary parts of the integrand in equation (5.14) must decay to zero as $\beta \to \infty$ for all real values of R and I. This requirement would not appear to pose any problem since the denominator in equation (5.14) is two orders higher than the numerator for the real component and four orders higher in the imaginary component. A problem does arise however, because in order to calculate G(r,t) for a particular value of t, equation (5.8) must be evaluated in increments of I from $0 \to \infty$. Letting $\beta \to \infty$ and $I \to \infty$ in equation (5.14) results in the following limits:

$$\begin{aligned} \lim_{\beta\to\infty\, I\to\infty} \Re\{Integrand(r,s)\} &= \frac{\alpha\beta^2}{\alpha^2\beta^4+I^2} \\ \lim_{\beta\to\infty\, I\to\infty} \Im\{Integrand(r,s)\} &= \frac{-I}{\alpha^2\beta^4+I^2} \end{aligned} \tag{5.18}$$

For small values of β, the β^4 term in the denominator is negligible compared to I^2. It is only after the β^4 term exceeds I^2 that it can carry the function toward zero. This means that as I becomes larger, the limit for the integration in β must be increased also, in proportion to $\sqrt{I}$. Since the integral will have to be evaluated for very large values of I, the limit on the integration will be very large also.

Another problem concerns the numerical evaluation of equations (5.11) and (5.12). The transfer function G(r,s) does not actually converge to a finite value, it is only the Euler transformation of G(r,s) that is convergent, as will be discussed shortly. In order to numerically determine the Euler transform of G(r,s) it is necessary to first calculate G(r,s), the numerical values of which quickly become unmanageably large for large values of s=R+Ij. In order to

minimize round off error, the integrals in equation (5.8) must be calculated with high precision, further pushing out the limit of β in the integration.

5.3.2 Improving the Convergence Properties of the Numerical Calculation

As previously discussed, it is not possible to numerically evaluate equation (5.8) directly because round-off error corrupts the numerical summation before the integral in β has converged with sufficient accuracy, for large values of I. The problem is the integrand, which oscillates and decays more slowly for large I. Now this problem would not exist if the first part of the integrand, the part in equation (5.15), could be made to decay to zero by itself, independently of the second part of the integrand which contains variable I. If this could be accomplished then the convergence of integral (5.8) would not depend on I, and convergence of the integral would be assured even as I→∞. Consider again equation (5.8), rearranged slightly to separate the oscillatory part of the integrand:

$$H_T(r,s) = K\int_0^{\infty} J_0(\beta r)\,J_0(\beta r_0)\,\beta\,\frac{\alpha}{s+[a+\beta^2]\alpha}\,d\beta \tag{5.19}$$

Now consider the oscillatory part of the integrand as a function of β:

$$D(\beta) = J_0(\beta r)\,J_0(\beta r_0) \tag{5.20}$$

As β→∞, $D_a(\beta)$ is found using equation (5.16):

$$D_a(\beta) = \lim_{\beta\to\infty} D(\beta) = \frac{(\cos(\beta r)+\sin(\beta r))(\cos(\beta r_0)+\sin(\beta r_0))}{\pi\beta\sqrt{rr_0}} \tag{5.21}$$

which decays as a first order power of β. The first order power of β in the denominator is just enough to cancel the β term in the numerator of the integrand, but not enough to guarantee convergence. Now define a new function $\bar{D}(\beta)$ by subtracting $D_a(\beta)$ function from $D(\beta)$:

$$\bar{D}(\beta) = J_0(\beta r)J_0(\beta r_0) - \frac{(\cos(\beta r)+\sin(\beta r))(\cos(\beta r_0)+\sin(\beta r_0))}{\pi\beta\sqrt{rr_0}} \tag{5.22}$$

This new function is also oscillatory at the same frequency as D(β), however it decays with a higher order of β. Figure 5.1 shows a plot of D(β) for r=3.0 and r_0=1.0, which is oscillatory and decaying as a first order inverse as expected. Figure 5.2 shows a plot of $\bar{D}(\beta)$ for β=0→8 indicating a rapid initial decay, and figure 5.3 shows $\bar{D}(\beta)$ for β=10→50, indicating that the rate of decay moderates for large β. The actual order of decay of $\bar{D}(\beta)$ is approximately $1/\beta^{3/2}$ when $\beta > 10$. Since the inverse power of β is greater than one, the new function will bring the integrand to zero independently of parameter I.

Rewriting equation (5.19) in terms of D(β) yields the following:

$$H_T(r,s) = K\int_0^{\infty} D(\beta,r,r_0)\beta\frac{\alpha}{s+[a+\beta^2]\alpha}d\beta \tag{5.23}$$

Figure 5.4 shows a plot of the real part of the integrand of equation (5.23) versus β for r=1.0, r_0=0.1, a=0.08, α=0.029, R=1.0, and I=2.0. Figure 5.5 shows the real integrand for the same values except that I=200. The figures show that the integrand decays with an increasing effective time constant for larger values of I. Figure 5.6 shows the real integrand with D(β) replaced by $\bar{D}(\beta)$, using the same values and I=200. The modified integrand clearly decays much faster than the unmodified integrand. Furthermore, the integrand always decays at least on the order of $1/\sqrt{\beta}$, independently of I, and for small values of I the rate of decay is considerably faster.

The modified integrand can be used to obtain a faster and more accurate solution to equation (5.19) in the following manner. Firstly, $D_a(\beta)$ has been defined from D(β→∞) as follows:

$$\overline{D_a}(\beta) = \frac{(\cos(\beta r)+\sin(\beta r))(\cos(\beta r_0)+\sin(\beta r_0))}{\pi\beta\sqrt{rr_0}} \tag{5.24}$$

The modified function $\bar{D}(\beta)$ can then be expressed as follows:

$$\overline{D}(\beta) = D(\beta) - \overline{D_a}(\beta) \tag{5.25}$$

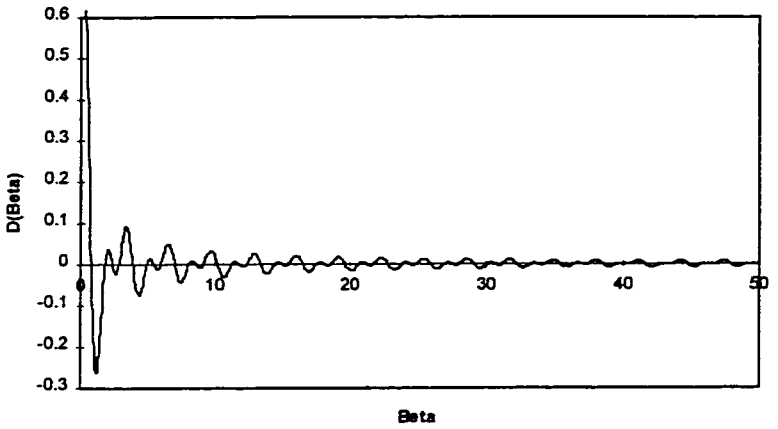

Figure 5.1: Plot of D(β) for r=3.0 and r_0=1.0

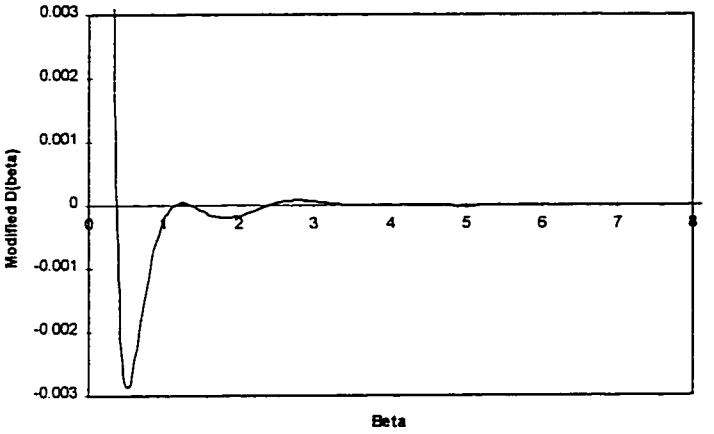

Figure 5.2: Plot of $\bar{D}(\beta)$ for β = 0→8

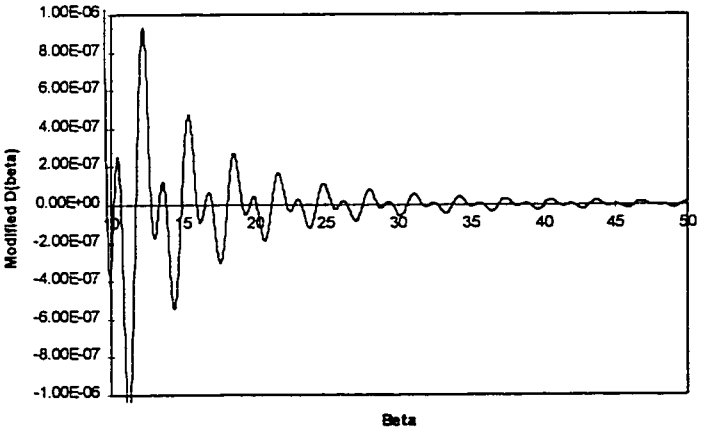

Figure 5.3: Plot of $\bar{D}(\beta)$ for β=10→50

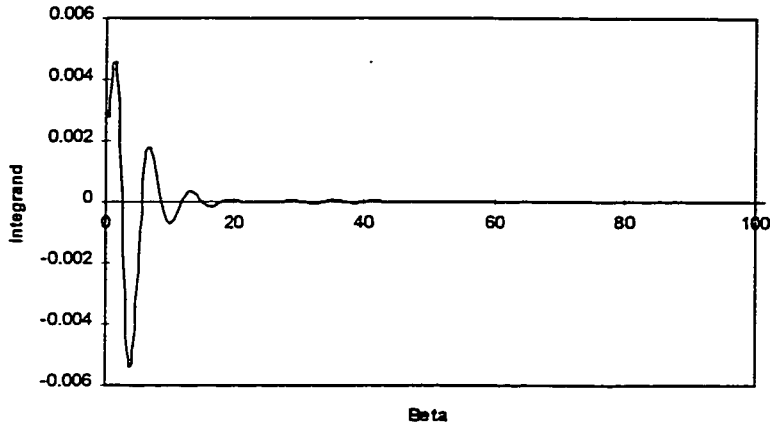

Figure 5.4: Unmodified Integrand for I=2

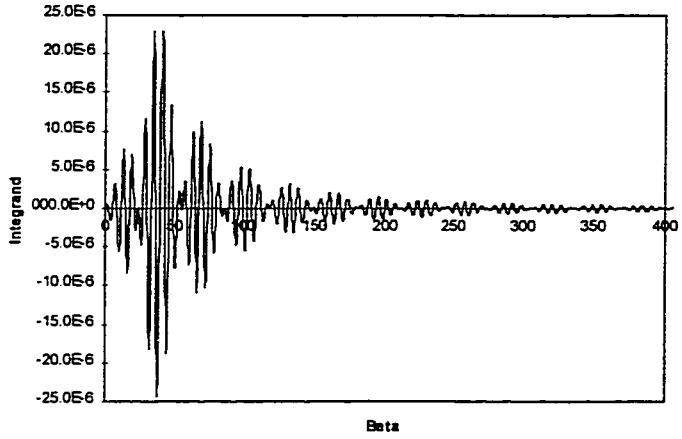

Figure 5.5: Unmodified Integrand for I=200

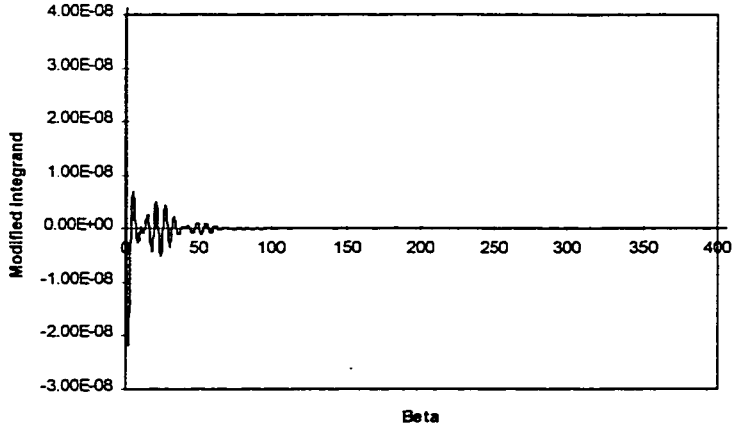

Figure 5.6: Modified Integrand for I=200

and equivalently:

$$D(\beta) = \overline{D}(\beta) + \overline{D_a}(\beta) \tag{5.26}$$

Now substitute equation (5.26) into equation (5.23) to give:

$$H_T(r,s) = K\int_0^{\infty}\left(\overline{D}(\beta) + \overline{D_a}(\beta)\right)\beta\frac{\alpha}{s+[a+\beta^2]\alpha}d\beta \tag{5.27}$$

Which expands to:

$$H_T(r,s) = K\int_0^{\infty}\overline{D}(\beta)\frac{\alpha\beta}{s+[a+\beta^2]\alpha}d\beta + K\int_0^{\infty}\overline{D_a}(\beta)\frac{\alpha\beta}{s+[a+\beta^2]\alpha}d\beta \tag{5.28}$$

The first integral in equation (5.28) contains the modified integrand which decays at the rate of $1/\sqrt{\beta}$ or faster. The second integral however contains the $\bar{D}_a(\beta)$ function which only just cancels the β term in the numerator as $\beta\to\infty$, and therefore has the same convergence problem as $D(\beta)$. The important difference however, lies in the ease of computation of $\bar{D}_a(\beta)$, which requires the calculation of one sine and one cosine function, as compared to $D(\beta)$ which requires the calculation of two Bessel functions. For comparison, an algorithm based on $\bar{D}_a(\beta)$ will run somewhere in the vicinity of 1000 times faster than an algorithm based on $D(\beta)$ for the same number of sample points and calculated precision. Equation (5.28) is therefore, a practical means of computing $H_T(r,s)$ numerically, to be then used in equations (5.11) and (5.12) to generate the time domain transfer function G(t).

5.4 The Transformation of the Inverse Transfer Function to the Time Domain

5.4.1 The Numerical Transformation Equation

The inverse transform of G(r,s) into the time domain transfer function G(r,t) is defined by the inverse Laplace transform equation:

$$G(r,t) = \frac{1}{2\pi j}\int_{\sigma-j\infty}^{\sigma+j\infty} e^{st}G(r,s)\,ds \tag{5.29}$$

where σ is a real number that is larger than the largest pole of G(r,s). Taking s=R+Ij, and assuming that R meets the conditions imposed on σ and that G(r,t) is a causal function,

equation (5.29) may be integrated along a vertical line on the complex plane, yielding the real integral:

$$G(r,t) = \frac{e^{Rt}}{\pi}\int_0^{\infty} \Re\{G(r,R+Ij)\}\cos(tI) - \Im\{G(r,R+Ij)\}\sin(tI)\,dI \qquad (5.30)$$

Equation (5.30) may be numerically evaluated by a number of methods. It is normally the case that higher order methods like Gaussian quadrature will produce more accurate estimates to an integral when a fixed number of data points are available. However this assumption is not necessarily true in the context of the Laplace inversion integral, because the primary source of error might not be due the numerical integration itself. There are two other sources of error, due to the inevitable processes of sampling in the time domain and sampling in the Laplace domain. Sampling in the Laplace domain occurs because of the necessity of numerically evaluating equation (5.8) to obtain $H_T(r,s)$. The evaluation of equation (5.8) is based on a fixed number of samples, which gives rise to a phenomenon called *aliasing*. A sampled-time signal cannot be completely reconstructed unless the sampling frequency is at least twice the system bandwidth, or in other words the sampling interval T must be less than 1/(2B), where B is the system bandwidth in Hz. This must be kept in mind when writing the algorithm to evaluate equation (5.8). The second source of error is the sampling in the Laplace domain, which is inevitable when numerically evaluating equation (5.39). Sampling in the s-domain yields a solution which is periodic in the time domain, therefore it is necessary to ensure that the maximum interval between samples ΔI is less than $2\pi/\tau$, where τ is the largest time value for which G(r,t) will be evaluated.

One possible solution to equation (5.30) is obtained by replacing the integral by the trapezoidal summation formula. This is the solution method proposed in a paper by Crump [103], which results in the summation:

$$G(r,t) = \frac{e^{at}}{T}\left[\frac{1}{2}G(r,R) + \sum_{k=1}^{\infty}\left\{\Re G\left(r,R+\frac{k\pi j}{T}\right)\cos\left(\frac{k\pi t}{T}\right) - \Im G\left(r,R+\frac{k\pi j}{T}\right)\sin\left(\frac{k\pi t}{T}\right)\right\}\right] \quad (5.31)$$

where a and T are empirical parameters satisfying the conditions T > t and a > α, such that:

$$|G(r,t)| \leq Me^{\alpha t} \quad (5.32)$$

The computational efficiency of the algorithm is improved if T is taken to be 2t, because then the sine and cosine terms disappear. In this case, equation (5.31) becomes:

$$G(r,t) = \frac{e^{Rt}}{2t}\left[\frac{1}{2}Q(r,R) + \sum_{k=1}^{\infty}\left\{\Re G\left(r,R+\frac{\pi j}{t}\right)(-1)^k - \Im G\left(r,R+\frac{(2k-1)\pi j}{2t}\right)(-1)^{k-1}\right\}\right] \quad (5.33)$$

The choice of the parameter *a* is critical to the convergence of equation (5.33). Equation (5.33) is the product of two functions, one that includes the term e^{Rt} and the other that includes the infinite series. As the product {Rt} becomes large then the first term becomes large, and the infinite series must become very small in order to converge to the same G(r,t). In order to minimize truncation error in the numerical calculation of equation (5.33), it not desirable that the ratio between the first and second products be very large or very small. A suitable ratio may be obtained by restricting the product Rt. It has been shown [83] that an Rt product equal to about 3.0 will yield a stable result over a wide range of the variable t. Thus, the parameter R is approximated by:

$$R = \frac{3}{t} \quad (5.34)$$

5.4.2 The Problems Associated with Transforming an Inverse Transfer Function

The Crump formula in equation (5.33) is not a practical inversion formula because of its typically slow convergence for most transfer functions. The slow convergence is particularly detrimental in the present application because of the fact that the s-domain transfer function G(r,s) must also be determined numerically for each value of s=R+Ij. A second problem with the Crump formula is that it will only converge to a solution if G(r,s) converges to zero as

s→R+∞j. For an inverse transfer function, G(r,s) never converges to zero as s→R+∞j. In fact, for most inverse transfer functions, including the ones that will be considered later in this thesis, G(r,s) goes to infinity as s→R+∞j.

The fact that G(r,s) must converge to zero as s→R+∞j in order for the time domain function to converge to finite values can seen by referring to equation (5.30). Unless the real and imaginary parts of G(r,s) converge to zero, the integrand will not decay to zero and so there will not be a finite limit for any value of t as the integration in variable I→∞. Notice however, that the sign of the integrand oscillates between positive and negative at the frequency of the sine and cosine terms. It is a fact that for all inverse transfer functions the cumulative integration oscillates between positive and negative values, with the positive and negative peaks approaching either a constant value or, more commonly, approaching infinity. The reason for this, as will now be explained, is that an inverse transfer function contains singularity functions which do not satisfy the existence criterion of the Laplace transform, and therefore do not actually 'exist' in the time domain. The divergence of the inversion integral for inverse transfer functions is therefore caused by the nature of the transfer function, rather than by the choice of solution algorithm which led to equation (5.33).

As was explained in chapter 2, the term 'inverse problem' normally is used to describe a type of problem that has particular characteristics, and that requires a special type of solution. The mathematical definition of an inverse problem is that the highest order derivative of the input variable be equal to or greater than the highest order derivative of the output variable. For a linear problem with one input variable x, and one output variable y, the mathematical form of the problem is as follows:

$$a_0 y + a_1 \frac{dy}{dt} + a_2 \frac{d^2y}{dt^2} + ...a_m \frac{d^m y}{dt^m} = b_0 y + b_1 \frac{dx}{dt} + b_2 \frac{d^2x}{dt^2} + ...b_n \frac{d^n x}{dt^n} \qquad (5.35)$$

where n≥m in the case of an inverse problem. Taking the Laplace transform of equation (5.35) with zero initial conditions, the transfer function G(s)=Y(s)/X(s) can be obtained:

$$G(s) = \frac{Y(s)}{X(s)} = \frac{b_0 + b_1 s + b_2 s^2 + ...b_n s^n}{a_0 + a_1 s + a_2 s^2 + ...a_m s^m} \tag{5.36}$$

Since n≥m for an inverse problem, the transfer function G(s) is not a proper fraction and so G(s)→∞ as s→R+∞j, as expected. Now as long as n is finite, G(s) can be expressed in partial fraction form as follows:

$$G(s) = c_0 + c_1 s + c_2 s^2 + ... c_i s^i + \frac{d_0 + d_1 s + d_2 s^2 + ...d_n s^k}{e_0 + e_1 s + e_2 s^2 + ...e_l s^l} \tag{5.37}$$

where k>l making the last term a proper fraction. Since the last term is a proper fraction, it behaves as an ordinary direct transfer function. That is, since the highest power of s is greater in the denominator than in the numerator, then G(s)→0 as s→R+∞j and so its inverse transformation converges to a finite result. As well as the proper fraction, there are I+1 additional terms in equation (5.37), where the value of I is equal to n-m. These terms will be called the *singularities* of the inverse transfer function, and they are the part of the transfer function which do not physically exist in the time domain, and so cause the failure of the inverse transformation equation (5.33). The balance of the transfer function will be called the *proper* transfer function, because of the fact that it converges to zero as s→R+∞j.

By analogy with equation (5.37), the numerical transfer function G(r,s) diverges because it contains singularity functions. Unfortunately, it is not possible to mathematically separate the singularities from the proper transfer function, as was done with the polynomial transfer function in equation (5.37). However it is possible to separate G(r,s) into its proper part and singularity part by an acceleration algorithm which filters singularities from the solution, as will now be derived.

5.4.3 Acceleration of the Numerical Transformation from Laplace to Time

In order to derive the acceleration algorithm, G(r,s) in equation (5.33) will be replaced by the proper transfer function 1/(s+1). Figure 5.7 shows the cumulative summation of equation (5.33) for G=1/(s+1) and t=1, where k is the number of terms in the summation and S_k is the cumulative sum. In the first place, notice that the derivative of the cumulative summation changes sign with each k. This is a result of choosing T=2t in the derivation above. Equation (5.33) converges to a value, but it does so slowly and in an oscillatory manner. It would seem that it might be possible to anticipate the final value by looking at the centre of the oscillations. The curve labelled 'averaged S_k' in figure 5.7 was obtained by averaging the S_k value with the S_{k-1} value, which produces a marked decrease in the range of the oscillations. The range of oscillations can be reduced still further by performing a second averaging operation on the averaged cumulative values, and a third averaging operation reduces the operations still further. The number of nested averages that can be taken depends on the number of successive approximations that are available. At k=2, only one nested average is possible:

$$f=\frac{T_1+T_2}{2} \tag{5.38}$$

where T_1 and T_2 are the first and second cumulative sums S_1 and S_2. At k=3, the average of the averages is:

$$f_2 = \frac{\frac{T_1+T_2}{2}+\frac{T_2+T_3}{2}}{2} = \frac{T_1+2T_2+T_3}{4} \tag{5.39}$$

Similarly for k=n, the $(n-1)^{th}$ nested average is given by [83]:

$$f_n = \frac{a_1T_1+a_2T_2+a_3T_3+.....a_nT_n}{b} \tag{5.40}$$

where the co-efficients a_i are given in table 5.1. The co-efficients in table 5.1 can be derived by a recursive formula for any k. Thus, if a_{ij} is the co-efficient in column I and row j, then:

$$a_{ij} = a_{i-1j-1} + a_{ij-1} \tag{5.41}$$

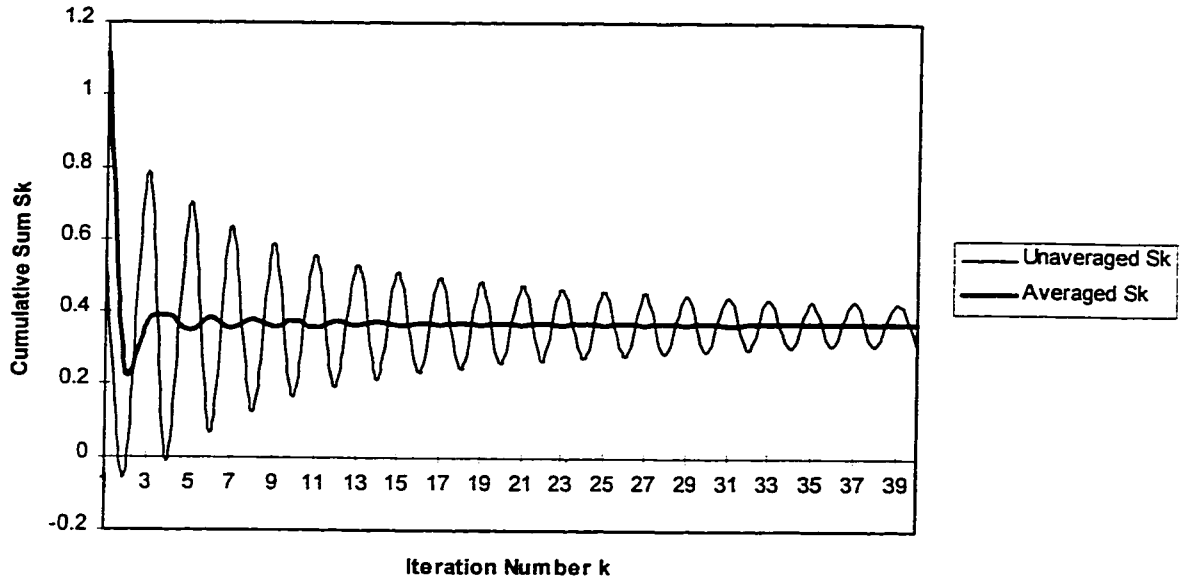

Figure 5.7: Unmodified and Averaged S_k vs. k

Table 5.1: Coefficients for the Accelerating Algorithm

a1	a2	a3	a4	a5	a6	a7	a8	b
1	1							2
1	2	1						4
1	3	3	1					8
1	4	6	4	1				16
1	5	10	10	5	1			32
1	6	15	20	15	6	1		64
1	7	21	35	35	21	7	1	128

The speed of convergence is fastest when the maximum number of averaging processes are performed on the data which is available. That is, when k=2 a single average of the two values is taken, when k=3 a second nested average is taken, and when k=n, n-1 nested averages are taken. The resulting series will be called the *accelerated* series, and when applied to the transformation equation (5.33) it will be called the *accelerated transformation*. The formula in equation (5.40) with co-efficients given by equation (5.41) is also known as the Euler transformation, which is defined as follows:

$$S^{a}{}_{k} = (q+1)^{-k-1}\left[q^{k}T_0 + \binom{k}{1}q^{k-1}T_1 + \binom{k}{2}q^{k-2}T_2 + \ldots + T_k\right] \tag{5.42}$$

where k is the iteration number, T_k is the k^{th} term of the unaccelerated series, and q=1. The advantage of using equations (5.40) and (5.41) instead of equation (5.42) is that the acceleration co-efficients are found recursively, rather than by the binomial terms. Calculating the binomial terms involves multiplying and dividing the very large numbers produced by the factorials, which causes numerical failure of the algorithm after only a small number of iterations.

Figure 5.8 compares the convergence of the accelerated transformation with the transformation using only one averaging process from figure 5.7. The convergence is several orders of magnitude faster, up until around iteration 36 when the accelerated algorithm suddenly fails. The failure of the accelerated algorithm is a result of the size of the coefficients given by equation (5.41) growing geometrically with the iteration number k. After k=35, the operations of adding and multiplying very large and very small numbers causes fatal truncation error. The number of iterations can be increased somewhat by using a compiler with quadruple precision to run the algorithm, however this is not necessary in practice since the accelerated algorithm converges extremely rapidly. Figure 5.9 shows the approximation error for the accelerated and single averaged transformations. The accelerated algorithm has converged beyond the numerical resolution of a 12 digit mantissa after 10 iterations.

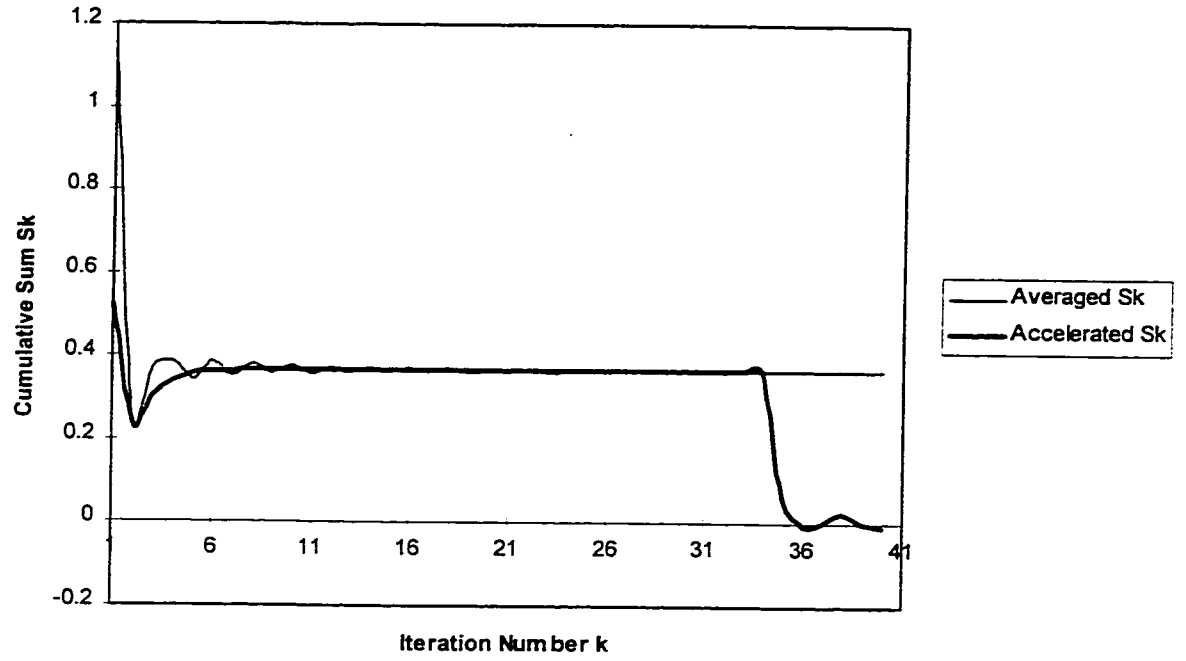

Figure 5.8: Averaged and Accelerated S_k vs. k

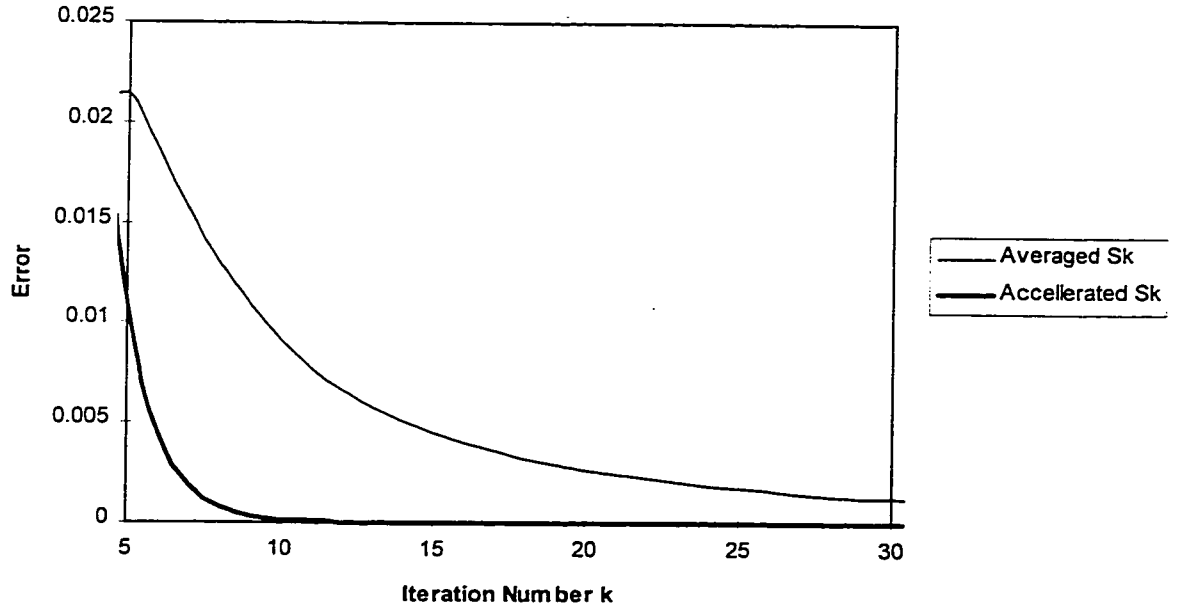

Figure 5.9: Error vs. k for Averaged and Accelerated S_k

A second important feature of the accelerated transformation is that it filters singularities from the time domain solution, and this is not just a lucky co-incidence. From a more abstract point of view, the accelerated transformation gives a physical interpretation to singularities that agrees with the analytical definition. In this sense, the accelerated transformation is a more complete representation of signals than the unaccelerated Laplace transformation which cannot properly handle singularity functions. The abstract perspective will not be dealt with in detail in this thesis, instead it will focus on the practical aspects of filtering singularities and increasing the order of convergence. The abstract perspective has been used however, to evaluate integral (5.32) in section 5.2.3, and so a discussion of this will be given at the end of this chapter.

To understand how the acceleration algorithm filters singularities from the time-domain solution, consider the transformation of the impulse function G(s)=1. Substituting G(R+Ij)=1 into equation (5.30) yields the following expression in the time domain:

$$G(t) = \frac{e^{Rt}}{\pi}\int_0^{\infty}\cos(tI)dI \tag{5.43}$$

When t=0, equation (5.52) is infinite, as expected for a unit impulse. When t≠0 equation (5.43) should be zero but it is not. Evaluating the integral in equation (5.43) when t≠0 yields:

$$G(t) = \frac{e^{Rt}}{\pi t}\sin\infty \tag{5.44}$$

which does not equal zero unless ∞ is a multiple of π. Equation (5.44) is not a physically correct interpretation of the impulse function in the time domain. Figure 5.10 shows the unaccelerated transformation of the unit impulse at t=1 by a plot of the cumulative sum versus iteration. As expected by equation (5.44), the transformation does not converge, rather it oscillates about zero indefinitely. Figure 5.10 also shows the accelerated transformation of G(s)=1 at t=1. The accelerated transformation converges to zero, and does so after only 3 iterations. Figure 5.11 shows the accelerated and unaccelerated transformations of a unit

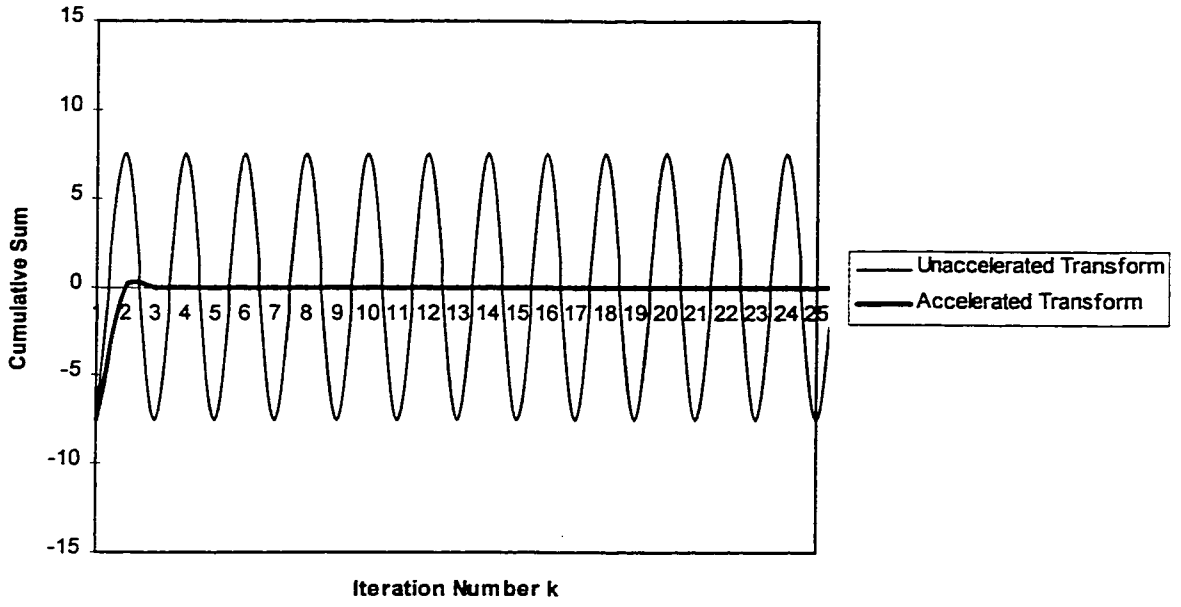

Figure 5.10: Convergence of an Impulse

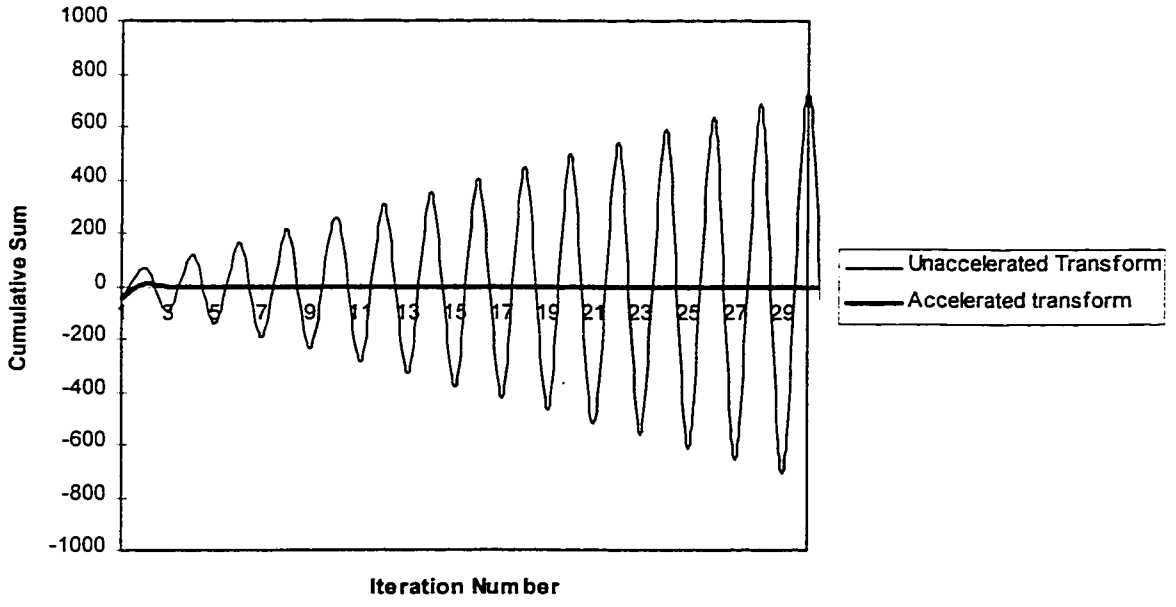

Figure 5.11: Convergence of Doublet

doublet G(s)=1 at t=1. The unaccelerated transformation oscillates about zero with an increasing amplitude, while the accelerated transformation converges rapidly to zero. Since all of the singularities in equation (5.37) transform to zero in the same way when $t \neq 0$, the accelerated transformation of equation (5.37) will converge to the time value of the last term only, and it will do so at an accelerated rate. When applied to G(r,s), the accelerated transformation filters the singularity functions from the transfer function and converges to the proper part of G(r,t) only. The only exception is when t=0, when the accelerated transformation is infinite.

5.5 Transforming the Singularities of the Inverse Transfer Function

The accelerated transformation is a practical means to transform the proper part of an inverse transfer function from the Laplace domain to the time domain. However, there are two elements to the transfer function which cannot be transformed in this way. The first is the value of G(r,t) when t=0, and the second is the singularity functions. The singularity functions cannot be identified in the time domain like the proper part of the transfer function, however they can be identified in the Laplace domain, using the transfer function G(r,s). Referring to the analytical transfer function in equation (5.37), it can be seen that as $s \rightarrow \infty$ the proper part of the transfer function disappears, leaving only the singularities:

$$G(s \Rightarrow \infty) \cong c_0 + c_1 s + c_2 s^2 + \ldots. \tag{5.45}$$

The co-efficients of the singularities can be identified by computing G(s) and curve fitting the polynomial in s for successively larger values of s. The variation in the calibrated co-efficients will eventually become zero for large values of s. The accuracy of this process is improved considerably if the degree of the singularity polynomial can be limited to first or second order. This can be accomplished by the method of regularization, as will be discussed shortly.

The last remaining element of G(r,t) which must be identified is G(r,t=0). This particular value of the proper part of the transfer function cannot be transformed directly because it is

superimposed onto the singularity functions at the origin. If $G^p(r,t)$ is the proper part of the transfer function G(r,t), then the initial value can be identified by the initial value theorem:

$$G^p(r,t=0) = \lim_{s\to\infty} sG^p(r,s) \tag{5.46}$$

Since $G^p(r,s)$ can be identified by subtracting all of the singularities of G(r,s), the initial value can be found.

5.6 Implementing the Inverse Transfer Function Solution in Real Time

5.6.1 The Form of the Solution

The process of calibrating the generalized thermal step response and calculating G(r,t) by numerical transformations to the Laplace domain and then back to the time domain is done off-line, before the machine is operated with the deflection control system. G(r,t) is evaluated at a finite number of t_k values and stored as a table of data In order to use G(r,t) on-line to transform measured temperature data into the heat input which produced it, a real-time convolution integration algorithm is required. The relationship between temperature and heat magnitude is expressed in the time domain as follows:

$$Q(s) = G(r,s)\,\Delta T(r,s) \tag{5.47}$$

In the time domain the relationship becomes:

$$Q(t) = \int_0^t G(r,t-\tau)\,\Delta T(r,\tau)\,d\tau \tag{5.48}$$

where $\Delta T(r,t)$ is the raw measured temperature difference at each of the measured node pairs. G(r,t) is consists of two parts, a proper part and singularities. Denoting the proper part by $G^p(r,t)$, the transfer function may be represented as follows:

$$G(r,t) = G^p(r,t) + A_0 u_i(t) + A_1 u_d(t) + \ldots\ldots \tag{5.49}$$

Where $U_i(t)$ and $u_d(t)$ are the time domain representations of a unit impulse and a unit doublet respectively, and A_n are the magnitudes of the singularities. Substituting equation (5.49) into equation (5.48) yields the following:

$$Q(t) = \int_0^t G^P(r,t-\tau)\,\Delta T(r,\tau)\,d\tau + A_0 \int_0^t u_i(t-\tau)\Delta T(r,\tau)\,d\tau + A_1 \int_0^t u_d(t-\tau)\Delta T(r,\tau)\,d\tau + \ldots\ldots \quad (5.50)$$

Because of the sifting property of the impulse functions, this equation reduces to:

$$Q(t) = \int_0^t G^P(r,t-\tau)\,\Delta T(r,\tau)\,d\tau + A_0\,\Delta T(r,t) + A_1\,d\frac{\Delta T(r,t)}{dt} + \ldots\ldots \quad (5.51)$$

The evaluation of equation (5.51) on-line requires the calculation of each of the terms. The first term is a convolution integral of the proper part of the transfer function with the time history of the temperature difference from τ=0 to τ=t. Using a numerical controller and data acquisition system, the temperature difference is sampled at finite time increments, which must be stored in the controller's memory in order to evaluate the integral. Because of the nature of a convolution integral, the two product functions in the integrand shift in phase for different values of time t. This means that the integral cannot be evaluated incrementally - the entire integration from τ=0 to τ=t must be re-evaluated for each Q(t) that is required. Since at least one new estimate of Q(t) is required for each control cycle, the convolution integral must be evaluated in every control cycle. The numerical integration can be performed by any method, however care must be taken to ensure that the points of measured temperature $\Delta T(r,t_k)$ co-incide with the table of transfer function values $G(r,t_k)$. Some integration methods, such as Gaussian quadrature, are not appropriate because they require sample points at irregular intervals. Since interpolation of either the measured data of the transfer function is not desirable, a better choice is an integration algorithm based on Simpson's rule, which makes use of samples at a constant time increment. As it will be shown shortly, it is possible to synchronize the temperature sampling with the control cycle and maintain a constant sampling and control interval.

5.6.2 The Finite Temperature Window

Another feature of the convolution integral that should be discussed is the limits of τ from τ=0-t. When the machine is first switched on the range of the integration is zero, and then as

t increases so does the range of the integral which must be evaluated. If the machine were running for several hours then many thousands of temperature samples would accumulate in the controller's memory and have to be integrated for each new estimate of $Q(t_k)$. In practice it is not necessary to store the complete time history of the measured temperature. This can be understood by referring to the integrand in equation (5.48), which is the product of $G(r,t-\tau)$ and $\Delta T(\tau)$. If τ is much smaller than t then $G(r,t-\tau)$ approaches $G(r,t)$. Any stable transfer function approaches zero as $t \rightarrow \infty$, therefore the values of $\Delta T(\tau)$ where τ is much smaller than t are multiplied by a transfer function that is approaching zero, and their contribution to the integral diminishes. This can be understood physically by the fact that the temperature effects of heat inputs diminish if they occur further back in time. After a certain amount of time has passed, a heat input will have no effect on the present temperature distribution. Because of this fact, it is not necessary to store an infinite amount of temperature data. The controller that has been developed stores a finite 'window' of temperature data that is integrated with the transfer function at each control cycle. The number of samples that is required for this window depends of the sampling rate and on the characteristics of the proper transfer function. Because it is desirable to have a constant control cycle frequency, the temperature window stores a fixed number of values, so that the calculation time of the numerical integration will be roughly constant for each cycle. When the machine is first turned on, the temperature window is loaded with zeros. As each new sample is taken it is added to the top of the window and all of the other values are shifted back by one, with the last one being discarded. In order for this process to work effectively, it is essential that the sampling increment be maintained relatively constant.

5.6.3 Processing the Singularities

As well as the convolution integral, there are a finite number of singularity terms in equation (5.51). In the time domain, the magnitudes of the singularities represent scaling factors for the present value of the measured temperature difference $\Delta T(r,t)$ and a finite

number of derivatives, also at present time t. The presence of singularities in an inverse transfer function can be understood with reference to figure 5.12, which is an example of the generalized step response with K=3.5, a=0.02, α=0.12, r=5.0, and r_0= 0.15. Since the temperature profile in figure 5.12 was produced by a unit step input, the transformation of the temperature profile by equation (5.51) must always equate to 1.0, for any value of t>0. Consider the case when $t=0^+$: the integration from $\tau=0-0^+$ is zero and figure 5.12 shows that the value of $\Delta T(r,t=0)$ is equal to zero. Equation (5.51) can only transform the temperature profile to 1.0 if some of the initial derivatives of $\Delta T(r,t=0)$ are non-zero and the scale factors A_n are selected appropriately. This shows how the singularities are an integral part of the transfer function, and in order to evaluate them the controller must be able to calculate the first n order derivatives of the temperature difference, where n is the highest order singularity that is present. The derivatives do not need to be stored however, since it is only the present value and not the history that is required in equation (5.51).

5.7 Regularization of the Inverse Transfer Function

The delay in the step response shown in figure 5.12 is typical of the measured temperature difference on a large machine structure. The delay leads to very undesirable properties of the convolution transfer function however. The convolution transfer function in equation (5.51) identifies instantaneous changes in the heat input Q(t) by operating on the derivatives of the temperature difference at the present time. It is clear from figure 5.12 that the temperature derivative at t=0 is very small, in fact it is almost zero. Conceptually, a transfer function based on this step response would have to contain several higher order singularities so as to incorporate the higher order derivatives which are changing at t=0 in response to the step input at t=0. While this is fine in theory, a practical temperature measurement apparatus cannot measure high order derivatives because of noise produced by the environment, by the temperature probe and circuit, and by the data acquisition system. Therefore, for the temperature profile in figure 5.12, the analytically exact transfer function cannot be

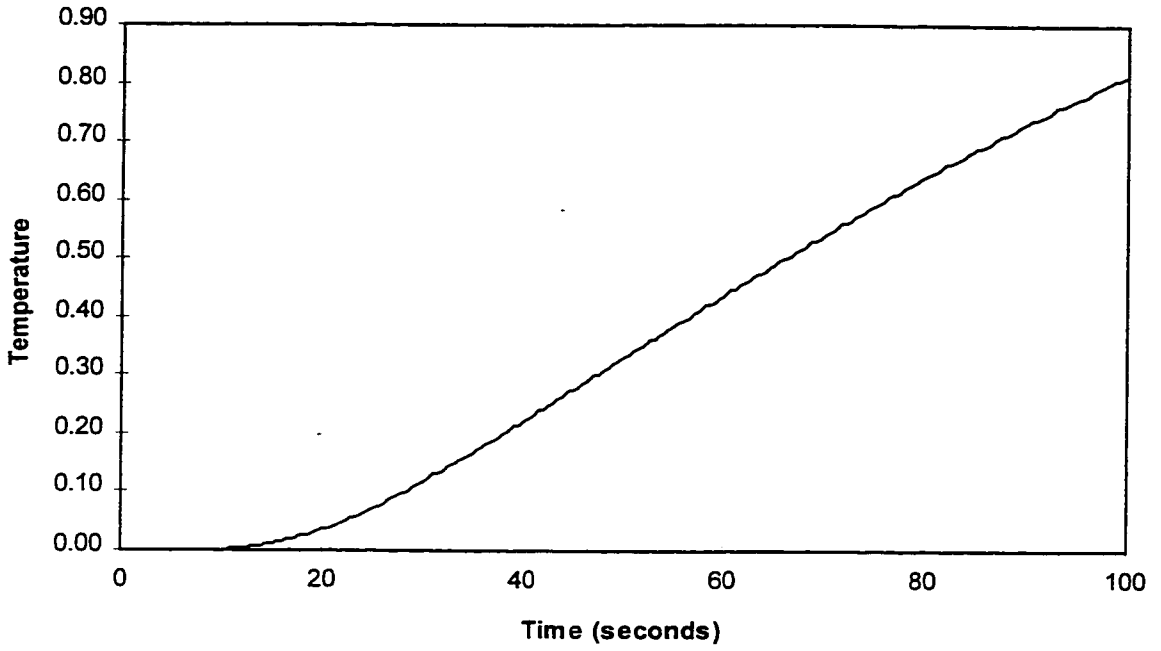

Figure 5.12: Typical Temperature Profile

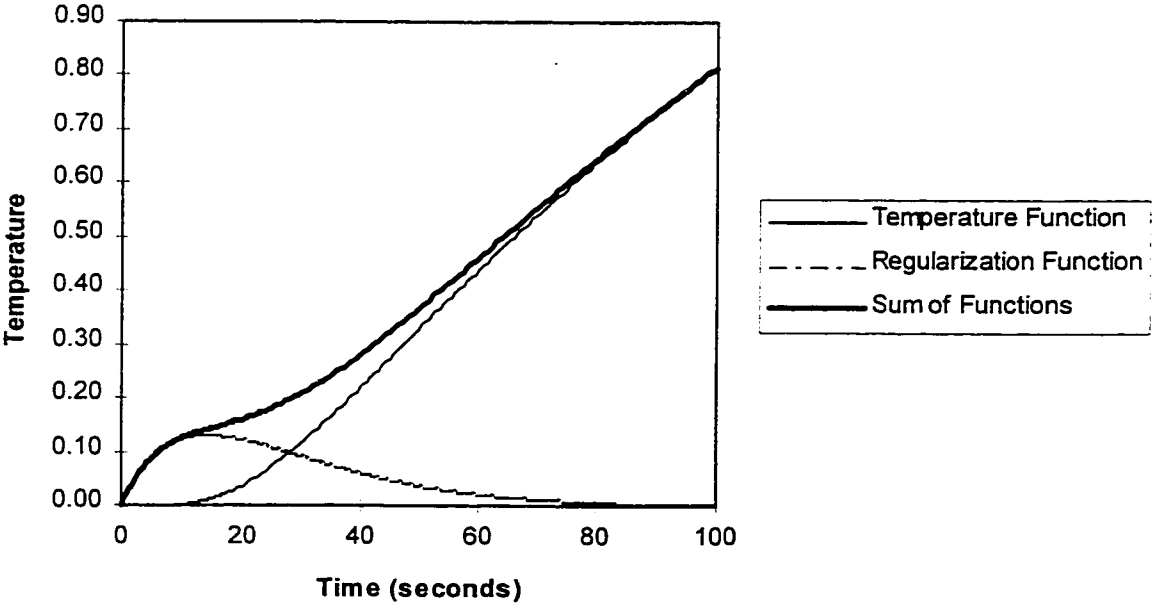

Figure 5.13: Example of Regularized Temperature Profile

implemented in a real system where measurement noise is a factor. This implies that some compromise must be made between the accuracy of the transfer function and its noise rejection characteristics. In other words, the calibrated step response which serves as the basis for the transfer function must be modified in some way. This process is called *regularization*, as was discussed in chapter 2, the difference here is that the regularization can be implemented in a more purposive way to directly re-tune the singularities of the transfer function to achieve the desired performance characteristics.

Figure 5.13 shows a plot of the function Ate^{-at} where A=0.025 and a=0.07, which we can assume is an analytical response to a step input for some hypothetical system. This function has an initial derivative of magnitude A, which is produced by this system in response to the step input. An inverse transfer function based on this function contains singularity functions, however the doublet predominates over all higher order singularities, which are equal to zero. Conceptually, the convolution transfer function does not need to consider any higher order singularities since the first derivative of the response, which is represented by the doublet term, is sufficient to identify the input.

Now consider the third function in figure 5.13, in which the temperature function and the regularization function are added together. The new function behaves exactly like the generalized step response except that the initial delay has been replaced by an initial derivative. The combined function in figure 5.13 is the regularized step response of the system, and it is from this function that a practical inverse transfer function can be derived. The regularization function has the form:

$$f_R = Ate^{-at} \tag{5.52}$$

where A and a are the empirical regularization parameters. The advantage of this method of incorporating regularization is that the designer has precise control over the form of time domain transfer function. To derive this relationship, consider the case of a generalized unit

step response, as in figure 5.13. At $t=0^+$ the contribution from the convolution integral and the term containing A_0 is zero, and therefore:

$$Q(t) = A_1 d\frac{\Delta T(r,t)}{dt} = 1 \tag{5.53}$$

Since the derivative of the generalized unit step response at $t=0^+$ is A, equation (5.53) can be solved for A_1:

$$A_1 = \frac{1}{A} \tag{5.54}$$

where A comes from equation (5.52), and A_1 is the magnitude of the doublet and the gain on the measured temperature derivative. The transfer function representation isolates the instability of the inverse heat conduction problem into one term, the term in equation (5.51) which contains A_1. This term is the source of the instability because the differentiation of the measured temperature greatly accentuates temperature measurement errors as compared to the other two terms. Equation (5.54) allows the stability of the transfer function to be precisely controlled, by establishing the gain on the temperature derivative within any required specification. The parameter a does not affect A_1, but it does affect A_0 and the proper transfer function $G^p(r,s)$. This parameter determines the time constant of the regularization term in equation (5.51), and it is used primarily to make a smooth transition in the regularized step response from the initial temperature derivative, back down to the unregularized curve, as in figure 5.13. It has been found that the single term in equation (5.52) does not give enough flexibility to make a smooth transition and a fast transition at the same time for the temperature profiles that will be used in this thesis. Hence, an alternate regularization term was investigated, which has the form:

$$f_R = (At+Bt^2)e^{-at} \tag{5.55}$$

It can be shown that:

$$A_1 = \frac{1}{A} \tag{5.56}$$

so there are two additional parameters B and a, to calibrate the transition from the initial slope A. It is the regularization term in equation (5.55) that will be used throughout this thesis. The parameters B and a will be chosen by trial and error, using a qualitative objective of making a fast but smooth transition from the initial slope back to the unregularized curve.

The transformation of the regularized step response to the Laplace domain follows from the linearity of the Laplace transform. If the regularized step response is $T_R(r,t)$, then:

$$T_R(r,t) = T(r,t) + f_R(t) \tag{5.57}$$

and so the transfer function $H_T(r,s)$ is found from:

$$H_R(r,s) = H_T(r,s) + sf_R(s) \tag{5.58}$$

where $f_R(s)$ is the Laplace transform of equation (5.55). The second term in equation (5.58) can be expressed as follows:

$$sf_R(s) = \frac{As}{(s+a)^2} + \frac{2Bs}{(s+a)^3} \tag{5.59}$$

CHAPTER 6: ESTIMATING HEAT GENERATION AND THEN THERMAL DEFLECTION ON A LINEAR PHYSICAL STRUCTURE

6.1 Introduction

This chapter outlines the procedure to be followed to build an operational system to estimate structural thermal deflection error from discrete temperature measurements in the vicinity of the heat source. The system that will be studied in this chapter is the linear physical test model that was designed in chapter 5. The first step is to identify the major heat sources in the structure and then calibrate the generalized thermal model. The real time algorithm for estimating the heat generation of the source will be implemented and validated on the physical model, using a number of test inputs. The thermal deflection models will then be calibrated, and the complete real time algorithm for estimating thermal deflection will be validated on the physical structure model.

6.2 Identifying the Heat Sources in the Structure

The first step of the procedure is to identify the major independent heat sources in the structure. The temperature increase in a real machine tool structure is large enough to be felt by touch, so it is not be too difficult to locate the areas of major heat generation using a thermocouple probe. An even better tool is a thermal imaging camera, such as the one used to generate the images in figures 5.1 and 5.7. There are normally between one and three major heat sources in a standard size machine tool, due primarily to the bearings, motor, and cutting process in declining order of importance. The heat that is generated by the cutting process can be transferred to the structure through the chips and cutting fluid, and through the cutting tool back into the spindle. There is no particular problem with identifying the chips and cutting fluid as a heat source, as long as they transfer their heat to the structure in a fairly predictable way. It is also important to run the machine under a variety of operating conditions in order to distinguish independent heat sources from dependant ones. The heat generated by bearings at opposite ends of a long spindle is an example of dependant heat sources that can be

identified by only one temperature measurement near one of the dependant sources. Independent sources can be superimposed on the same position on the structure, as for example when the spindle bearing and cutting tool are in close proximity so that the heat generated by each seems to originate from the same location. In this case the two independent sources can be lumped together into one, identified by the same temperature measurement. Some heat sources, though significant in temperature, may not produce any significant thermal deflection. This might occur if the heat is channelled quickly out of the structure, or even by accidents of geometry and kinematics. It is probably good practice to identify all of the major temperature hot points as sources, and then look at their contribution to the thermal deflection at a later stage of the process.

Figure 5.7 shows the thermal image of the test structure. The image identifies four heat sources, two that can be seen in the picture and two located symmetrically on the other side. The heat sources are all dependant and therefore may be treated as one source, requiring only one measured temperature difference. The best practice is normally to place the two measured temperatures where the temperature gradient is largest, and as close as possible to the source to minimize the delay. Since the heat source is on the surface of the test structure it would be possible to place the probes much closer to the source than could be done with a real machine tool. In order to make the analysis more realistic, the measured points were chosen at one and two inches from the outer edge of the electric heating pad. The locations of the measured points is shown schematically in figure 5.6, which is repeated in figure 6.1.

6.3 Calibrating the Generalized Thermal Step Response

Figure 6.2 shows the temperature difference profile measured on the structure for a step input of magnitude 280 W, which shall be non-dimensionalized to Q=1.0. The temperature difference was measured using two thermistors and a pair of Wheatstone bridge circuits, activated by a regularized power supply. The analog voltages representing resistance variations

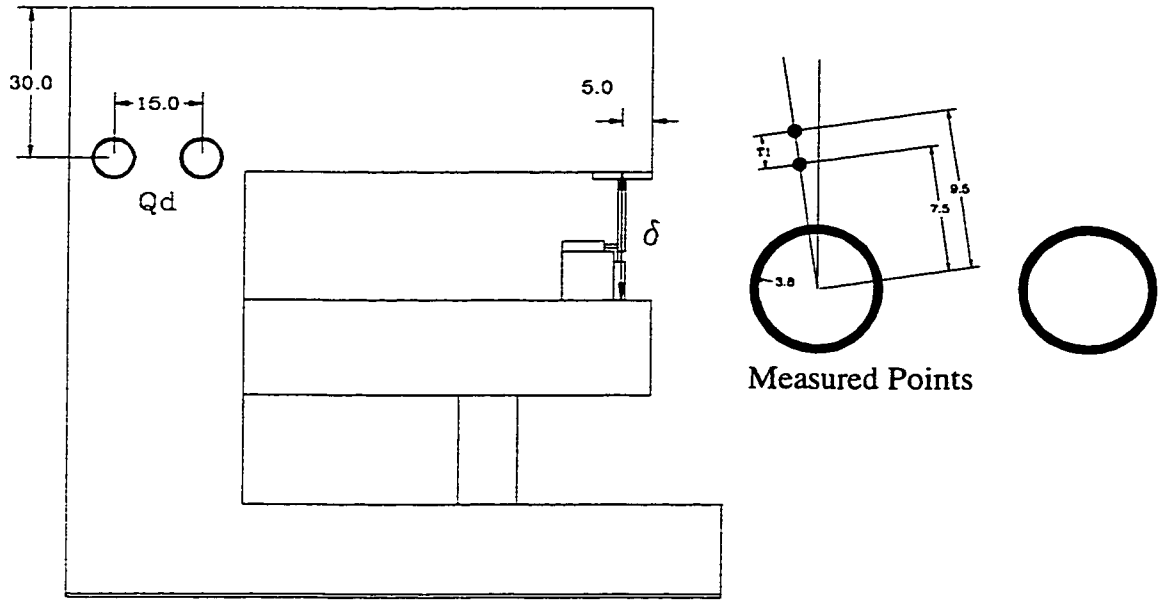

Figure 6.1: Schematic of Model Setup
(Dimensions in Centimeters)

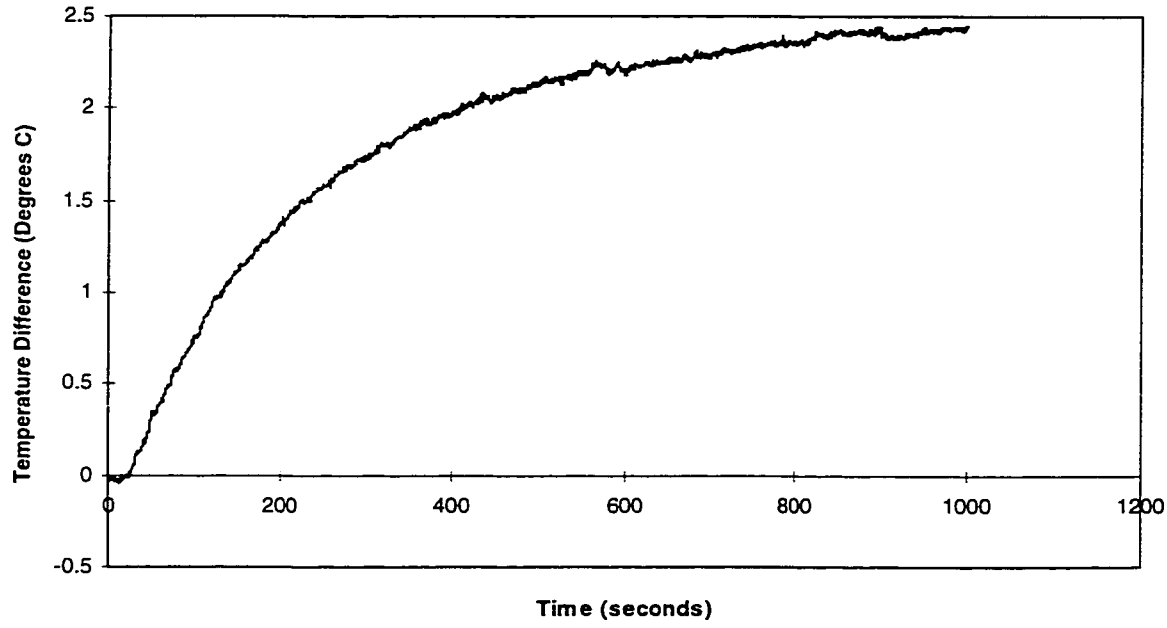

Figure 6.2: Measured Temperature Difference for q=1.0

in the thermistors were sampled in blocks of 1000 at the rate of 1 - 1.5 kHz, and the samples were then averaged within each block to yield one temperature estimate at the rate of about 2 Hz. The process of averaging a large number of samples produces a more stable temperature estimate. All of the processing on the sample blocks is done by the data acquisition card itself, independently of the main CPU which receives only the processed temperature estimates at the rate of 2 Hz. This leaves the main CPU free to perform other operations in parallel with the data acquisition and processing.

The system delay in figure 6.2 is on the order of 20 seconds long, which is quite large in comparison with the rise time. The delay time is an important characteristic of the temperature difference profile since it represents the interval in which no useful information is transmitted to the control system following a change in heating conditions. The effect that this has on the performance of the control system cannot be fully assessed however, until the relationship between the heat input and the deflection error is determined. It will be shown shortly that it is the ratio of the temperature delay to the effective time constant of the thermal deflection error that is the most useful number for assessing the inherent stability of the uncompensated control system transfer function. Figure 6.3 shows the calibrated generalized thermal step response, with calibrated parameters:

$$\begin{aligned} r_0 &= 0.12 \\ r &= 5.12 \\ a &= 0.01565 \\ \alpha &= 0.1173 \\ K &= 3.498 \end{aligned} \tag{6.1}$$

The calibration of the parameters was done in MATLAB visual programming, and part of the Matlab visual program is given in figure 6.4. The function F(t,u) in the figure is a matrix containing the function to be calibrated and the function differentiated with respect to each of its parameters, u. The initial guess is contained in the matrix labelled [vg]. The numerical data to be calibrated comes from an external file STEVE.DAT. MATLAB uses a variant of the simplex method to find a local minimization of the difference between the function and the

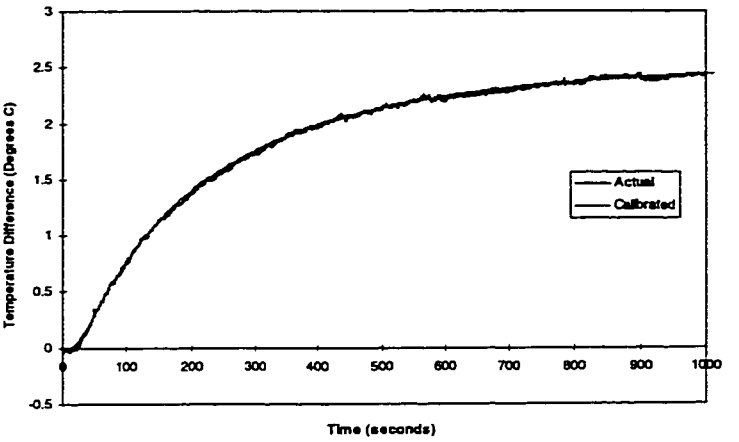

Figure 6.3: Measured Temperature Difference with Calibrated Generalized Step Response

Input temperature input data from the file steve.dat

$data := READPRN(steve\_dat)$

Extract the useful portion of the data following t=0, where the input begins after sample 66

$i := 1..3500$

$t_i := (data^{\langle 0 \rangle})_{i+66} - (data^{\langle 0 \rangle})_{66}$

$tem_i := (data^{\langle 1 \rangle})_{i+66} - (data^{\langle 1 \rangle})_{66}$

Define a matrix of 12 data points on which to calibrate the model: $n = \begin{pmatrix} 5 \\ 15 \\ 35 \\ 50 \\ 75 \\ 150 \\ 250 \\ 350 \\ 450 \\ 600 \\ 800 \\ 1000 \end{pmatrix}$

Define the fixed parameters: $r1 := 0.12$

$r := 5.12$

F(t,u) is the matrix containing the function to be calibrated.
The variables u are the calibration parameters, t is the time

$$F(t,u) := \begin{bmatrix} \int_0^{50} \frac{\beta \cdot u_2}{\beta^2 + u_0} \left[1 - e^{-u_1 \cdot t \cdot \left(\beta^2 + u_0\right)}\right] \cdot J0(r \cdot \beta) \cdot J0(r1 \cdot \beta)\, d\beta \\ \int_0^{50} \frac{\beta \cdot u_2}{\left(\beta^2 + u_0\right)^2} \left[\left[1 + u_1 \cdot t \cdot \left(\beta^2 - u_0\right)\right] \cdot e^{-u_1 \cdot t \cdot \left(\beta^2 + u_0\right)} - 1\right] \cdot J0(r \cdot \beta) \cdot J0(r1 \cdot \beta)\, d\beta \\ \int_0^{50} \left[u_2 \cdot t \cdot \beta \cdot e^{-u_1 \cdot t \cdot \left(\beta^2 + u_0\right)}\right] \cdot J0(r \cdot \beta) \cdot J0(r1 \cdot \beta)\, d\beta \\ \int_0^{50} \frac{\beta}{\beta^2 + u_0} \left[1 - e^{-u_1 \cdot t \cdot \left(\beta^2 + u_0\right)}\right] \cdot J0(r \cdot \beta) \cdot J0(r1 \cdot \beta)\, d\beta \end{bmatrix}$$

Define the function variables and begin the calibration

$i := 0..11$

$vx_i := t_{(n_i)}$

$vy_i := tem_{(n_i)}$

$vg := \begin{pmatrix} 0.025 \\ 0.0841 \\ 2.07 \end{pmatrix}$

$p := genfit(vx, vy, vg, F)$

Print the calibrated parameters: $p = \begin{pmatrix} 0.01565 \\ 0.1173 \\ 3.49842 \end{pmatrix}$

Figure 6.4: Mathcad Subroutine for Calibrating the Thermal Model

data at the eleven selected points in matrix [n]. There are three calibration parameters in figure 6.4, a, α, and K. What is not shown in figure 6.4 is the iterative part of the program for finding the optimal value of r. Figure 6.4 represents a sort of subroutine that finds the optimal a, α, and K for given values of r and r_0. This is done for several values of r, and a performance criterion is evaluated for each calibration. The r value which optimizes the performance criterion is the optimal r value. Calibrating r separately from the other three parameters was found to be faster and more reliable than a single optimization with four parameters. The performance criteria that was used is the root-mean-square of the error. The value of r_0 was chosen arbitrarily rather than calibrated because it was found that the calibration of the other four parameters gives sufficient flexibility, and thus the fifth parameter is redundant. Figure 6.3 shows that the calibrated generalized step response fits the measured data with high accuracy in all aspects of the temperature curve, including the delay, the rise, and the steady-state. This is expected because of the mathematical derivation of the generalized base equation.

Figure 6.5 shows a plot of the difference between the calibrated generalized step response and the measured temperature profile. The signal in figure 6.5 is actually the cumulative noise from environmental and instrumentation sources, rather than a true error in the calibrated generalized step response. It has a cumulative mean approaching zero, and its magnitude and spectral composition are independent of the magnitude of the measured temperature, up until $T=T_{max}$ in figure 6.3. The generalized model rejects the temperature system noise because it is incompatible with the mathematical form of the model. In this way, the generalized model is able to extract the useful part of the real measured data from the random and systematic noise. Figure 6.6 shows the spectral composition of the noise, with a plot of the magnitude of the discrete Fourier transform of the noise, versus frequency. Figure 6.6 shows that the noise energy is distributed equally over the relevant bandwidth, approximating the 'white noise' model. The highest frequency component in figure 6.5 is about 2 Hz, corresponding to the

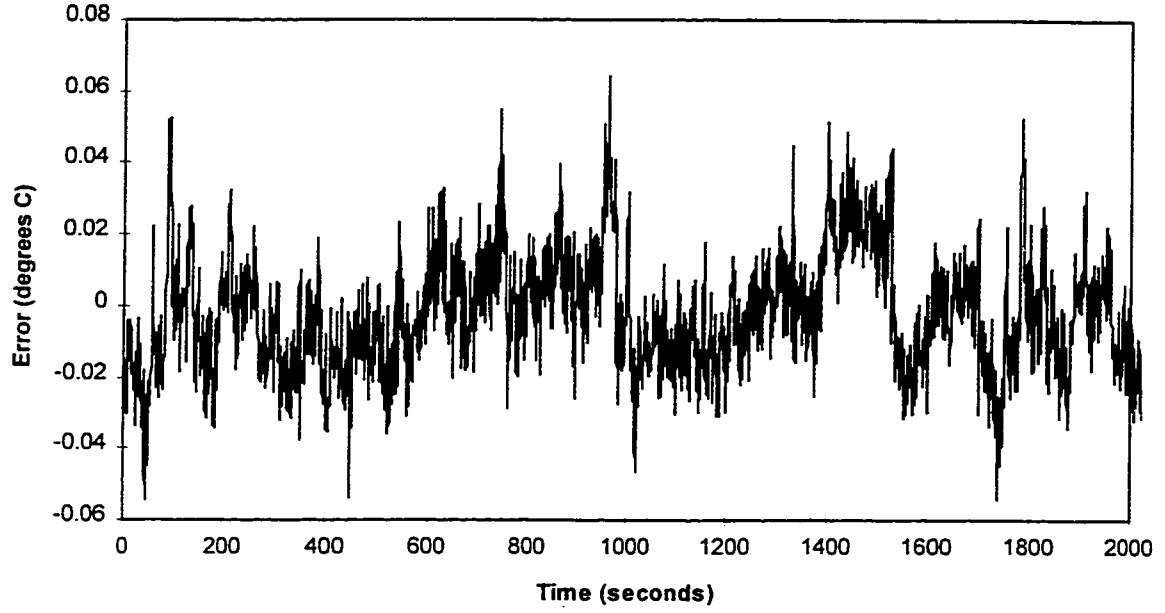

Figure 6.5: Plot of Noise for q=1

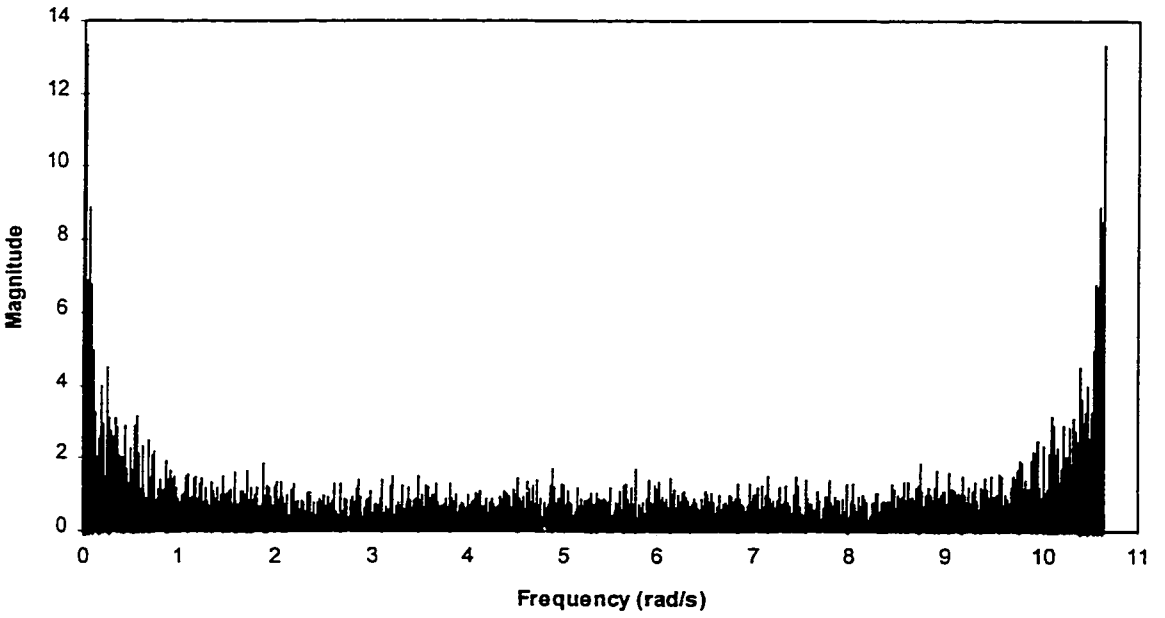

Figure 6.6: Magnitude Plot of DFT of Noise

sampling time of approximately 0.5 seconds. This high frequency noise is due to instrumentation and sampling effects as well as environmental noise. The low frequency noise which is clearly evident in figures 6.5 and 6.6 is a greater concern however, because it is potentially more damaging to the performance of the control system. Such low frequency noise is a product of environmental fluctuations in the vicinity of the measured temperature points. The thermistors on the experimental model were covered in insulating material about 1.5 cm in diameter to minimize the effect of local air currents on the temperature readings, otherwise the noise would have been considerably larger. Nevertheless, environmental noise dominates over instrumentation noise in all of these experiments. Low frequency noise is a particular concern because it requires a special low frequency filter that introduces a large time delay into the system. This point will be considered in more detail shortly.

6.4 Selecting the Temperature Derivative Gain and Regularization of the Step Response

A complete discussion of the allowable temperature derivative gain will have to wait until the thermal deflection step response is calculated in a later section. Figure 6.5 shows the maximum derivative of the noise is around $\Delta T=0.05$ degrees C divided by $T=0.5$ seconds, which equals 0.1. A derivative gain of 155 would therefore produce a maximum noise amplitude of 15.5 degrees C per second. While this might seem to be a very high gain for undesirable noise, it has been shown that the thermal deflection transfer function is itself a low pass filter, which will attenuate much of this noise in the final result [79]. Thus, using $A=1/155=0.00644$, and $B=0.00135$ and $a=0.0859$, figure 6.7 shows the regularization function, and the regularized step response. The parameters B and a were selected so as to make a smooth but fast transition, as shown in the figure. Figure 6.8 shows how the regularization function in equation (5.55) alters the step response.

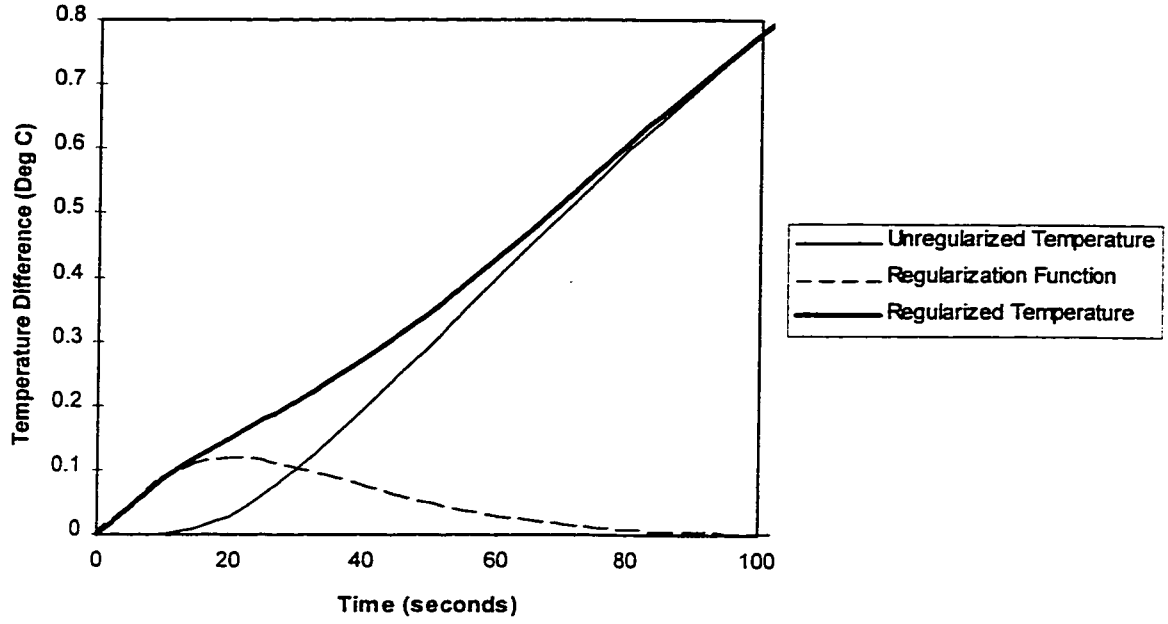

Figure 6.7: Calibrated Generalized Step Response with and Without Regularization

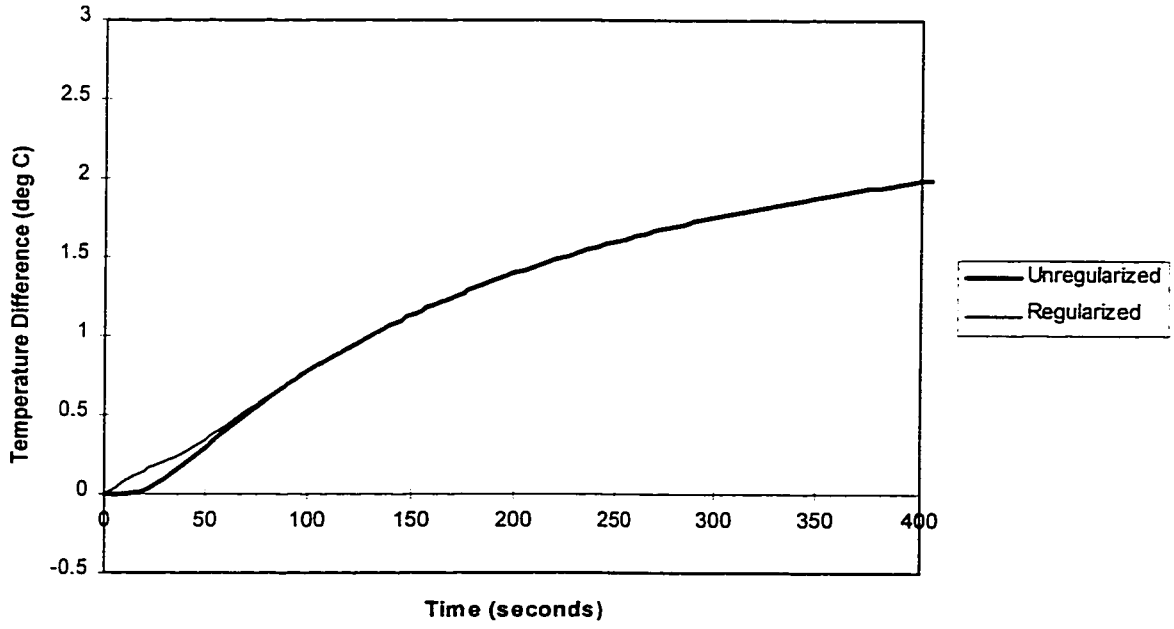

Figure 6.8: Regularized and Unregularized Step Response

6.5 The Calculation of the Time Domain Transfer Function

The procedure for calculating G(r,t) was developed in chapter 5, but it is useful now to extract the important equations from previous chapters, and compile them together here for future reference. The generalized step solution in the time domain was given in equation (5.3):

$$T(r,t) = Kq\int_0^\infty \frac{\beta}{\beta^2+a} J_0(\beta r) J_0(\beta r_0)\left[1-e^{-(a+\beta^2)\alpha t}\right] d\beta \tag{6.2}$$

The direct transfer function in the Laplace domain $H_T(r,t)$ was derived from the generalized step solution, and expressed as equation (5.8):

$$H(r,s) = K\alpha\int_0^\infty \frac{\beta\, J_0(\beta r)\, J_0(\beta r_0)}{s+[a+\beta^2]\alpha} d\beta \tag{6.3}$$

A practical numerical equation for calculating $H_T(r,s)$ for all s=R+Ij and $I \neq \infty$ was derived as equation (5.28), which can also be expressed by its real and imaginary components as follows:

$$\begin{aligned}
\Re\{H(r,s)\} &= K\alpha\int_0^\infty \beta\overline{D}(\beta)\frac{R+\alpha(a+\beta^2)}{(R+\alpha[a+\beta^2])^2+I^2} d\beta - K\alpha\int_0^\infty \beta\overline{D_a}(\beta)\frac{R+\alpha(a+\beta^2)}{(R+\alpha[a+\beta^2])^2+I^2} d\beta \\
\Im\{H(r,s)\} &= -K\alpha\int_0^\infty \beta\overline{D}(\beta)\frac{I}{(R+\alpha[a+\beta^2])^2+I^2} d\beta + K\alpha\int_0^\infty \beta\overline{D_a}(\beta)\frac{I}{(R+\alpha[a+\beta^2])^2+I^2} d\beta
\end{aligned} \tag{6.4}$$

where (equation (5.22)):

$$\overline{D}(\beta) = J_0(\beta r) J_0(\beta r_0) - \frac{(\cos(\beta r)+\sin(\beta r))(\cos(\beta r_0)+\sin(\beta r_0))}{\pi\beta\sqrt{rr_0}} \tag{6.5}$$

and (equation (5.24)):

$$\overline{D_a}(\beta) = \frac{(\cos(\beta r)+\sin(\beta r))(\cos(\beta r_0)+\sin(\beta r_0))}{\pi\beta\sqrt{rr_0}} \tag{6.6}$$

This is the equation that will be used to calculate the transfer function $G^P(r,t)$. The regularization part of the step response was transformed to the Laplace domain as equation (5.59):

$$F_R(s) = sf_R(s) = \frac{As}{(s+a)^2} + \frac{2Bs}{(s+a)^3} \tag{6.7}$$

which can be evaluated in terms of its real and imaginary components for any value of s=R+Ij.

The inverse transfer function G(r,s) is derived from the direct transfer function in equation (5.12), which after including the regularization term becomes:

$$\Re\{G_R(r,R+Ij)\} = \frac{\Re\{H(r,R+Ij)+F_R(R+Ij)\}}{\Re\{H(r,R+Ij)+F_R(R+Ij)\}^2+\Im\{H(r,R+Ij)+F_R(R+Ij)\}^2}$$

$$\Im\{G_R(r,R+Ij)\} = \frac{-\Im\{H(r,R+Ij)+F_R(R+Ij)\}}{\Re\{H(r,R+Ij)+F_R(R+Ij)\}^2+\Im\{H(r,R+Ij)+F_R(R+Ij)\}^2} \quad (6.8)$$

Equations (6.4) (6.7) and (6.8) are used to calculate the proper regularized transfer function $G^P_R(r,s)$. The numerical integration was done using Gaussian quadrature in block increments until the maximum value of the integrand within the block is below a threshold value. The transformation to the time domain was done using the accelerated Crump formula discussed in chapter 5, to a tolerance of 1E-05, in increments of 0.5 seconds beginning from t=0.5. The transformed transfer function $G^P(r,t)$ is shown in figure 6.8, where r=5.12. The magnitudes of the singularities, A_0 and A_1 were found with a precision of 1E-04 by equation (6.7) using Gaussian quadrature in block increments.

6.6 The Real Time Process of Estimating the Heat Generation

6.6.1 The Temperature Window

The rate of decay of the transfer function in figure 6.9 determines the size of the temperature window that must be stored by the controller. Although the transfer function appears to decay quite rapidly, there is actually a small residual that lingers for some time. Truncating the window at 150 seconds results in a steady-state error of about 2%, which is unacceptable. Using a temperature window of 600 seconds results in a steady-state error from truncation of less than 0.05%, but then there are 1200 temperature samples which must be stored with a 0.5 second sampling time. For a given sampling time there is a maximum number of samples that can be processed. On a 60 MHz Pentium PC, the convolution integral

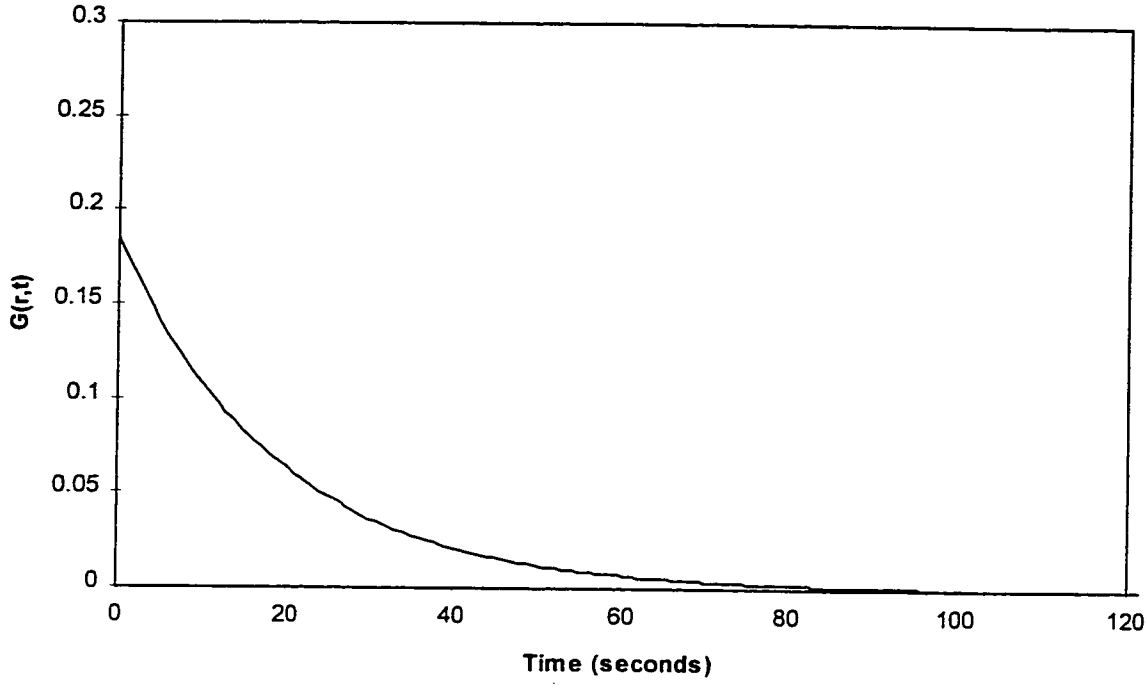

Figure 6.9: Time Domain Transfer Function $G_P(r,t)$ for r=5.12

requires about 0.1 seconds with a 1200 sample window, leaving 0.4 seconds for the thermal deflection and control system calculations. Furthermore, a 0.5 second sampling time system produces more stable temperature samples than a system with a smaller sampling time because of the averaging process done by the data acquisition processor independently of the main CPU. There is in fact no advantage to using a smaller sampling interval, so the CPU may as well use the time to greatest advantage, rather than just sit idling while it is waiting for another sample. In an optimal parallel system the main CPU and the data acquisition CPU would finish their respective tasks at the same instant, a goal which will never be achieved here. The temperature window that will be used in this thesis is therefore a linear buffer 1200 samples long. As mentioned previously, as each new sample is added to the top of the buffer all of the other samples are incremented down by one with the last one being discarded.

6.6.2 Estimating the Temperature Derivative

As mentioned previously, the main source of instability of the inverse transfer function G(r,s) is the term containing the derivative of the measured temperature difference. The simplest method for calculating a derivative is the formula:

$$\frac{\Delta f_k}{\Delta T} = \frac{f_k - f_{k-1}}{T} \tag{6.9}$$

where f_k is the k^{th} sample and T is the sampling time. Figure 6.10 shows the derivative of the measured temperature difference in figure 6.2, using the first order derivative formula from equation (6.9). As expected, the signal noise was amplified by the differentiation in comparison with the useful signal, leaving the useful signal completely unrecognizable. Higher order expressions for the derivative are more accurate and attenuate noise, however it can be shown that all higher order derivatives can also be expressed as first order derivative followed by a digital filter. In light of this, it is more effective to start with the differentiated signal in figure 6.10 and then design a filter which will remove the unwanted frequency components.

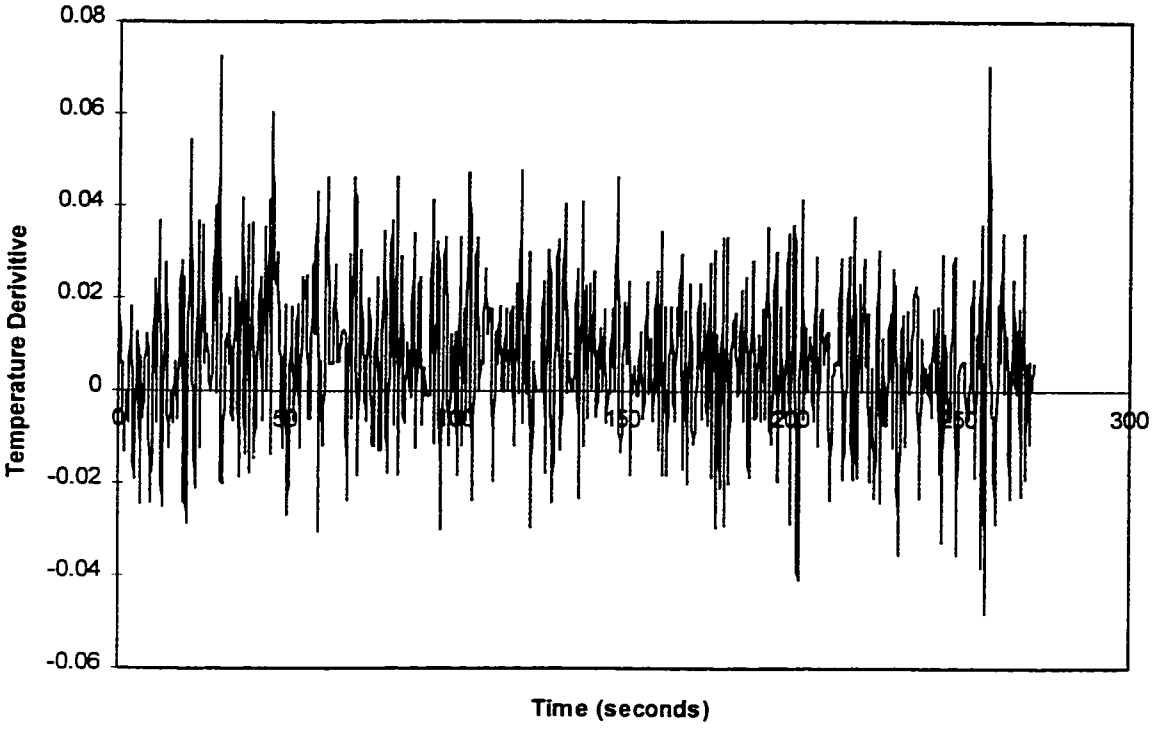

Figure 6.10: Derivitive of T(r,t)

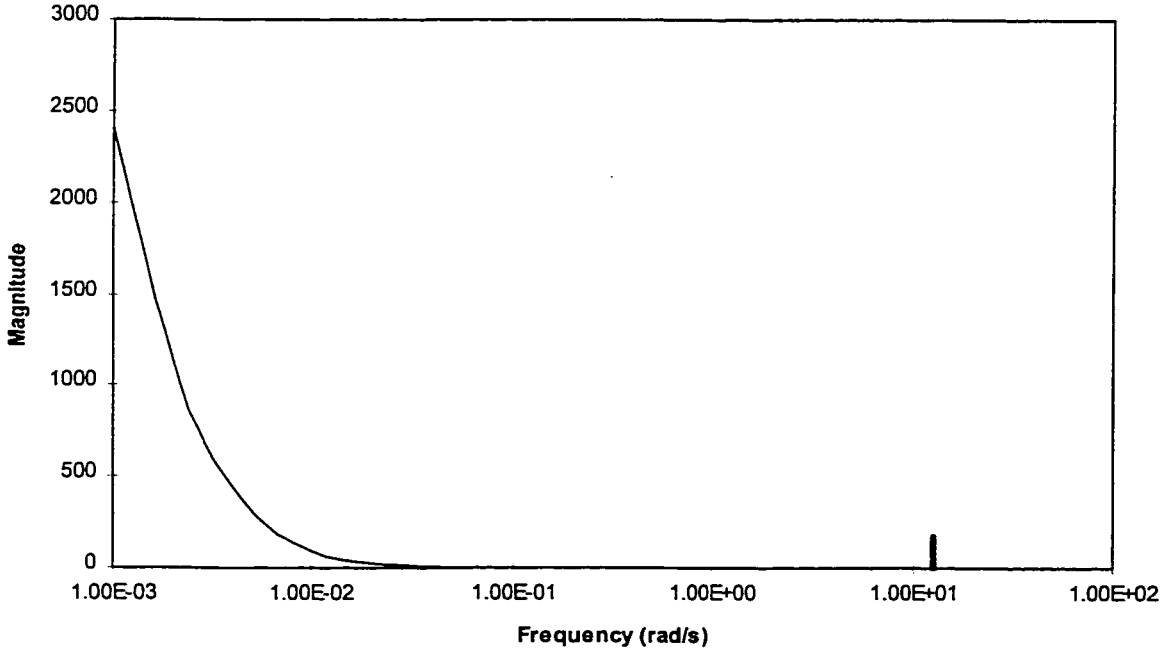

Figure 6.11: Magnitude of Inverse Transfer Function G(r,s)

All real signals are usually processed in some way to eliminate noise, which normally originates in the data acquisition and sampling process by a number of mechanisms. Discretization of an analog signal produces noise at the sampling frequency as the signal jumps between discrete storage levels. This type of noise can be minimized by using a data acquisition card with a large bit storage for each sampled data value. The card used in these experiments uses a 12 bit representation, which is excellent for this application. Lower frequency noise may be produced by the data acquisition itself, both from power supply fluctuations and changes in the measured variable introduced by the measurement apparatus. All of the noise sources just discussed are much higher in frequency than the spectrum of the useful signal. Figure 6.11 shows the frequency spectrum of the useful signal, which is the calibrated temperature difference step response T(r,s). Notice that the magnitude scale is not in decibels. The sampling frequency is marked on the figure, 12.56 rad/s, corresponding to 2 Hz. Since the frequency spectrum of the useful signal approaches zero at ω=12.56 rad/s, noise at this frequency can be easily removed by a suitable filter, without distorting the magnitude spectrum of the useful signal. The figure shows that an ideal low pass filter will not introduce any significant distortion for cut-off frequencies up to about 0.3 rad/s.

It is clear from figure 6.11 that the high frequency noise introduced by the data acquisition system may be filtered without distorting the useful temperature signal. However the frequency spectrum of the noise shown in figure 6.6 shows that low frequency noise persists, even below 0.05 Hz or 0.314 rad/s. The low frequency noise components are evident on inspection of figure 6.5. The source of this high frequency noise was found not to originate from the data acquisition process, but rather from environmental sources. Random air currents over the area of the temperature measurement causes small fluctuations in the temperature of the measured points that is detectable by the measurement apparatus. Insulating the surface of the structure around the thermistors reduces the noise, however it also reduces the temperature gradient, making the measurements more difficult to resolve, and it increases the thermal deflection

produced by the heat source by increasing the temperature. A compromise solution is to apply a 1.5 cm. diameter insulating pad over each thermistor, shielding it from direct air currents. The temperature differences shown in this thesis were all made using the 1.5 cm insulating pads.

6.6.3 Design of the Derivative Filter

Since it is not possible to completely filter the noise in figure 6.5 without distorting the temperature spectrum of the useful signal, a compromise solution will have to be achieved. Since any significant magnitude distortion is not acceptable, the cut-off frequency of the low pass filter is chosen to be 0.05 Hz or 0.314 rad/s, which is right at the edge of the system bandwidth in figure 6.11. Since the cut-off frequency is so close to the system band-edge a very sharp cut-off rate will be required. A FIR filter is normally preferred in digital applications because of its inherent stability and ease of design. The IIR filter however, is more computationally efficient, and allows for a much sharper cut-off transition for the same number of terms. Hence, a third order Butterworth IIR filter will be used here. The continuous transfer function for a third order Butterworth filter is:

$$FF(s) = \frac{1}{s^3 + 2s^2 + 2s + 1} \tag{6.10}$$

The continuous transfer function is transformed to the z-domain using the bilinear transformation:

$$s \rightarrow \frac{2}{T}\frac{z+1}{z-1} \tag{6.11}$$

which yields the discrete transfer function:

$$FF(z) = \frac{(z+1)^3}{1441.5z^3 - 3783.3z^2 + 3339.1z - 989.2} \tag{6.12}$$

from which a recursive formula can be derived.

Figure 6.12 shows the derivative of the measured temperature difference from figure 6.10, filtered by the discrete transfer function in equation (6.12). The noise component is considerably attenuated, however the low frequency components, those below 0.05 Hz, persist. There is another undesirable feature in figure 6.12 which is more subtle, but actually far more detrimental to the ultimate objective of implementing a control system. The measured temperature difference contains an initial delay of about 20 seconds, as seen in figure 6.2, and a slightly shorter delay is expected in the temperature derivative. However figure 6.12 shows that the initial delay has actually increased somewhat in the filtered derivative. The increased delay is an inevitable by-product of filtering the derivative, and so filtering effectively increases the system delay. This will be dealt after the thermal deflection transfer functions have been presented and discussed. It will be seen that the controller will introduce an artificial positive delay, by which it will attempt to cancel the negative delay that is inherent to the system, including the delay produced by the derivative filter.

6.7 Results of the Real Time Heat Estimation Program

The procedure for transforming measured temperature difference samples into an estimated heat generation function in real time is now complete. The solution is obtained by numerically evaluating equation (5.5) for a window of 1200 temperature difference samples. The convolution integral is evaluated by Simpson's second order method using samples spaced by T=0.5 seconds. The total computation time for the entire algorithm, which was implemented in real time in C++ is less than 0.125 seconds. Figure 6.13 shows the estimated Q(t) from the measured temperature profile in equation (8), without filtering of the temperature difference derivative. The ideal estimate is a constant line of magnitude 1.0, which is also shown in the figure. Although the ideal signal is not apparent in figure 6.13, the cumulative mean of the signal is actually 1.0, and the oscillations are the result of amplified noise. While not very aesthetic, the estimate in figure 6.13 will be filtered by the second part of the

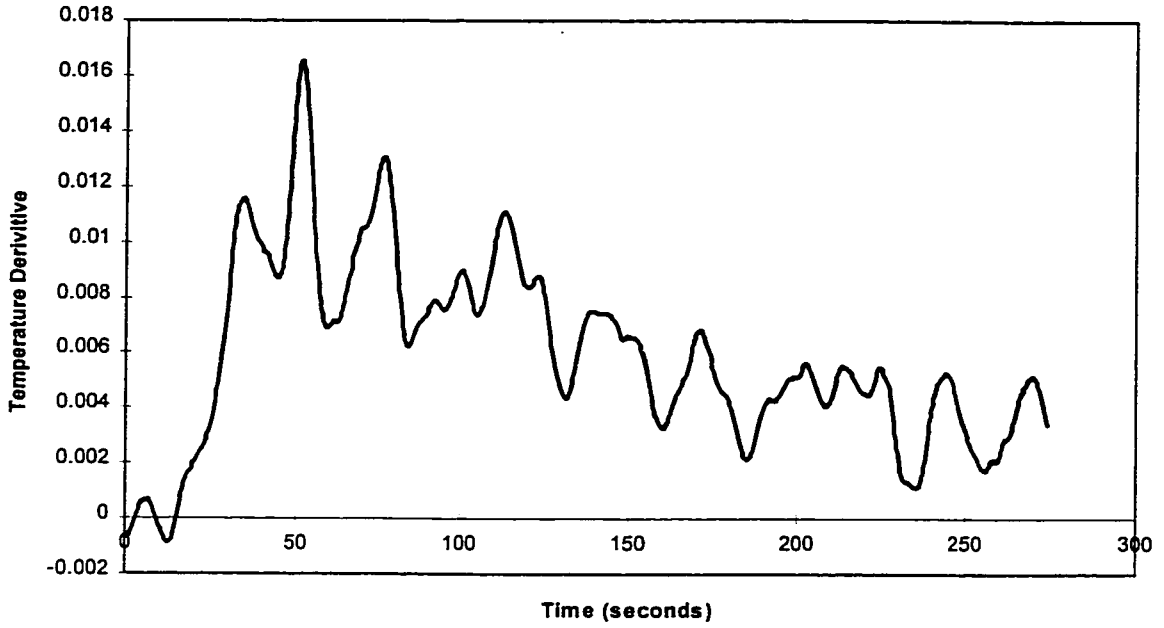

Figure 6.12: Derivitive of T(r,t) with filtering

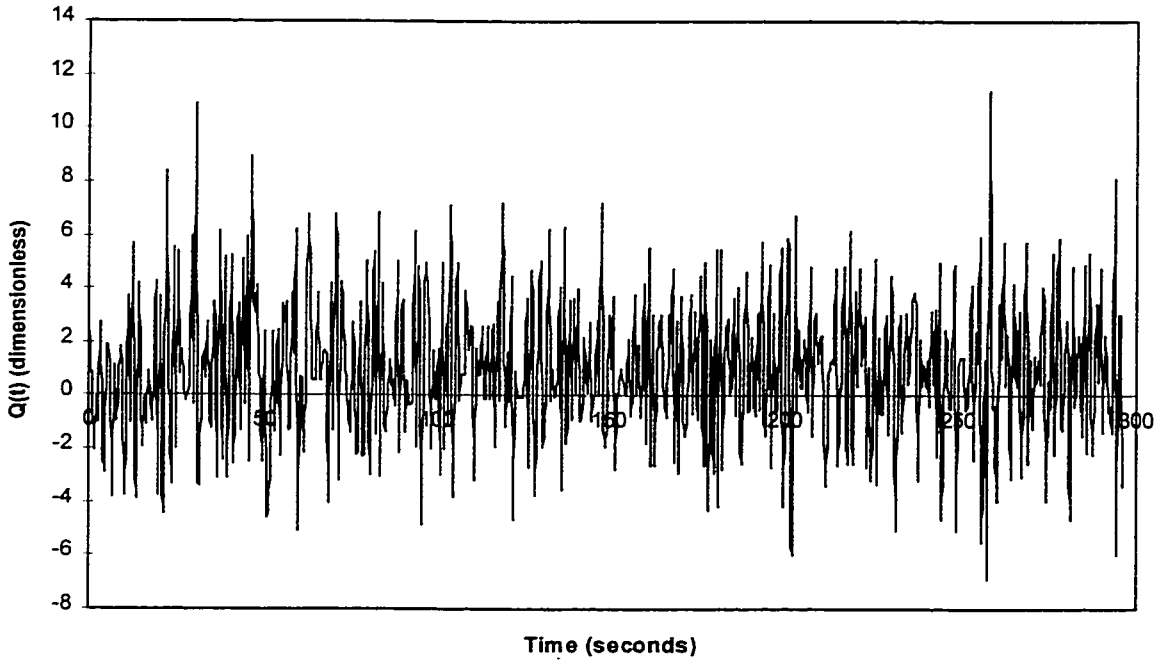

Figure 6.13: Estimated Q(t) Without Filtering

complete transfer function, the thermal deflection transfer function, which acts as a low pass filter itself.

Figure 6.14 shows the same estimate of the heat generation as in equation 6.13, but this time using the derivative filter given by equation (13). Figure 6.14 is much closer to the ideal estimate, but it too contains unwanted noise. Further filtering is unnecessary however, as will be seen shortly. The estimated Q(t) requires 30.76 seconds to reach the correct value of 1.0, which constitutes the effective system delay for G(r,t). The cumulative mean of Q(t) in figure 6.14 is less than 0.05% in steady state, indicating very little steady-state distortion of the processed signal.

The derivation thus far is based on the assumption of a linear thermal model. The main potential sources of non-linearity are radiation effects and joint interaction. Since the two-component experimental structure is not expected to exhibit significant nonlinearity, and radiation heat transfer is negligible at the operating temperature of the experimental structure, the linear assumption was assumed to be justified. Figure 6.15 shows the measured temperature difference at the same measured points as before, for a dimensionless heat input of Q=0.5. The measured temperature profile is compared with the temperature profile predicted by the calibrated generalized model, using the expression for the general solution, equation (6.2). Figure 6.16 shows the measured temperature difference at Q=0.25, compared with the temperature difference determined from calibrated equation (6.2). These two figures confirm that the linearity hypothesis is valid, since the cumulative mean of the difference between the predicted and the actual temperature differences is approximately zero. A zero cumulative mean indicates that the difference between the curves is due entirely to noise, while the signal itself maintains the same ratio as the ratio of the heat input magnitudes.

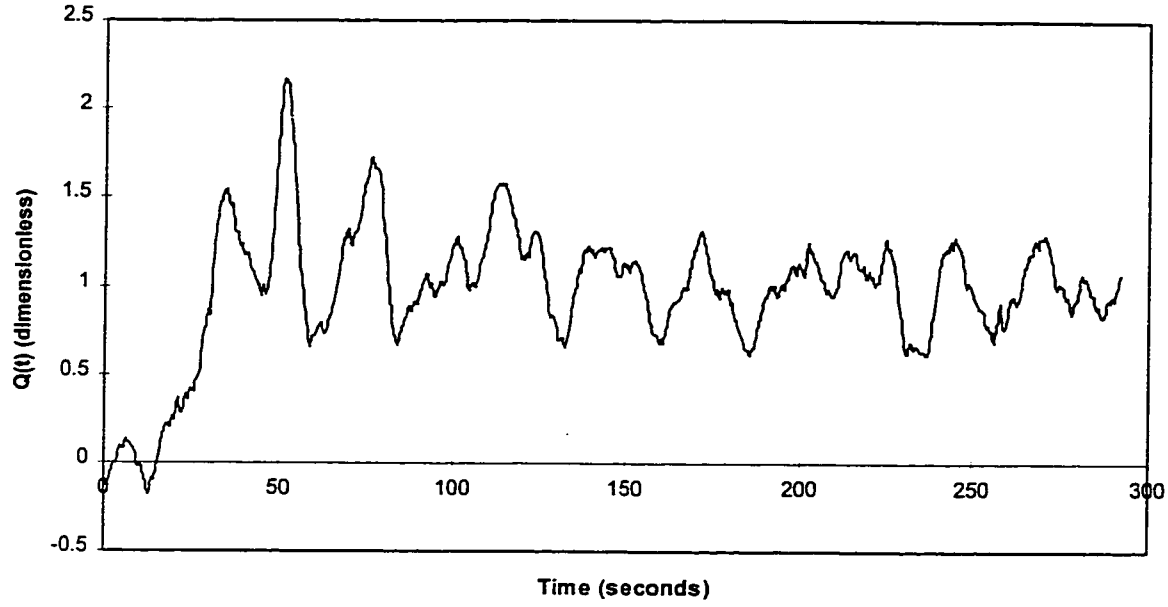

Figure 6.14: Estimated Q(t) with Derivitive Filtering

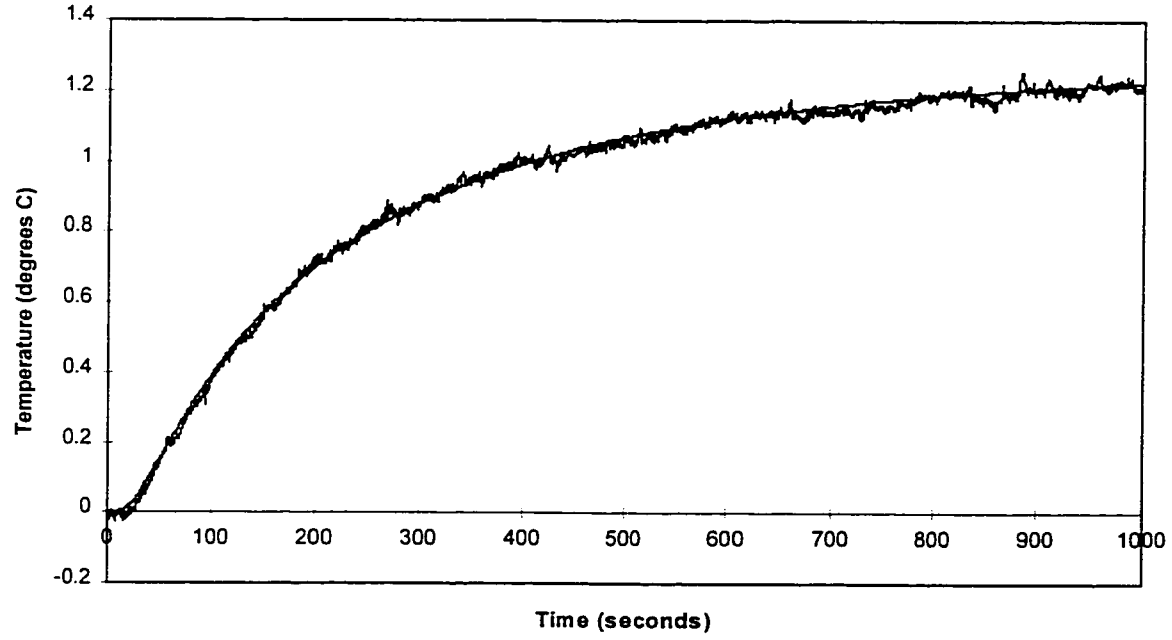

Figure 6.15: Measured Temperature Difference and Temperature Difference Estimated with Calibrated Model (Calibrated at Q=1.0) for Input Q=0.5

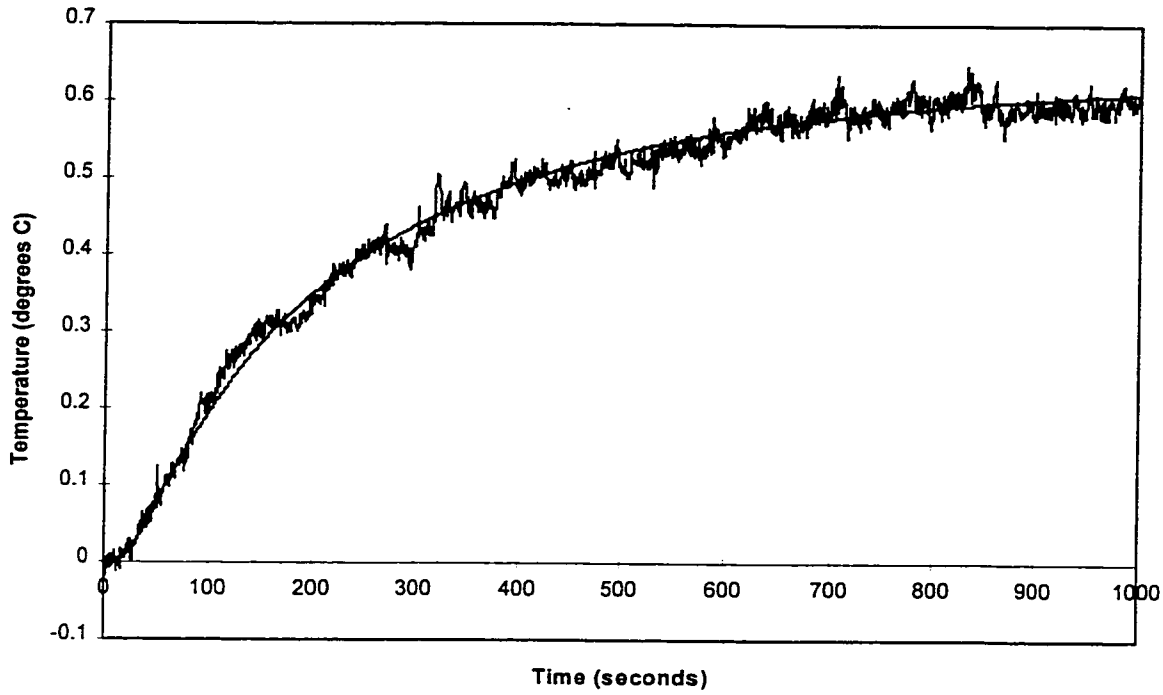

Figure 6.16: Measured Temperature Difference and Temperature Difference Estimated from Calibrated Model (Calibrated at Q=1.0) for Q=0.25

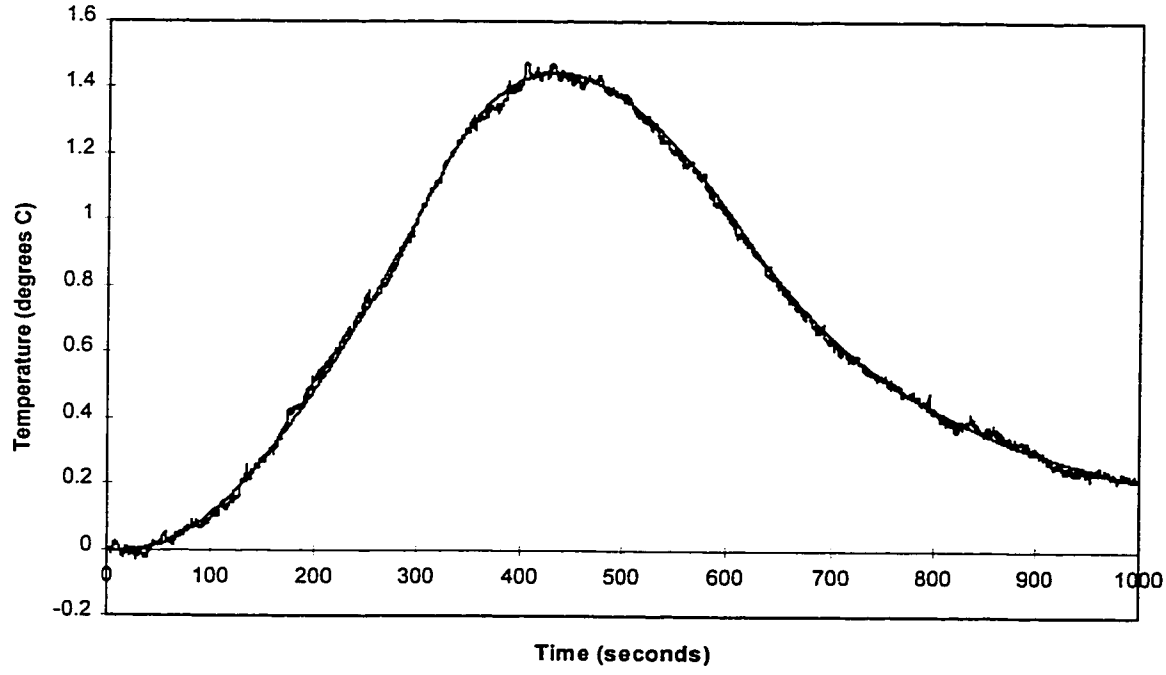

Figure 6.17: Measured Temperature Difference and Temperature Difference Estimated with Calibrated Model (Calibrated for Q=1.0) for Triangular Input

6.8 Discussion of the Heat Estimation Results

An obvious feature of figures 6.2, 6.15, and 6.16 is that the noise magnitude in not linear along with the temperature difference. In fact, the noise amplitude remains constant independent of the magnitude of the temperature which is being measured from q=0 up until q=1. The model was also tested up to q=2, and the linearity of the temperature difference was found to be maintained. The amplitude of the noise actually increased when the temperature difference exceeded 3.5 degrees C, probably the result of changing air flows on the surface of the structure at high operating temperatures.

Although the transfer function G(r,t) was calculated on the basis of a single step response, the linearity of the Laplace transform implies that the transfer function is valid for any input. Figure 6.17 shows the measured temperature difference for a triangular heat input, beginning from zero at t=0, increasing linearly to q=1.0 at t=300 seconds, and then decreasing linearly to zero at t=600 seconds, after which it remains constant at zero. The temperature difference predicted by calibrated equation (6.2) is also shown in the figure, and again the mean difference between the two curves is about zero.

The three measured temperature differences in figures 6.15, 6.16 and 6.17 were processed by the convolution transfer function G(r,t) as the samples were collected and the results are shown in figures 6.18, 6.19, and 6.20, for q=0.5, q=0.25, and the triangular input respectively. These figures also show the correct Q(t), and again the average difference between the two curves approaches zero as time goes to infinity. These estimated inputs will be used to estimate the thermal deflection for the same Q inputs in the next section.

6.9 Deriving The Thermal Deflection Model

The second part of the transfer function relating the measured temperature $\Delta T(t)$ to the thermal deflection $\delta_x(t)$ and $\delta_y(t)$ is the direct transfer functions $H_x(s)$ and $H_y(s)$, where:

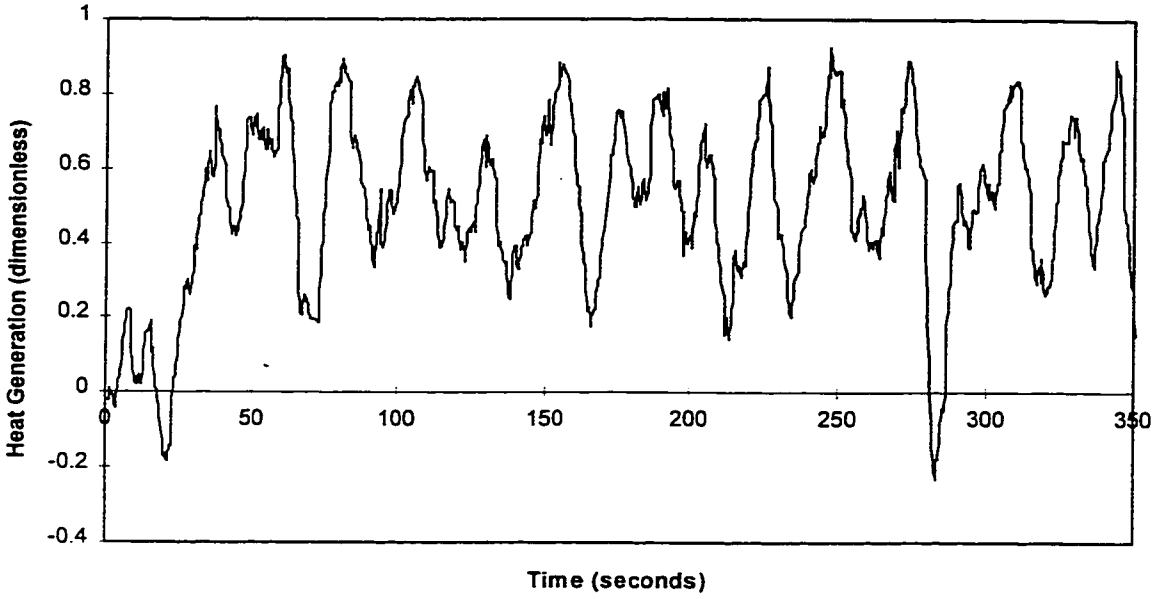

Figure 6.18: Estimated Q(t) for Q=0.5 (Model Calibrated at Q=1.0)

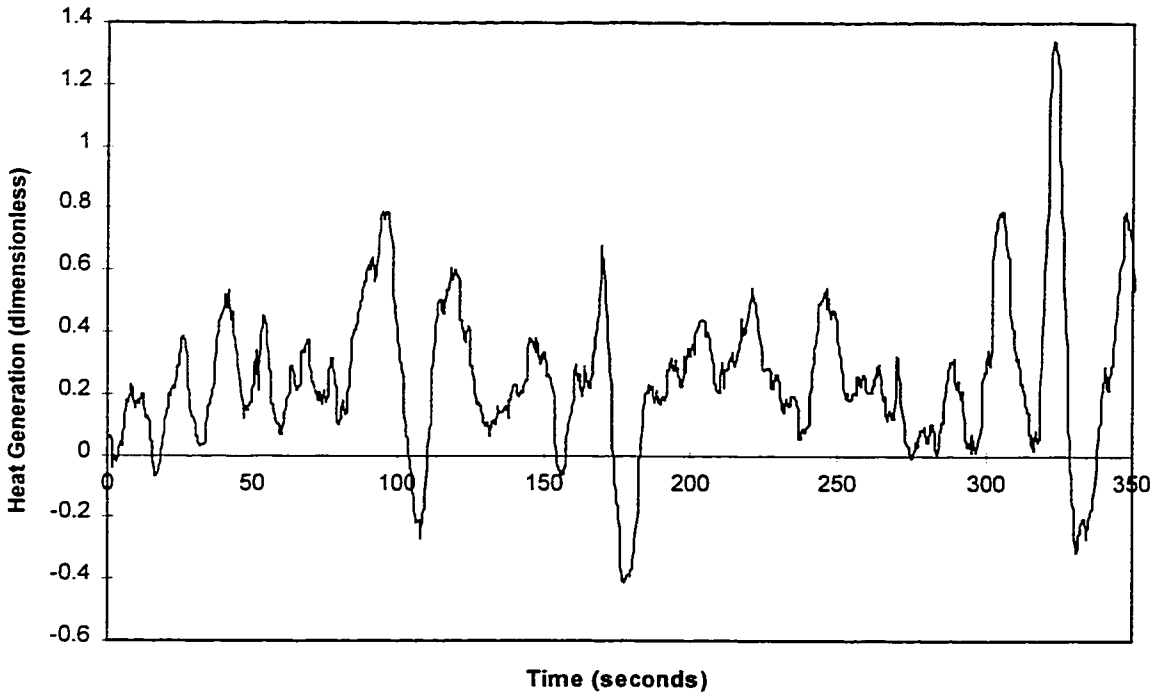

Figure 6.19: Estimated Q(t) for Q=0.25 (Model Calibrated at Q=1.0)

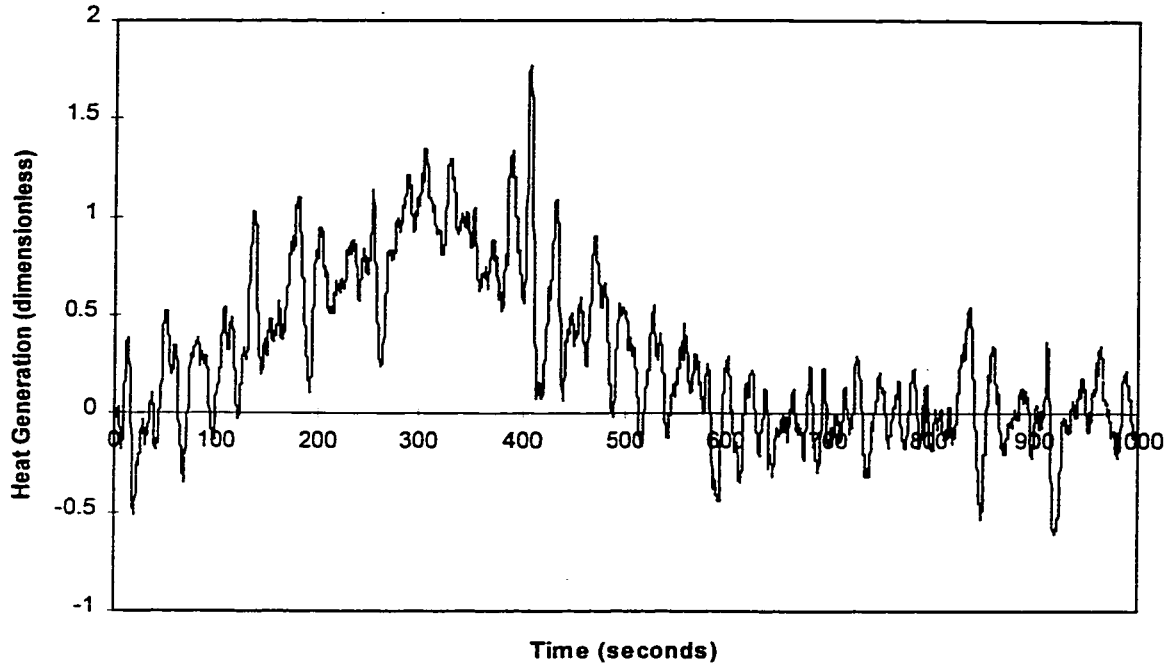

Figure 6.20: Estimated Q(t) for Triangular Input (Model Calibrated at Q=1.0)

$$H_x(s) = \frac{\delta_x(s)}{Q(s)}$$

$$H_y(s) = \frac{\delta_y(s)}{Q(s)}$$

The direct transfer functions are determined in the same general manner as with the inverse transfer function, by calibrating an analytical model of the step response in the time domain with measured data, and then transforming the calibrated model to the Laplace domain. The accuracy of the thermal deflection model is not as critical as in the case of the temperature model because it is not subjected to an inverse solution. Nevertheless, any inaccuracy that is inherent to the thermal deflection model cannot be compensated by the control system, so it is important to devise a calibrated analytical model that is as accurate as possible. The sources of inaccuracy in the thermal deflection model may be divided into two types. The first type is non-linear error, which is produced by, for example, joint interaction, radiation effects, non-linear measurement and instrumentation noise. This type of inaccuracy cannot be dealt with in a linear model, and so it represents an optimal error bound which can only be approached with a linear transfer function. The second type of inaccuracy is linear error, that is error which increases linearly with the magnitude of the input. This second type of inaccuracy results from an inadequate linear model, which does not exactly match the measured data on which it was calibrated. Since we are now dealing with a direct problem, there is no excuse for introducing any significant linear error into the direct transfer function, since linear error can always be reduced by incorporating more parameters into the analytical model. The objective then is to reduce the range of the linear error to within the scope of the non-linear error, thereby realizing an optimal linear system.

The finite-element and experimental results have shown that the thermal deflection in a large machine structure is never an underdamped system. Hence, a reasonable analytical model for the step response in the time domain is as follows:

$$\delta(t) = A_1 - A_1 e^{-a_1 t} + A_2 - A_2 e^{-a_2 t} + \ldots\ldots + A_n - A_n e^{-a_n t} \tag{6.14}$$

The derivative of equation (6.14) at t=0 is:

$$\delta'(t) = A_1 a_1 + A_2 a_2 + \ldots\ldots + A_n a_n \tag{6.15}$$

This form ensures that $\delta(0)=0$, however it cannot easily accommodate an initial delay without some of the A_n co-efficients being negative. It will be shown that the initial derivative of the thermal deflection step response is zero, therefore a better form for the step response is as follows:

$$\delta(t) = A + B - Ae^{-at} - Be^{-bt} + Dte^{-dt} \tag{6.16}$$

The derivative of equation (17) at t=0 is:

$$Aa + Bb + D \tag{6.17}$$

which can be made equal to zero if D=-Aa-Bb. The analytical form in equation (6.16), with 6 analytical parameters was found to be sufficiently accurate in all of the cases in which it was used.

6.10 Calibrating the Thermal Deflection Model

Figure 6.21 shows the measured thermal deflection in the y-direction for a step thermal input of magnitude Q=1.0. The steady-state thermal deflection is 242.4 microns, which is around 2.7 times larger than the maximum deflection of the real machine tool shown in figure (5.1). Figure 6.22 shows the thermal deflection in the x-direction for the same step input of magnitude q=1.0. The maximum x-deflection is 77.6 microns. The analytical model in equation (6.16) was calibrated with measured thermal deflection data using MATHCAD visual programming, as shown in figure 6.3. The calibrated values of the parameters in equation (6.16) are:

$$\begin{array}{ll} A = 10.546 & a = 5.90E\text{-}04 \\ B = 67.08 & b = 9.14E\text{-}04 \\ D = -0.0414 & d = 0.00435 \end{array} \tag{6.18}$$

for the x-deflection, and:

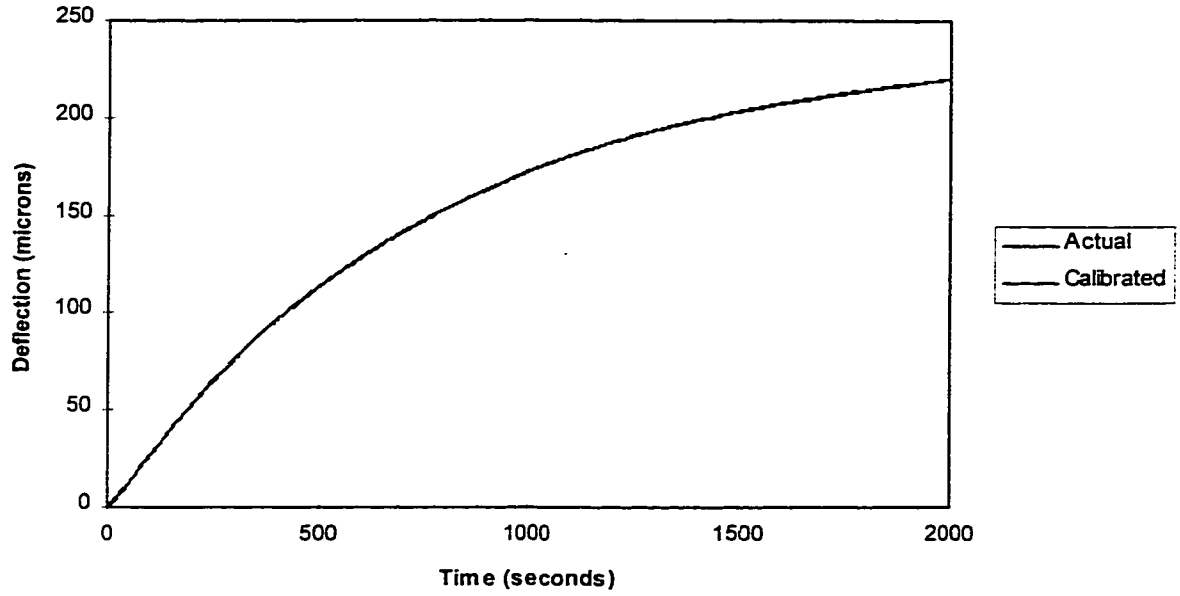

Figure 6.21: y-Deflection with Calibrated Model

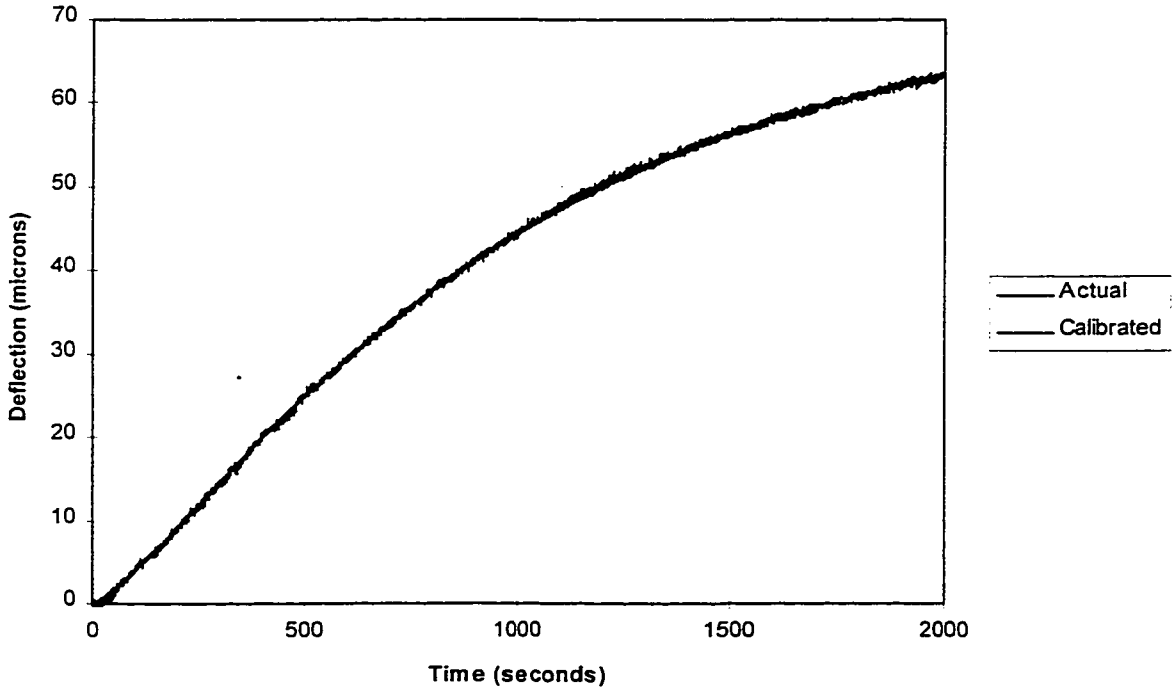

Figure 6.22: x-Deflection with Calibrated Model

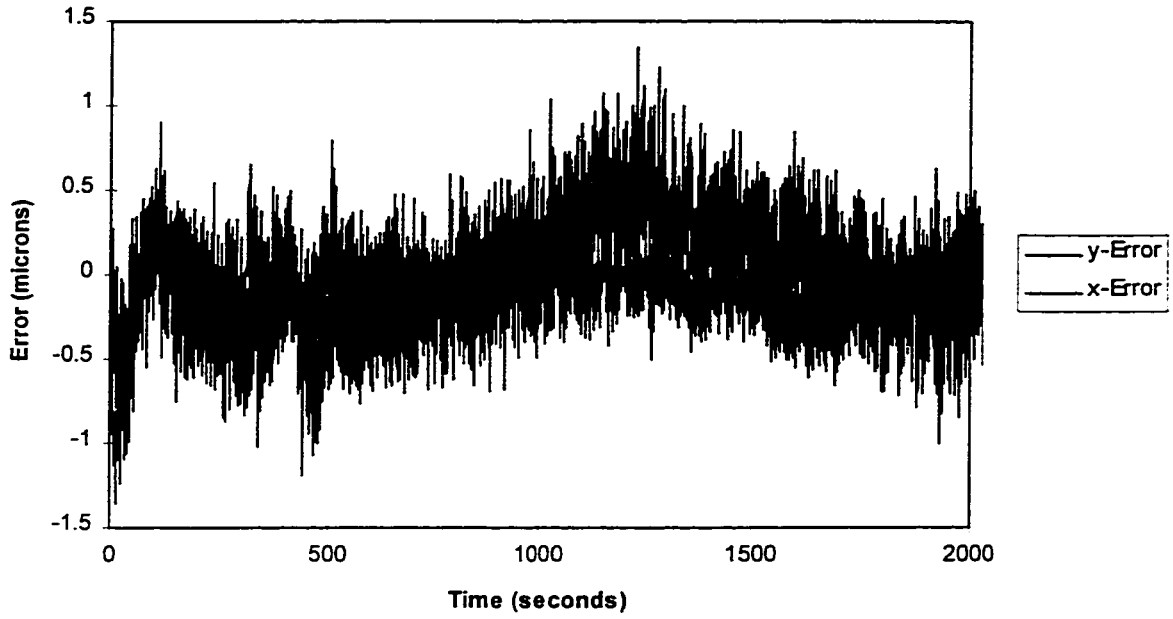

Figure 6.23: Deflection Error

$$\begin{array}{ll} A = 100.43 & a = 9.09E\text{-}04 \\ B = 141.96 & b = 1.57E\text{-}03 \\ D = -0.01000 & d = 0.00903 \end{array} \qquad (6.19)$$

for the y-deflection. The calibrated analytical step responses are shown in figures 6.21 and 6.22 along with the measured thermal deflection data. The difference between the two curves in figures 6.21 and 6.22 is the thermal deflection modelling error, shown in figure 6.23. The error plots shown in figure 6.23 include both linear and non-linear error components. The combined total error is less than ±1.5 microns, which is within the band of the non-linear error caused by measurement noise, and below the specified nominal resolution of the LVDTs, which is ±2 microns. Increasing the accuracy of the analytical model by increasing the number of terms and parameters will therefore not improve the accuracy of the transfer function.

Figure 6.24 shows the magnitude of the DFT of the y-deflection noise, and figure 6.25 shows the magnitude of the DFT of the x-deflection noise. The noise is approximately white noise over most of the useful frequency range, as shown in the figures. There is a low frequency peak, which is apparent also from figure 6.23 as a low frequency movement. The low frequency noise does not affect the linear accuracy of the calibrated model, as will be seen shortly.

6.11 The Thermal Deflection Transfer Function

The analytical step response in equation (6.16) transforms to the Laplace domain to define the following transfer function:

$$H(s) = \frac{\delta(s)}{Q(s)} = \frac{c_0 + c_1 s + c_2 s^2 + c_3 s^3}{(s+a)(s+b)(s+d)^2} \qquad (6.20)$$

where:

$$\begin{aligned} c_0 &= Aabd^2 + Babd^2 \\ c_1 &= 2Babd + Bbd^2 + Dab + Aad^2 + 2Aabd \\ c_2 &= 2Bbd + Aab + Db + Da + Bab + 2Aad \\ c_3 &= D + Bb + Aa \end{aligned} \qquad (6.21)$$

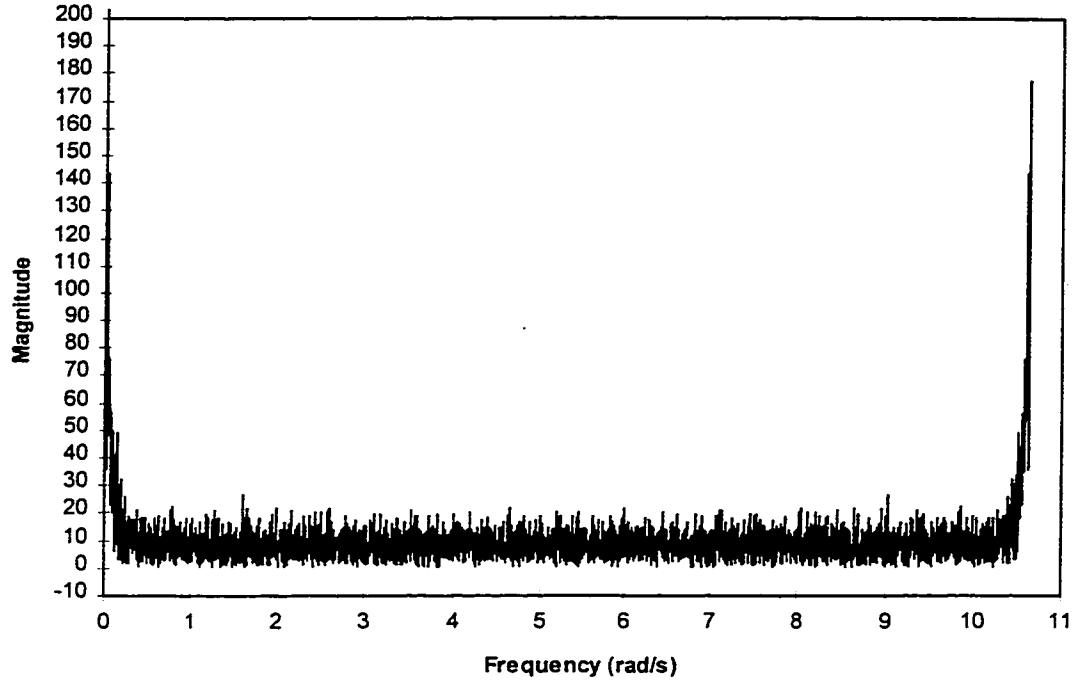

Figure 6.24: DFT of y-axis Deflection Noise

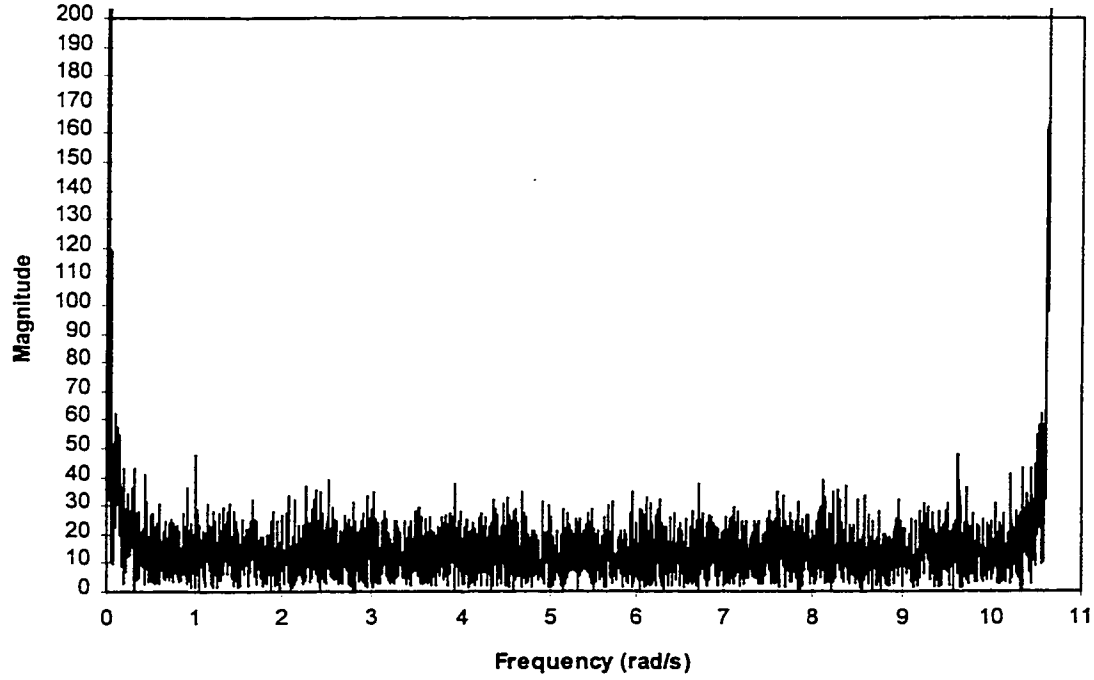

Figure 6.25: DFT of x-Axis Deflection Noise

This transfer function could be transformed back to the time domain to define a time domain transfer function H(t), which could be used to solve the direct problem using a convolution integral, as was done to solve the inverse problem previously. Being a direct transfer function, equation (6.20) does not contain any singularity functions, so the time domain transfer function reduces to the convolution integral only. It turns out that the time domain solution using a convolution is not a very practical method of calculating the thermal deflection in this case. Figures 6.26 and 6.27 show the time domain transfer functions $H_x(t)$ and $H_y(t)$, based on the calibrations of equations (6.18) and (6.19). The transfer functions were transformed analytically, based on equation (6.20). The figures show that the transfer functions approach zero as $t \to \infty$, confirming that the transfer functions are stable. However, the time constants for this decay are very large. Even after 4000 seconds the transfer functions still have not approached sufficiently close to zero to allow for the truncation of the tail end. Using the convolution approach, the controller would have to maintain a window of at least 1500 seconds of stored input values $Q(t_k)$ in order to achieve an accurate estimate of the thermal deflection. Using every estimated $Q(t_k)$ with a sampling time of 0.5 seconds would require that 3000 values be stored and processed with every control cycle. Since this much data could not be processed in 0.5 seconds, it would be necessary to discard some of the sampled data, keeping only one in five or less, which naturally will affect the accuracy of the solution. In order to avoid the problem of maintaining and processing a large window of data, a different approach to evaluating the thermal deflection transfer function will be used.

6.12 A Real Time Analytical Solution of the Thermal Deflection Transfer Function

6.12.1 The Criterion for the Solution

Before attempting to derive a real time solution to the thermal deflection transfer function, it is important to recognize the limitations of any solution. In the first place, the input to the transfer function is the estimated heat generation Q(t), which was shown for several inputs in figures 6.13, 6.17, 6.19, and 6.20. The estimated Q(t) is a delayed and distorted representation

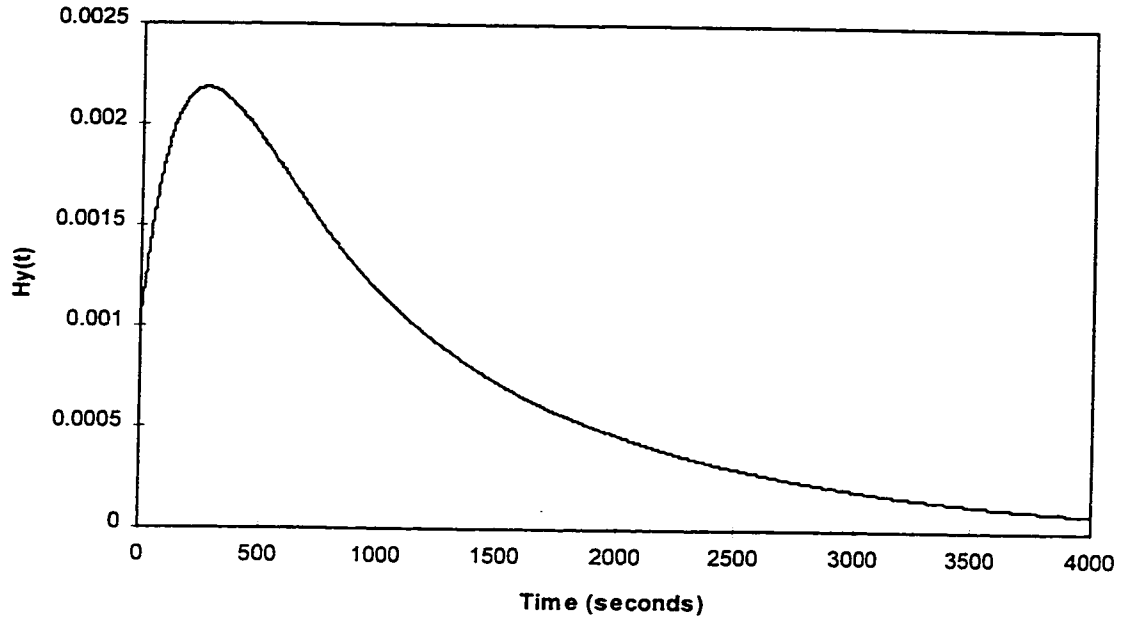

Figure 6.26: Time Domain Transfer Function $H_y(t)$

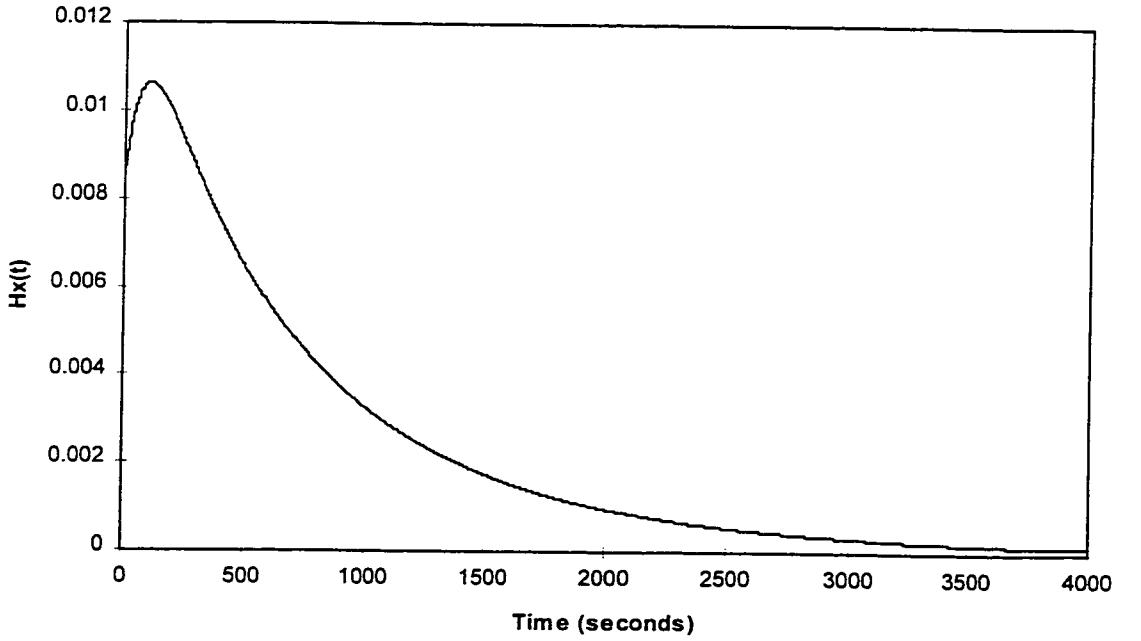

Figure 6.27: Time Domain Transfer Function $H_x(t)$

of the actual heat generation, and this error will be carried over to the deflection solution, even though it will be significantly altered by the dynamics of the thermal deflection model. Furthermore, the estimated heat generation is determined at only a finite number of discrete points, with no information available about the behaviour of the heat input between estimated points. This does not pose a significant problem where the sample period is much smaller than the time constant of the thermal deflection step response. Figures 6.21 and 6.22 show that the thermal deflection time constants for the present model are around 20 minutes, and they are normally even larger than that for an actual machine structure which is usually more massive than the present model. A sampling time of 0.5 seconds makes for an excellent approximation to a continuous system. Nevertheless, in order to derive an analytical solution it is necessary to assume at least a piece-wise continuous analytical form for the input function. The analytical form that will be used is the familiar staircase function, or zero-order hold of the sampled heat magnitude values.

In order to minimize the data which must be stored and processed, the solution should be an incremental one. That is, the algorithm should be able to store the thermal deflection at the end of each time step, and then determine and add to it the additional thermal deflection produced during the next time step. The thermal deflection transfer function in equation (6.20) is inadequate for this type of solution because it is based on the assumption that the initial conditions of all derivatives of the input and output variables are zero. The objective now is to derive a more general solution that can accommodate non-zero initial conditions at $t=0^-$. By the nature of such a solution it cannot be expressed in the form of a transfer function, as will be seen shortly.

6.12.2 The Derivation of the Analytical Solution

The derivation of the general solution begins with the transfer function in equation (6.20). Cross-multiplying results in the equation:

$$\left(d_0 + d_1 s + d_2 s^2 + d_3 s^3 + s^4\right)\delta(s) = \left(c_0 + c_1 s + c_2 s^2 + c_3 s^3\right)Q(s) \tag{6.22}$$

where the c_i co-efficients are defined by equation (6.21) and the d_0 co-efficients are defined as follows:

$$\begin{aligned} d_0 &= abd^2 \\ d_1 &= ad^2 + bd^2 + 2abd \\ d_2 &= 2bd + ab + d^2 + 2ad \\ d_3 &= 2d + a + b \end{aligned} \tag{6.23}$$

Assuming zero initial conditions, the above equation transforms into a differential equation in the time domain:

$$\delta'''' + d_3\delta''' + d_2\delta'' + d_1\delta' + d_0\delta = c_3 q''' + c_2 q'' + c_1 q' + c_0 q \tag{6.24}$$

The transfer function would be re-obtained if the differential equation (6.24) were transformed to the Laplace domain with zero initial conditions. A more general solution may be obtained however, by transforming the differential equation to the Laplace domain with non-zero initial conditions. In this case, a continuous function f(t) transforms to the Laplace domain as follows:

$$\mathcal{L}\{f(t)^n\} = s^n F(s) - s^{n-1} f(0) - s^{n-2} f'(0) - \ldots\ldots f^n(0) \tag{6.25}$$

The Transformation of all of the terms of equation (6.24), collecting powers of s and then solving for $\delta(s)$ results in a general equation that is a function of all of the initial derivatives of δ and of Q. The general equation can be simplified somewhat by recognizing that a zero order hold representation of the input implies that all initial derivatives of Q(t) are zero at $t=0^-$. Making use of this simplification, the general solution with initial conditions is:

$$\delta(s) = \frac{c_0 + c_1 s + c_2 s^2 + c_3 s^3}{d_0 + d_1 s + d_2 s^2 + d_3 s^3 + s^4} Q(s) + \frac{e_0 + e_1 s + e_2 s^2 + e_3 s^3}{d_0 + d_1 s + d_2 s^2 + d_3 s^3 + s^4} \tag{6.26}$$

where:

$$
\begin{aligned}
e_0 &= \delta_0''' + d_3\delta_0'' + d_2\delta_0' + d_1\delta_0 - c_1 q_0 \\
e_1 &= \delta_0'' + d_3\delta_0' + d_2\delta_0 - c_2 q_0 \\
e_2 &= \delta_0' + d_3\delta_0 - c_3 q_0 \\
e_3 &= \delta_0
\end{aligned}
\tag{6.27}
$$

nd the denominator co-efficients are given by equation (6.23). Notice that all of the derivatives of q_0 have been made zero in equation (6.27). The denominator can be refactored back to the form in equation (6.20) to yield:

$$
\delta(s) = \frac{c_0 + c_1 s + c_2 s^2 + c_3 s^3}{(s+a)(s+b)(s+d)^2} Q(s) + \frac{e_0 + e_1 s + e_2 s^2 + e_3 s^3}{(s+a)(s+b)(s+d)^2} \tag{6.28}
$$

In order to use equation (6.28) to generate a solution for δ(t) in real time, it must be transformed into a solution in the time domain. Figure 6.28 shows hypothetical input data representing Q(t) and the output function δ(t). Notice that the discrete estimated points Q(kT) have been extrapolated to the staircase function shown in the figure. Prior to each transition at t=kT the derivatives of the analytical function δ(t) are, in general, non-zero. The analytical input which is applied at each kT is a step of magnitude Q(kT). The form of the solution given in equation (6.28) incorporates all of the previous step inputs into the initial conditions at $t=kT^-$, that is the time just prior to the application of the input at t=kT. Assuming that all of the derivatives are known at $t=kT^-$, it is not necessary to retain any information about the previous step inputs. Therefore, the analytical solution for the present time step is equal to the step response of equation (6.28). Notice that the first term on the right in equation (6.28) is the transfer function H(s) from equation (6.20). Applying the step input Q(s)=1/s to this transfer function and transforming to the time domain yields the calibrated unit step response from which the transfer function was derived:

$$
\delta_1(t) = A + B - Ae^{-at} - Be^{-bt} + Dte^{-dt} \tag{6.29}
$$

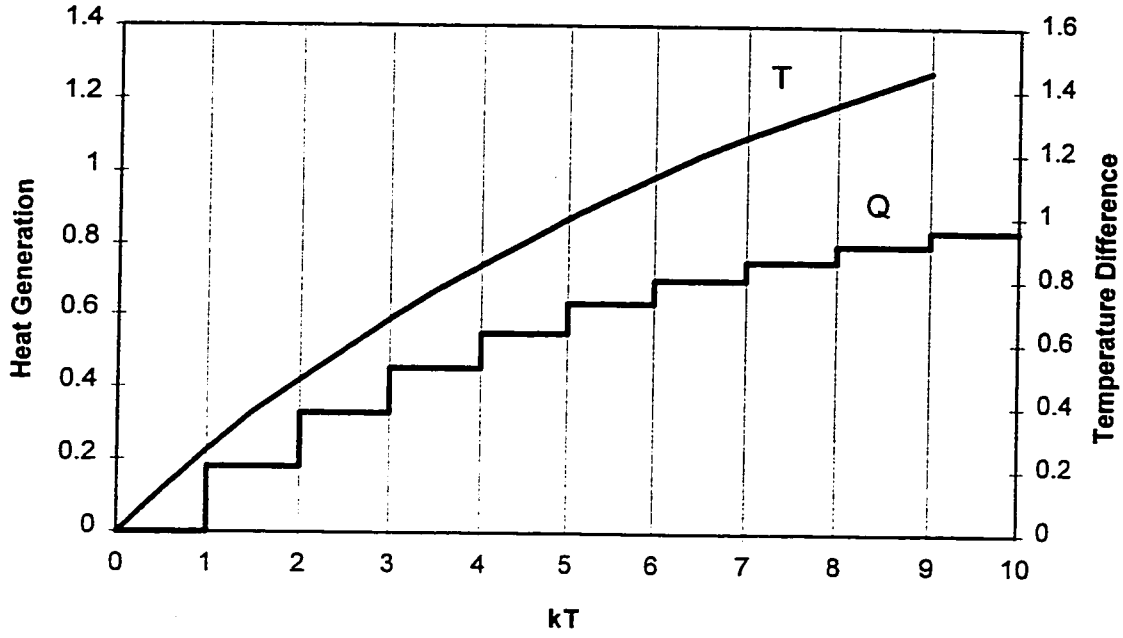

Figure 6.28: Input Data Extrapolated to Staircase Function

The second part of equation (6.28) is the part which accommodates the initial conditions. Before it can be transformed to the time domain it must be expanded into partial fractions. The process of expanding the term involves very tedious algebraic manipulation that will not be documented here. The unexpanded function is:

$$\delta_2(s) = \frac{e_0 + e_1 s + e_2 s^2 + e_3 s^3}{(s+a)(s+b)(s+d)^2} \tag{6.30}$$

Which expands in partial fraction form to:

$$\delta_2(s) = \frac{AA}{s+a} + \frac{BB}{s+b} + \frac{DD}{(s+d)^2} + \frac{EE}{s+d} \tag{6.31}$$

where:

$$AA = \frac{e_3 a^2 - e_2 a^2 + e_1 a - e_0}{(a-d)^2(a-b)}$$

$$BB = \frac{e_3 b^3 - e_2 b^2 + e_1 b - e_0}{(b-d)^2(b-a)}$$

$$DD = \frac{e_3 d^3 - e_2 d^2 + e_1 d - e_0}{(d-b)(a-d)} \tag{6.32}$$

$$EE = \frac{(2d-b-a)e_0 + (ab-d^2)e_1 + (bd^2+ad^2-2abd)e_2 + (d^4-2bd^3-2ad^3+3abd^2)e_3}{((b-d)(a-d))^2}$$

The function in equation (6.31) transforms to the time domain as follows:

$$\delta_2(t) = AAe^{-at} + BBe^{-bt} + DDte^{-dt} + EEe^{-dt} \tag{6.33}$$

The complete step response is obtained by adding together equation (6.29) multiplied by the magnitude of the step input q, and equation (6.33):

$$\delta(t) = Aq + Bq + (AA-Aq)e^{-at} + (BB-Bq)e^{-bt} + (DD+Dq)te^{-dt} + EEe^{-dt} \tag{6.34}$$

The co-efficients AA, BB, DD, and EE are defined by equation (6.32), which is in turn a function of the parameters e_k in equation (6.27). The e_k parameters are a function of the d_k parameters in equation (6.23), but they are also a function of the initial derivatives of δ and the initial value of Q. The initial values describe the condition of the system just prior to the application of the input, that is at $t=kT^-$ in figure 6.28. These values must be evaluated at the

previous time step, based on the previous input and initial conditions. The procedure then is as follows: starting from a zero initial condition and a step input at t=0, calculate $\delta(T)$ and derivatives of $\delta(T)$ up to the third derivative. These values become the initial derivatives for the second time step, beginning with a step input of magnitude q=Q(T) at t=T. The procedure is repeated at each additional time step. Keep in mind that calculating these derivatives does not introduce any error because this is an analytical system that is free from measurement noise. The solution after n time steps will in fact be an exact analytical solution for the deflection model with the staircase input shown schematically in figure 6.28. With a sampling time on the order of 0.5 seconds, the sampled input solution very nearly approximates the continuous one.

The value of $\delta(T)$, $\delta`(T)$, $\delta``(T)$, and $\delta```(T)$ are found by differentiating equation (6.34) and plugging in t=T. These define the initial derivatives of the next time step as follows:

$$\begin{aligned}
\delta(T) &= Aq + Bq + (AA-Aq)e^{-aT} + (BB-Bq)e^{-bT} + (DD+Dq)Te^{-dT} + EEe^{-dT} \\
\delta'(T) &= a(Aq-AA)e^{-aT} + b(Bq-BB)e^{-bT} + (DD+Dq)e^{-dT} - d(DD+Dq)Te^{-dT} - dEEe^{-dT} \\
\delta''(T) &= a^2(AA-Aq)e^{-aT} + b^2(BB-Bq)e^{-bT} + d^2(DD+Dq)Te^{-dT} - 2d(DD+Dq)e^{-dT} + d^2EEe^{-dT} \\
\delta'''(T) &= a^3(Aq-AA)e^{-aT} + b^3(Bq-BB)e^{-bT} - d^3(DD+Dq)Te^{-dT} + 3d^2(DD+Dq)e^{-dT} - d^3EEe^{-dT}
\end{aligned} \tag{6.35}$$

All of the equations for the incremental analytical solution are now in place. The only constant variables in the algorithm are the calibration parameters defining the model: A, B, C, D, and a, b, c, d. The solution is obtained by evaluating in sequence: the d_k from equation (6.23); the e_k from equation (6.27) using the d_k and stored values of the initial derivatives; the variables AA, BB, DD, and EE from equation (6.32); and finally the thermal deflection and its derivatives for a step of magnitude q=Q(kT) from equation (6.35). The value $\delta(T)$ is the current estimate of the thermal deflection, and also is used along with its derivatives in equation (6.35) to define the initial conditions for the next time step. Despite the large number of equations, this solution is extremely fast because there is a very small amount of data to be carried over and processed from one time step to the next. Furthermore it is an exact solution because there is no truncation of the input function. A program that is based on this algorithm

was written in C++ and combined into one module with the program written earlier to estimate Q(kT). Before proceeding to the results, it is useful to first investigate the relationship between the inverse solution for the heat generation based on G(r,s) and the direct solution for the thermal deflection that was just derived, based on H(s).

6.13 Analysis of the Measurement Transfer function

The final objective of this chapter is to develop a practical method of estimating the thermal deflection due to one source from a single temperature difference measurement. The heat generation function Q(t) is an internal state variable that will never be used by the controller in real time. Thus, it is the combined transfer function G(r,s)H(s) and not the individual components that is the system of interest. The combined transfer function will now be called the *measurement* transfer function because it operates in a control system as an indirect measurement of the thermal deflection.

A Bode diagram of the inverse transfer function G(r,s) is shown in figure 6.29. The magnitude plot shows a DC gain of -9.8 dB, with the gain increasing linearly with the logarithm of the frequency after about 8.0E-03 rad/s or 1.3E-3 Hz. The absolute gain is arbitrary because it depends on the units that are used for the input and output variables, in this case temperature is measured in degrees Celsius and the heat generation magnitude is dimensionless. The noteworthy feature of figure 6.29 is that the magnitude gain increases linearly with the logarithm of the frequency, becoming extremely large for very high frequencies. This is characteristic of all inverse problems, and it is the source of the instability of the solution. The gain at 0.1 rad/s or 0.63 Hz is about 30 dB higher than the DC gain, and the gain at the sampling frequency of 2 Hz or 12.6 rad/s is 60 dB higher than the DC gain. This means that the 2 Hz noise is amplified one thousand times more than the useful signal, which can be assumed to be a DC input. This is in agreement with the result shown in figure 6.13, where the transformation of an unfiltered temperature difference by G(r,s) produced an

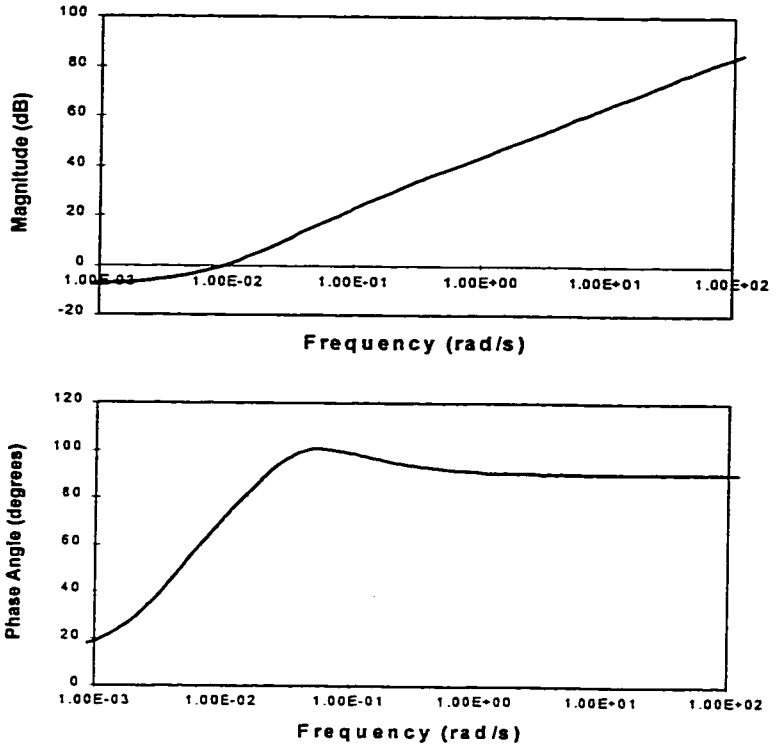

Figure 6.29: Bode Diagram of G(s)

estimate for Q(t) that was completely obliterated by amplified noise. Figure 6.29 also indicates that the noise amplification problem becomes worse for higher sampling rates, approaching infinity as the sampling rate becomes vary large.

Figures 6.30 and 6.31 show the bode diagrams of the thermal deflection transfer functions $H_x(s)$ and $H_y(s)$ respectively. The Bode diagrams of the thermal deflection transfer functions are characteristic of a low pass filter, with the gain approaching negative infinity decibels as the frequency becomes very large. This is a desirable characteristic because it tends to filter the high frequency noise that is amplified by the inverse transfer function. The $H_x(s)$ transfer function has a better characteristic than the $H_y(s)$ transfer function because the transition from the constant gain to the beginning of the cut-off region occurs at a lower frequency. This is reflected in figures 6.32 and 6.33, which show Bode diagrams of the measurement transfer functions $G(r,s)H_x(s)$ and $G(r,s)H_y(s)$ respectively. Both measurement transfer functions have a constant DC gain and a constant high frequency gain with a transition region. The unstable increasing amplitude gain of the inverse transfer function has been attenuated by the filtering characteristics of the thermal deflection transfer function. This would indicate that there is no practical limit on the cycling frequency of the controller because the noise amplification problem that is inherent to the inverse problem does not get any worse if the cycling frequency is increased above 2 Hz. The figures also show that the high frequency noise close to the 2 Hz sampling frequency is attenuated more than the lower frequency noise in the transition region. This is completely the opposite situation to the case of the Q(t) estimate in figure 6.13, where it was the high frequency noise that dominated the error in the Q(t) estimate. Since Q(t) is a hidden state variable that is calculated by the controller but is not processed independently of the thermal deflection transfer function, the noise in the Q(t) estimate should not be a concern to the control system designer, rather it is the behaviour of the measurement transfer functions in figures 6.32 and 6.33 that must be taken into consideration.

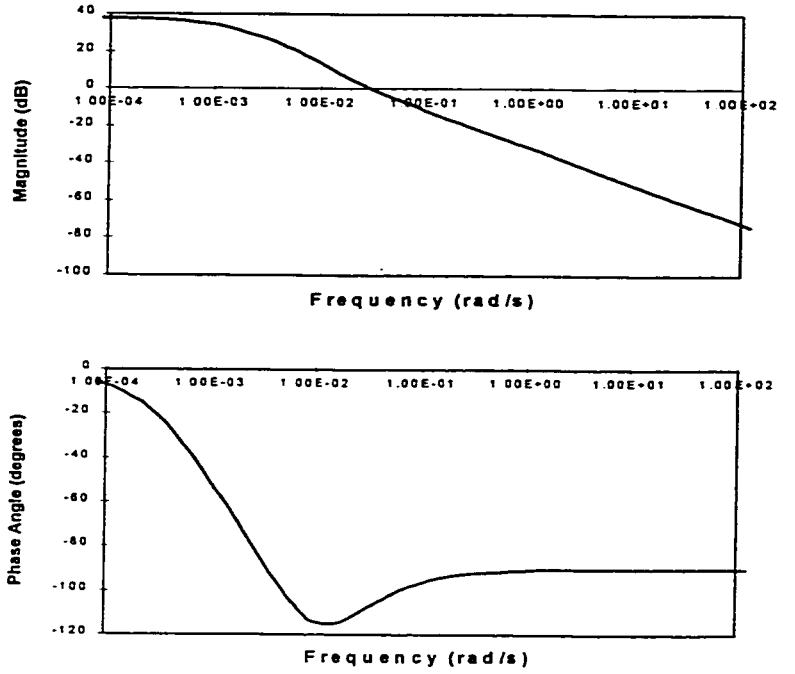

Figure 6.30: Bode Diagram of $H_x(s)$

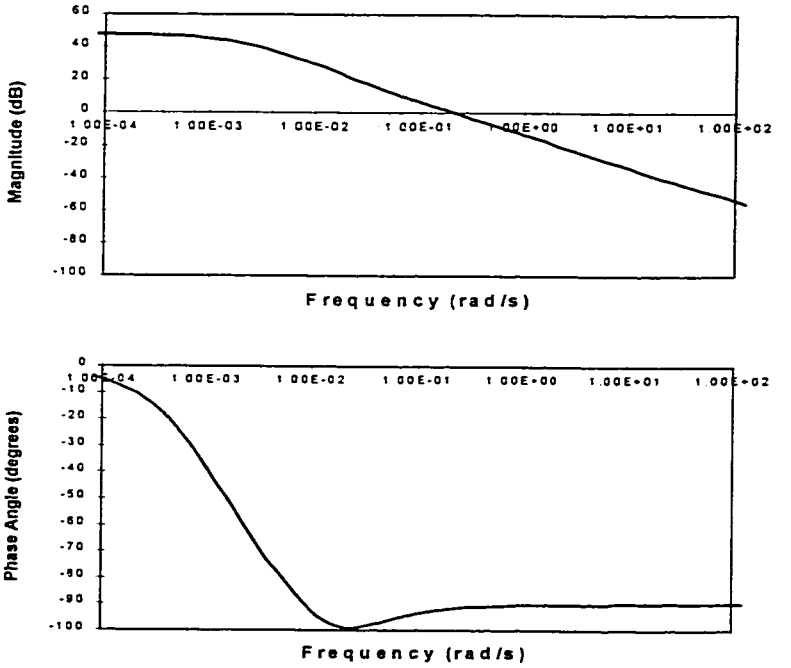

Figure 6.31: Bode Diagram of $H_y(s)$

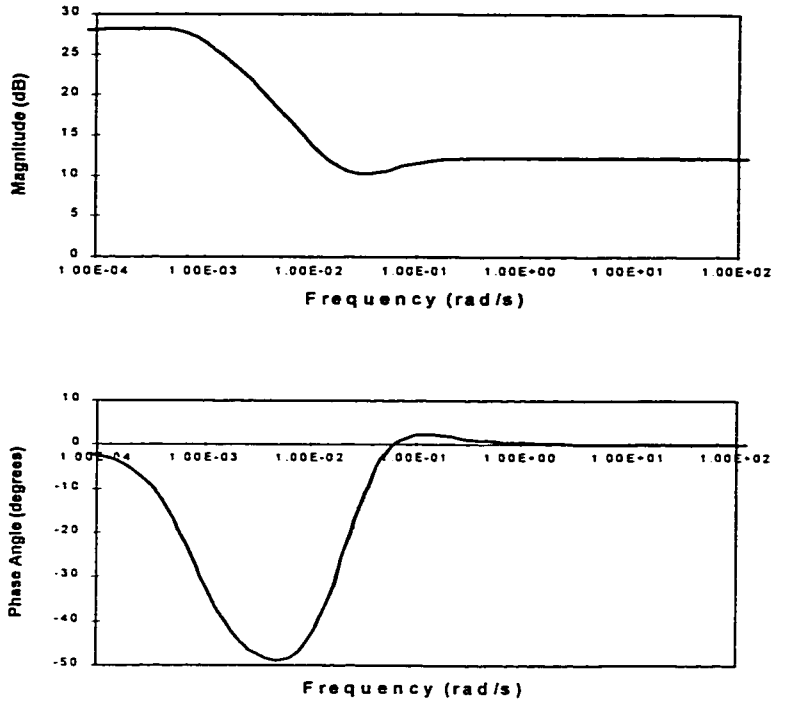

Figure 6.32: Bode Diagram of $G(s)H_x(s)$

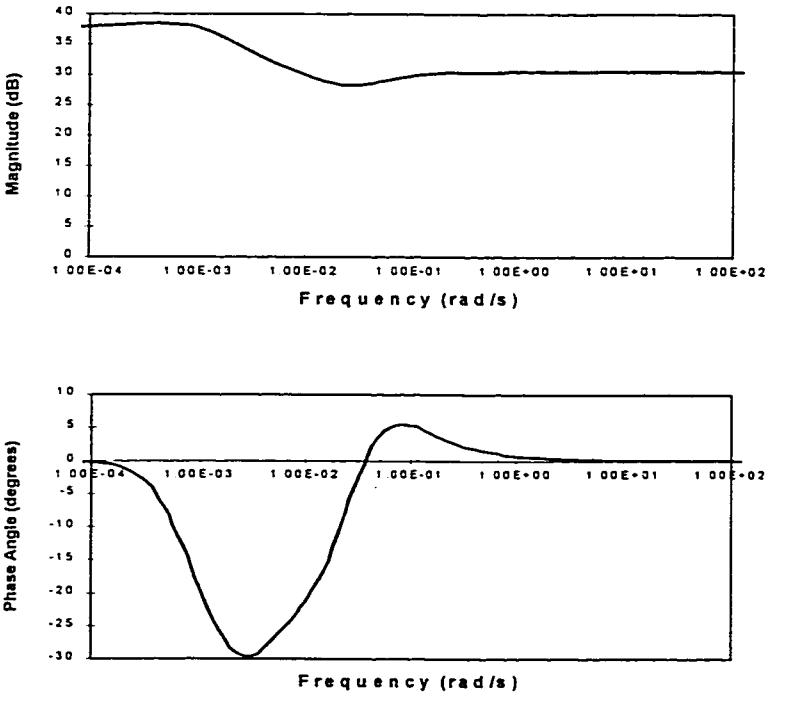

Figure 6.33: Bode Diagram of $G(s)H_y(s)$

A comparison of figures 6.32 and 6.33 shows that the noise amplification is greater for the $G(r,s)H_y(s)$ transfer function than for the $G(r,s)H_x(s)$ transfer function. In the first place, the constant high frequency gain is 16 dB lower than the DC gain for the $G(r,s)H_x(s)$ transfer function, but only 8 dB lower for the $G(r,s)H_x(s)$ transfer function. This translates into a signal to noise amplification ratio of 5.3 and 2.5 respectively. Secondly, the transition region for the $G(r,s)H_x(s)$ transfer function is slightly shorter that 2 decades, while for the $G(r,s)H_y(s)$ transfer function it is slightly longer than 2 decades. These differences are inherent to the characteristics of the physical model. The general appearance of figures 6.32 and 6.33 is common to all large structures, however the particular characteristics vary from one machine to the next, and for different axes of the same machine. If the noise characteristics of the measurement transfer function are not satisfactory, then filtering of the input temperature signal may be required. Filtering must be applied with caution however, since real time filtering introduces a phase lag which increases the net system delay. A more directed approach is to use derivative filtering only, since most of the high amplitude noise produced by the inverse transfer function comes from the temperature derivative term.

6.14 The Real Time Implementation of the Measurement Transfer Function

Figure 6.34 and 6.35 show the estimated thermal deflections $\delta_x(t)$ and $\delta_y(t)$ for a measured unit step temperature difference. The estimation was done in real time, using a sampling rate of 2 Hz, with derivative filtering of the measured temperature difference. The figures also show the actual thermal deflection, measured on the structure in real time. The estimated thermal deflection is very close to the actual thermal deflection with the greatest difference occurring near t=0 seconds. Figures 6.36 and 6.37 show the same estimated and measured thermal deflections for the first 200 seconds after the application of the step input, showing the initial lag in the estimate relative to the measured thermal deflection. The estimated deflection profiles appear to be shifted in time relative to the actual profiles. This shift is a result of the initial delay in the estimated Q(t), which was shown in figure 6.13, which

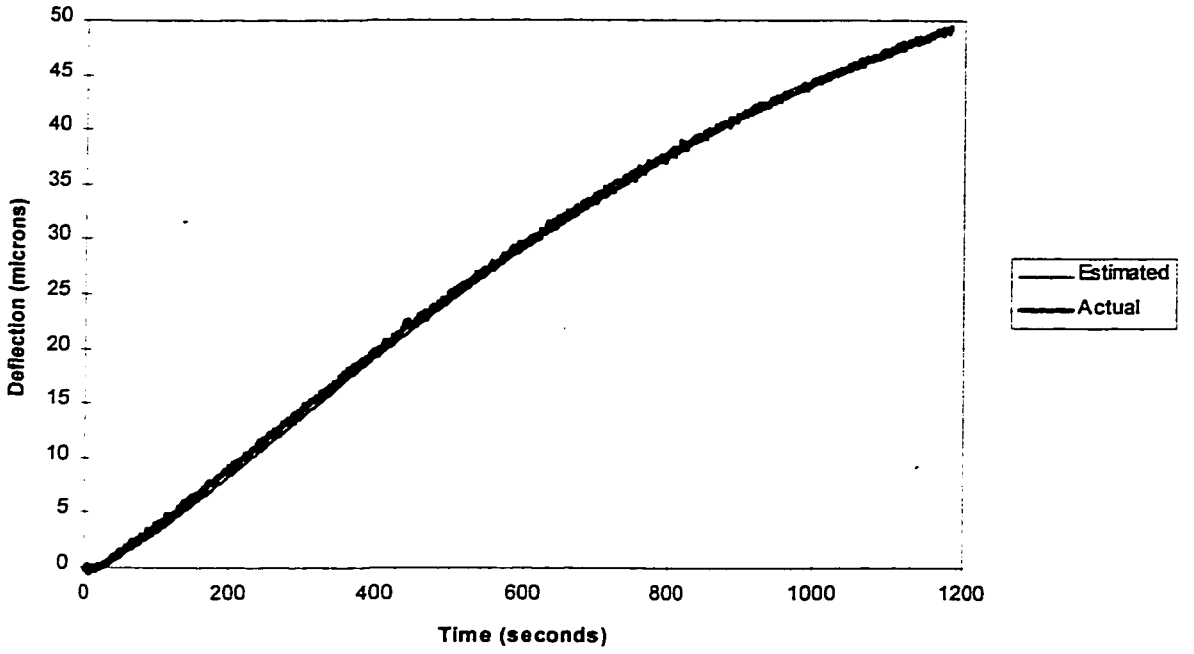

Figure 6.34: Estimated x-Deflection with q=1.0

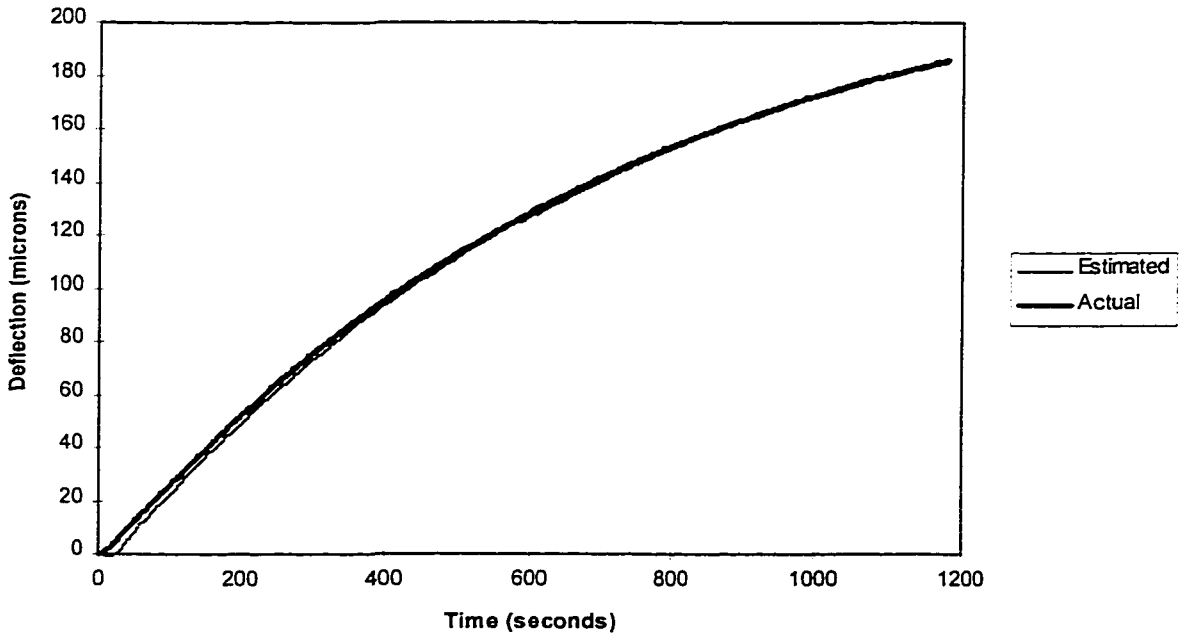

Figure 6.35: Estimated y-Deflection with q=1.0

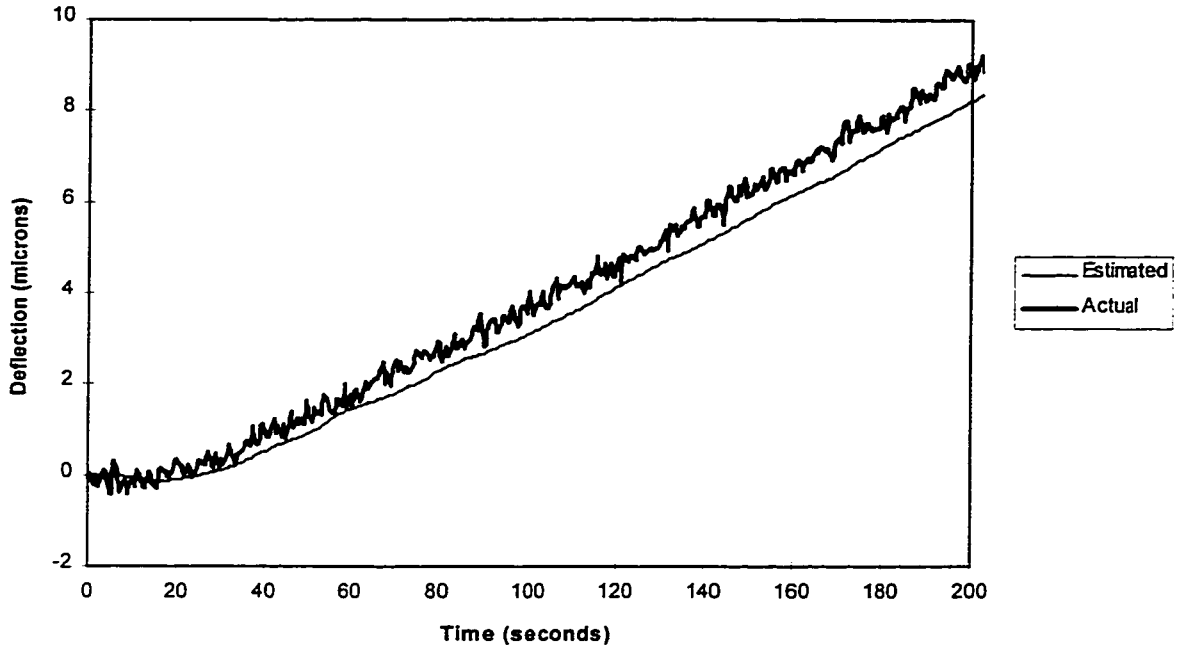

Figure 6.36: Estimated x-Deflection for the first 200 seconds with q=1.0

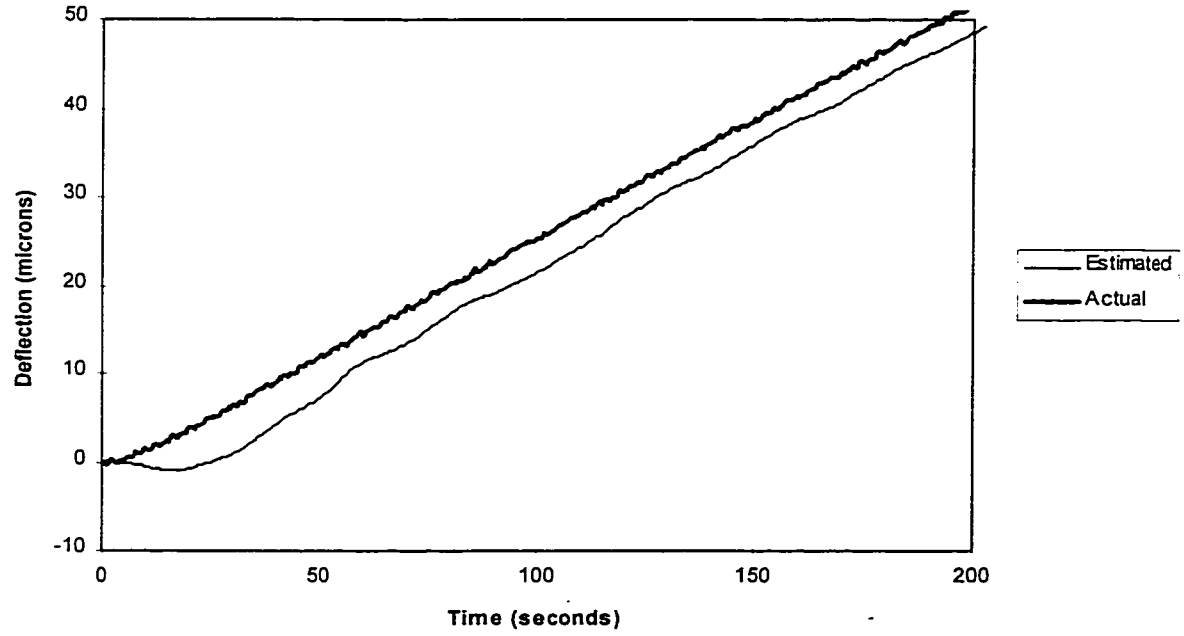

Figure 6.37: Estimated y-Deflection for First 200 Seconds with q=1.0

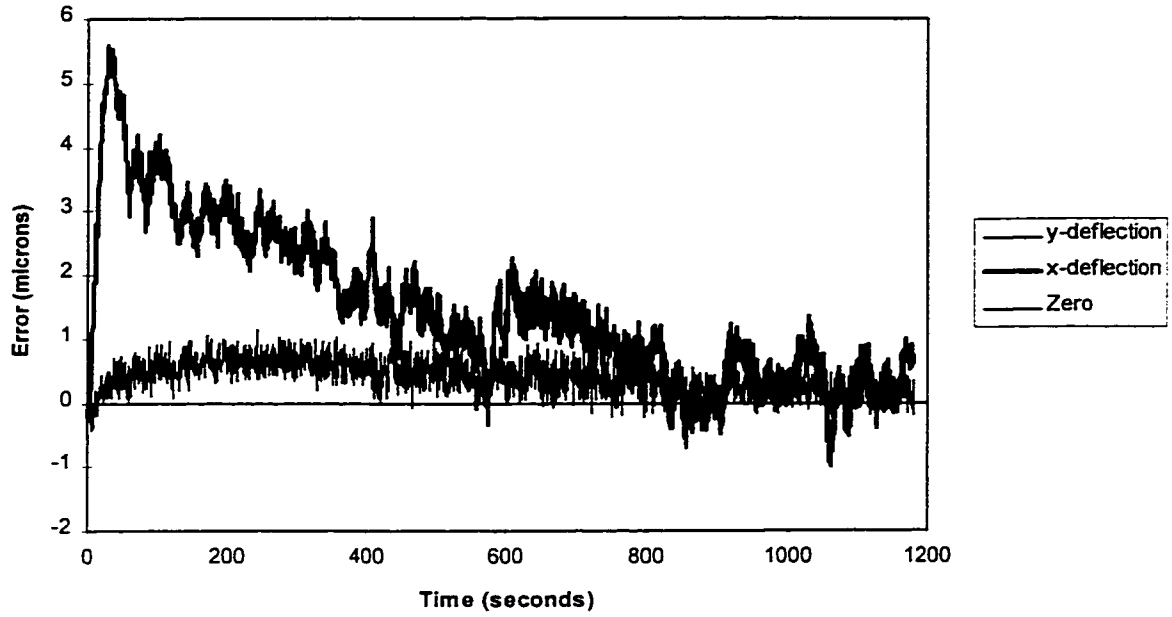

Figure 6.38: Deflection Error for q=1.0

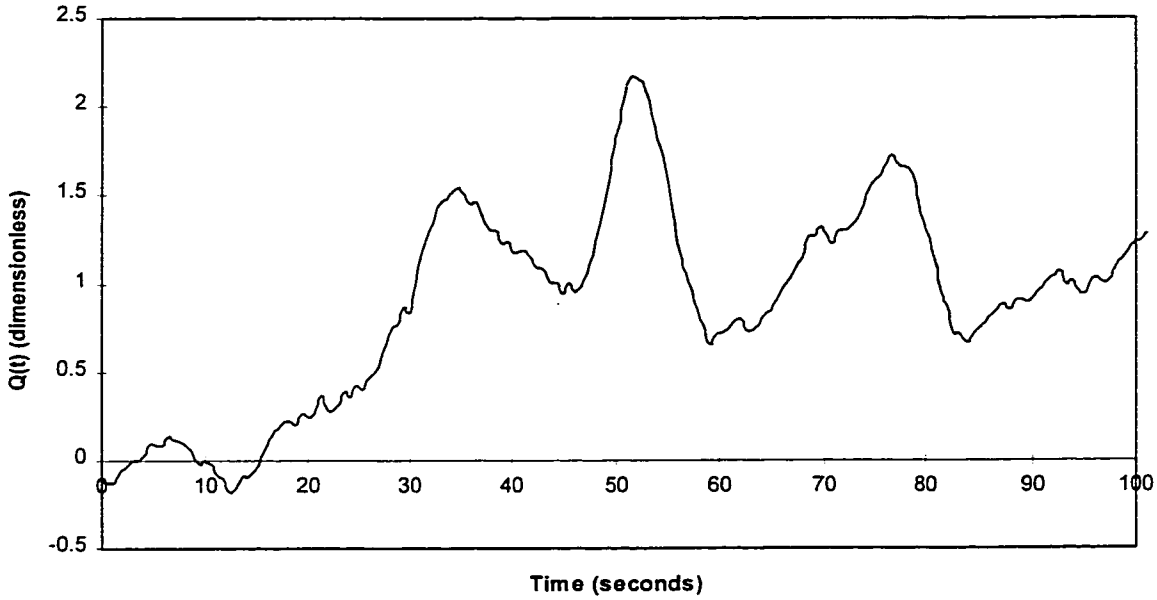

Figure 6.39: First 100 seconds of Estimated Q(t)=1.0

produces a corresponding delay in the estimated thermal deflection. The shift in the thermal deflection reduces with time because the input remains constant at 1.0 and the effect of the initial delay diminishes. Figure 6.38 shows the difference between the estimated and actual thermal deflection in the x-direction and in the y-direction, which represents the error in the estimation process. The steady state error band approaches 2 microns in the y-direction in steady-state, however there is an initial error exceeding -5 microns which expands the overall error band to around 7 microns. It is the initial error that is most pronounced, dominating the overall error band.

Figure 6.13 shows that the total system delay for the Q(t) estimation, including the derivative filter, is about 30 seconds, which is the time for the Q(t) estimate to reach its final value of 1.0. Figure 6.39 is a close-up view of the estimated Q(t) from figure 6.13. Now the estimate would be closer to the actual Q(t) if it could be shifted backward in time, as shown in figure 6.40. The estimate in figure 6.40 has not been changed relative to figure 6.39, except to recognize that the effects being detected at the present time are actually the result of inputs which occurred at some time in the past which have been held up by the system delay. For a linear system, the system delay is invariant with the magnitude and type of input, thus if the shifted estimate in figure 6.40 is actually better than the real estimate in figure 6.39, then it should also be a better estimate for any other Q(t). The negative time shift shown in figure 6.40 will be called the *artificial delay*, and if chosen properly the artificial delay can be made to cancel the system delay, resulting in an improved estimate of Q(t) and therefore an improved estimate for the thermal deflection. The one major problem with using an artificial delay is that it creates a band where no information about Q(t) is available, as shown in figure 6.40. The duration of this 'silent region' is equal to the length of the artificial delay. Since a complete time history of Q(t) is required, it is necessary to fill in this region with some sort of assumed or extrapolated values. Figure 6.41 shows a few possibilities for filling in the silent region. One possibility is to assume a constant value equal to 0.5, another possibility is to

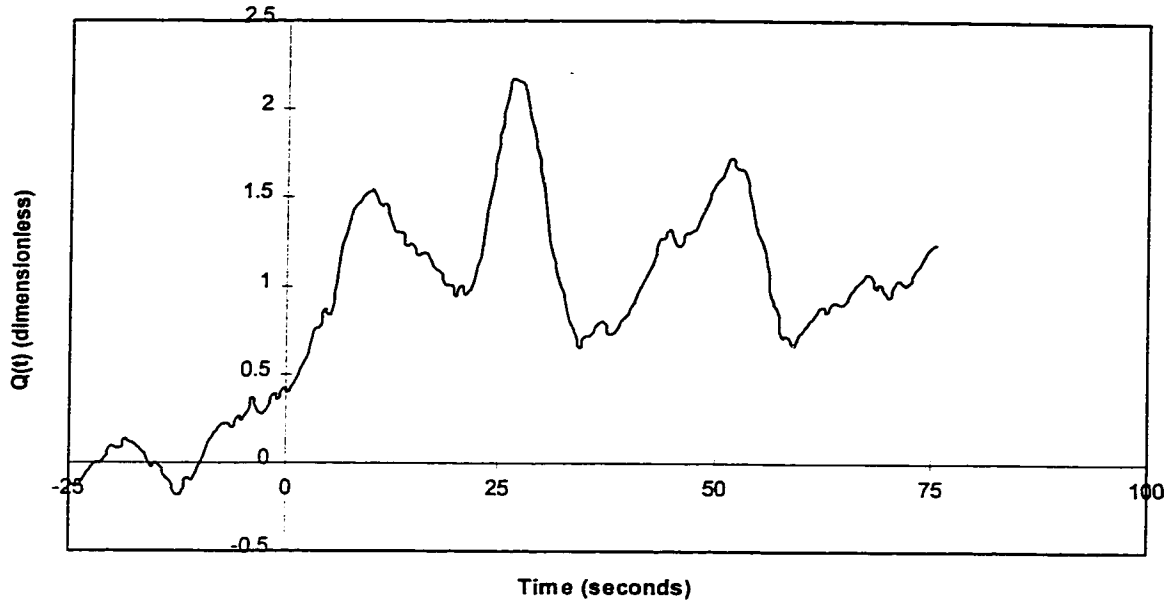

Figure 6.40: Estimated Q(t)=1.0 Shifted backward by 25 seconds

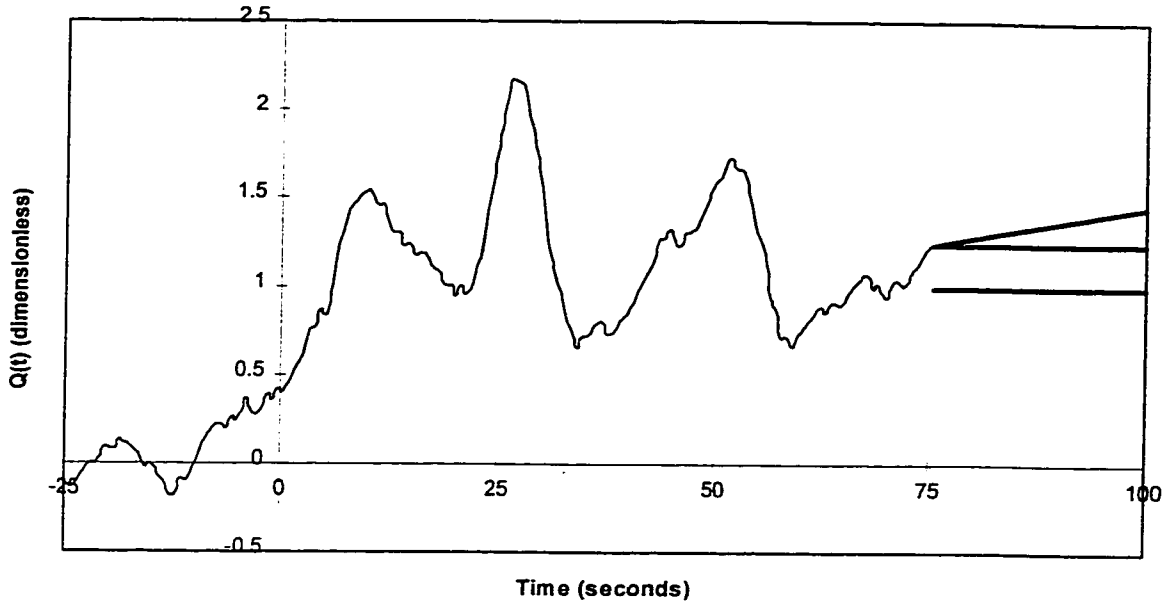

Figure 6.41: Shifted Estimated Q(t) showing Three Possible Filler Functions

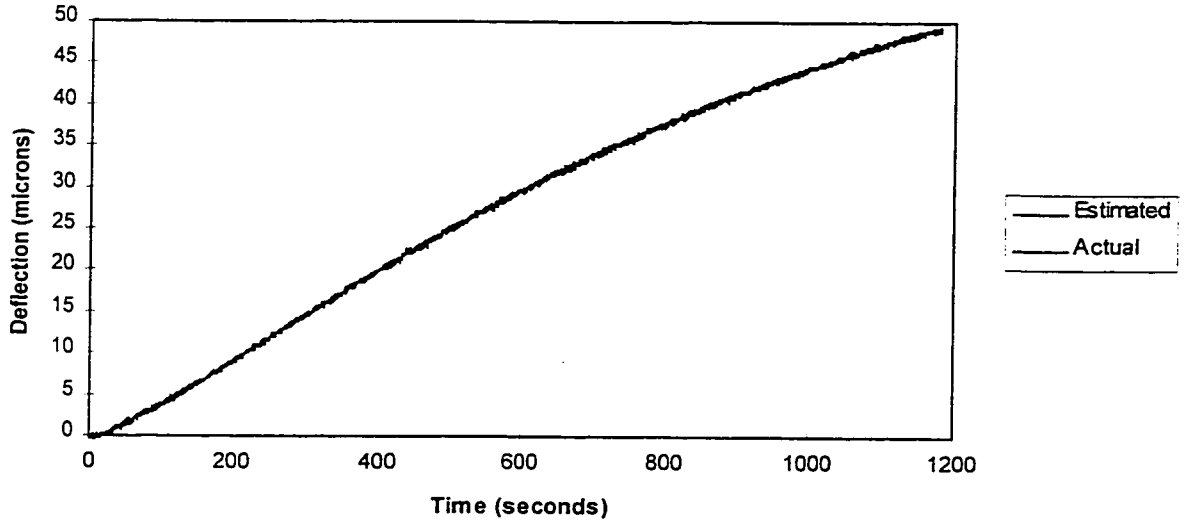

Figure 6.42: Estimated x-Deflection with 10 Second Artificial Delay with q=1.0

extrapolate the last known value of Q(t), and the final possibility shown in figure 6.41 is to extrapolate the last known derivative. There are many other possibilities, however the fact is that no direct information can be obtained about Q(t) in this region, so any assumed or extrapolated values will introduce some error. It was found that assuming values arbitrarily produced unreliable results, and extrapolating the derivative introduced too much noise, thus the best compromise is to extrapolate the last known value of Q(t) into the silent region.

Since the artificial delay with last value extrapolation increases the overall noise in the output, the optimal solution is not necessarily to cancel the whole of the system delay. Increasing the artificial delay has the effect of reducing the initial error to a step input, at the cost of increased error in the steady-state because of noise. If the objective is to minimize the overall error band for a step input then the optimal artificial delay will produce initial and final error bands which are equal. However, if a machine tool is to be operated for long periods of time, and only infrequently subjected to a sudden large step input, some other solution may be optimal. Figures 6.42 and 6.43 show the estimated and actual thermal deflection for a unit step input, using an artificial delay of 10 seconds in the real time estimation algorithm, and figure 6.44 shows the error. The 10 second delay has reduced the initial maximum error to less than 4 microns, and the overall error band is about 5 microns. Furthermore, the initial error drops within the steady state error band within 40 seconds of the input, as opposed to 500 seconds in the case of zero artificial delay, and there is very little increase in the system noise at steady-state. Increasing the artificial delay above 10 seconds brings much less improvement in the initial error and increases the steady-state noise considerably, hence the 10 second artificial delay is chosen for the best overall performance.

6.15 Results of the Thermal Deflection Estimation Algorithm for Various Inputs

Figure 6.45 shows the estimated thermal deflection along with the actual thermal deflection for the measurement algorithm with 12 second delay, and an input of q=0.5. Figure

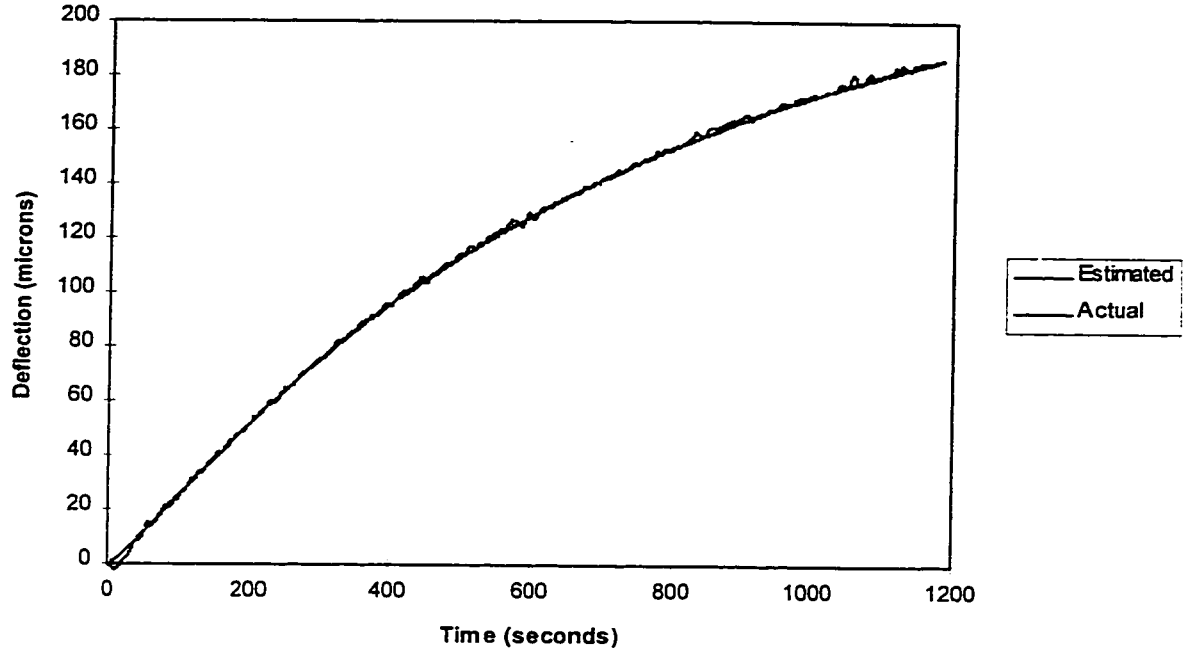

Figure 6.43: Estimated y-Deflection with 10 Second Artificial Delay with q=1.0

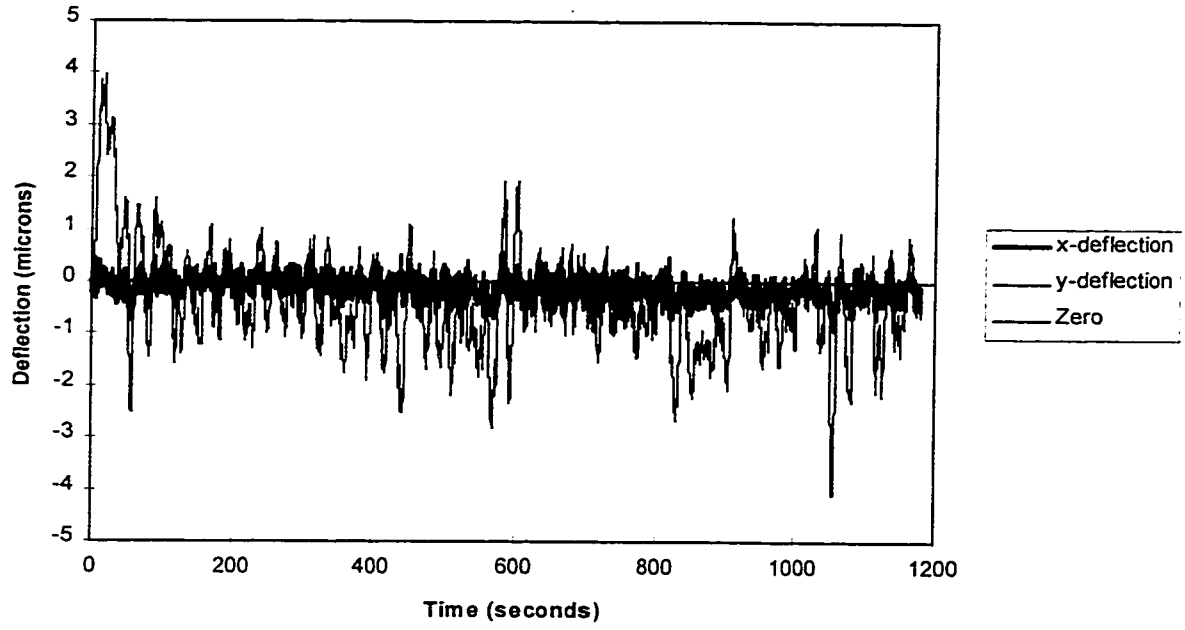

Figure 6.44: Error in Deflection Estimate with 10 Second Artificial Delay with q=1.0

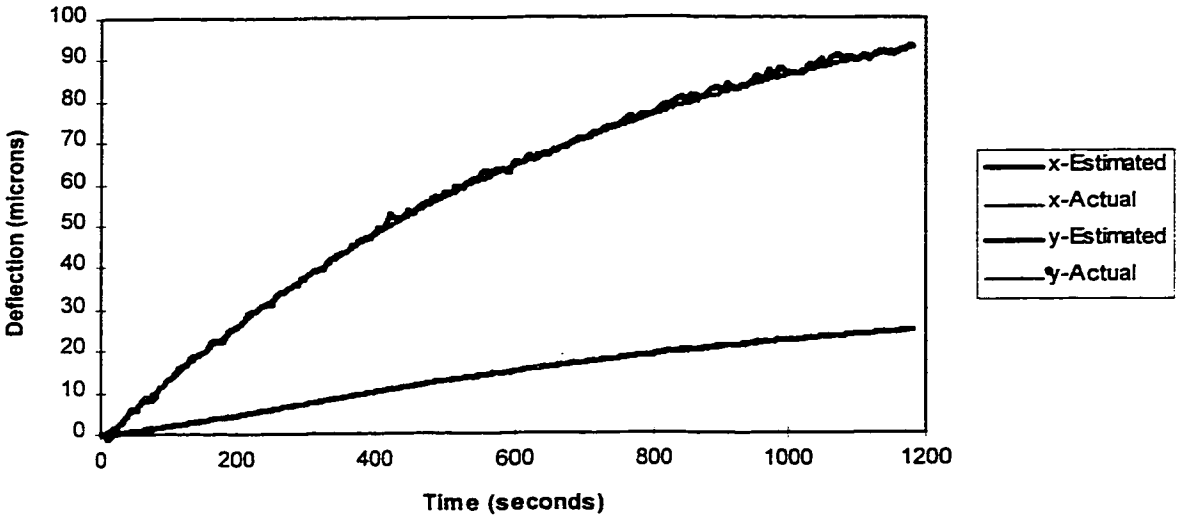

Figure 6.45: Estimated Deflection with Artificial Delay of 12 seconds for q=0.5

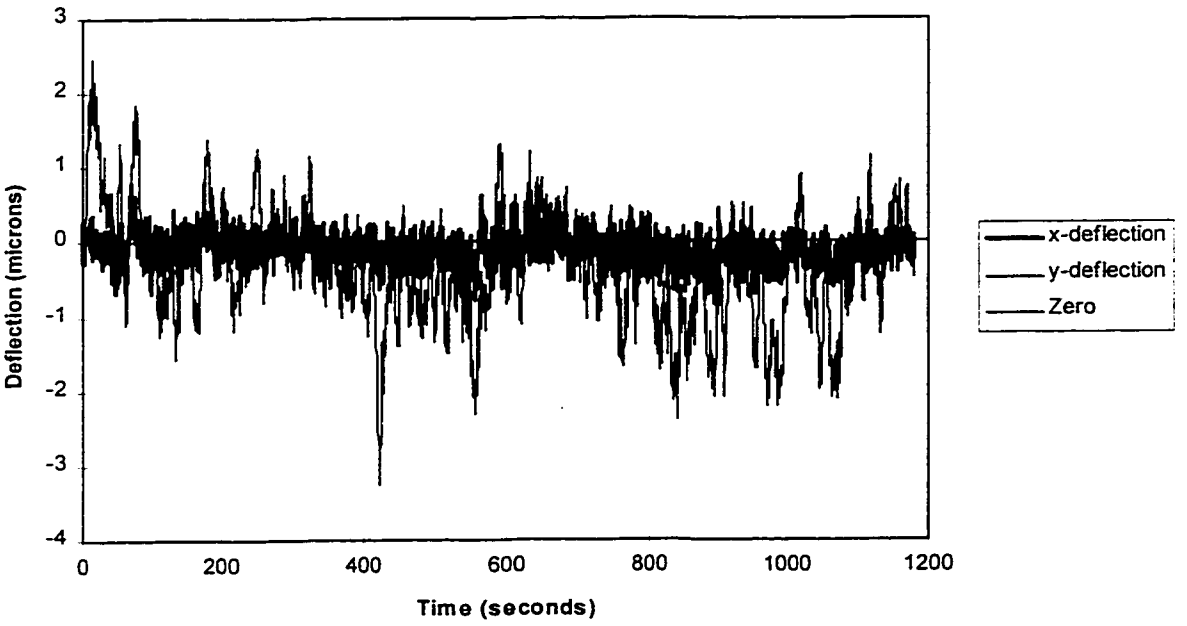

Figure 6.46: Deflection Estimate Error with 12 second Delay for q=0.5

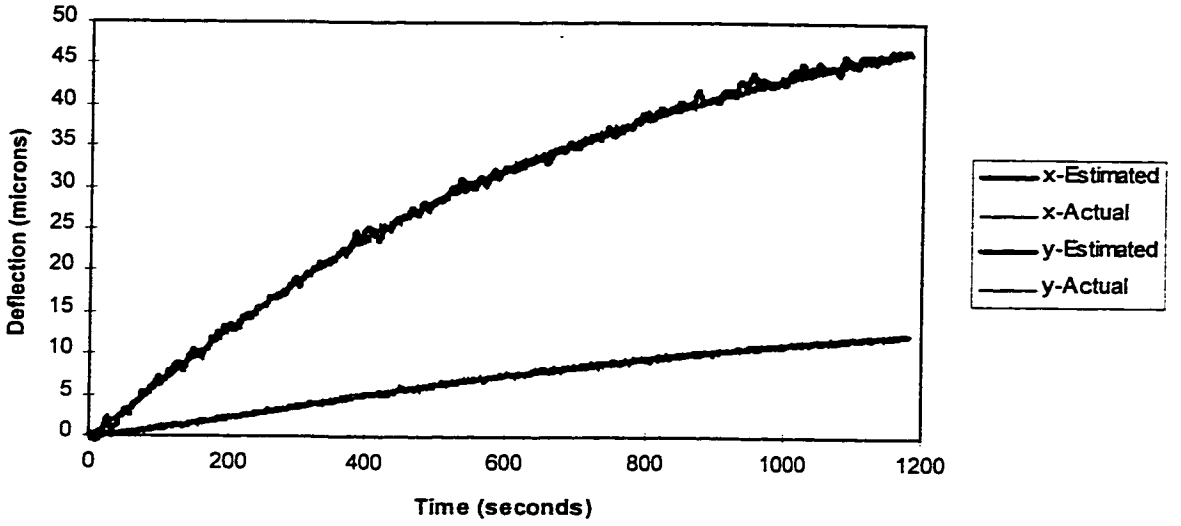

Figure 6.47: Estimated Deflection with 12 Second Artificial Delay for q=0.25

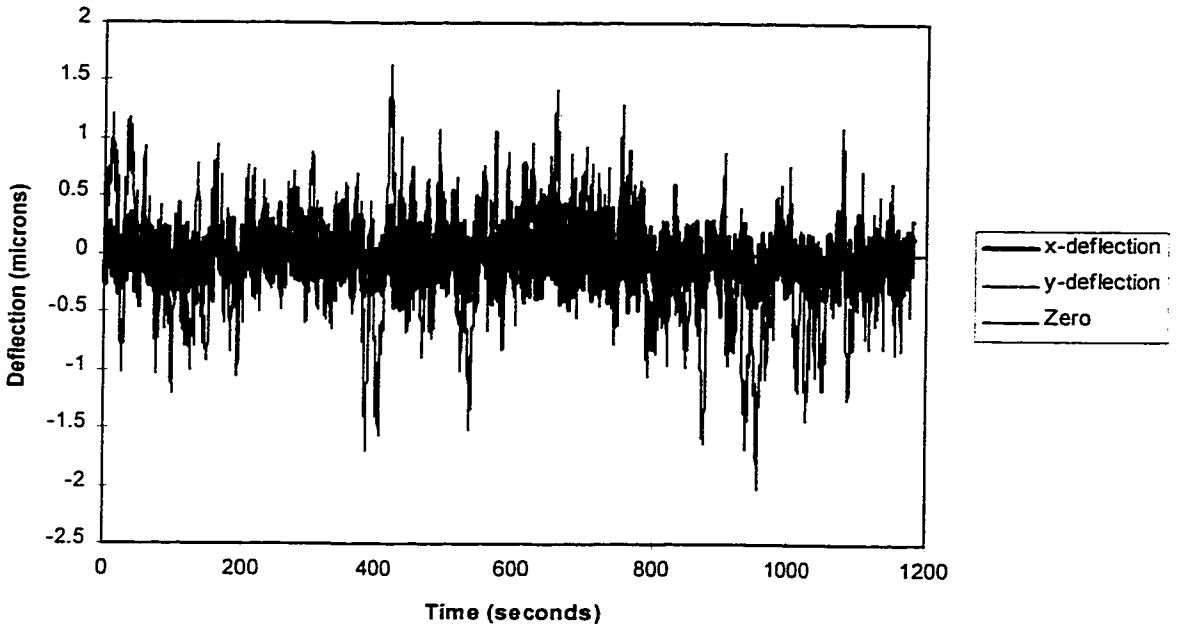

Figure 6.48: Thermal Deflection Error with 12 second Artificial Delay for q=-.25

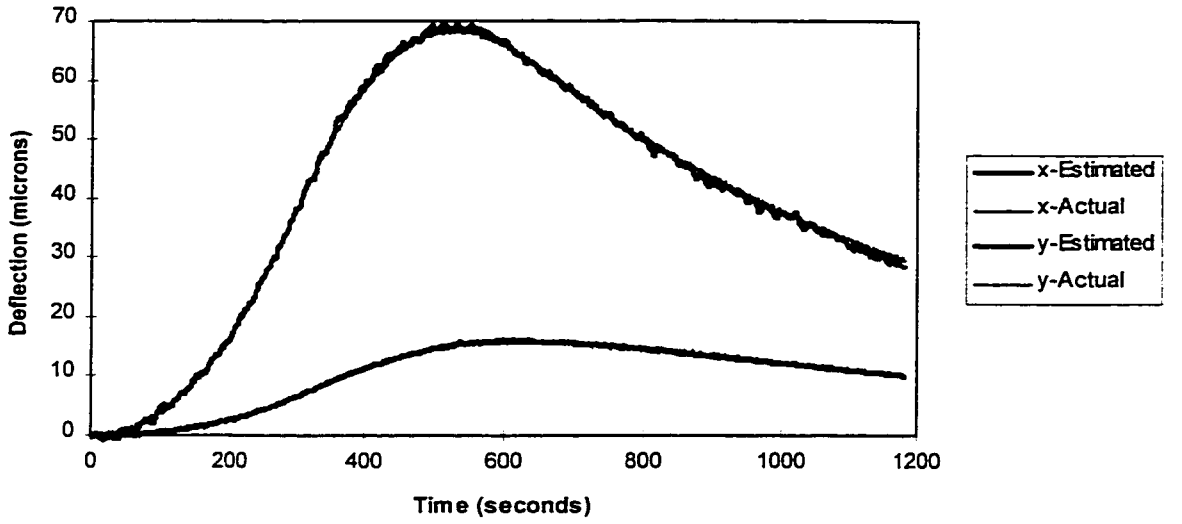

Figure 6.49: Estimated Deflection with 12 Second Artificial Delay for Triangle Input

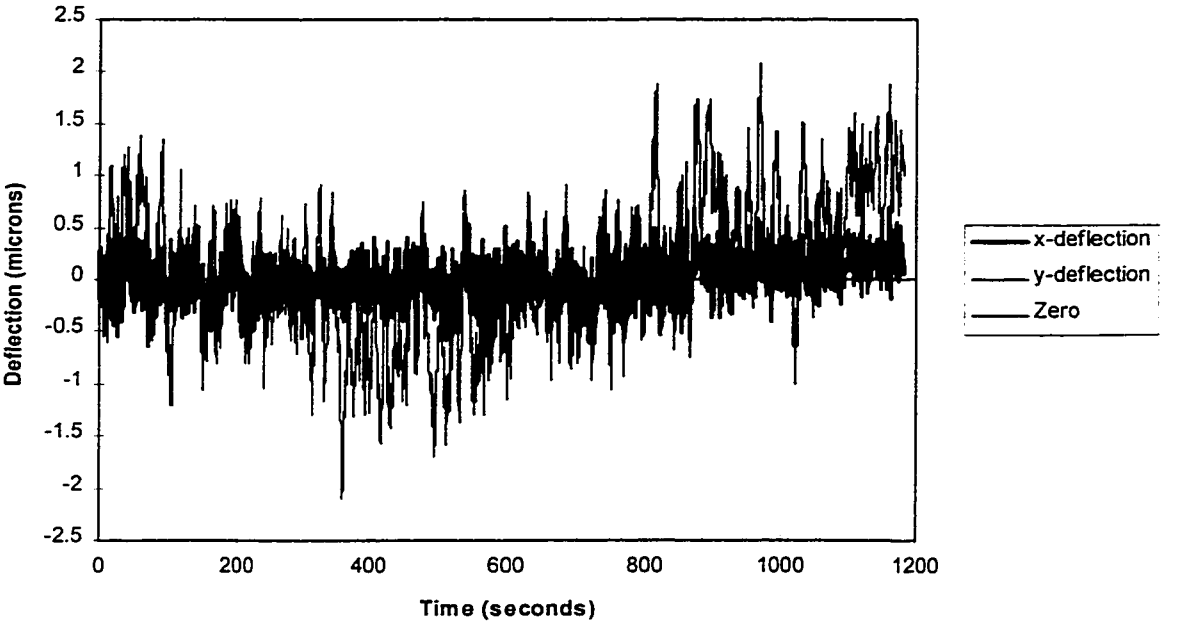

Figure 6.50: Estimated Deflection Error with 12 Second Artificial Delay for Triangle Input

6.46 shows the estimation error, which has an error band of about 5 microns. Since the actual thermal deflection is on the order of 125 microns, the estimate is accurate to around 4% of the maximum input. Figure 6.47 shows the estimated and measured thermal deflection for an input of q=0.25, and figure 6.48 shows the estimation error. The range of the estimation error is about 3.5 microns or 5.6% of the maximum thermal deflection. Figure 6.49 shows the estimated and actual thermal deflection for a triangular heat input which increases linearly from zero to 1.0 in the time interval from t=0 to t=300, and then decreases linearly to zero in the time interval from t=300 seconds until t=600 seconds. Figure 6.50 shows the estimation error for the triangular input. There is no large initial error in the estimated thermal deflection for the triangular heat input because there is no abrupt change in the input. The abrupt change in slope are reflected in the estimation error, as can be seen in figure 6.50. The range of the estimation error is about 4 microns, or 5.7% of the maximum thermal deflection.

The results show that the measurement transfer function and solution algorithm is accurate within a maximum error range of 6 microns. The results also confirm that the estimated thermal deflection is reliable for any input, with the worst case inputs shown in the figures above. Thermal inputs that include abrupt changes in value or derivative are the most difficult to deal with because of the inherent system delay that can only be partially compensated by the artificial delay. The analysis of the system delay above reveals that it imposes a definite limitation on the estimation algorithm because there will always be a period of time following a change in the input during which no useful information about the input can be obtained. The extrapolation of the previous input into this silent region is the principal source of estimation error. This means that every system will have an inherent estimation error range which cannot be improved by further processing of the input signal. The only way to improve the estimates above the results given above is to reformulate the system itself. If the temperature measurement probes had been placed closer to the heat source then the smaller initial delay in the temperature difference would have produced a smaller system delay and a

more accurate estimate. This shown the importance of placing the measurement probes as close as possible to the heat source, although there will always be some practical limit.

It is important to note that the system that was analysed here probably represents a worst case in terms of the estimation error. Evaluating the effectiveness of the estimation for a particular system can be understood by conceptually dividing the measurement transfer function into its two parts, the inverse transfer function G(r,s) and the thermal deflection transfer function H(s). The system delay is produced by the inverse transfer function, which produces a Q(t) which is shifted back in time by some effective delay, and the output of G(r,s) is the input to H(s). The initial deflection error is the amount of deflection that occurs in the real system as a result of the actual Q(t) during the time interval of the system delay. Thus, the magnitude of the inherent, or unavoidable estimation error depends not only on the system delay that is associated with the inverse transfer function G(r,s), but also the time constant of the thermal deflection transfer function H(s). A useful value for assessing a system is the temperature difference delay to a unit step input, divided by the effective time constant of the thermal deflection unit step response. That is:

$$E_e = \frac{\tau_{Td}}{\tau_{dd}} \tag{6.36}$$

where τ_{Td} is the effective temperature delay to a step input, and τ_{dd} is the effective time constant of the thermal deflection step response. The value of E_e in this case is:

$$\begin{aligned} E_e^x &= \frac{12.0}{1230} = 0.00976 \\ E_e^y &= \frac{12.0}{760} = 0.0157 \end{aligned} \tag{6.37}$$

The E_e ratios in this model are quite large because of the large temperature delay in this model relative to the time constant of the thermal deflections. In the next chapter, a model with a more realistic E_e ratio will be considered.

CHAPTER 7: ESTIMATING THERMAL DEFLECTION ON A NON-LINEAR COMPUTER SIMULATED STRUCTURE

7.1 The Source of the Non-Linearity

One may identify the three main potential sources of nonlinearity in estimating the thermal deflection of machine structures as arising from (1) radiation effects, (2) measurement noise, and (3) joint effects. Radiation is a common source of nonlinearity for thermal problems at elevated temperatures, but it is normally negligible at low temperatures where convection and conduction are the dominant mechanisms of heat transfer. It was shown in chapter 7 that temperature and thermal deflection in the physical model is linear within the resolution of the measurement apparatus, and therefore no significant nonlinearity may be attributed to this source. Measurement noise as a source of nonlinearity was also considered in some detail in chapter 6. It was found that the temperature and deflection measurement noise is approximately white noise, with energy fairly evenly distributed over the system bandwidth. Several methods of minimizing system noise were presented, including regularization and derivative filtering. It was found that the nonlinearity introduced by measurement noise can be effectively controlled so that maximum error is within a defined range that can be made sufficiently small to meet the objectives of this thesis, stated in chapter 3.

The final potential source of nonlinearity to be considered is the joint effect, a phenomenon which was described in detail in chapter 4. To summarize briefly, the joint effect is produced by the interaction between the contact pressure in fixed and sliding joints with the thermal resistance of the contact interface [12]. When the thermal expansion of the machine structure changes the contact pressure of an interface between two machine components, the heat flux through the joint is redistributed, changing the overall temperature distribution and the resulting thermal deflection. In chapter 4 the contact stiffness was shown to be nonlinear, hence if the redistribution of the heat flux is significant, the relationship between the measured temperature difference and the thermal deflection will exhibit a certain amount of nonlinearity [104]. Since

the procedure that was developed in chapter 7 to estimate thermal deflection from measured temperature points is based on the assumption of a linear model, a significant joint effect will cause a systematic error that cannot be dealt with by the procedure of chapter 6.

7.2 The Adaptive Model of a Nonlinear System

A block diagram representing the real system and the real time model with nonlinear effects is shown in figure 7.1. The figure shows schematically that the stress distribution in the contact region, which is a subset of the global stress distribution, changes the relationship between the heat input and the temperature distribution in the real system by changing the thermal contact resistance. In this case, any constant parameter model is only a 'snapshot' of the actual system for one particular contact stress distribution, and any deviation from that distribution will introduce an error in the model. In order to reproduce the joint effect in the thermal deflection model, it is necessary to the modify the parameters of the thermal deflection model in accordance with the actual contact pressure distribution, as shown in figure 7.2. The thermal deflection model shown in figure 7.2 is called an adaptive model and it is generally a nonlinear system. Implementing an adaptive model in this case requires a knowledge of the relationship between the contact pressure distribution and the parameters of the thermal deflection model. The thermal deflection model implemented in chapter 7 can be represented as a fifth order linear differential equation with constant co-efficients. There are two major obstacles to implementing adaptive parameter variation with this model. In the first place, the relationship between the co-efficients of the differential equation and the contact pressure would have to be determined experimentally, by varying the contact pressure distribution and then recalibrating the co-efficients of the model. In the second place, the adaptive model requires a real time estimate of the contact pressure, something which is not directly measurable in a real machine tool in operation. Thus, while the adaptive approach is useful for visualization, it is not a practical solution that could be implemented in practice.

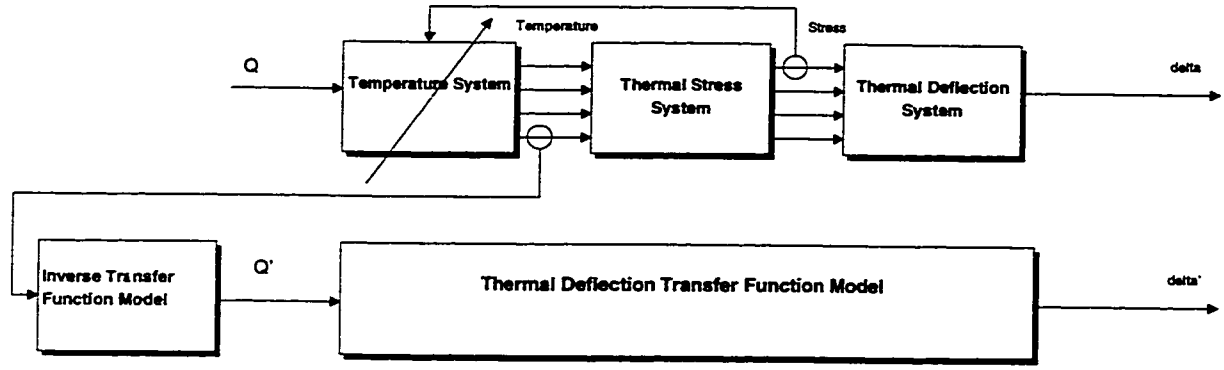

Figure 7.1: Block Diagram of Nonlinear Machine Tool System with Linear Model

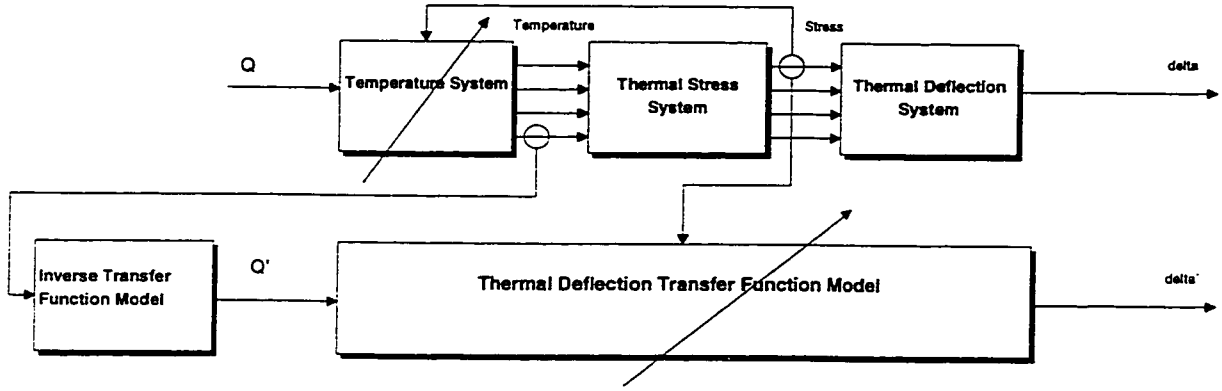

Figure 7.2: Block Diagram of Nonlinear Machine Tool System with Adaptive Model Using Measured Contact Pressure

In order to approach a realizable solution, consider the schematic model in figure 7.3. There are two sets of temperature measurements shown in the figure, one to estimate the heat generation and the other to estimate the contact pressure distribution. This scheme is an improvement over that shown in figure 7.2, because it provides a mechanism for indirectly estimating the contact pressure distribution from temperature measurements. The problem which remains is how to establish a reliable model relating measured temperatures to the contact pressure. This relationship is not an obvious one since the temperature, even in the vicinity of the source, depends on factors other than the contact pressure. Furthermore, the adaptive model does not lend itself easily to empirical type models because the contact pressure is difficult to measure, even off-line, and calibrated empirical models depend on the availability of known input and output data.

7.3 The Equivalent Model Using Contact Element Flux Generators

The solution which will be implemented in this chapter is based on the configuration shown in figure 7.3, however the mechanism will be based on the generalized model that has already been developed in this thesis. In order to make use of the generalized model, the thermal deflection system of a machine structure with a nonlinear joint must first be transformed conceptually into a form which can be more effectively modelled. Figure 7.4 shows a schematic drawing of a discrete model of a machine structure with one heat source in the column, and with a joint consisting of nine contact elements at the interface between the column and knee. The arrows in the figure indicate the direction of heat flux in the linear structure, from the heat source in the column through the contact surface, and into the knee. The thermal deformation of the structure produces contact stress in the contact elements which can be either positive or negative. Since the joint thermal contact resistance is proportional to the contact pressure, shown in chapter 4, the effect of the higher contact pressure is to increase the heat flux through those elements, and the effect of the lower contact pressure is to reduce the heat flux through those elements. This is the nonlinear aspect of the system. From the point of view of the thermal

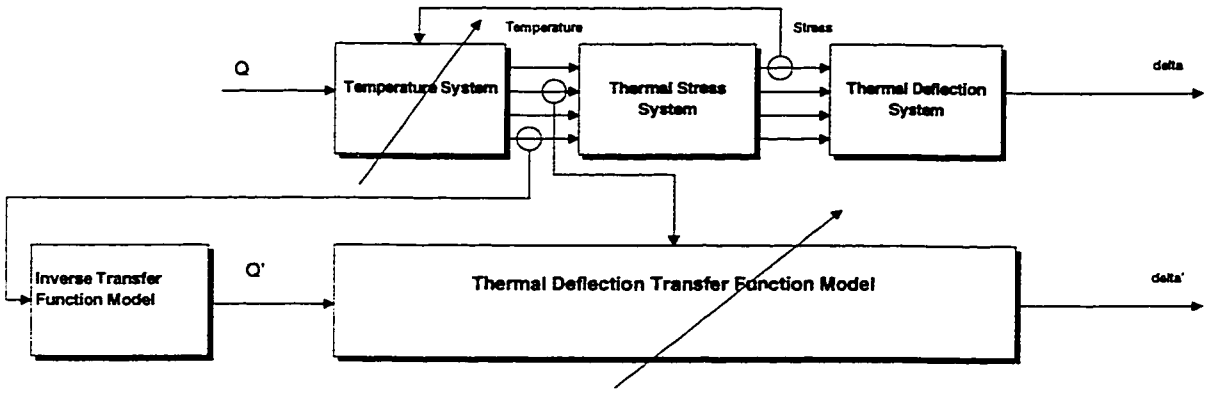

Figure 7.3: Block Diagram of Nonlinear Machine Tool System with Adaptive Model Using Measured Temperature

deflection system, the effect of the contact pressure is simply to rechannel the heat flux through the contact joint, with the resulting changes in the temperature distribution and in the thermal deflection. The other effects of the contact joint relate to the mechanical stiffness of the structure, which have only an incidental impact on the thermal deflection. Thus, an equivalent thermal deflection system is shown in figure 7.5, now with the contact elements replaced by hypothetical heat flux generators, each channelling the incremental heat flux magnitude that results from the increase or decrease in the contact pressure of that contact element. Since the machine tool test structure in figure 4.13 has been shown to be a linear thermal system, the individual incremental heat fluxes shown in figure 7.5 may be linearly superimposed onto the global heat flux shown in figure 7.4.

The above analysis indicates that, from a thermal deflection point of view, the heat flux generators shown in figure 7.5 are equivalent to the nonlinear contact elements. This can be better understood by considering that the thermal deformation of the structure depends on the following three factors: (1) the temperature distribution, (2) the co-efficient of thermal expansion of the structure, and (3) the stiffness of the structure. The nonlinear contact elements only affect factors (1) and (3). Furthermore, it can be shown that for the configuration of figure 4.13 the nonlinearity of the contact does not affect the overall stiffness of the structure to any appreciable extent. Several finite-element models were tested, using various combinations of loading and joint geometry, with the conclusion that the equivalent stiffness between the points of application of the cutting force is linear. Hence, the only significant factor which is appreciably affected by the nonlinearity of the contact elements is the temperature distribution. Considering heat flux generators in the place of contact elements to generate the same temperature distribution is therefore equivalent. In the case of the finite-element system shown above, nine flux generators are required to replace the nine contact elements with zero error. In a physical system the flux generator would be continuous rather than being composed of finite

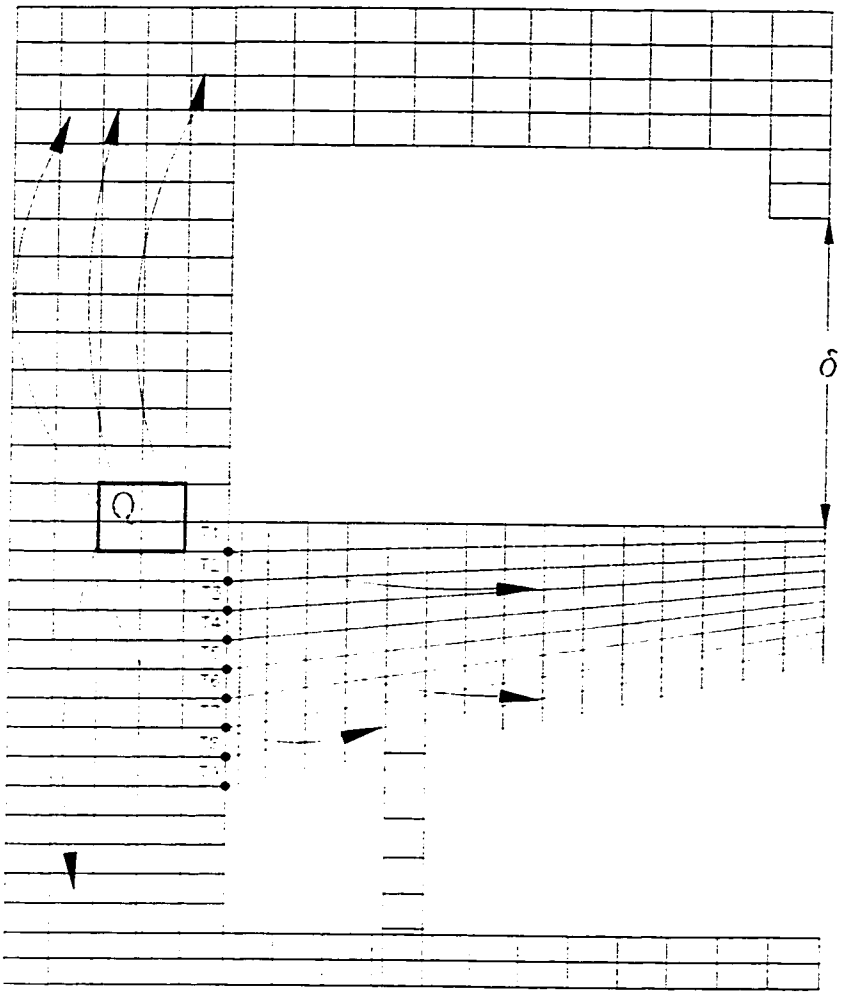

Figure 7.4: Schematic Drawing of Finite-Element Model Showing Linear Heat Flux

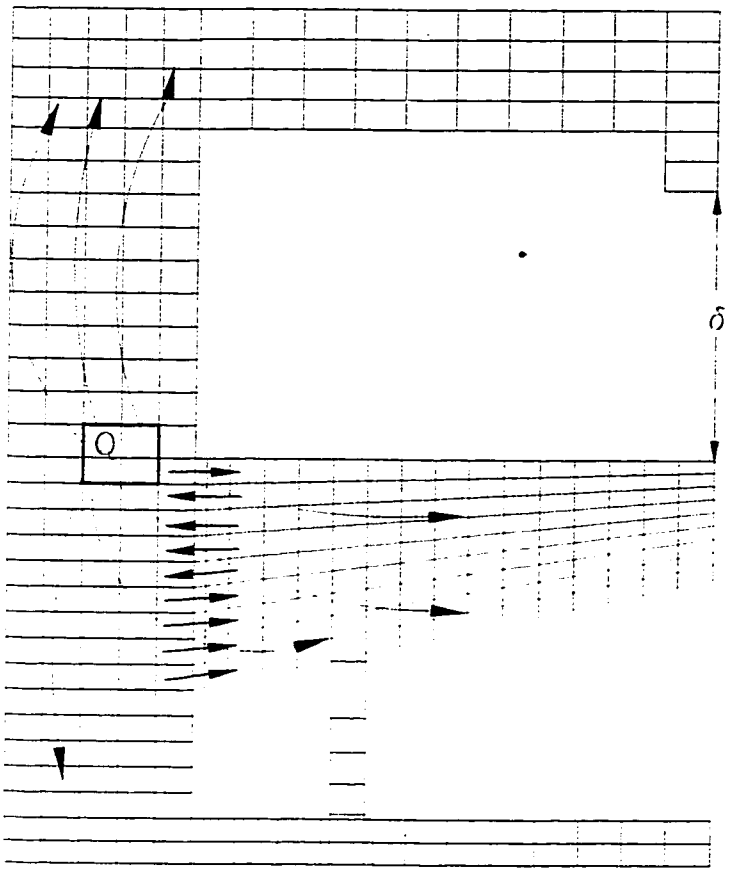

Figure 7.5: Schematic Drawing of Finite-Element Model with Disturbance Heat Flux Elements

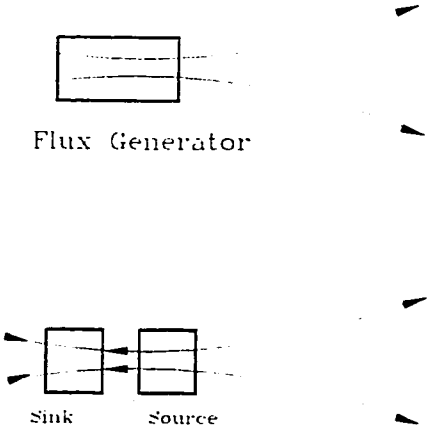

Figure 7.6: Schematic Drawing of Flux Generator and Source-Sink Combination

sized elements, however it could be adequately represented by a large number of smaller flux generators, with flux magnitudes approaching zero.

The advantage of representing the contact joint by thermal flux generators rather than by mechanical elements is that the equivalent system can be modelled by the powerful generalized approach presented in chapter 4. The nine heat flux generators shown in figure 7.5 may be modelled as paired heat source - heat sinks, as shown in figure 7.6. The magnitude of the heat generation of each source-sink pair corresponds to the actual deviation of the heat flux through the element which is produced by the nonlinearity of the contact. The magnitude of each source can be estimated from temperature measurements, using the procedure derived in chapter 6 and implemented in chapter 6. The thermal deflection due to each source can also be modelled using the procedure described in chapter 6. One of the main advantages of this type of modelling is that the nonlinearity has been eliminated from the modelled system. Both the temperature field and the thermal deflection that is produced by the main source and the fictitious source-sink pairs can be superimposed linearly. The nonlinear aspect of the problem is the behaviour of the conceptual source-sink pairs, however this behaviour is not predicted by the model, it is estimated from on line temperature measurements.

7.4 The Procedure for Estimating Thermal Deflection in a Nonlinear System

7.4.1 The Linearized Model

A linearized model of a nonlinear system is obtained by linear extrapolation of a single system response to one particular input. This input is often called the *reference input*, and the system response to this input is called the *reference output*. A linearized model is exactly correct only for the reference input since linear extrapolation of a nonlinear model introduces a certain amount of error. The amount of error depends on the nature of the system, however in general, the error increases when the system variables deviate from their reference values. For many systems that contain only a small amount of nonlinearity, the linearized model is acceptable over

the useable range of the system variables. For systems with appreciable nonlinearity, the linearized model is often a convenient starting point that is refined by adaptive parameter variation or other methods. Since a procedure for estimating the linear thermal deflection has already been developed in this thesis, the procedure that will be followed is to obtain a first estimate of the thermal deflection from a linearized model, and then refine the estimate with a correction model. The linearized model is obtained by the same procedure that was explained in chapter 7: (1) define two temperature measurement nodes close to each independent heat source; (2) calibrate the temperature difference step response and define the inverse transfer function; (3) calibrate the thermal deflection model; (4) implement the transfer function solutions in the real time algorithm. The step input is used as the reference input because it is probably the most common type of thermal input in a machine structure. The reference step magnitude could be approximately half of the maximum heat generation of the source, however if the machine is known to operate within a particular thermal input range most of the time then better results may be obtained by using a different reference magnitude. In the experiments that follow, the half-maximum reference will be used.

7.4.2 Estimating the Heat Generation of the Contact Sources

The next step of the procedure is to define and estimate the heat generation of the fictitious heat source-sink pairs in figure 7.5. As was discussed above, the heat generation of the source-sink pairs represents the deviation in the heat flux through the joint from the linearized or reference input, due to the nonlinearity of the contact joint. Hence, when the reference input is applied to the system, the linearized heat flux is equal to the actual heat flux, and the heat generation of the contact sources is equal to zero. Figure 7.4 shows a measured temperature node adjacent to each fictitious contact source. Assuming that the main heat source, Q(t) in figure 7.4, can be accurately estimated by the linear procedure, the temperature of each of the measured nodes in figure 7.4 can also be estimated by the generalized direct thermal model. Now if there is no deviation from the linearized heat flux distribution through the joint then the

measured temperature at each of these nodes will be equal to its estimated value. If there is a deviation from the linearized heat flux distribution then this will be reflected in a temperature deviation at the measured point. Hence, the difference between the estimated temperatures using the linearized model and the actual measured temperatures is the temperature change induced by the contact joint, or from the other perspective it is the change induced by the fictitious sources. It is this temperature difference that shall be used to identify the magnitude of the fictitious sources, using a similar procedure to that which was developed in chapter 6.

Before applying the procedure of chapter 7 to estimate the generation of the contact sources, it is important to identify and discuss certain differences between the fictitious contact sources and real sources. In the first place, the temperature response of the contact sources is not an absolute temperature, but rather a deviation from a reference temperature. The reference temperature is determined from the estimated heat generation of the main source Q(t). The first new consideration is whether the nonlinearity of the contact joint will affect the estimation of Q(t). As was discussed in chapter 6, a heat estimate based on a temperature difference near the source is very insensitive to more distant heat sources since the temperature gradient that is produced by a source decays much more rapidly than the absolute temperature. Using the perspective of fictitious contact sources, one would not expect a significant contribution from these sources to the temperature difference measured near the main source. The finite-element results show that the temperature difference used to estimate Q(t) in the test structure is linear within the numerical resolution of the finite-element program. The second new consideration is the process of estimating the reference temperature at each of the measured nodes. The model relating heat generation to temperature is simply the direct transfer function corresponding to the inverse transfer function G(r,s) and the parameters are calibrated from the measured temperature responses to the reference input at each of the measured nodes in figure 7.5. The on-line solution for the transfer function can be obtained in one of two ways: (1) using the

general temperature solution in equation (5.1) and the calibrated parameters, or (2) using the convolution integral approach developed in chapter 6.

The next consideration is the magnitude of the temperature deviation that is to be expected near the contact nodes. It was shown in chapter 7 that the temperature measurement error associated with the data acquisition process is nonlinear. That is, the magnitude and spectral composition of the measurement error is independent of the magnitude of the measured temperature, so for small measured temperatures the disruptive effect of the measurement noise is potentially more significant. It will be shown that the temperature deviation is of the order of one degree Celsius, which is large enough to be accurately detected in the presence of measurement noise. However, it is not feasible to look at the deviation of a temperature difference because the resulting signal would be overwhelmed by measurement noise. This poses a serious problem of source dependance, particularly given the close proximity of the sources in figure 7.4. The implication is that the temperature deviation of each of the measured points in figure 7.4 is the linear superposition of the contribution from all of the contact sources and it is not possible to estimate any one source independently of the others.

The final consideration to be looked at here is the nature of the heat source-sink pair, and the applicability of the generalized thermal model to such an unusual heat source. The generalized model rests on a calibrated base equation that is mathematically similar to the real process, as explained in chapter 4. The difference between a source-sink pair and an ordinary source relates to overall pattern of heat flux and temperature distribution. For one particular point however, the mathematical form of the temperature profile is not greatly altered. Furthermore, since the source-sink pair have equal and opposite magnitudes they are dependant sources that are rightly lumped together into one single source. It will be shown that the generalized model provides an excellent representation for the contact source-sink pairs.

7.4.3 Modelling the Thermal Deflection Produced by the Contact Sources

Once the relative magnitudes of the contact sources have been determined, the next step is to estimate the thermal deflection that is produced by their temperature distribution. The total thermal deflection is the superposition of the linearized thermal deflection produced by the main source and the nonlinear deflection produced by each of the contact sources. The most difficult aspect is determining how much of the overall thermal deflection is produced by each one of the contact sources, and this is done through calibration of the thermal deflection models associated with each one of the heat sources. It is not possible to activate one contact source at a time because any application of contact pressure in a real structure will invariably affect the entire joint. Thus, the thermal deflection models must be calibrated simultaneously using some sort of error minimizing scheme, and the number of calibrated inputs must be equal to or greater than the number of contact sources. In practice, the nine contact sources shown in figure 7.5 are not necessary, they can be effectively lumped together into a smaller number of independent sources. This so because of the close proximity of the sources and the flexibility of the generalized solution, explained in chapter 4.

7.4.4 The Algorithm for Estimating Thermal Deflection in a Nonlinear System

Figure 7.7 shows a block diagram of the real time process for estimating the thermal deflection in a nonlinear system. In the figure there are three sets of temperature measurements serving as the inputs to the estimation algorithm. Input ΔT represents the temperature difference measured near the main source Q(t) and T_1 and T_2 represent two measured temperatures in the vicinity of the contact joint. The first process is the estimation of Q(t) through the calibrated convolution transfer function, represented by Block 1. Block 1 in figure 7.7 is the only truly linear process since it is unaffected by the contact joint. Block 2 represents the algorithm which calculates the linearized thermal deflection $\delta(t)$, using the incremental solution presented in section 6.7. Block 3 represents two separate algorithms, which estimate the linearized temperature profiles at T_1 and T_2 using the direct thermal model. The linearized temperature is

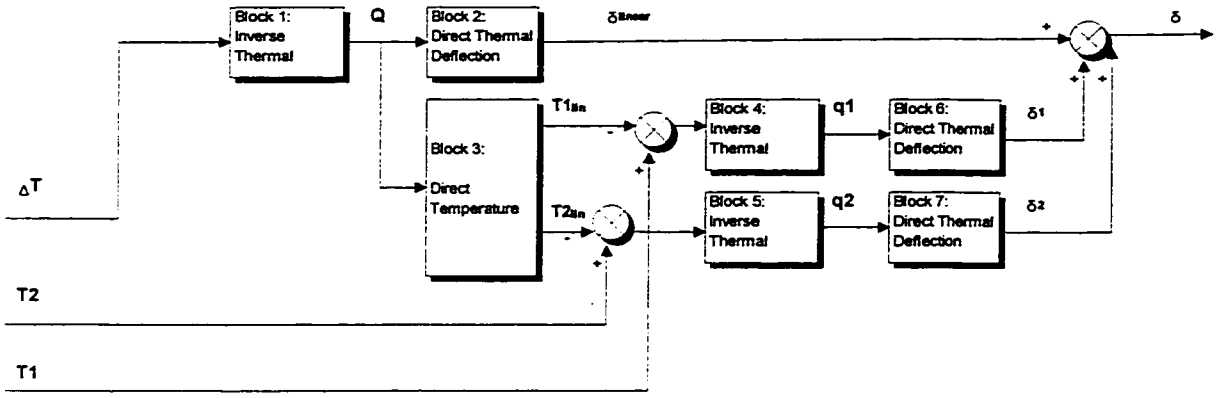

Figure 7.7: Block Diagram of Nonlinear Estimation Algorithm

subtracted from the measured to obtain the temperature deviations δT_1 and δT_2. Blocks 4 and 5 represent the same inverse algorithm as in Block 1, now being used to estimate the disturbance heat generation q_1 and q_2. The estimated thermal inputs are transformed into deflections $\Delta\delta_1$ and $\Delta\delta_2$ which are added to the linearized thermal deflection δ.

7.4.5 Calibrating the Temperature Models

The calibration of the temperature models corresponding to blocks 1 and 3 in figure 7.7 has already been explained in chapter 7 and needs no further discussion here. Blocks 4 and 5 define the inverse relationship between the temperature deviations δT_1 and δT_2 and the conceptual heat sources q_1 and q_2, and the calibration of these models poses a particular problem since the procedure that was employed in chapter 7 is no longer applicable. The empirical calibration of a model depends upon the availability of experimental system response data corresponding to known inputs. In the case of blocks 4 and 5, neither the input variable nor the output variable is directly available, as will now be explained. This lack of information entirely defies the concept of empirical modelling, and it in this regard that the fundamental difference between a purely empirical model and the generalized model truly emerges.

In chapter 7, it was reasonable to assume that well defined heat inputs could be generated, for example by starting the rotation of a bearing or applying power to a motor in a predetermined way. In the present case the controllable input is the main source Q(t) and not the fictitious sources $q_1(t)$ and $q_2(t)$, which merely react to the effects produced by the main source. What this means is that the input variable is always unknown, both in magnitude and in its functional character. Furthermore, since the output variable is a temperature difference in time rather than a temperature difference in space, it is no longer reasonable to assume that measured temperature near one source in independent of the other sources. If more than one fictitious source is considered then the measured temperatures are composed of contributions from each of the contact sources, and it is not immediately possible to separate the contributions from each

source. Now since the contact sources are fictitious, one might ask why it is not possible to just assume that the nonlinearity is produced by a single source, eliminating the interdependence. In practice it is not possible to adequately represent the flux redistribution that is produced by most contact joints with only a single source, so in order to produce an adequate estimate of the nonlinear thermal deflection it is essential to deal with the interdependence problem.

The first of these problems to be considered is the determination of the input heat functions q_{ti}. Looking at a thin contact element, the heat conduction through the element is given by:

$$q_t = \frac{dT}{\bar{R}} \tag{7.1}$$

where q_t is the total heat conducted through the element, R is the thermal contact resistance, and dT is the temperature difference across the element. In chapter 5 is was shown that the thermal resistance is approximately proportional to the inverse of the contact pressure, thus:

$$q_t \propto P_c\, dT \tag{7.2}$$

where P_c is the contact pressure at the element. If the nonlinear deviation in the heat flux is called q, then:

$$q \propto \delta P_c\, dT \tag{7.3}$$

where δP_c is the change in the contact pressure from the linear value. If dT is approximately constant then:

$$q \propto \delta P_c \tag{7.4}$$

This analysis is simplified because it neglects the interaction among the contact elements and the interaction between the contact elements and the linear substructure. Nevertheless, it shows that the heat generation of the contact sources is proportional to the deviation from the linearized contact pressure for at least some of the range of δP_c. The advantage of using a finite-element test system rather than a physical one is that it makes it possible to look at any variable in the system, even those that are inaccessible in a physical system. In the experimental results that follow, the behaviour of the contact pressure will be plotted for known inputs to the main

heat source, and the results used to define a suitable functional relationship between the main source Q(t) and the contact sources q_i. This relationship must be a general one however, since the same process cannot be repeated in the case of a real machine tool.

The second problem to be considered is the determination of the output variable corresponding to the calibration input. Because of the superposition of the temperature distributions from each contact heat source, it is not possible to isolate the temperature contribution from each source individually at any given point on the structure, hence there is not a single unique solution to the problem. It is important to recognize the significance of this statement because it illustrates the fundamental difference between a purely empirical model and the calibrated generalized model. The fact that the pure temperature response to a single contact source cannot be identified is a practical limitation on the ability to measure certain system variables. Specifically, the problem arises because it is not possible to activate the contact sources one at a time, they must be activated together producing a jumble of temperature responses at the same point in space. There is no information contained in the measured temperature data to indicate the relative contribution from each source. The temperature rise at a point near one contact source may be the result of heat generation by that source or it may be a delayed response to the heat generation of another, more distant source. Any calibrated empirical model inherently makes an assumption regarding these relative contributions, and this assumption is not necessarily correct. The situation is analogous to a linear system of equations where the determinant of the co-efficient matrix is equal to zero. There are an infinite number of calibrated solutions, but only one of these solutions can be physically correct.

The inherent advantage of the generalized model is that its mathematical form is similar to the mathematical form of the actual physical system. The missing information regarding the relative contribution from each source at a given point is therefore built into the model before

it is calibrated. The general model for the temperature profile at a point was given by equation (5.1) and is repeated here:

$$T(r,t) = K\alpha \int_0^{\infty} \beta J_0(\beta r) J_0(\beta r_0) e^{-(a+\beta^2)\alpha t} \int_0^{t} q(\tau) e^{(\beta^2+a)\alpha t} d\tau d\beta \qquad (7.5)$$

where q(t) is the heat generation of one contact source and the other parameters are defined in chapter 5. The temperature at a given point is the linear superposition of the temperature profiles due to each of the contact sources, estimated by equation (7.5). To understand how the generalized model can break down the temperature profile into its constituent parts consider figure 7.8, which shows two measured points near two heat sources. The typical temperature profiles produced by each of the sources at the measured points for step inputs at t=0 is also shown in the figure. Notice that temperature response to the q_1 input is felt at T_1 before it is felt at T_2 because the temperature delay is larger at greater distances from the source. Now, if the q_1 temperature model were calibrated to produce the T_1 temperature profile shown in figure 7.8 then the temperature model would automatically predict the delayed response at T_2. In this way, the relationships between q_1 and T1, and q1 and T2 are not independent. The predefined mathematical relationship forces the calibration parameters to converge to the mathematically correct solution, as will be shown shortly.

The model for the temperature at any point T_j is the linear superposition of the generalized models relating the q_i to T_j. That is:

$$T_j = \sum_{i=1}^{n} T_i(q_i, r_j) \qquad (7.6)$$

where the $T_i(q_i,r_j)$ are the generalized models corresponding to each q_i. Now, there is only one generalized model for a particular source q_i , which corresponds to equation (7.5). The same calibrated model predicts the contribution from its source onto each of the measured points by changing the value of parameter r in equation (7.5), called r_j in equation (7.6).

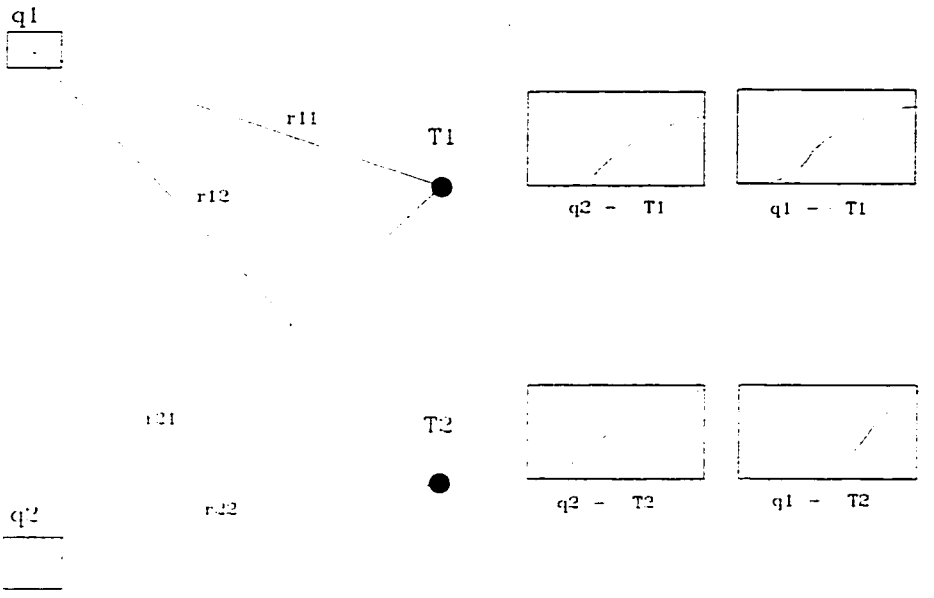

Figure 7.8: Schematic Drawing of Two Contact Heat Source System

In the procedure presented in chapter 7, the variable r in equation (7.5) was treated as an ordinary empirical parameter. In the present case, the missing information in the calibration data requires that parameter r be treated as a fixed variable rather than a calibration variable. Restricting the r parameter reduces the flexibility of the generalized model to conform to the measured data, but it serves a different purpose in this case. Parameter r is used to establish the mathematical form of the system model by defining the inter-relationship between all of the temperature profiles that are produced by one contact source. In order that the mathematical form be accurate, the selected values of r should be realistic for the geometry under consideration. The procedure that will be used here is to assume the locations of the contact sources, and then estimate the distance from the centre of the source to the measured points. The sources will be assumed to be located at equidistant positions along the contact joint. For m contact sources there are 3m calibration parameters for the thermal model: K, a, and α for each contact source. These 3m parameters must be solved simultaneously, using the m temperature profiles for the calibration.

The algorithm for calibrating the contact source parameters is shown in figure 7.9 for the case where m=2. The parameters used in figure 7.9 are a_1, a_2, α_1, α_2, $K_1q_1^{<1>}$, $K_1q_2^{<1>}$, $K_2q_1^{<2>}$, and $K_2q_2^{<2>}$, where the subscript indicates the heat source number and the superscript indicates the calibration input. There must be at least as many calibration inputs as there are contact sources, two of each in this case. The calibration inputs that will be used in this chapter are step inputs, one with a greater magnitude and one with a lesser magnitude than the reference input. The first four of the parameters, a_1, a_2, $\alpha_{1, \text{ and } \alpha 2}$, shall be called the real parameters and the other four are called the product parameters. In the first block of figure 7.9 initial values are assumed for the four real parameters and the four product parameters. The product parameters are formed because the heat magnitudes cannot be separated from the temperature gain at this point. Block 2 represents the MATLAB calibration algorithm for the <1> calibration input, and block 3 represents the calibration for the <2> calibration input. Since the calibrated parameter values

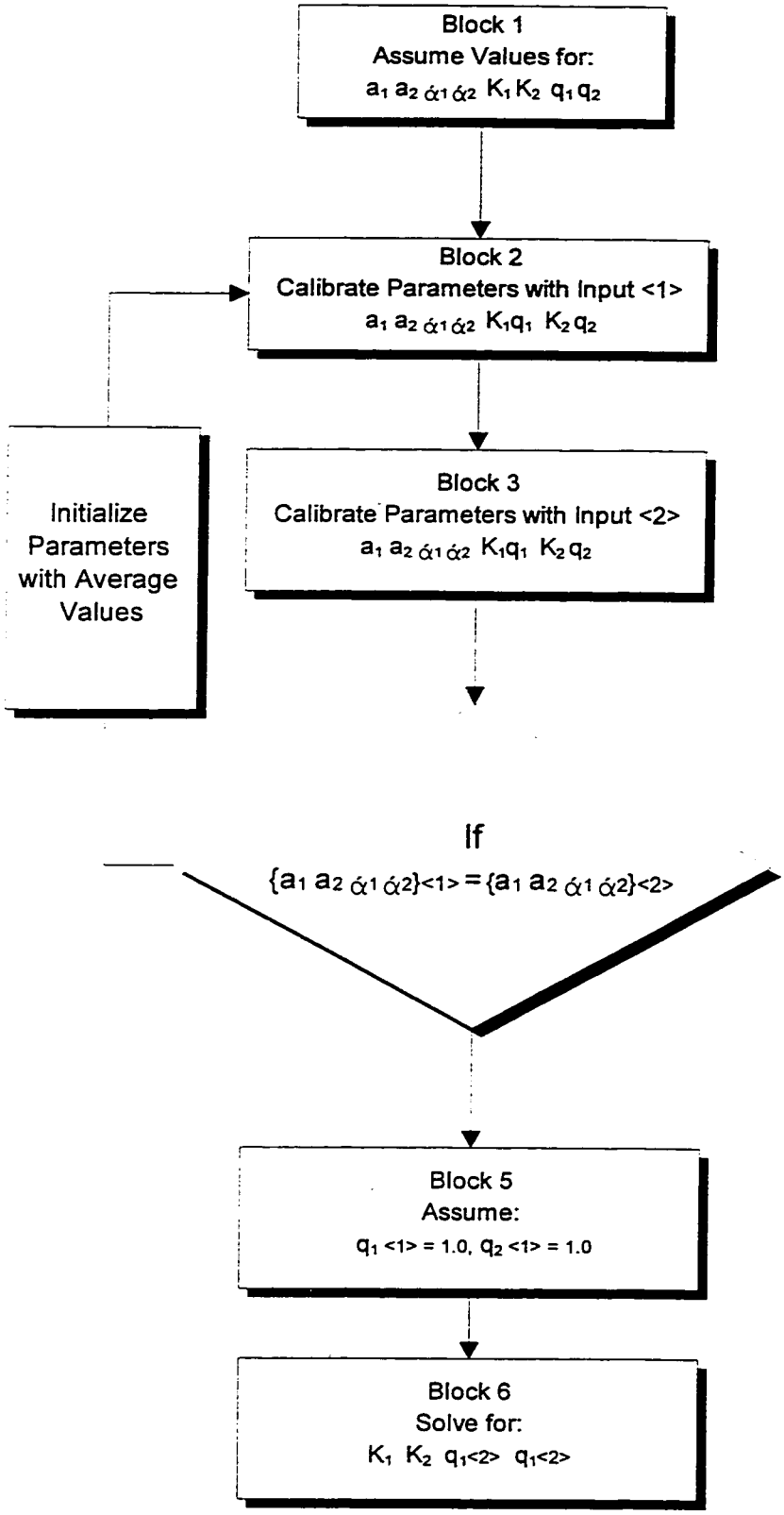

Figure 7.9: Thermal Calibration Flowchart

depend on the initial guess, the two sets of calibrated values will not necessarily be equal. Block 4 represents the control loop which checks whether the a and α parameters are close enough to be considered equal, otherwise the two calibrated values for each parameter are averaged and the process begins again with the averaged parameter values as the initial guess. When the two calibration blocks converge to the same a and α parameters the control moves to block 5 which assumes a reference heat magnitude of 1.0 for both $q_1^{<1>}$ and $q_2^{<1>}$, so that K_1, K_2, $q_1^{<2>}$ and $q_2^{<2>}$ may be calculated independently. Selecting reference values for the heat sources does not affect the result since the heat generation is an internal variable to the estimation transfer function.

7.4.6 Modelling the Thermal Deflection from the Contact Sources

A separate thermal deflection model is required for each contact heat source. Using the form of equation (6.16), there are 6 empirical parameters for each contact heat source for a total of 6m parameters. As with the thermal model these parameters must be solved simultaneously since the total thermal deflection is the superposition of the individual contributions from each of the contact sources. Since the thermal deflection model is entirely empirical, the model does not necessarily assume the correct mathematical form, as in the case of the thermal model. However the fact that the heat generation can be accurately identified by the procedure of section 7.4.5 greatly simplifies the calibration of the thermal deflection models. It will be shown that it is sometimes possible to isolate the contribution from one heat source by inducing the saturation of the other sources. This technique is particularly useful when there are only one or two contact sources.

7.5 Implementation of the Nonlinear Procedure

7.5.1 The Nonlinear System Model

Before settling on the final design of the nonlinear computer simulation model, a large number of finite-element models of machine tool structures had been investigated, using different configurations and different heat source locations, in order to identify the type of

machine tool that is prone to exhibit a high degree of nonlinearity. Several general principles emerged from this study, which will now be summarized:

1. The stiffness of the structure can affect the nonlinearity, however there is no definite correlation that could be established. Stiffening the structure sometimes increases the nonlinearity of the thermal deflection and sometimes it decreases it, depending on the configuration of the model which is being tested.

2. Thick walled structures have a greater percent nonlinearity than thin walled structures when other factors are the same. Changes in the thermal resistance of a contact joint affect the heat flux in proportion to undisturbed heat flux through the joint. Thick walled structures distribute the heat flux more efficiently than thin walled structures, so that the thick walled structure increases the heat flux through the joint, which increases the nonlinearity of the structure. Using the same reasoning, a structural material with higher conductivity or a lower convection coefficient would also exhibit a greater percent nonlinearity.

3. The location of the heat source is the most important factor affecting the nonlinearity of the thermal deflection. As stated above, the greater the heat flux through the joint the greater will be the effect of changes in the thermal resistance of the joint. Placing a heat source close to a joint has a dual effect; in the first place it increases the heat flux through the joint, and secondly it tends to increase the thermal deformation in the vicinity of the joint which induces larger changes in the contact pressure. It was found that no significant nonlinearity could be induced in the finite-element models unless there was a major heat source located close to the contact joint, within about 100-200 mm.

Making use of these three general rules, the finite-element test model was designed in chapter 5 with a 25 mm wall thickness and with the major heat source located close to the contact joint, as shown by its finite-element grid in figure 7.10. The finite-element grid was developed using the ALGOR finite-element modelling package [84], and the nonlinear solution

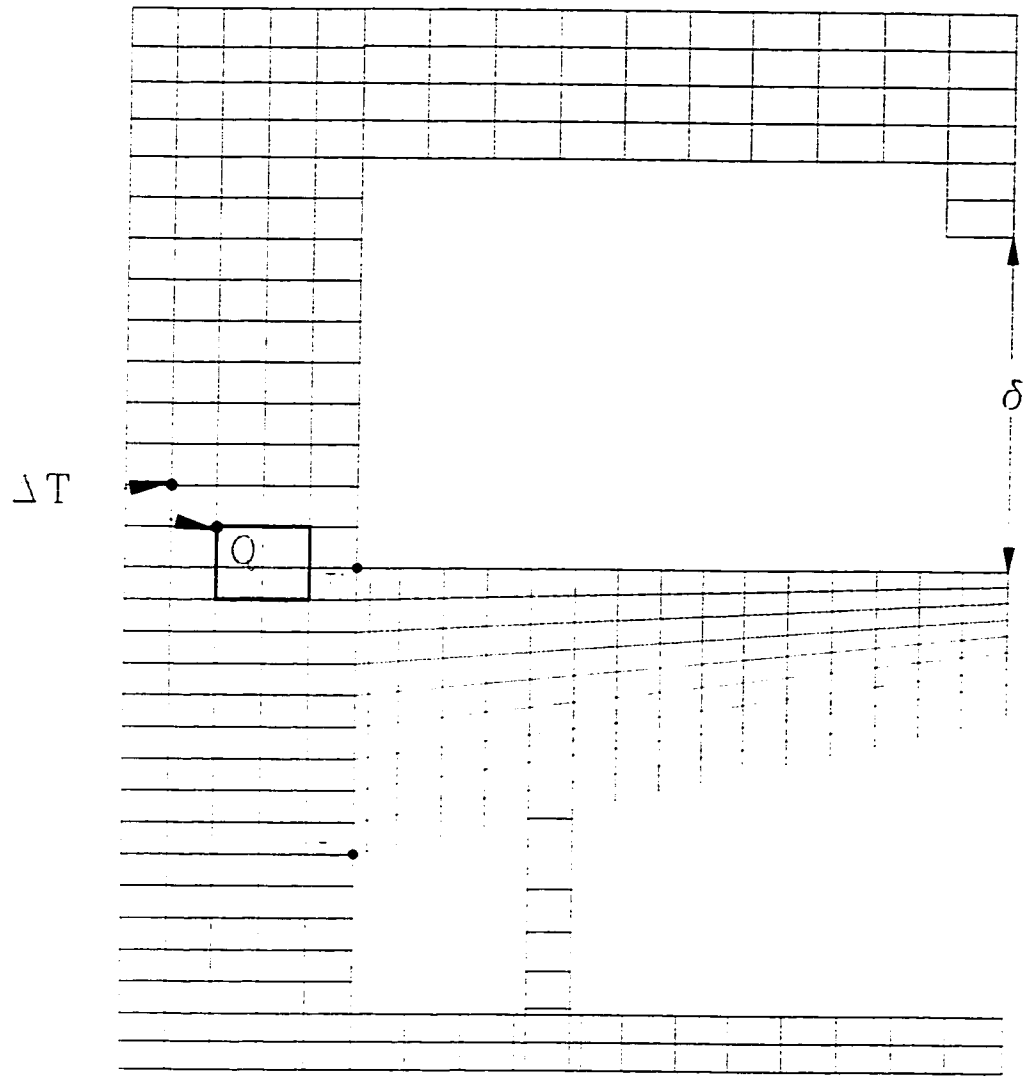

Figure 7.10: Finite-Element Grid of Test Model

algorithm incorporates the ALGOR finite-element processing package. Particular attention has been paid to the modelling of the joint contact, so as to simulate realistic joint nonlinearity, as would be encountered in a real machine tool under actual operating conditions. The finite-element grid in figure 7.10 indicates the location of the heat source, and the points of measured deflection.

Figure 7.11 shows a cross-sectional view of the heat source. In order to more realistically represent the type of heat source that would be encountered in a real machine tool, the heat source has been placed on the inside of the structure, at the base of the internal bracket shown in the figure. There is on average 6 centimetres of material between the surface of application of the heat generation and the outside surface of the machine, which is a realistic geometry for a bearing.

7.5.2 Estimating the Linearized Thermal Deflection

Since all machine tools have joints, all machine tools exhibit a certain amount of thermal deflection nonlinearity. It is the amount of nonlinearity that determines whether the model can be dealt with the linear procedure of chapter 7, or whether nonlinear correction is necessary. The procedure of chapter 7 is therefore the first step in the process of estimating the thermal deflection in a nonlinear machine tool system. If the error in the linear model introduced by nonlinearity is considered acceptable, then no further modelling is necessary. If the nonlinear error is unacceptable then the nonlinear correction algorithm in figure 7.7 must be implemented.

Figure 7.12 shows the temperature distribution in the finite-element structure with a heat input of 395 watts, which is now defined as the maximum heat input of dimensionless magnitude 2.0. This figure was generated by the nonlinear finite-element algorithm, however it is equivalent to the thermal image of the linear structure which was shown in figure 5.7. The temperature distribution identifies the location of the major heat source near the interface

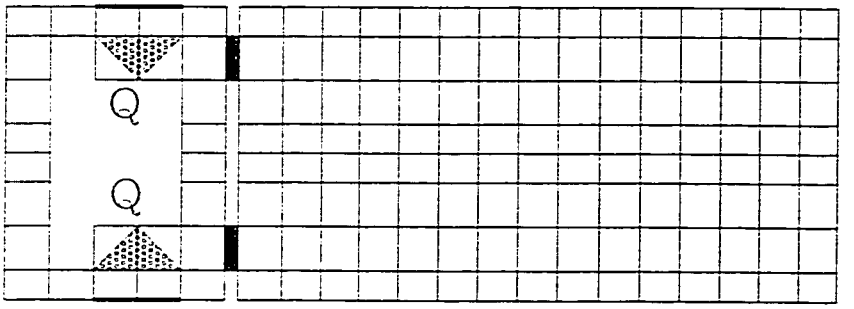

Figure 7.11: Vertical Cross-Section View of Column Showing Heater Arrangement

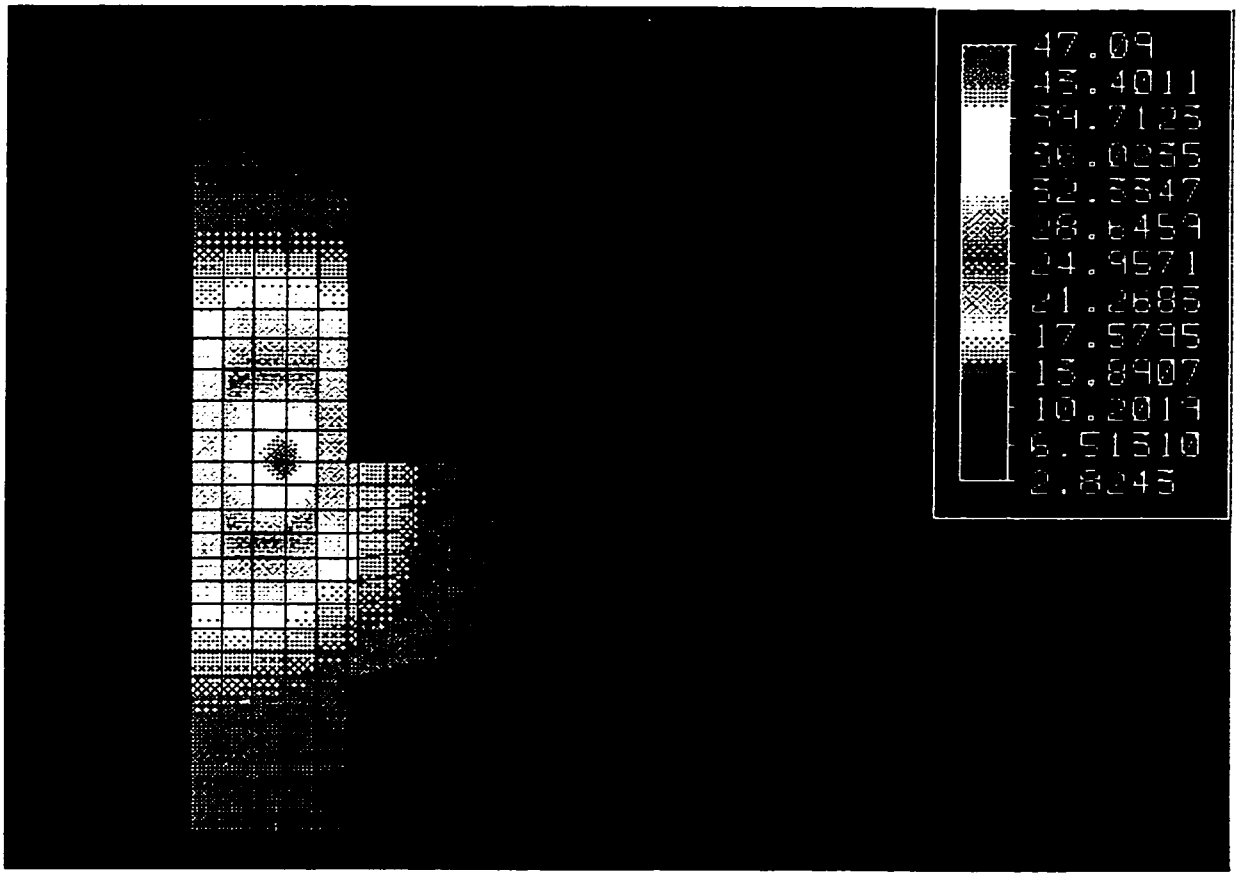

Figure 7.12: Steady-State Temperature Distribution in the Finite-Element Test Model for Heat Input Q=2.0

between the column and knee of the machine. Figure 7.10 shows the locations of the two measured points near the heat source which will be used to define the inverse transfer function. The next step is the choice of the reference input for the linearized solution. In the absence of any specific information regarding the machines operational duty range, the reference input shall be defined as a step input with magnitude one half of the maximum, or Q=1.0 in dimensionless terms. Figure 7.13 shows the temperature difference between the measured nodes following the application of the reference input at t=0. The figure also shows the calibrated generalized step response obtained from equation (6.2), with:

$$\begin{aligned} K &= 3.372 \\ a &= 3.20 \\ \alpha &= 0.000212 \\ r &= 0.19 \\ r_0 &= 0.12 \end{aligned} \tag{7.7}$$

Figure 7.14 shows the actual and calibrated temperature difference for the first 30 seconds, magnifying the difference between the two curves. The most obvious characteristic of the actual temperature difference is that there is no initial delay. Since the generalized model cannot accommodate a system without an initial delay there is a small deviation between the two curves. It should be pointed out that the deviation is not due to a flaw in the generalized model, it is actually a flaw in the finite-element model. The combination of a finite grid and time step masks the initial delay at locations close to the heat source. It was shown using simple models that the initial delay at this distance from the source can be reproduced with a finite-element model, however the model must have such a fine mesh density and small time increment that it is impractical to use as a test model. The calibrated generalized model is probably a better representation of the actual system corresponding to the finite-element model, since it forces the finite-element data to conform to the proper mathematical form. The uncorrected finite-element temperature response will continue to be used for the actual system model despite this inherent flaw. The particular form of the finite-element response will also be used to illustrate some points about regularization that were raised in chapter 6.

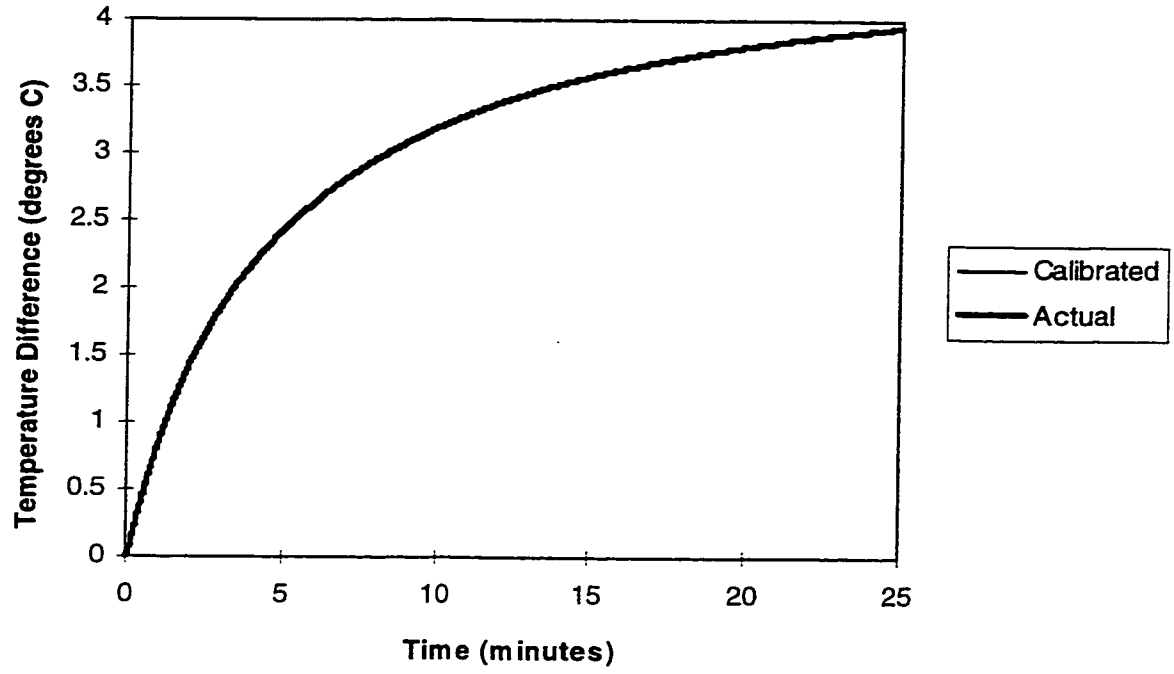

Figure 7.13: Temperature Difference for Main Source with Calibrated Model

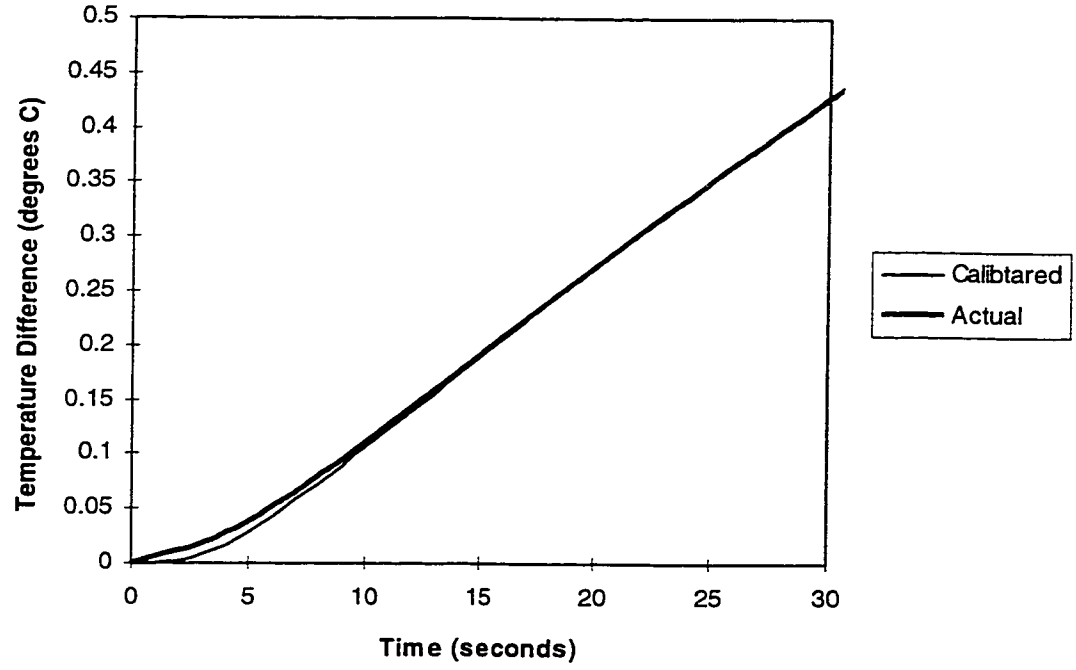

Figure 7.14: Temperature Difference for Main Source (first 30 seconds)

Figure 7.15 shows the difference between the actual and calibrated temperature difference. The measurement noise is negligible, as expected for a finite-element model, so the difference represents the calibration error. The figure also shows the regularization model from equation (6.2), using regularization parameters:

$$\begin{aligned} A &= 5.59E\text{-}03 \\ B &= 8.25E\text{-}06 \\ a &= 0.290 \end{aligned} \tag{7.8}$$

The regularization model has been calibrated such that the regularized step response is equal to the actual temperature response. This is only possible because the initial derivative of the temperature difference is 0.00544, which produces an acceptable doublet singularity of 183.75. In theory, if the regularized temperature difference is equal to the actual temperature difference, and there is no temperature measurement noise, then there will be zero estimation error. This is not the case in practice, as will now be shown.

Figure 7.16 shows the regularized temperature difference, and figure 7.17 shows the proper part of the transfer function G(r,t) corresponding to figure 7.16. The singularities are:

$$\begin{aligned} A_0 &= -57.121 \\ A_1 &= 183.75 \end{aligned} \tag{7.9}$$

The thermal deflection step responses measured between the points shown in figure 7.10 for Q=1.0 were calibrated using the model from equation (6.2), resulting in the following empirical parameters for the x-deflection:

$$\begin{aligned} A &= -0.1695 \qquad a = 0.00890 \\ B &= -1.255 \qquad b = 0.00129 \\ D &= -0.004785 \qquad d = 0.0097 \end{aligned} \tag{7.10}$$

and y-deflection parameters:

$$\begin{aligned} A &= 3.845 \qquad a = 0.0123 \\ B &= 2.355 \qquad b = 0.00142 \\ D &= -0.0354 \qquad d = 0.0338 \end{aligned} \tag{7.11}$$

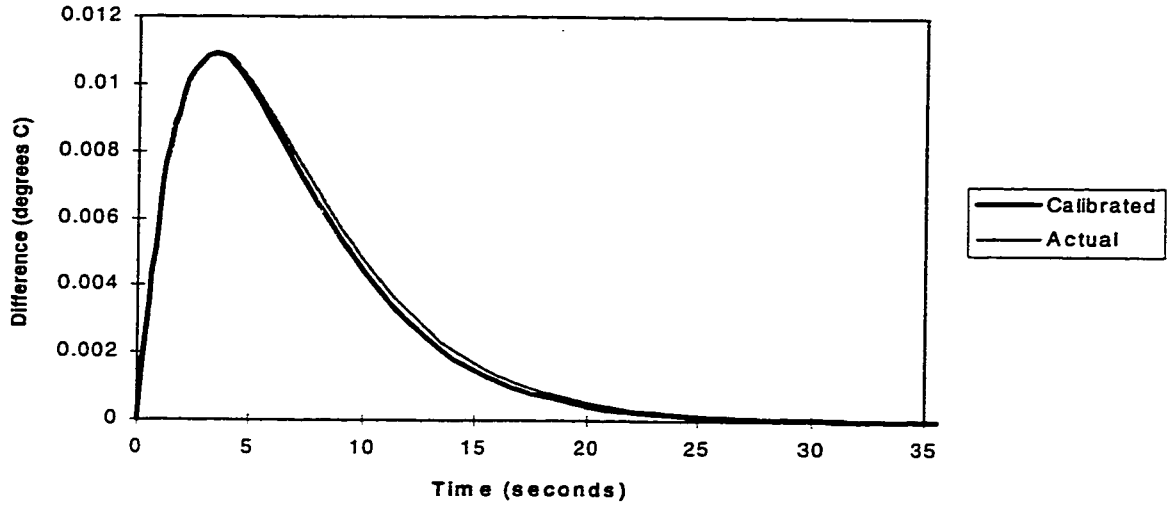

Figure 7.15: Difference Between Actual and Calibrated temperature Difference, Showing Regularization Model

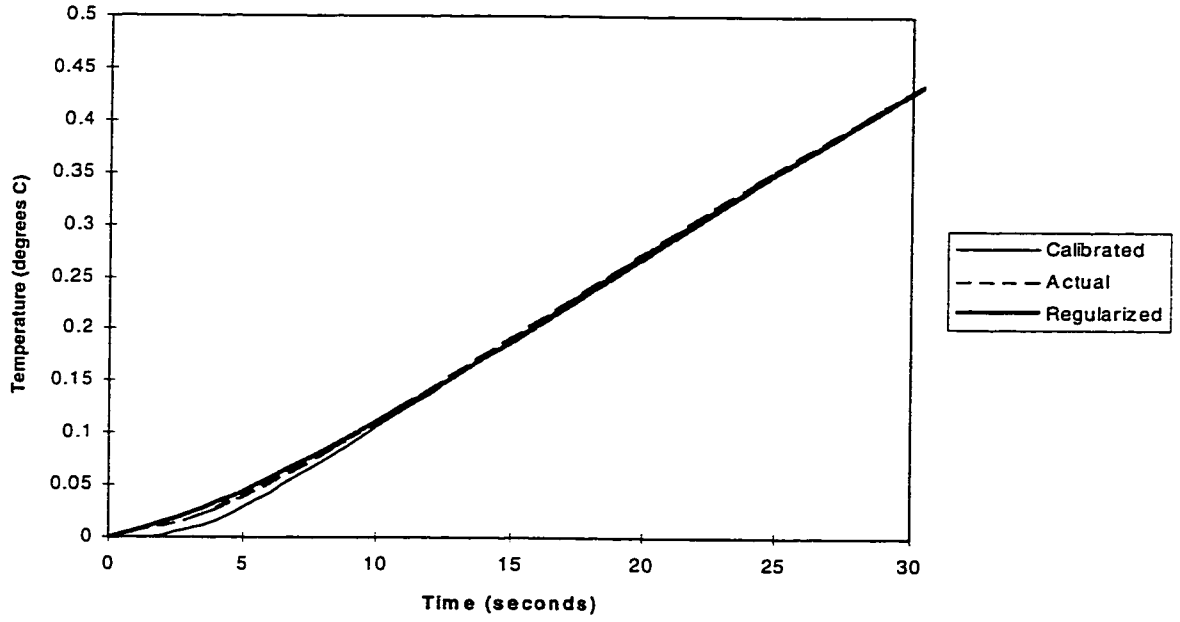

Figure 7.16: Regularized Temperature Difference

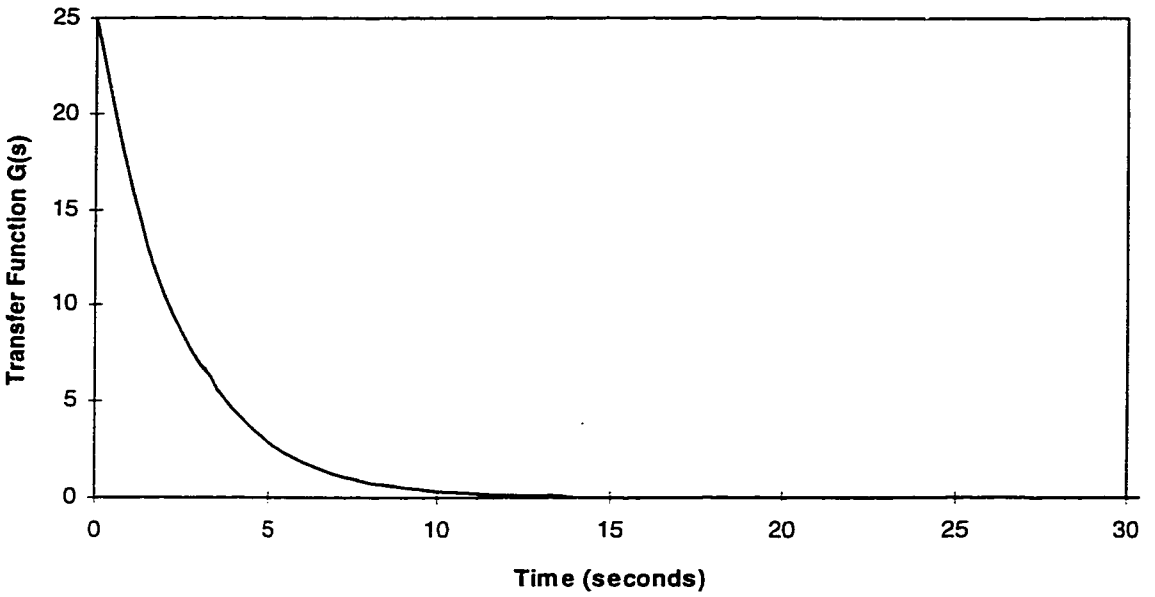

Figure 7.17: Numerical Transfer Function G(r,t)

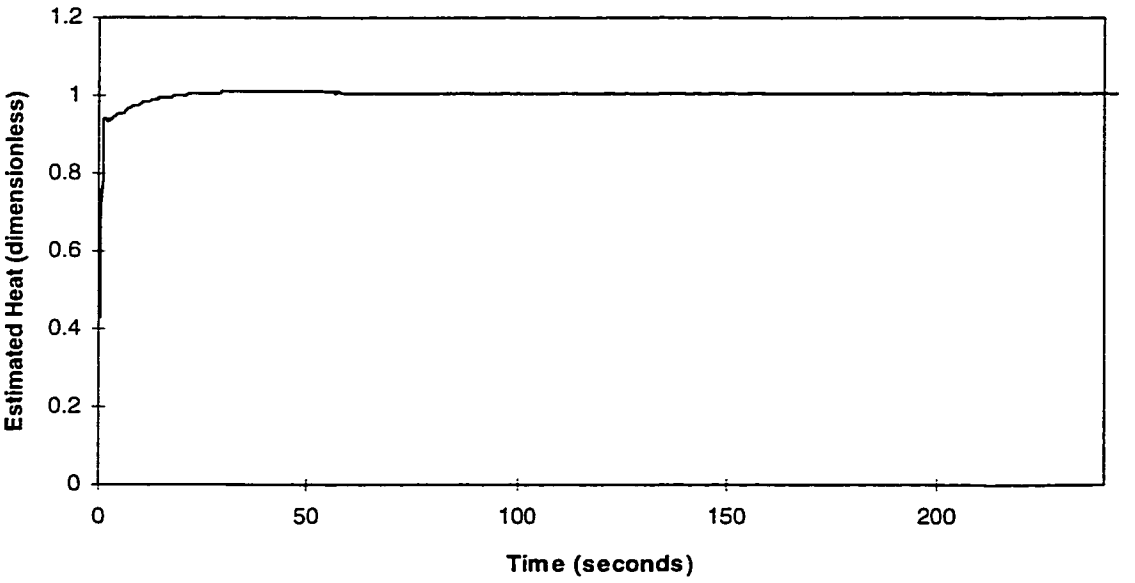

Figure 7.18: Estimated Heat Generation Q=1.0

The maximum difference between the actual and calibrated curves is less than 0.1 microns.

The linearized thermal deflection estimation algorithm is the same algorithm that was discussed in chapter 6. Since the regularized and actual temperature step responses are almost identical, there is no significant estimation delay that is due to the regularization. Thus, the artificial delay in the solution algorithm is chosen to be zero. Figure 7.18 shows the estimated heat generation, corresponding to the temperature difference in figure 7.13. As expected, the estimated heat generation rises quickly to the correct value of 1.0 and there are no detectable high frequency components in the estimate. What might not have been expected however, is the transition region from zero to about 30 seconds which is evident in the figure, and a steady-state error of about 0.7% that is not clearly evident in the figure. Figure 7.19 shows the estimated and actual thermal deflection, and figure 7.20 shows the estimation error. It should come as a surprise that the estimation error range is as large as 1.6 microns, given the facts that the estimation is for the reference input Q=1.0, the regularized and actual step responses are close to identical, and there is zero measurement noise. The source of the error is numerical inaccuracy in evaluating the convolution integral and the temperature derivative on-line with a finite sampling rate. Increasing the sampling rate to above 2 Hz would reduce the estimation error in figure 7.20, which would approach zero as the sampling rate approaches infinity. A sampling rate that is higher than the controller cycling frequency could be achieved with a more expensive data acquisition system capable of accurately multi-sampling during each control cycle period. However such a system would not improve the accuracy of the estimation in practice, since the range of the error induced by random noise has been shown to exceed 1.6 microns. Nevertheless, it shows how any effort to reduce the error associated with random noise must be accompanied by a system of multi-sampling to reduce the error associated with the finite temperature sampling.

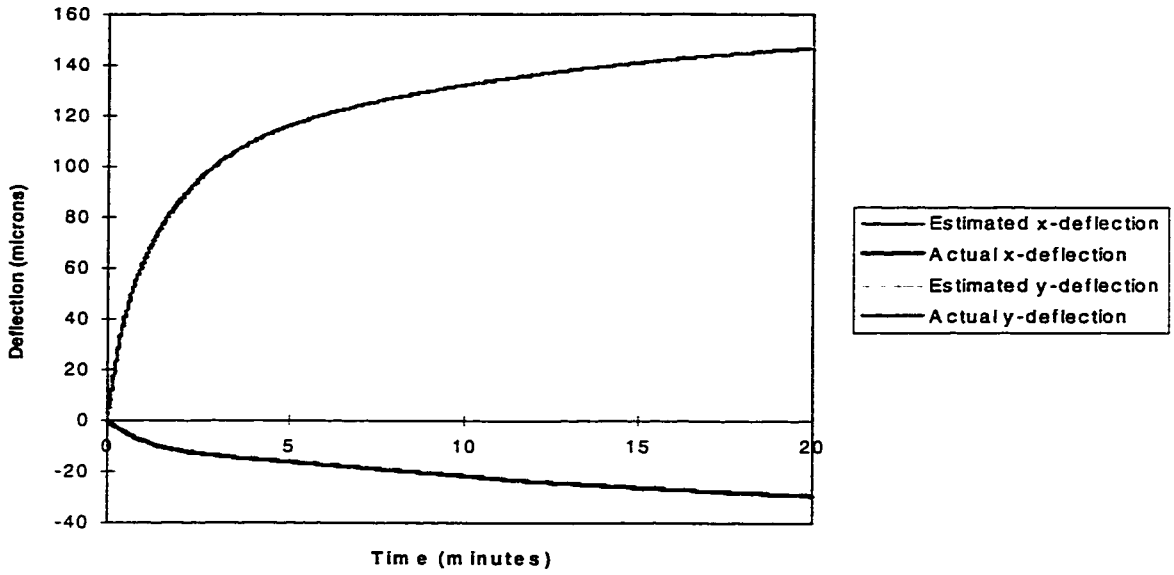

Figure 7.19: Actual and Estimated Thermal Deflection for Q=1.0 (Model Calibrated for Q=1.0)

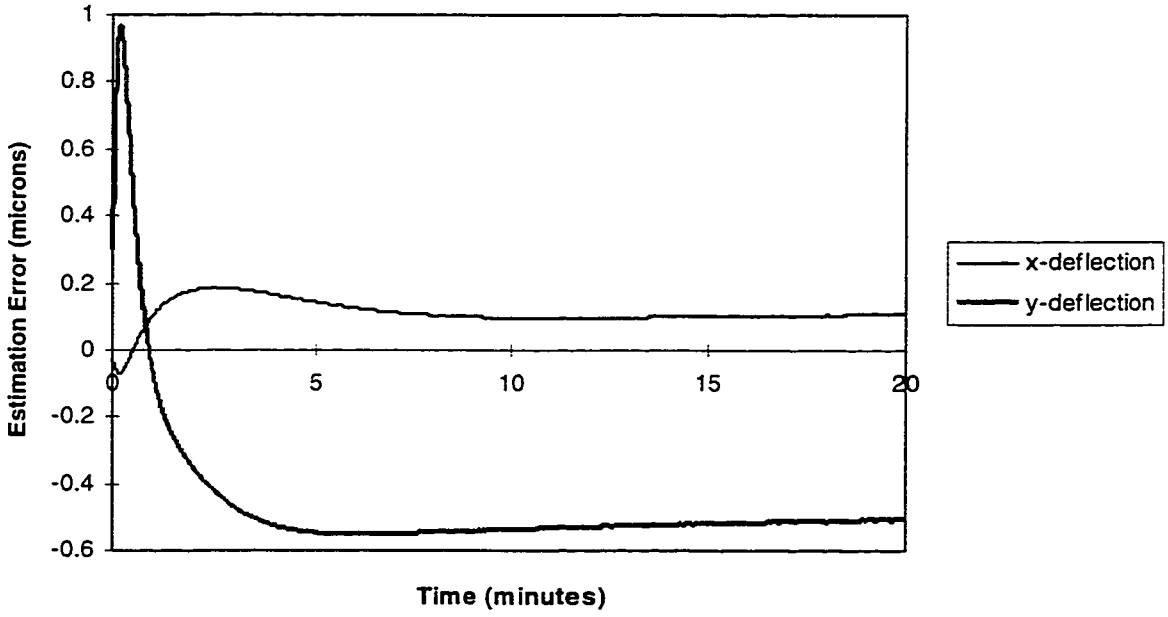

Figure 7.20: Estimation Error for Q=1.0 (Model Calibrated for Q=1.0)

The error which is caused by a finite temperature sampling rate readily explains the initial error shown in figure 7.20. It does not adequately explain the steady-state error however, since the measured temperature and temperature derivative are approaching constant values. There is another phenomenon at work here, which can be seen by referring back to equation (7.9), where the magnitude of the impulse singularity was found to be -57.121. As already stated, the steady-state temperature derivative is zero, thus the approximation to the thermal deflection is found from equation (5.62) by taking the temperature derivative to be zero and the steady-state temperature to be constant:

$$Q(t) = \Delta T_{ss} \left(\int_0^t G^{p}(r,t-\tau)\, d\tau + A_0 \right) \tag{7.12}$$

where Δt_{ss} is the steady-state temperature difference, equal to 4.133 degrees Celsius. Since the steady-state Q(t) is the constant value 1.0, the bracketed term in equation (7.12) must be equal to 0.5/4.133 = 0.1210. It now becomes apparent why the steady-state round-off error is so large for this particular model. Since A_0 = -57.121, the steady-state value of the integral must be equal to +57.242, and the addition of these two is only accurate to three significant figures. Because the integral must be approximated using a finite number of samples it is prone to inaccuracy, which becomes accentuated when the difference is taken. The solution is to readjust the regularization parameters so as to reduce the value of the A_0 term. As was explained in chapter 7, there are no definite rules for choosing the a and B regularization parameters, however ensuring that A_0 is reasonably small is one of the objectives of this process, for the reasons just shown. Since the estimation error is within the range of the expected error induced by noise for the data acquisition system discussed in chapter 7, this discussion is academic at this time and so the regularization parameters may be left as they are.

7.5.3 Evaluating the Linearized Model

Figure 7.21 shows the estimated thermal x-deflection for a step input of magnitude Q=2.0, along with the actual deflection in the x-direction, calculated with the finite-element model.

Similarly, figure 7.22 shows the estimated and actual y-deflection corresponding to the same input. The difference in the estimated and actual deflections indicate a high degree of nonlinearity in the system. Figure 7.23 shows the estimation error of the linearized system model. The error range is 10 microns in the y-direction and 1.5 microns in the x-direction, which represents nonlinearity of 3.4% and 2% respectively. While the percentage nonlinearity is not high, the resulting error is unacceptably high. Furthermore, since the nonlinear error is a systematic error it is partially additive with the other error sources, including measurement noise. The analysis of numerous machine tool configurations that was described earlier indicates that 3.5% is quite a high percentage nonlinearity, and 5% is probably the extreme outer limit for any configuration that is realistic for a machine tool structure. Figure 7.23 shows that the 3.5% nonlinearity is unacceptable for this machine tool, since the objectives of this thesis, stated in chapter 1, cannot be satisfied unless the nonlinear error is reduced considerably.

7.5.4 Estimating the Nonlinear Thermal Deflection

7.5.4.1 Calibrating the Contact Sources

One of the advantages of a finite-element test model for the nonlinear estimation procedure is that it allows us to look at the system more closely, identifying general characteristics and processes that may be common to all machine tools that exhibit a high percentage nonlinearity. Before looking at the specific model under consideration, the essential characteristics of the structure that are a precondition to high percentage nonlinearity will be identified. The single most important condition that is common to all machine tool configurations that exhibit significant nonlinearity is that there is a major heat source located close to a large joint contact. This condition will be used a basic assumption in the analysis that follows.

Figure 7.24 shows the contact pressure distribution at the contact joint for a zero thermal load. The static contact pressure is approximately uniform at about -27 psi, which represents the clamping force that is present in a real machine tool. Figure 7.25 shows the steady-state contact

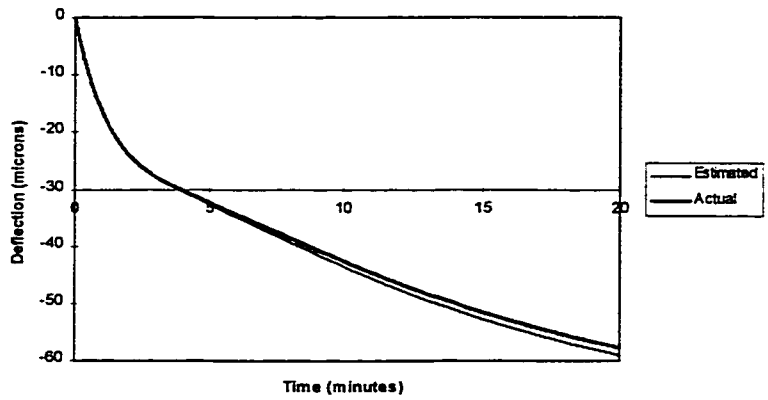

Figure 7.21: Estimated x-Deflection for Q=2.0 (Model Calibrated for Q=1.0)

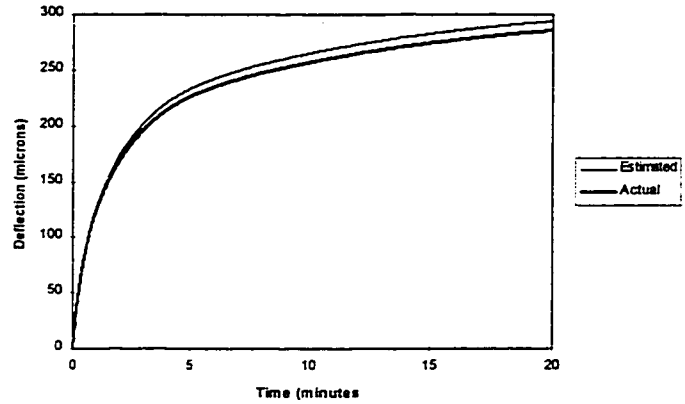

Figure 7.22: Estimated y-Deflection for Q=2.0 (Model Calibrated for Q=1.0)

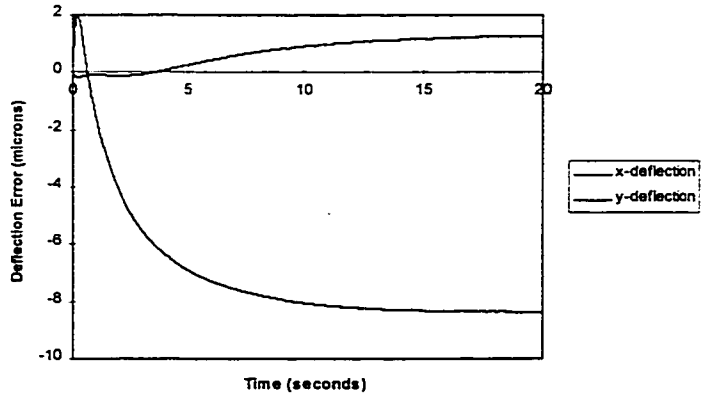

Figure 7.23: Nonlinear Estimation Error for Q=2.0 (Model Calibrated at Q=1.0)

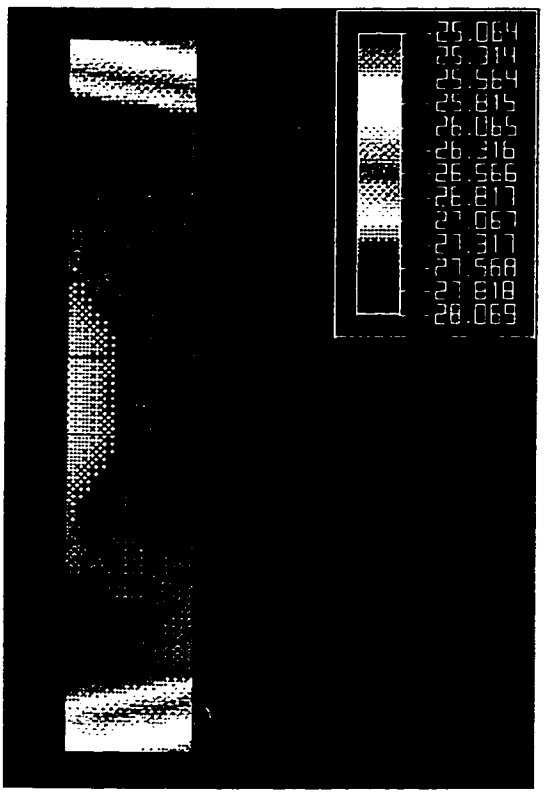

Figure 7.24: Pressure Distribution Q=0

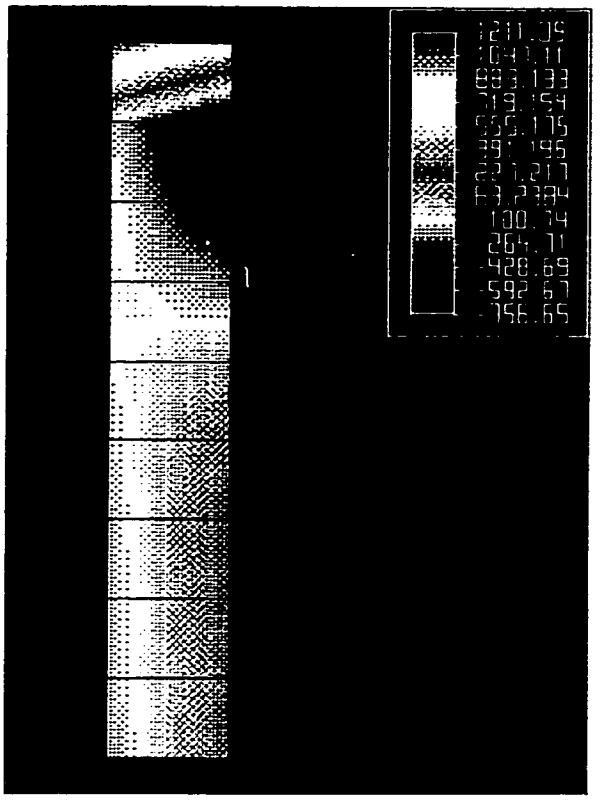

Figure 7.25: Pressure Distribution Q=2.0

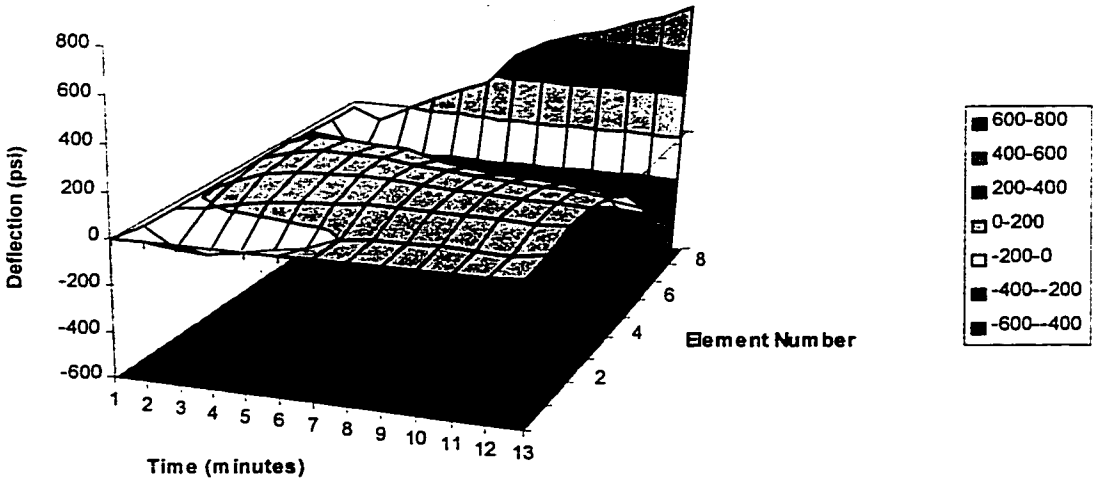

Figure 7.26: Contact Pressure Distribution at Joint Interface for Q=2.0

pressure distribution for the maximum heat input Q=2.0. The contact pressure of each contact element is determined by averaging the pressure over the surface area of the element. Figure 7.26 is a three-dimensional surface plot showing the contact pressure at each contact element as a function of time for a step heat input of magnitude 2.0 applied at t=0. The elements are numbered 1 through 9, corresponding to the element numbers in figure 7.4 The figure shows that the elements numbered 1 through 4 have positive values in steady-state and for most of the time after t=0. The elements numbered 5 through 8 are negative in steady-state and for most of the time after t=0. The last element is positive in steady-state. Positive contact pressure means that the surfaces are separating. As described in chapter 5, when the surfaces separate they are assumed to be contacting over a different, smaller area that allows a negligibly small heat flux. Hence, the effect of the joint is to cut off the flow of heat through elements 1 to 4, and to increase the conductivity of elements 5 to 7. This pattern of increasing the conductivity on one half of the joint and decreasing the conductivity on the other half of the joint is the most typical situation which is seen in practice. The other, less common situation is where the conductivity is increased or decreased over the entire contact area. Both of these situations can be conveniently modelled by lumping all of the contact elements into two fictitious heat sources. One of these sources shall be used to increase the heat flux through the lower half of the contact, and the other source will be used to decrease the heat flux through the upper half of the contact. It will be shown that the two source model gives an adequate representation for the contact elements.

Figure 7.27 shows the same contact pressure versus time that was shown in figure 7.26, but this time using line graphs for each contact element. The important point to notice from this figure is that the contact pressures reach their steady-state values very quickly. All of the elements with a negative steady-state contact pressure reach 75% of their maximum value within one minute after the application of the heat input at t=0. It will be seen shortly that the absolute temperature and the nonlinear temperature deviation in the contact zone have time

constants that are many minutes long. By comparison, the contact pressure may be adequately represented as a step input by neglecting the relatively short transition region. This is important because it was shown in equation (7.4) that the heat generation magnitude of the fictitious sources is proportional to the contact pressure. Figure 7.27 shows that a reference step input to the contact sources can be approximately generated by applying a step input to the main source. The contact pressure response to a step input in the main source shown in figure 7.27 is typical when the main heat source is located nearby to the contact joint. Since the location of the heat source nearby to the contact joint is a precondition for a nonlinear system, the conclusion drawn from figure 7.27 is a general conclusion that is applicable to any machine tool system with significant joint nonlinearity.

Figure 7.28 shows the assumed locations of the contact heat sources and the positions of the measured temperatures in the contact zone. Figure 7.29 shows the temperature profiles measured at these points for a step heat input of Q=1.0. Figure 7.30 shows the same temperature profiles, this time scaled to show the initial delays. The generalized model was calibrated from this data, resulting in the calibrated parameters for the T1 and T2 temperature models. The difference between the actual temperature step responses and the generalized models is negligible at the calibration input Q=1.0. An incremental direct solution based on equation (6.34) was implemented, using these calibrated models. Figure 7.31 shows the linearized estimate for T1 for a step input Q=2.0, calculated with equation (6.34). Figure 7.31 also shows the actual temperature response at T2 for Q=2.0, determined by the nonlinear finite-element algorithm. Figure 7.32 shows the actual and linearized temperature response at T2 for the same input Q=2.0. Figure 7.33 shows the difference between the linearized estimate and the actual T1 and T2 profiles for the Q=2.0 input, and figure 7.34 shows the difference between the linearized estimate and the actual T1 and T2 profiles for the Q=0.5 input. The temperature profiles in figure 7.33 and 7.34 are the temperature deviations produced by the joint nonlinearity for the Q=2.0 and Q=0.5 step inputs respectively. From the other perspective, they are the

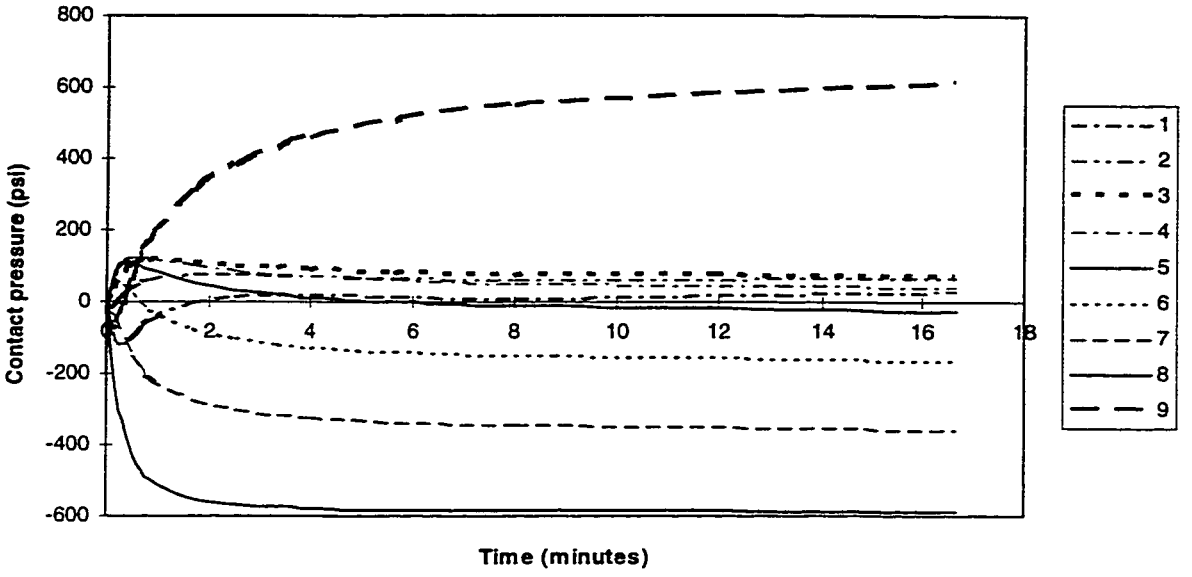

Figure 7.27: Contact Pressure of Contact Nodes for Q=2.0

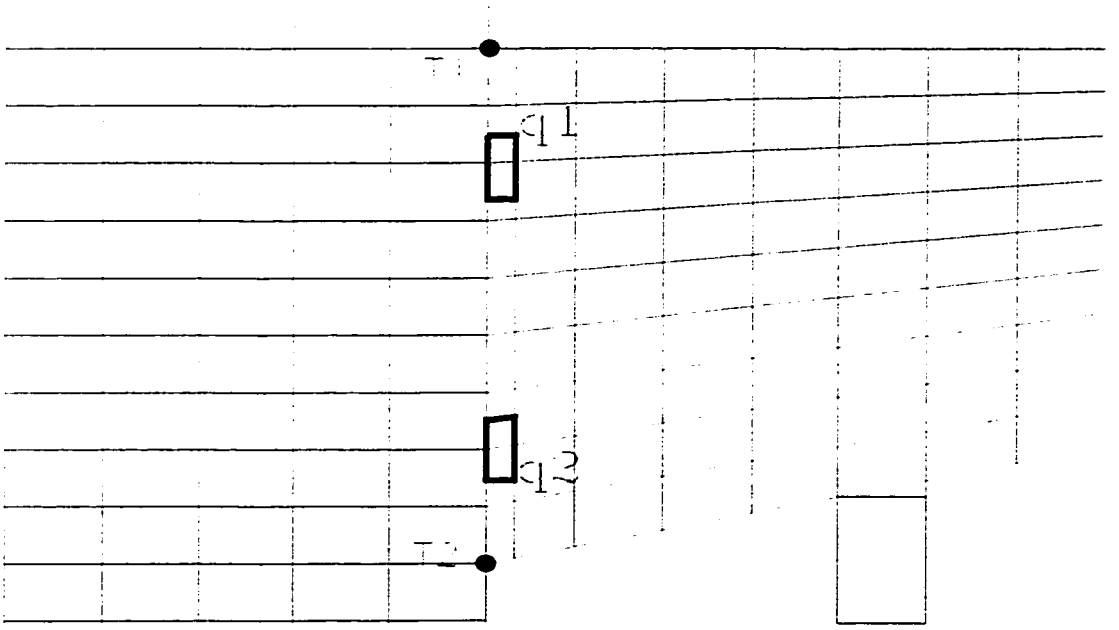

Figure 7.28: Assumed Locations of Contact Sources

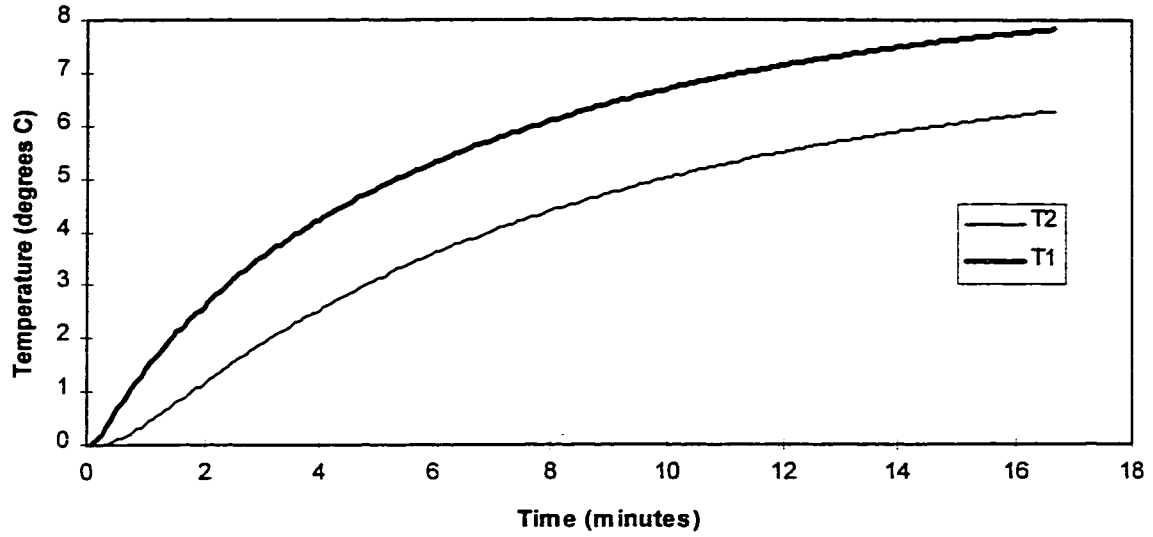

Figure 7.29: Contact Zone Temperatures for Q=1.0

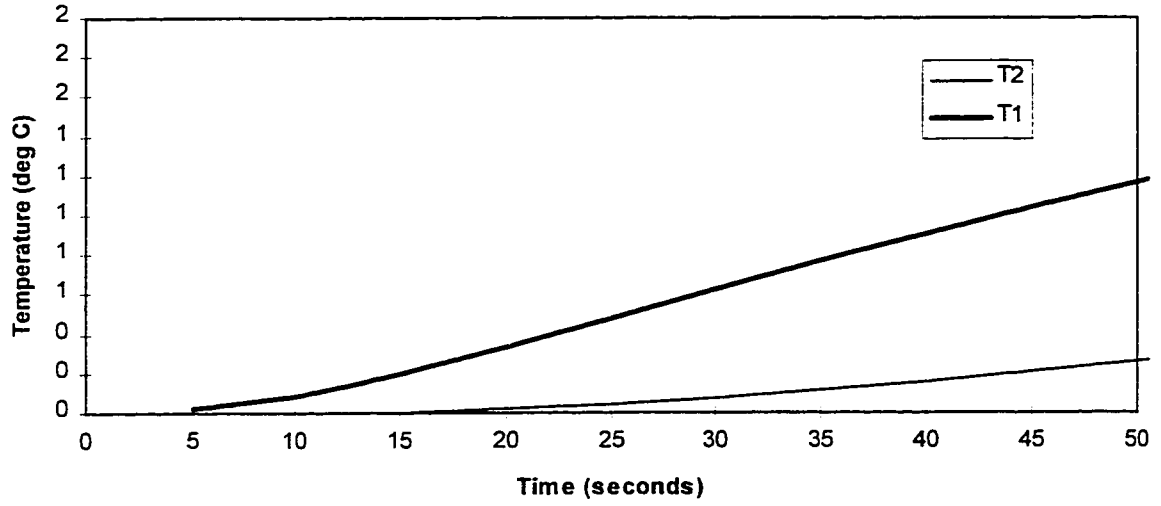

Figure 7.30: Contact Zone Temperatures for Q=1.0 (firsr 50 seconds)

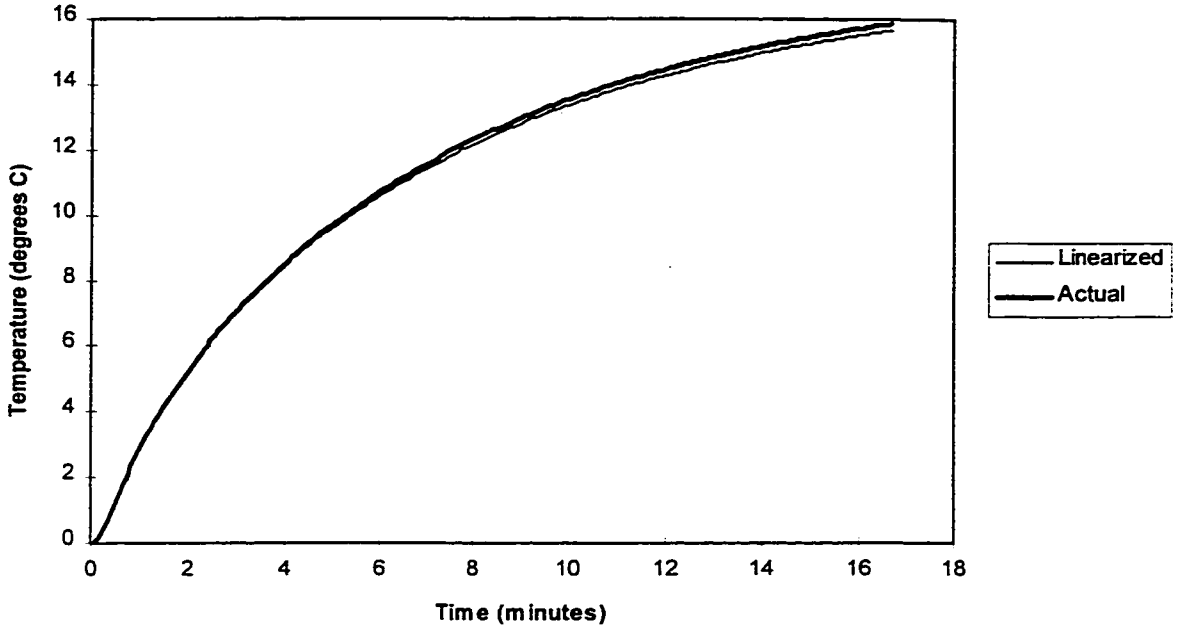

Figure 7.31: Actual and Linearized T1 for Q=2.0

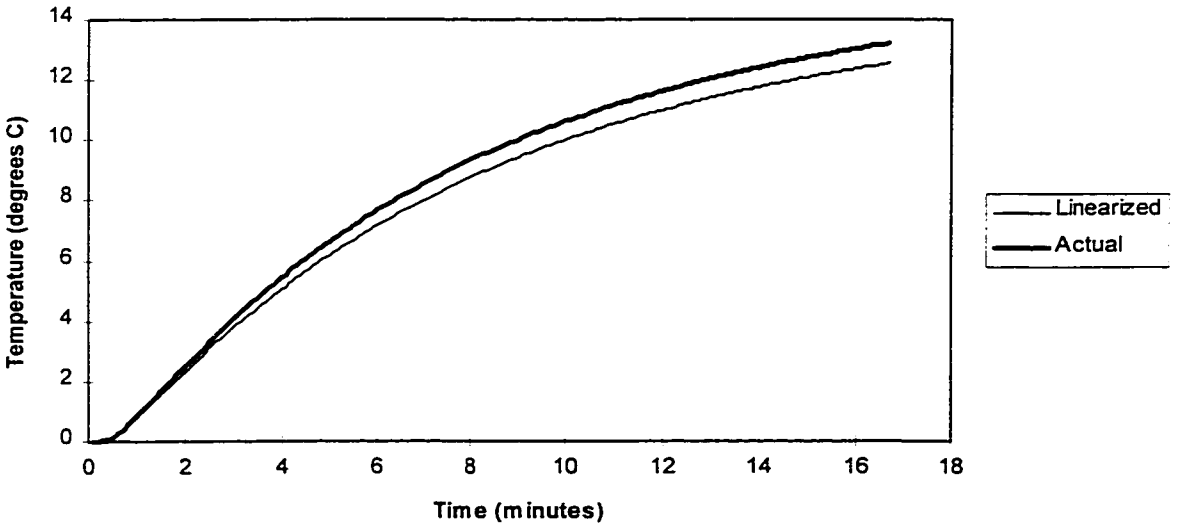

Figure 7.32: Actual and Linearized T2 for Q=2.0

temperature deviations produced by the contact heat sources. It is these temperature deviations that are the inputs to the contact heat source estimation algorithm.

The temperature deviations for the Q=2.0 and Q=0.5 step inputs shown in figures 7.33 and 7.34 are the calibration inputs corresponding to <1> and <2> in figure 7.9. Before calibrating the generalized model, it is necessary to assume the size of the contact sources, and estimate the distance from the centre of the sources to the measured temperature points T1 and T2, shown in figure 7.25. The Generalized model is not sensitive to the size radius r_0 when $r \geq 2r_0$, so r_0 is selected somewhat arbitrarily to be $r_0=0.12$. The distance from the source locations to the measured points is determined by the geometry of the structure and the assumed locations of the contact sources. Figure 7.35 shows a solid model of the contact area, indicating the locations of the fictitious heat sources and the measured temperature points. The distances r_{ij}, where i is the source and j is the measured point, were determined to be:

$$\begin{aligned} r_{11} &= 4.89 \qquad r_{12} = 12.47 \\ r_{22} &= 6.21 \qquad r_{21} = 10.84 \end{aligned} \tag{7.13}$$

These values are important because they help to define the mathematical form of the system model. With these r and r_0 values, the empirical parameters were calibrated using the procedure shown in figure 7.9. The calibrated parameters for source 1 and source 2 with a tolerance of 3 significant digits are as follows:

$$\begin{aligned} a_1 &= 0.025 \qquad a_2 = 0.0361 \\ \alpha_1 &= 0.0841 \qquad \alpha_2 = 0.0799 \\ K_1 &= 0.00874 \qquad K_2 = 3.73 \\ q_1^{Q=2.0} &= 1.0 \qquad q_2^{Q=2.0} = 1.0 \\ q_1^{Q=0.25} &= 32.92 \qquad q_2^{Q=0.25} = -0.124 \end{aligned} \tag{7.14}$$

where the subscript indicates the contact source index. These values for K and q were determined under the assumption that q_1 and q_2 are both equal to 1.0 when Q=2.0. The relative heat magnitudes in equation (7.14) are misleading because they seem to indicate that the heat generated by source 1 is much larger than source 2, when in fact it is exactly the opposite that

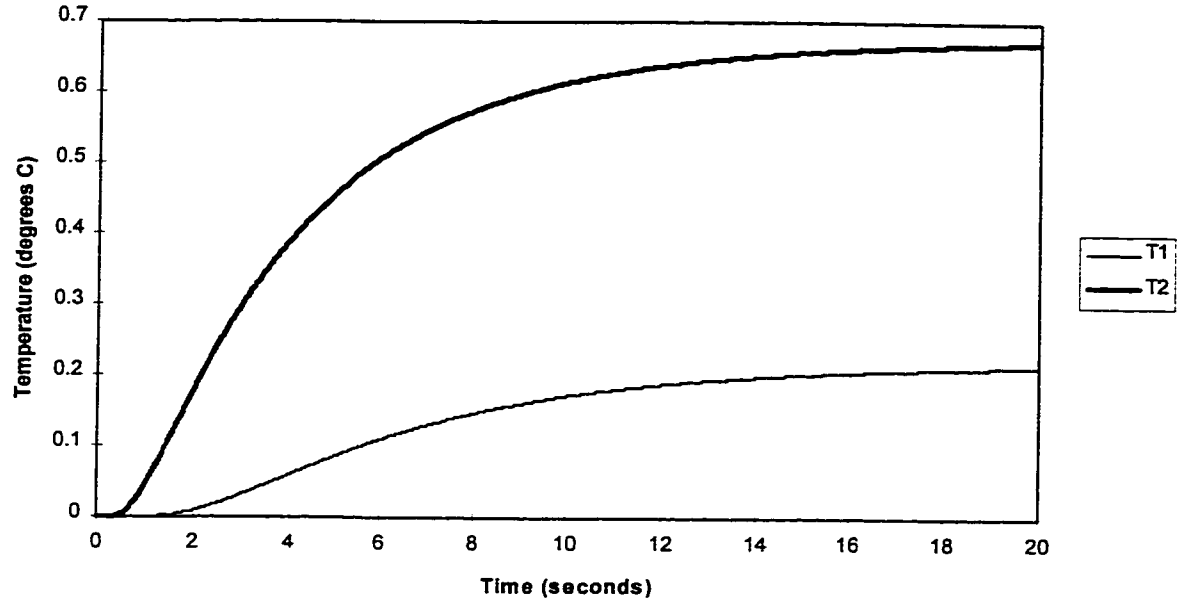

Figure 7.33: Nonlinear Temperature Deviation for Q=2.0

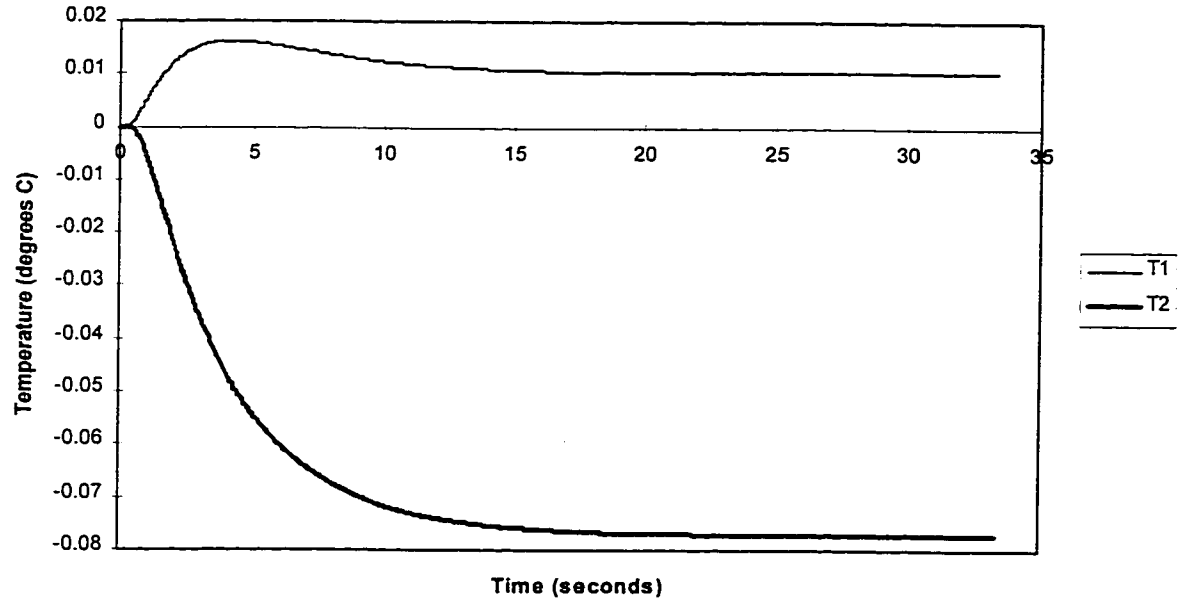

Figure 7.34: Nonlinear Temperature Deviation for Q=0.5

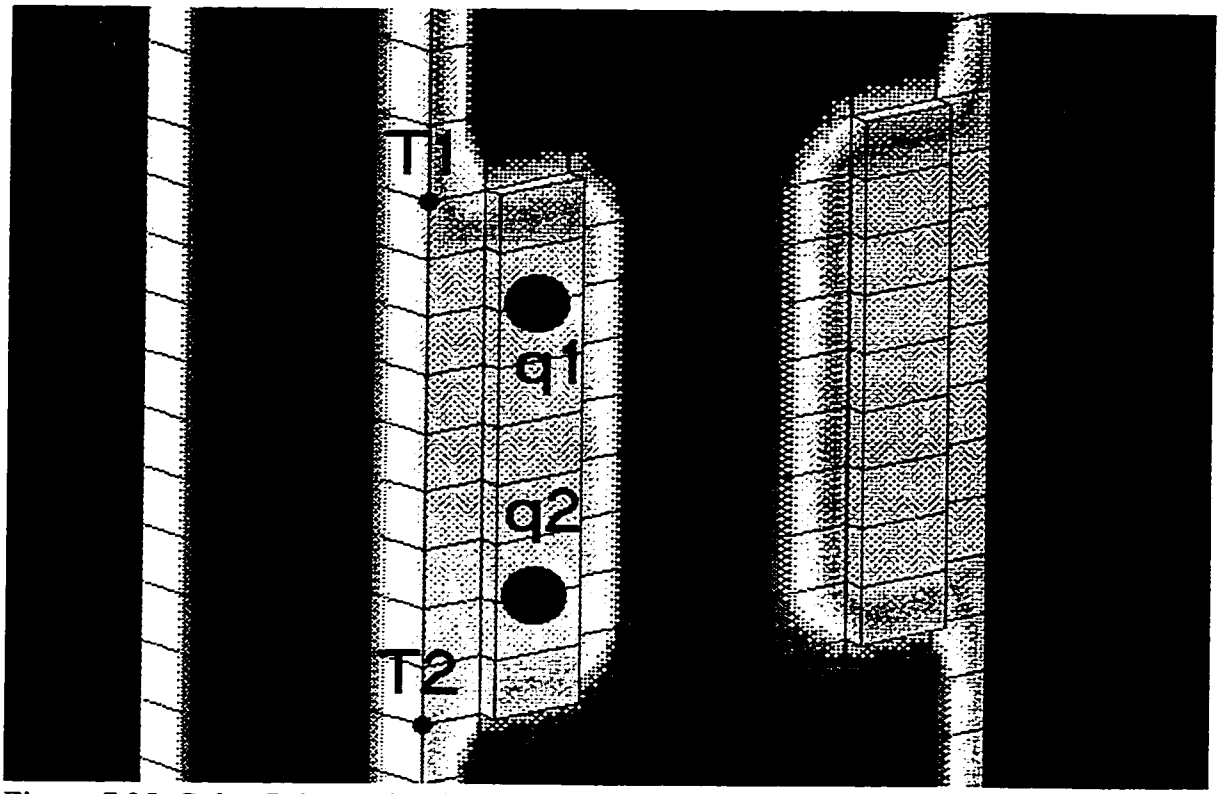

Figure 7.35: Color Enhanced Solid Model Showing the Geometry of the Contact Sources

is the case. Without changing the validity of the model, the parameters can be redefined by making $K_1=K_2$ instead of fixing $q_1=1.0$. It is reasonable to assume that the dimensionless gain of each source should be the same since the sources are in similar locations within the structure and therefore should produce similar effects. Under this new definition the parameters of equation (7.14) become:

$$\begin{array}{ll} a_1 = 0.025 & a_2 = 0.0361 \\ \alpha_1 = 0.0841 & \alpha_2 = 0.0799 \\ K_1 = 3.73 & K_2 = 3.73 \\ q_1^{Q=2.0} = 2.3E{-}04 & q_2^{Q=2.0} = 1.0 \\ q_1^{Q=0.25} = 0.0289 & q_2^{Q=0.25} = -0.124 \end{array} \tag{7.15}$$

It is important to mention this redefinition does not affect the outcome of the model in any way, it merely makes it easier to interpret the parameters. Figure 7.36 shows the calibrated temperature profile at T1 and T2 for a heat input of 2.0, along with the actual temperature deviations that were used to calibrate the model. The estimated temperature at each point is actually the sum of the temperature contributions from the generalized model of each of the two contact sources. Figure 7.37 shows the calibrated model and the actual temperature profiles for the Q=0.5 input. The results show that the two source model fits the actual data very well for the calibrated inputs. The figures also show that a one source model could not have represented the system as accurately because the one generalized thermal model could not have produced the overshoot in the T1 temperature profile that is evident the figures. From the perspective of the fictitious sources, the overshoot is the result of the superposition of the two linear temperature profiles from the two contact sources. Figure 7.38 shows the temperature step responses T11 and T22 corresponding to the q_1 and q_2 contact sources respectively. T11 is the temperature response at node 1 due to an input at q_1, and T22 is the temperature response at node 2 due to an input at q_2 These are the temperature step responses that would be produced if the contact sources could be activated independently. The figure also shows the regularized step responses for T11 and T22, using the following regularization parameters:

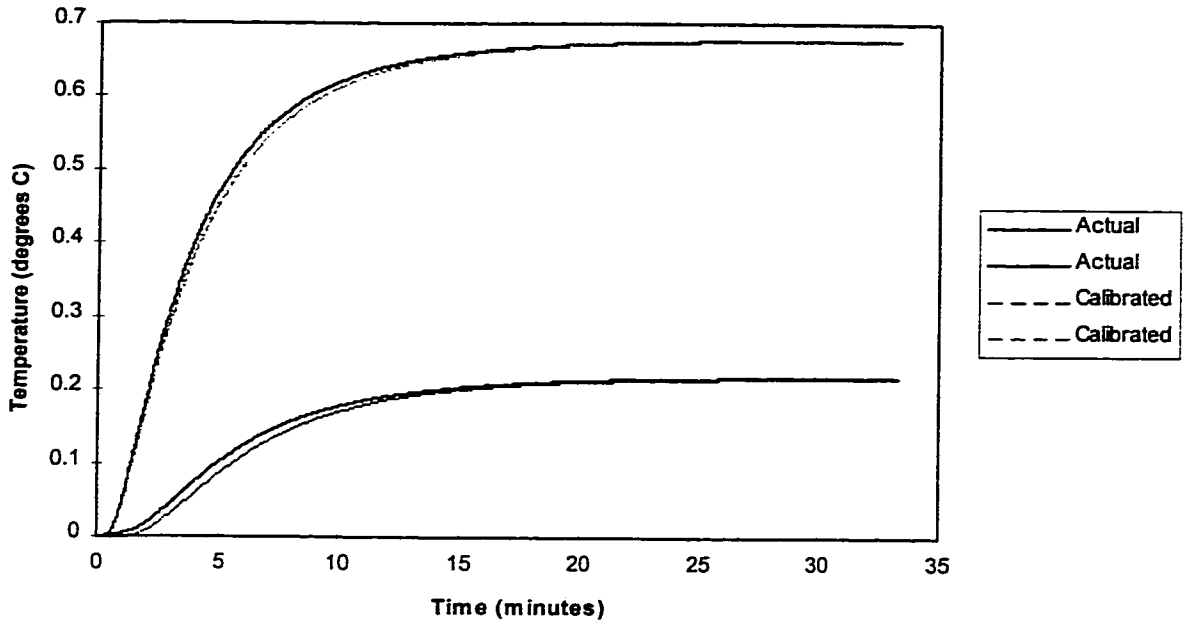

Figure 7.36: Calibrated Model of Temperatures T1 and T2 for Q=2.0

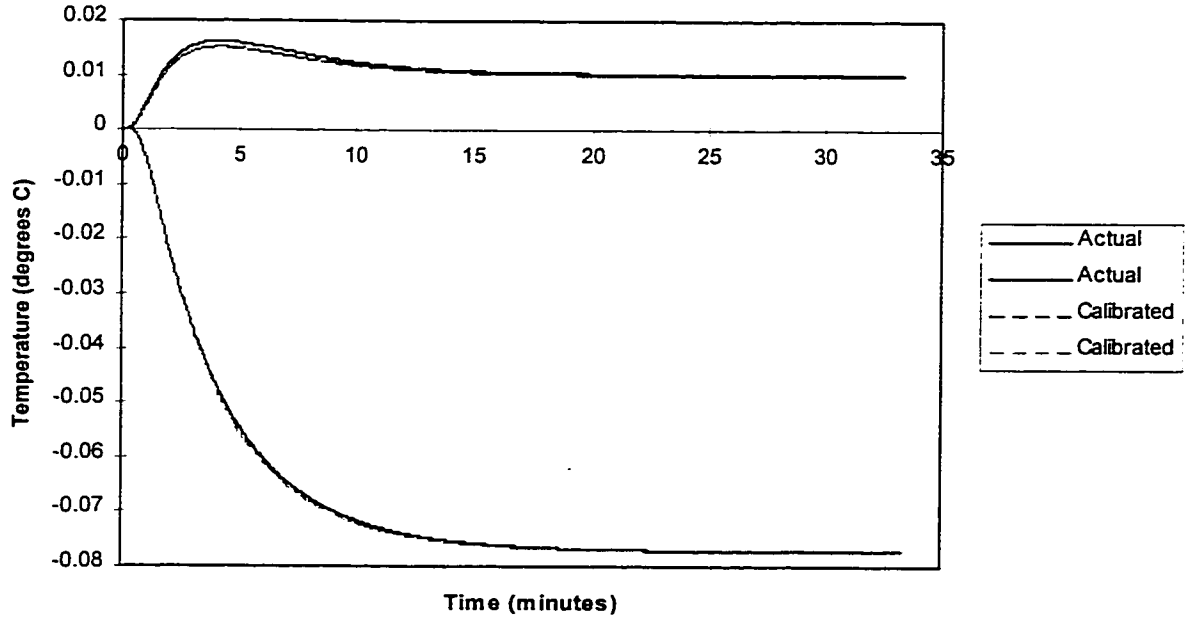

Figure 7.37: Calibrated Model of Temperatures T1 and T2 for Q=0.5

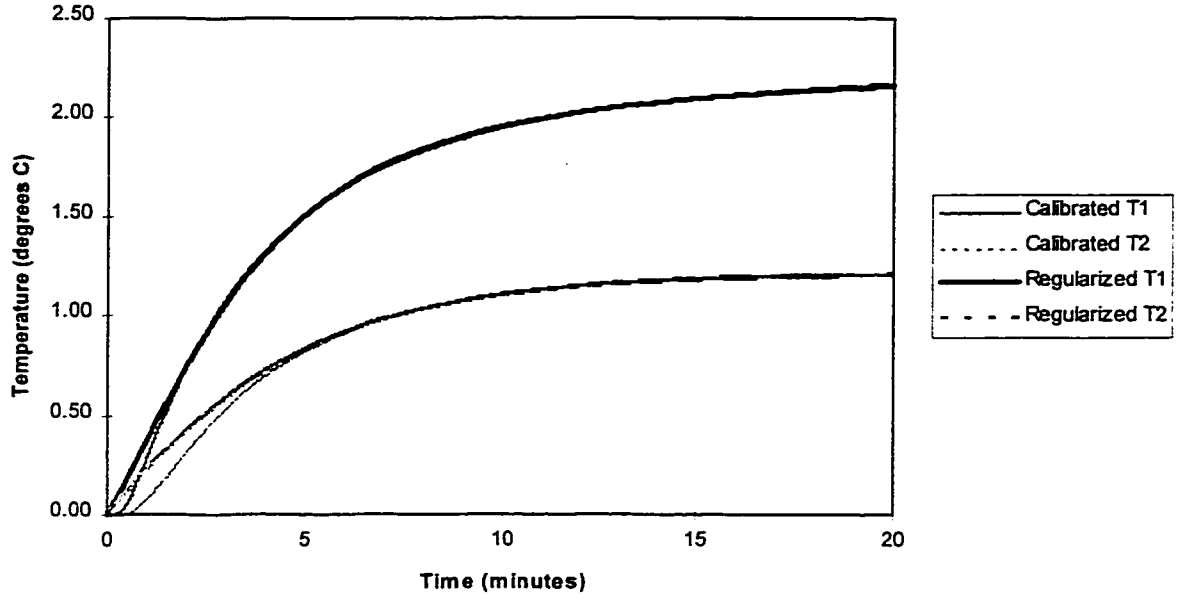

Figure 7.38: Regularized Temperature Models for T11 and T22

$$\begin{aligned} A_1 &= 0.00203 & A_2 &= 0.00369 \\ B_1 &= 7.34E\text{-}04 & B_2 &= 1.26E\text{-}04 \\ a_1 &= 0.0574 & a_2 &= 0.0268 \end{aligned} \tag{7.16}$$

The transfer functions are determined in the usual way, resulting in time domain transfer functions with the following singularities for the q_1 model:

$$A_0 = -1.349 \qquad A_1 = 183.90 \tag{7.17}$$

and for the q_2 model:

$$A_0 = -0.3492 \qquad A_1 = 281.46 \tag{7.18}$$

The thermal deflection in the x any y directions is shown in figure 7.39 for the Q=2.0 step input, and in figure 7.40 for the Q=0.5 step input. There are four models required for calibration, relating q_1 and q_2 to the thermal deflections in x and in y. The calibration of the thermal deflection models can be simplified considerably by noting from equation (7.15) that the heat generation of the q_1 source is negligible for the Q=2.0 input. Hence, the x and y thermal deflections in figure 7.39 are produced entirely by the q_2 source, which can be calibrated without any interference from the q_1 source. It was found that the fourth order model in equation (6.16) is not adequate for modelling the thermal deflections in figure 7.39 with sufficient accuracy. Thus, a sixth order model was used with the following step response:

$$\delta(t) = A + B - Ae^{-at} - Be^{-bt} + Dte^{-dt} + Ete^{-et} \tag{7.19}$$

With the q_2 models already calibrated, the q_1 models can be calibrated from the Q=0.5 thermal deflection data with the contribution from q_1 identified and removed, using equation (6.16). The calibrated parameters are for the q_1 source:

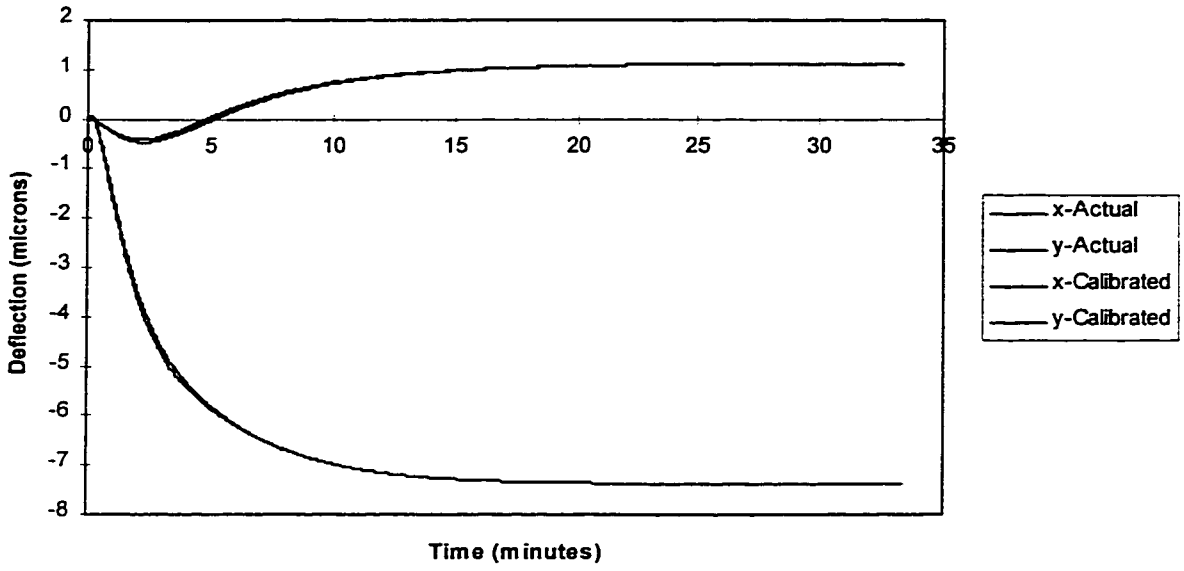

Figure 7.39: Calibrated Nonlinear Deflections for Q=2.0

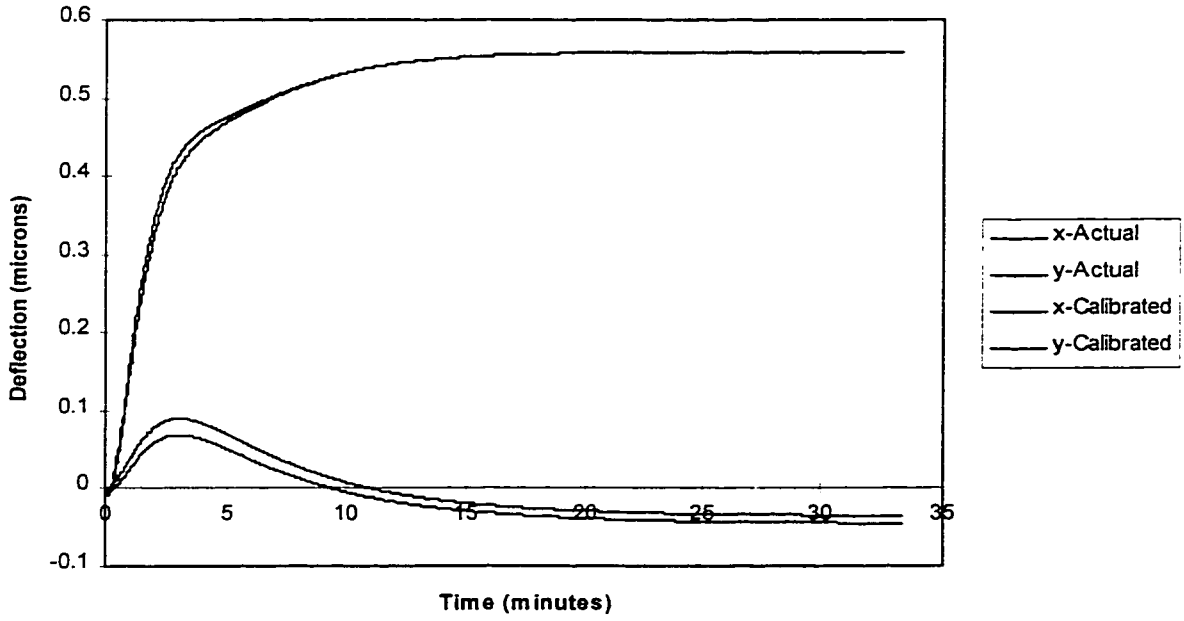

Figure 7.40: Calibrated Nonlinear Deflections for Q=0.5

x-deflection

A = 0.787	a = 0.00971
B = 1.20	b = 0.00441
D = -0.0145	d = 0.00849

y-deflection

A = -0.241	a = 0.00312
B = -6.29	b = 0.00462
D = 0.0357	d = 0.0123

(7.20)

and for the q_2 source:

x-deflection

A = -0.737	a = 0.0120
B = 1.87	b = 0.00289
D = -0.0135	d = 0.0077
E = 0.0178	e = 0.0191

y-deflection

A = -0.111	a = 0.0022
B = -7.27	b = 0.00489
D = -0.123	d = 0.0157
E = 0.179	e = 0.0201

(7.21)

The calibrated deflections are shown in figures 7.39 and 7.40 along with the actual thermal deflections.

7.6 Estimating the Thermal Deflection in Real Time

The block diagram of the real time process was shown in figure 7.7. There are three sets of temperature measurements: the temperature difference near the main source, and the two temperatures in the contact zone. These three measurements are used to estimate the heat generation of the main source Q_d, and the two contact sources q_1 and q_2. The total estimated thermal deflection is the sum of the estimated deflection produced by each of these three sources. The sampling time increment is chosen to be 2 seconds, which is four times larger than the sampling time for the linear model in chapter 6. A larger sampling time is required for the nonlinear algorithm since it includes three inverse transfer functions instead of one, and it must also estimate the temperature at T1 and T2 to calculate the temperature deviation, as shown in

figure 7.7. The numerical procedures for implementing the process blocks in figure 7.7, are identical to those explained in chapter 6.

7.7 Estimating the Thermal Deflection for Noncalibrated Inputs

The objective of the nonlinear thermal deflection estimation method is to accurately estimate thermal deflection for any real input duty cycle. Three inputs have been chosen to test the performance of the method. The first test input is a step of magnitude Q=1.5. Since this input is between the two calibration inputs it tests the ability of the algorithm to interpolate the calibration inputs. The second input is a step of magnitude Q=3.0, which tests the ability of the algorithm to extrapolate the calibration inputs. The third input is a step input of magnitude 1.0 in addition to a constant force input applied to the table of the machine tool model. Contact stress which originates from other sources or mechanical inputs influences the thermal deflection by inducing nonlinearity into the system. Because the contact source approach is a general system approach, it should not matter whether the nonlinearity is induced by the calibration heat source or from some other source or input. Any nonlinearity will induce temperature effects that are detectable at the measured nodes T1 and T2, and transformed into an equivalent contact heat flux. The third input will test the ability of the algorithm to extrapolate the calibration inputs into other sources of nonlinearity. The purpose of these tests is to evaluate the real time nonlinear estimation algorithm, which corresponds to blocks 3 through 7 in figure 7.7. The actual heat input is applied to block 3 rather than the estimated heat input, so as to isolate the nonlinear aspect of the algorithm for validation.

Figure 7.41 shows the temperature deviation from the linearized temperature for the Q=1.5 step input at T1 and T2. Figure 7.42 shows the nonlinear thermal deflection which is the difference between the actual measured deflection and the linearized deflection. This is the minimum error that would result from a linearized estimation of the thermal deflection, 2.5 microns in the y-direction and 0.5 microns in the x-direction. This is the error that is due entirely

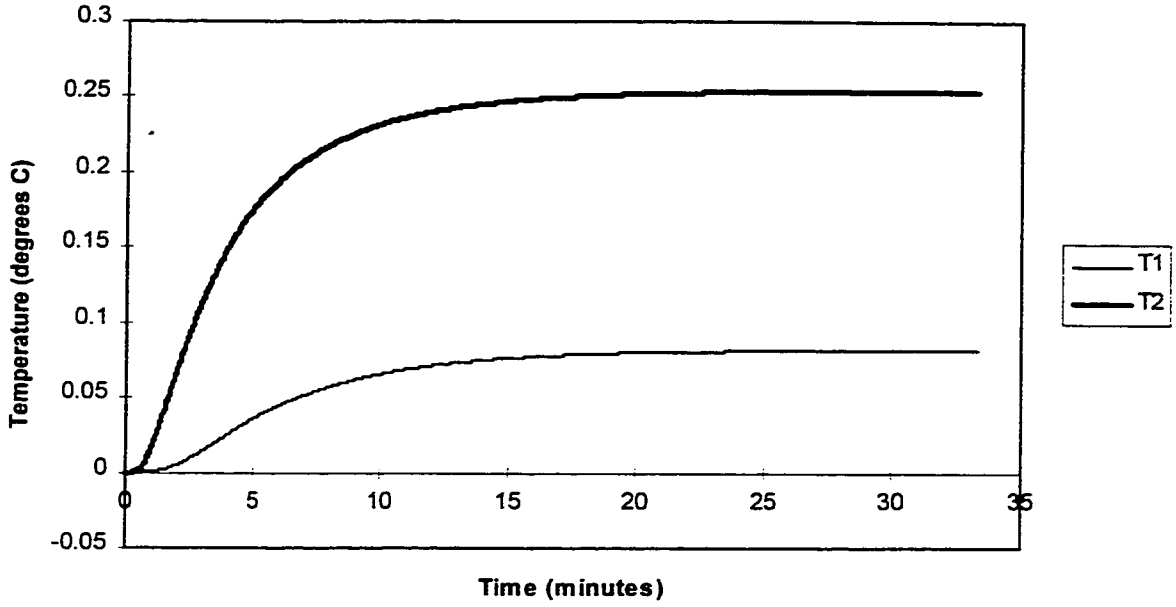

Figure 7.41: Nonlinear Temperature Deviation for Q=1.5

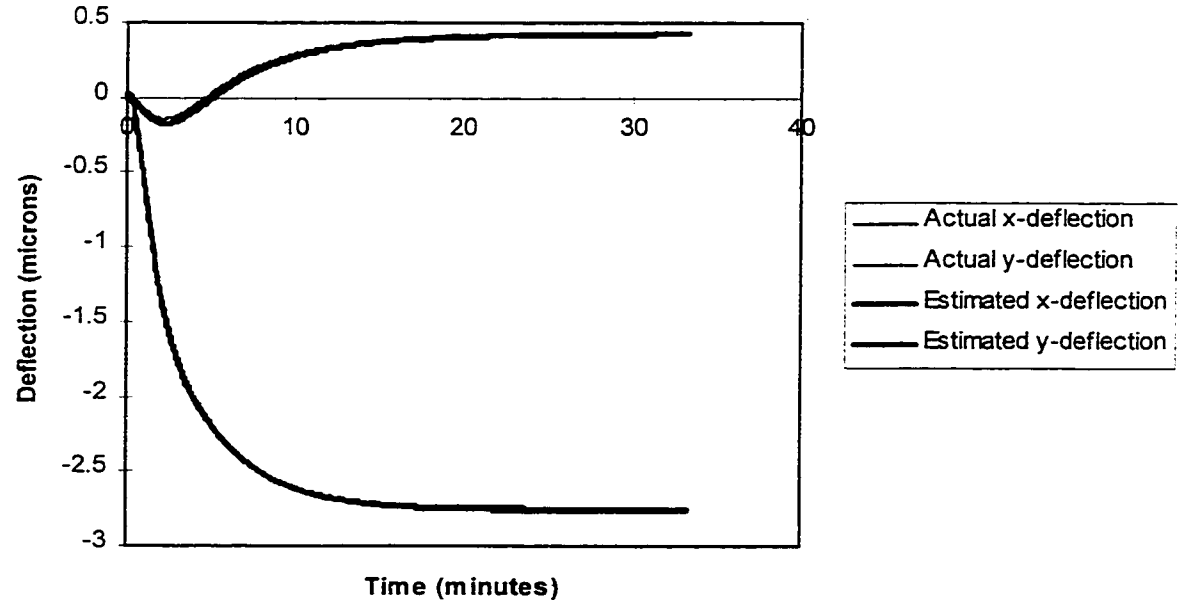

Figure 7.42: Actual and Estimated Deflection for Q=1.5

to the nonlinearity of the problem, without any numerical or noise induced error. Figure 7.42 also shows the estimated thermal deflection, using the nonlinear algorithm. The two curves are so close that they are virtually identical, which demonstrates how effectively the nonlinear algorithm interpolates the calibration data to estimate uncalibrated inputs. Figure 7.43 shows the difference between the estimated and actual nonlinear deflection. The nonlinear error has been reduced to within 0.06 microns in the x and y directions, which is completely negligible, and the nonlinear error for this input is essentially zero.

Figure 7.44 shows the temperature deviation that results from the Q=3.0 step input. The maximum temperature increase in the structure for this input is about 79 degrees Celsius, which is not unreasonable, as can be seen by the temperature distribution in the real milling machine in figure 5.1. Machine tools are sometimes operated at extreme conditions that produce unusually high thermal loads. Since the model will normally be calibrated in the usual operating range of the machine, the purpose of this test input is to investigate the performance of the method under extreme conditions. Figure 7.45 shows the nonlinear thermal deflection which results from this input. It is clear from the maximum y-deflection of 23 microns that a linear model is totally unsatisfactory for this machine tool model under these input conditions. The estimated thermal deflection is also shown in figure 7.45, and again the agreement between the curves is excellent. Notice in particular that the shape of the deflection curves is quite a bit different from the Q=1.5 and Q=2.0 cases, indicating that this is not at all a linear system. The difference between the curves is shown in figure 7.46, in which the maximum deflection has been reduced to within 0.5 microns in the y-direction and 0.1 microns in the x-direction, a reduction to less than 2.5% of the original nonlinear deflection. This test case demonstrates that the estimation algorithm can extrapolate beyond the calibration inputs as well as interpolate between them.

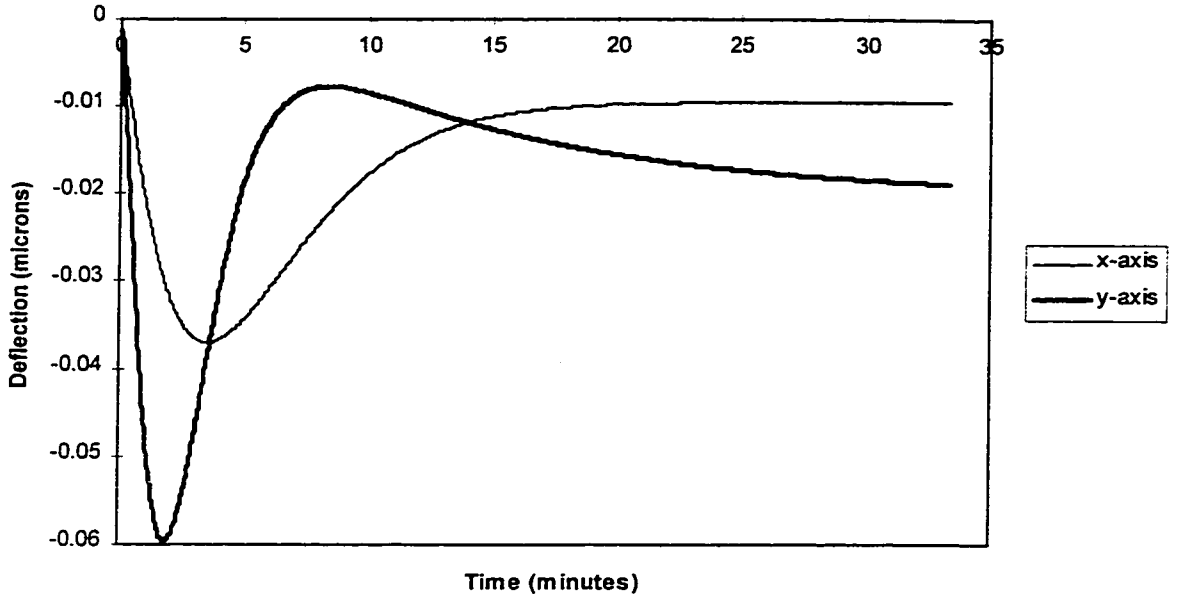

Figure 7.43: Deflection Estimation Error for Q=1.5

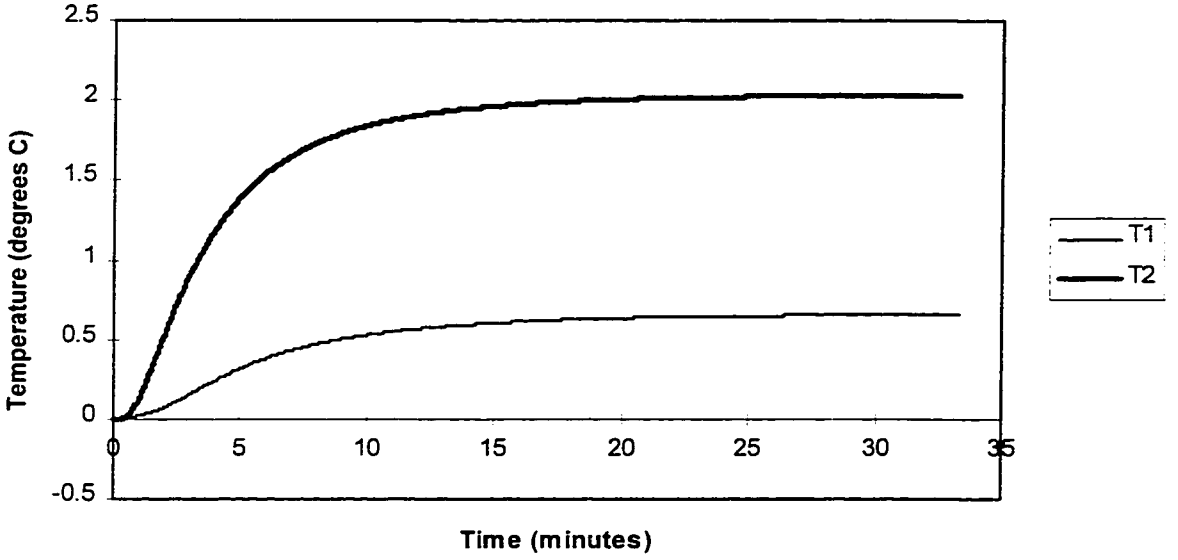

Figure 7.44: Temperature Deviation for Q=3.0

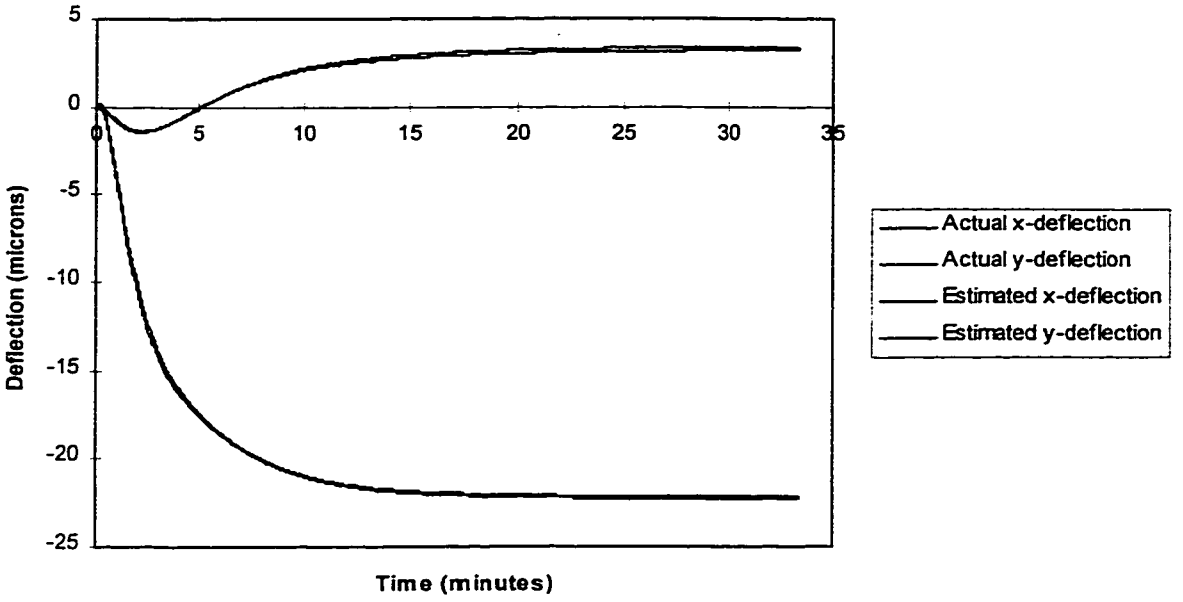

Figure 7.45: Actual and Estimated Nonlinear Deflection for Q=3.0

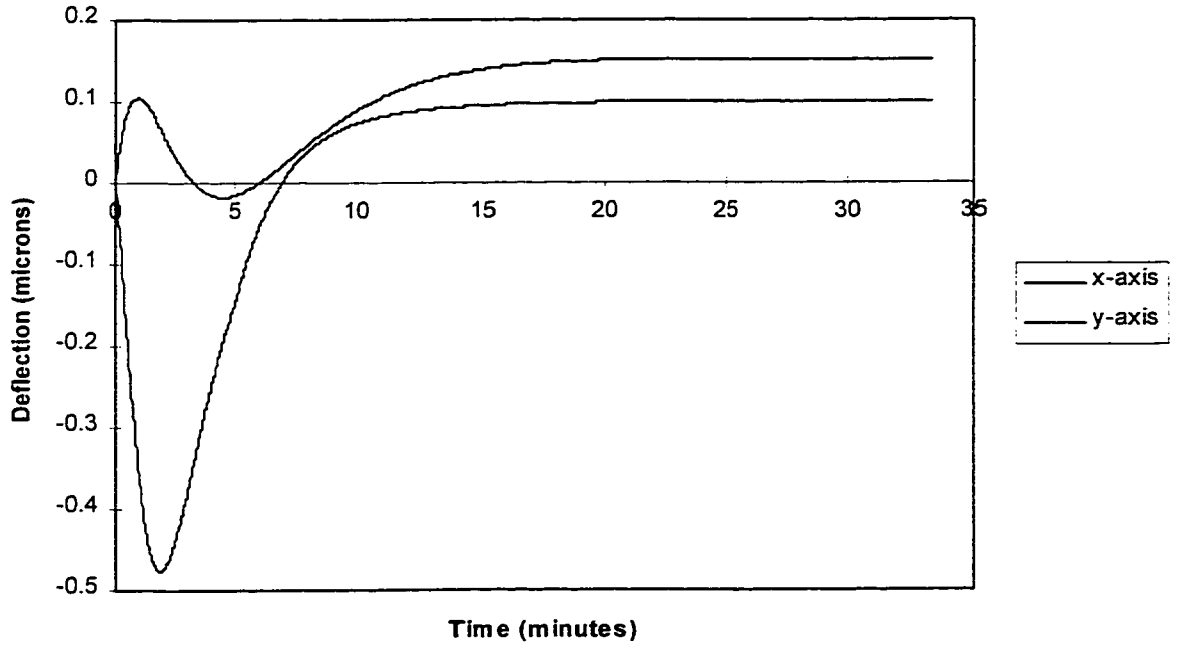

Figure 7.46: Nonlinear Deflection Estimation Error for Q=3.0

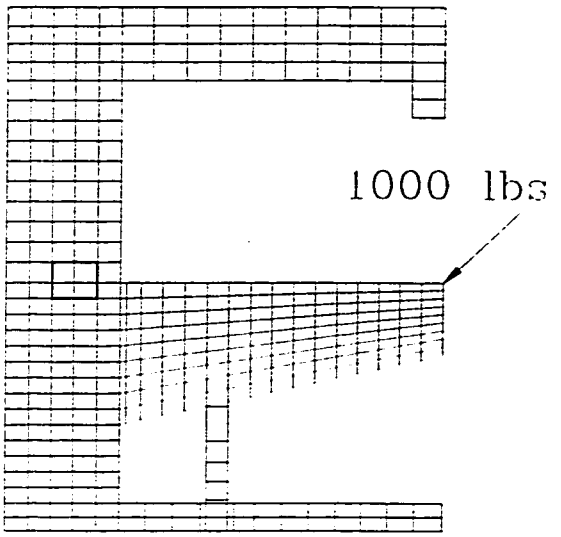

Figure 7.47: Finite Element Test Model indicating the Force Input

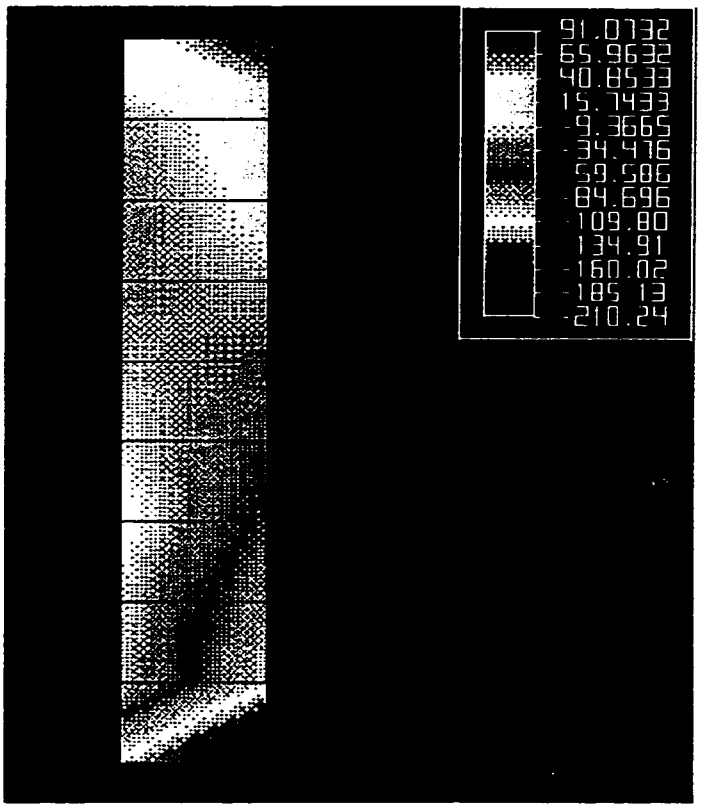

Figure 7.48: Contact Pressure Distribution for Q=2.0 and Constant Force

Figure 7.47 shows the finite-element test model with a constant force of 1000 pounds applied to the end of the table and a step heat input of Q=1.0. The force is equally distributed over the edge of the table, representing, for example, a large work piece mounted at a 45 degree angle relative to the table. Figure 7.48 shows the steady-state contact pressure distribution that results from the force and heat combination. A comparison of figure 7.48 with figure 7.25 shows that large external forces significantly affect the contact pressure distribution. Figure 7.49 shows the temperature deviation at T1 and T2, and Figure 7.50 shows the nonlinear thermal deflection. In the absence of the external force, the nonlinear deflection would have been zero since Q=1.0 is the reference input. However, figure 7.50 shows that the 1000 pound force input induced a nonlinear thermal deflection of more than 3.5 microns. For comparison, the static deflection produced by mechanical deformation from this force is 0.538 microns in the x-direction and 4.84 microns in the y-direction. Thus, the static deflections and the thermoelastic nonlinearity induced into the thermal deflection are on the same order of magnitude. Since the static deflection of the table occurs instantaneously on the application of the force, it does not cause any machining error. The nonlinear thermal deflection is more troubling because the effect is time and load variant, which means that it changes from the time that the piece is loaded and reference points are taken. Figure 7.50 shows the estimated nonlinear deflection along with the actual nonlinear deflection. The curves are so close as to be nearly indistinguishable. Figure 7.51 shows the estimation error, which rises to a maximum of 0.07 microns in the y-direction and 0.02 microns in the x-direction. These results show that the nonlinear model is capable of accurately identifying and estimating the effects of other sources for which no calibration data was available. This result shows the power of combining empirical data with a mathematically correct model of the structure. In the next chapter, the effect of measurement noise on the accuracy and stability of the thermal deflection estimation will be considered

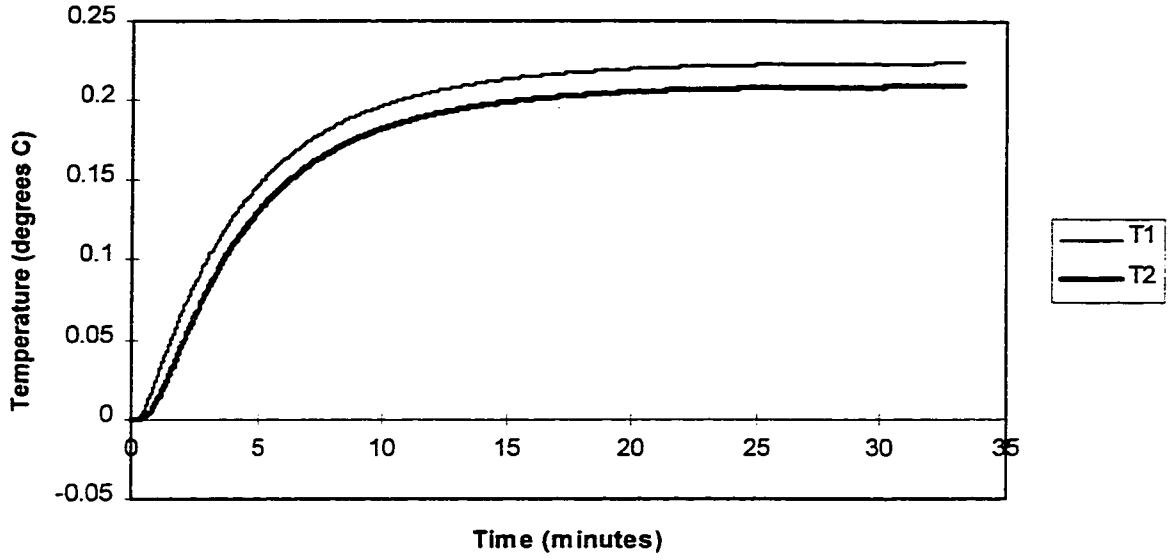

Figure 7.49: Nonlinear Temperature Deviation for Constant Force Input

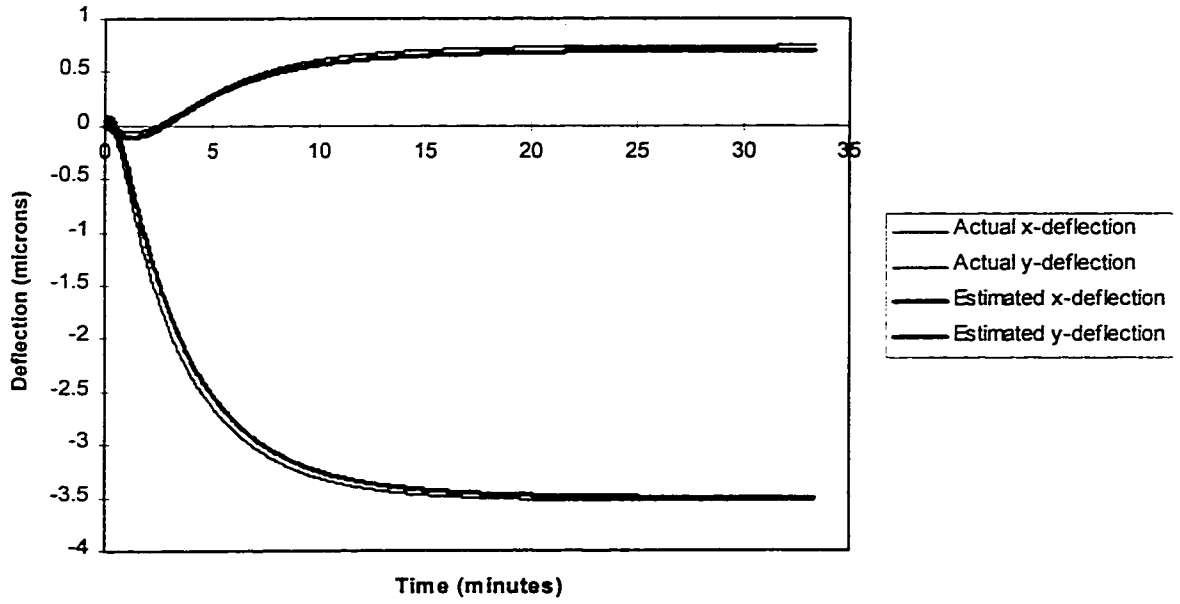

Figure 7.50: Actual and Estimated Thermal Deflection for Constant Force Input, Q=1.0

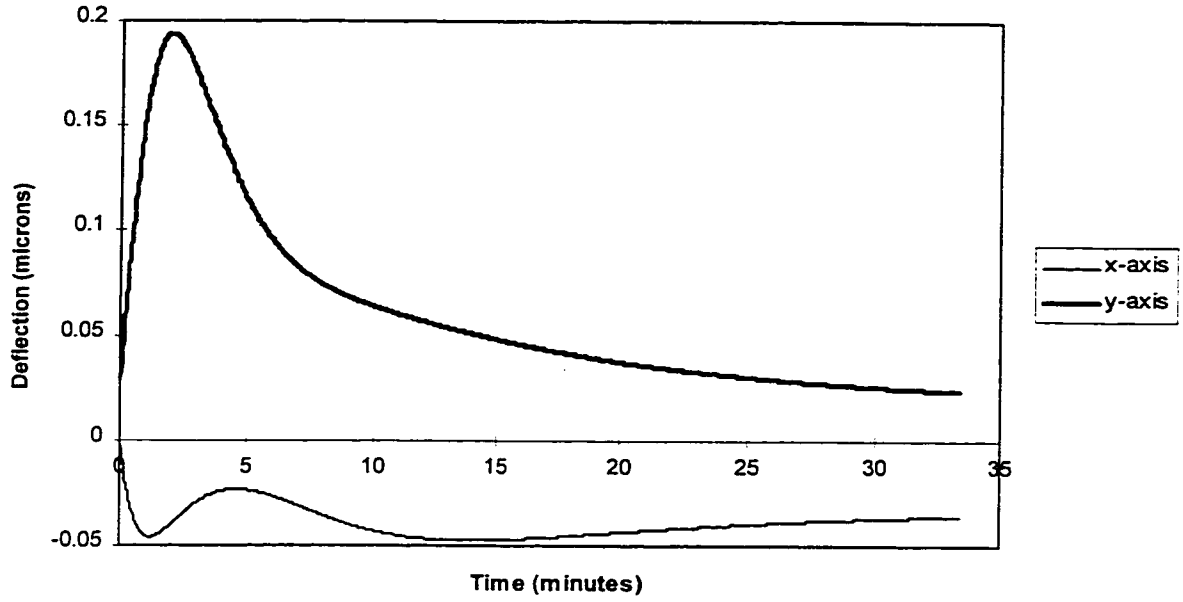

Figure 7.51: Nonlinear Deflection Estimation Error for Constant Force Input, Q=1.0

CHAPTER 8: THE THERMAL DEFLECTION CONTROL SYSTEM

8.1 Introduction

The real-time thermal deflection control system shown described in chapter 3 is comprised of two processes: estimation and compensation. The estimation procedure was demonstrated in chapter 6 for the linear case and in chapter 7 for the non-linear case. What remains to be developed is the position control actuator to compensate for the estimated thermal deflection. The most effective actuation would be achieved by a motor control system, such as would be available for NC type machines. Most commercial NC controllers can be programmed to respond to external signals from the thermal deflection controller. Because of the relatively large time constant of thermally induced error, the dynamics of the motor control are negligible, and so the thermal deflection error is dominated by the estimation error. Many production machines are not NC, and even among NC machines the numerical control is often not implemented on all three axes. For these machines with less than three axis numerical control and where thermal deflection error is a factor on a non-NC axis, some other form of actuation is required, possibly in addition to motor control on the NC axis or axes.

Several non-NC actuation methods have been tested in the literature as discussed in chapter 3. The ideal actuator would achieve acceptable performance at minimal expense and inconvenience, without being bulky or introducing additional compliance to the structure. The most promising method of actuation in terms of cost and convenience is heating and cooling elements placed strategically on the structure. The first disadvantage of heat control elements is that the time constant of the actuator is comparable to the time constant of the track position, which means that the dynamics of the actuators will not be negligible in the control system design. The second disadvantage of heat control elements is that there will inevitably be cross-coupling between the actuators and the adjacent controlled axes. These problems produce a significant decrease in the bandwidth of the closed loop system and a propensity for

overshooting with faster control, which can produce significant control error unless handled carefully.

The best heat control compensator in terms of performance would have capacity for heating and cooling within the range required by the control system, so that the actuator would form a linear system, capable of passing both positive and negative inputs. Although thermoelectric cooling elements are commercially available, the cost and complexity of a cooling actuator is considerably higher than for an actuator which generates positive heating only. A system employing only positive heating would be far more economical and would not require any external heat sink. It would also be inherently non-linear and create additional challenges for the control system designer.

Two compensation approaches will be implemented in this chapter, one based on NC position control, and the other based on positive heating elements alone. Since the NC position control problem is a simple one, the results will be simulation only, implemented on the non-linear machine tool model that was presented in chapter 7. The positive heater compensation will be implemented on the physical model that was presented in chapter 6. The heating elements will be resistance type electric heaters because of their low cost and ease of implementation. The actuation mechanism will be heater control on all three axes, with the control on one axis being zero because of model symmetry.

8.2 Motor Controlled Actuation for NC Machines

Figure 8.1 is a schematic block diagram showing the proposed thermal deflection control system to be implemented on an NC machine tool with three-axis position control. The block labelled G(s) represents the inverse transfer function that was developed and implemented in chapters 5 and 7. The block H(s) represents the thermal deflection transfer function that was developed and implemented in chapters 6 and 7. The estimated thermal deflection δ^e is negated,

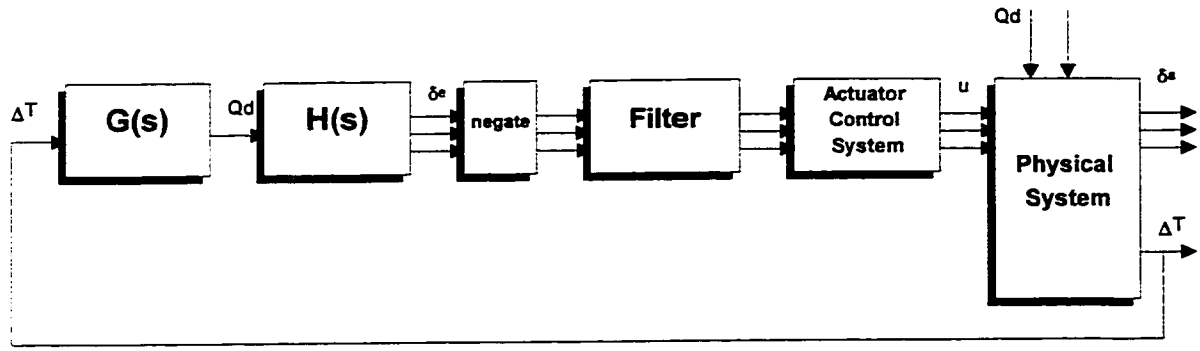

Figure 8.1: Block Diagram of Three-Axis Thermal Deflection Control System with NC actuation

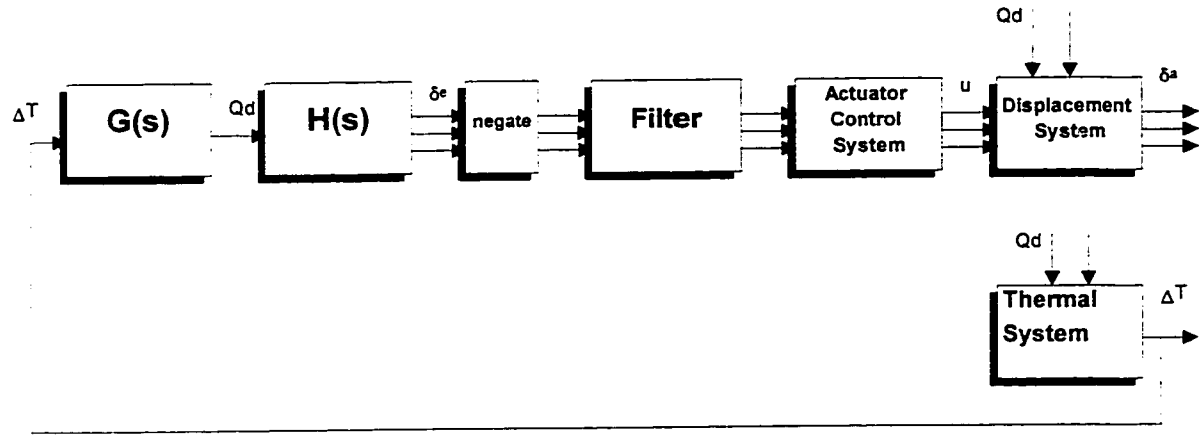

Figure 8.2: Block Diagram of Thermal Deflection Control System with NC Actuation Indicating Open Loop

filtered, and fed into the actuator control system of the NC machine tool. The filter removes high frequency noise that might cause long term damage to the NC drive motors and cause a deterioration in the surface finish of the work. The design of this filter is somewhat arbitrary because the relationship between position control noise and surface finish depends on the feed rate, the type of operation, and the geometry of the cutting tool.

Figure 8.1 shows that there is no direct feedback of the actual position δ^a, only an indirect feedback through the measured temperature difference ΔT, as explained in chapter 3. Since the forward control loop does not introduce any thermal input to the system the measured temperature is unaffected by the feedback, and so the system can be redrawn as an open loop system, as shown in figure 8.2. Furthermore, the dynamics of the NC actuator control system are negligible compared to the dynamics of the estimated thermal deflection δ^e. Thus, for all practical purposes, the control error is equal to the estimation error after filtering, and that is how it will be simulated here.

8.3 The Simulated Test Case for NC Actuator Control Applied to a Nonlinear Machine Structure

Figure 8.3 shows the heat disturbance test input, which was applied to the non-linear machine tool model that is shown in figures 7.10 and 7.11. The input is a triangular pulse with a maximum amplitude of 2.0 and a total duration of 10 minutes. Figure 8.4 shows the resulting non-linear temperature deviation profiles of the measured nodes, determined by the finite-element algorithm developed in chapter 7. This temperature deviation is caused by the system nonlinearity, as explained in chapter 7. Figure 8.5 shows the nonlinear thermal deflection for the same input, calculated by processing the temperature distribution with the thermal deflection finite-element model. The curves in figure 8.5 represent the deflection error that results from system nonlinearity, explained in chapter 7, and the figure also shows the estimated nonlinear deflection, determined by the algorithm that was developed in chapter 7. The performance of the nonlinear estimation algorithm is evaluated by the estimation error, shown in figure 8.6. As

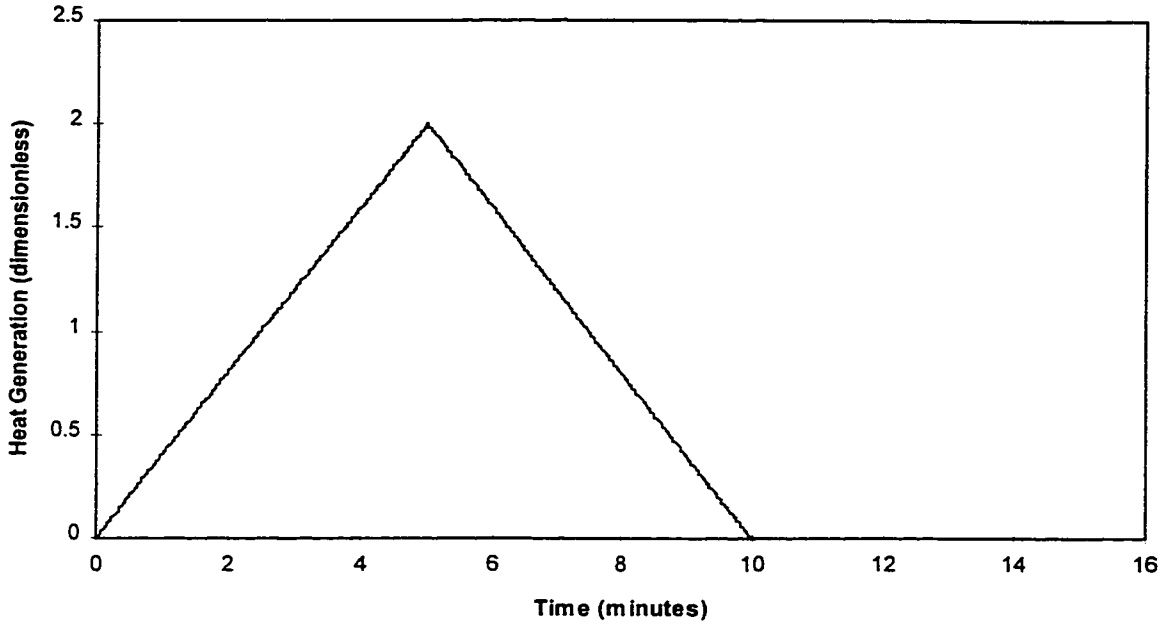

Figure 8.3: Triangular Heat Generation Test Function

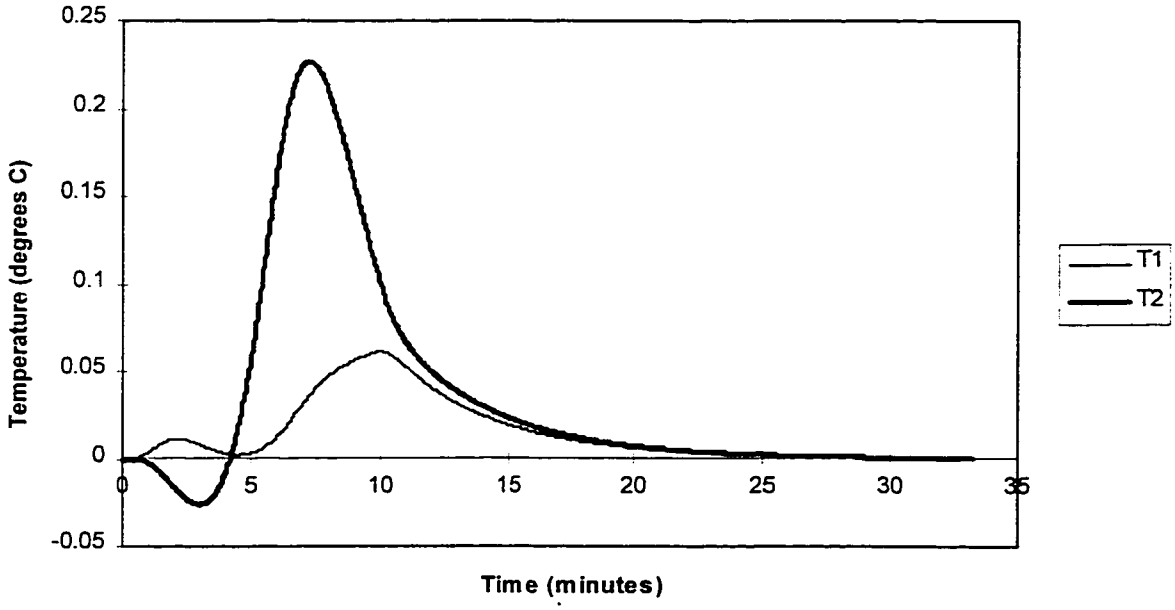

Figure 8.4: Temperature Deviation for Thermal Triangle Input

expected from the verification results of chapter 8, the estimation error is significantly smaller than the actual nonlinear deflection shown in figure 8.5.

The temperature profiles in figure 8.4 are unrealistic because they do not contain any measurement error. In order to better simulate the operation of the control system as it would be employed on an actual machine tool, a simulated measurement error should be superimposed onto the temperature profiles. Measurement noise will be generated from actual temperature measurements taken from the physical model shown in figure 6.1, using a high pass filter to remove the DC bias. Figure 6.5 shows the actual temperature measurement error using thermistor probes on the surface of the real structure, which is filtered and reproduced here as figure 8.7. Figure 8.8 shows the temperature profiles from figure 8.4 with the measurement noise superimposed. Figure 8.9 shows the estimated thermal deflection, determined by processing the temperature profiles with the algorithm that was developed in chapter 7. Figure 8.10 shows that the nonlinear estimation error is contained within the range of ±0.4 microns, while the noiseless estimate in figure 8.6 is within the range ±0.15 microns. This may be somewhat surprising given the fact that the inputs to the estimation algorithm, T1 and T2, do not exceed 0.24 degrees C and 0.07 degrees C respectively, and the range of the temperature noise is about 0.12 degrees C. The reason why the measurement noise is not transmitted to the output is because the thermal deflection system acts as a low pass filter, blocking transient fluctuations in the measured temperature and transmitting only the long term trend.

The position compensation is realized on an NC machine as a sequence of discrete steps, where the minimum resolution is defined by the characteristics of the stepper motor controller. For the purpose of this simulation it will be assumed that the minimum resolution is 0.5 microns. It is apparent from figure 8.10 that the deflection estimate is well filtered so that no further linear filtering is necessary. However it is prudent to implement a hysteresis to prevent rapid switching about a set point. This means for example that when the error exceeds +0.5

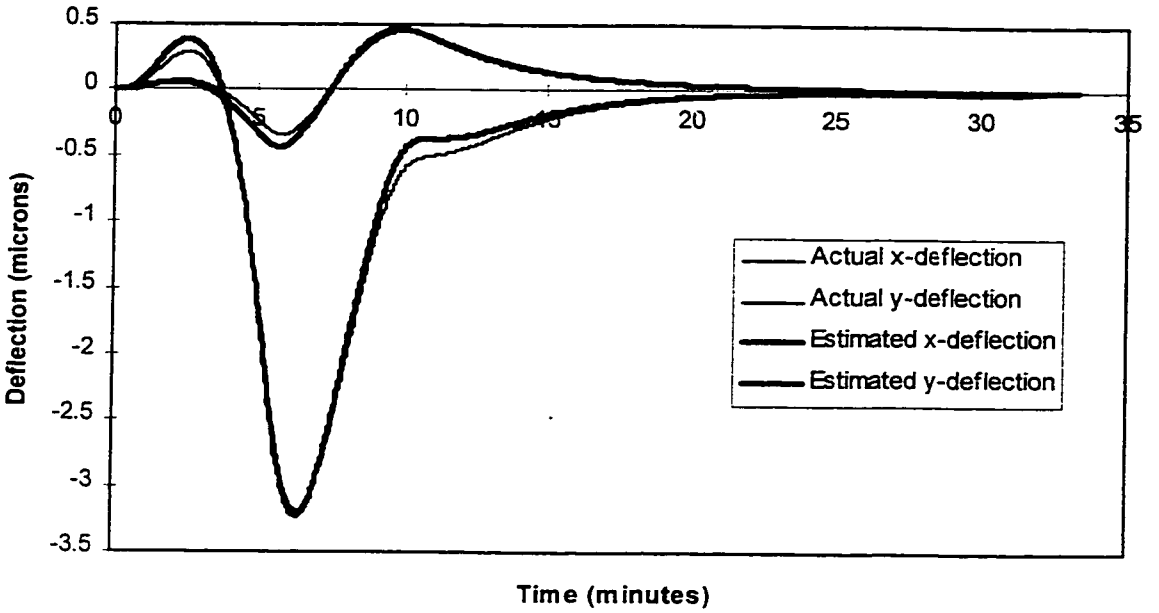

Figure 8.5: Actual and Estimated Nonlinear Deflection for Trianglular Heat Input

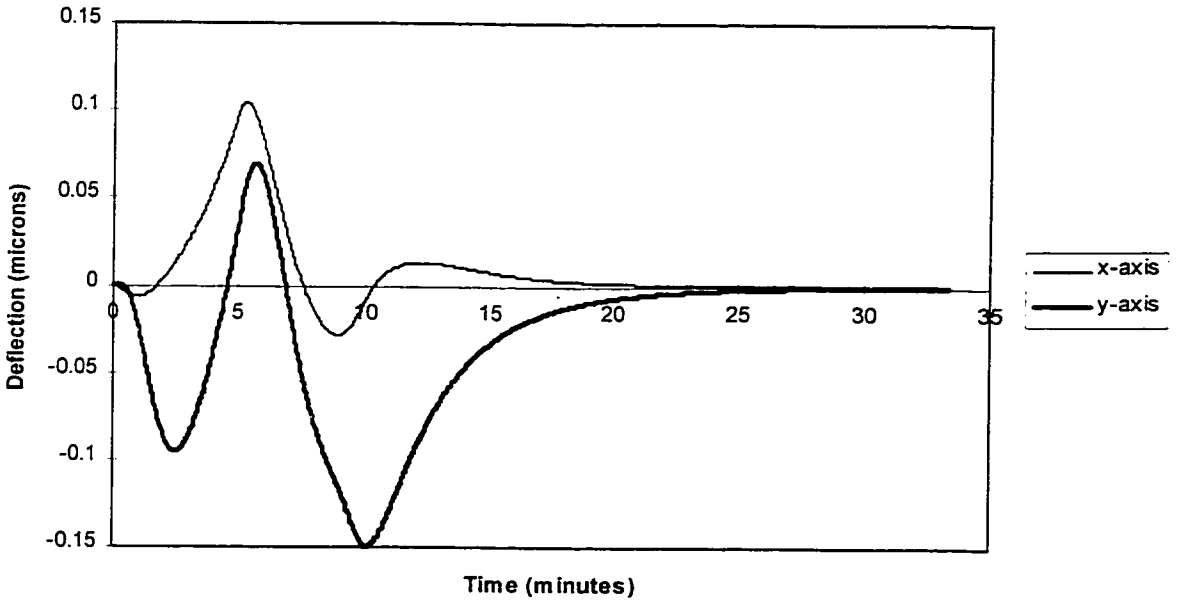

Figure 8.6: Nonlinear Deflection Estimation Error for Triangular Heat Input

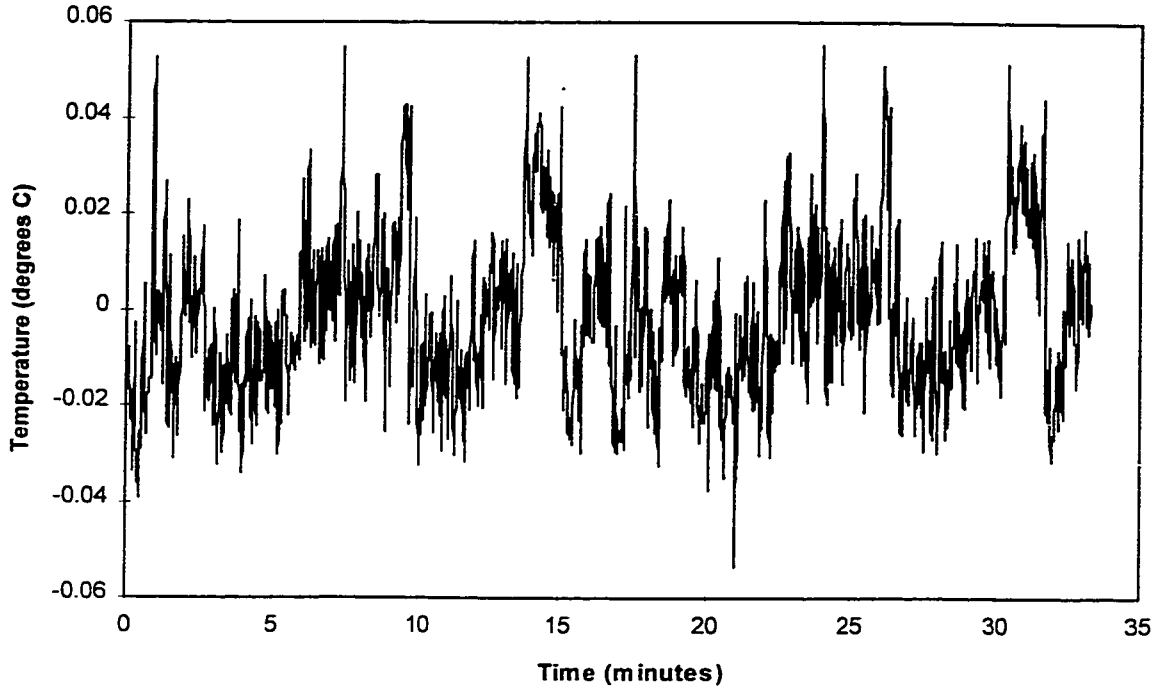

Figure 8.7: Temperature Measurement Noise for a Thermistor Probe

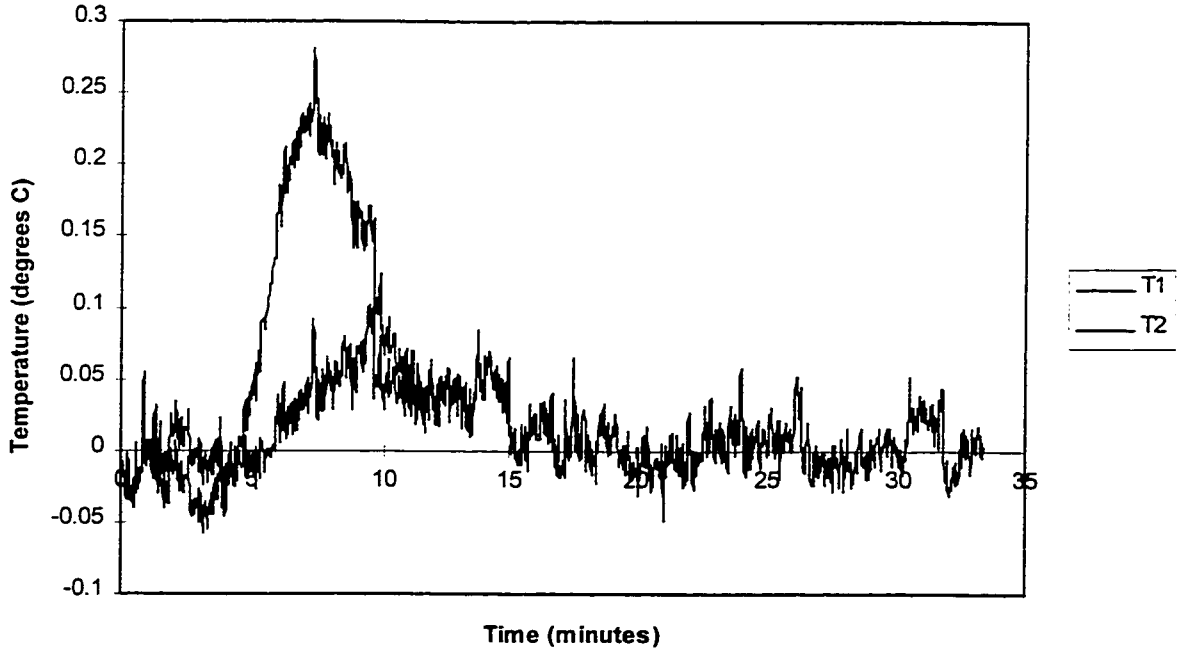

Figure 8.8: Nonlinear Temperature Deviation with Superimposed Measurement Noise

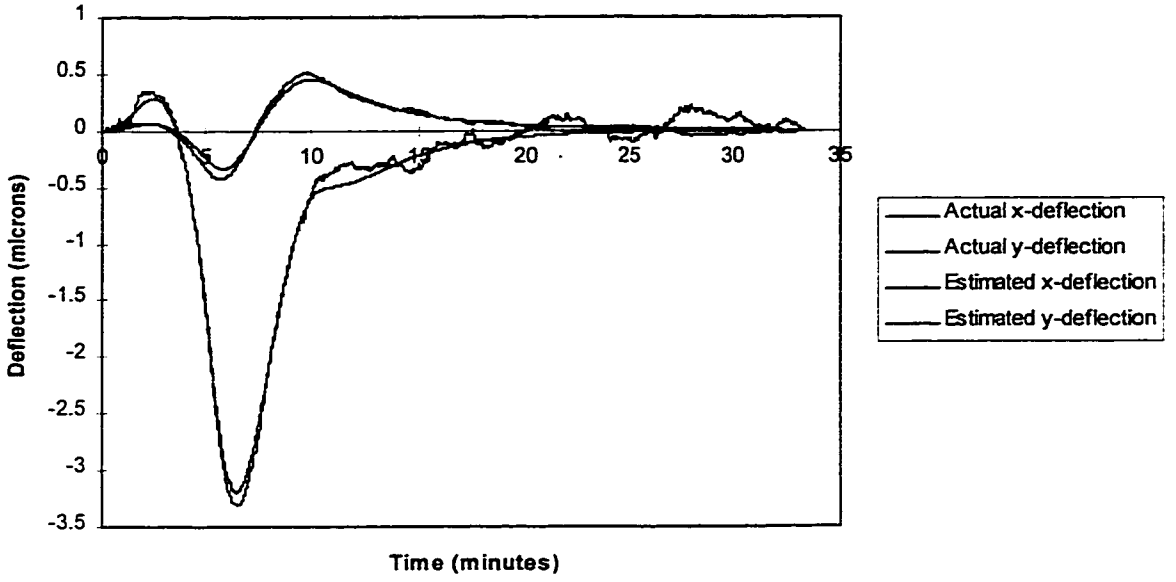

Figure 8.9: Actual And Estimated Nonlinear Deflection Incorporating Simulated Temperature Measurement Noise

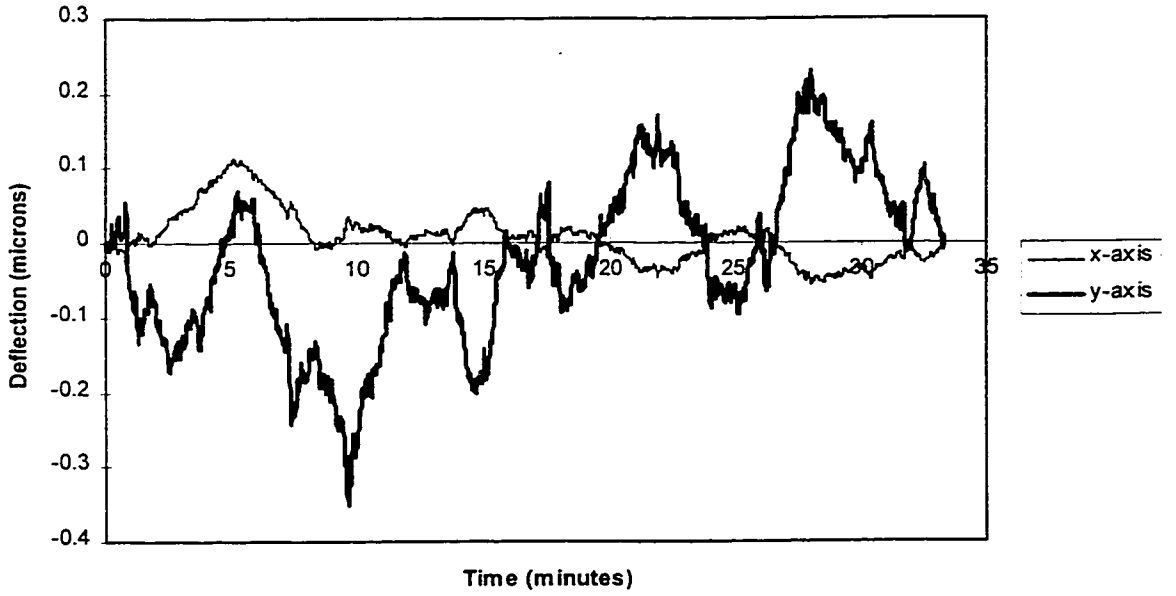

Figure 8.10: Nonlinear Deflection Estimate Error Incorporating Simulated Temperature Measurement Noise

microns the NC controller will move -0.5 microns, but will not reposition again until the error is ±0.5 microns from the new set point. Figure 8.11 shows the thermal deflection error after compensation by the NC controller, which is always within a range of +0.6 μm to -0.5 μm.

8.4 Actuation Using Resistance Electric Heaters on a Linear Physical Model

The advantage of heater compensation is that it can be used to control non-NC machine tool axes without any complicated or expensive additional apparatus. The problems derive from the short bandwidth of the compensation transfer functions and the cross-coupling between controlled axes. As a consequence, not all machine tools can be compensated using heating elements, and in others the compensation is not very effective, even assuming ideal conditions.

As an example of heater control, consider the columnar structure shown in figure 8.12a, which might represent an industrial turning machine. The position of point x can be shifted to the right by the application of heat to Q1, or to the left by the application of heat to Q2. The application of equal heating to Q1 and Q2 would produce a positive deflection along the axis of the column. However, no combination of heating will produce a significant negative deflection along the axis of the column for these heaters or for any other heater positions. Hence, positive heating actuation could not be used to control the thermal deflection along the columnar axis of this structure. Now consider figure 8.12b, which has the configuration of an overhead milling machine or a press drilling machine. The application of heat to Q1 would deflect point b along the negative y-axis and the application of heat to Q2 would deflect point b along the positive y-axis. Both heaters will also produce deflection along the positive x-axis. The effect of Q3 and Q4 is similar to Q1 and Q2, except that the deflection primarily affects point a instead of point b. If the controlled variable is the relative displacement of point a to point b, then both positive and negative displacements are possible along the x and y axes. However the fact that the heaters produce deflection along more than one axis implies a coupled

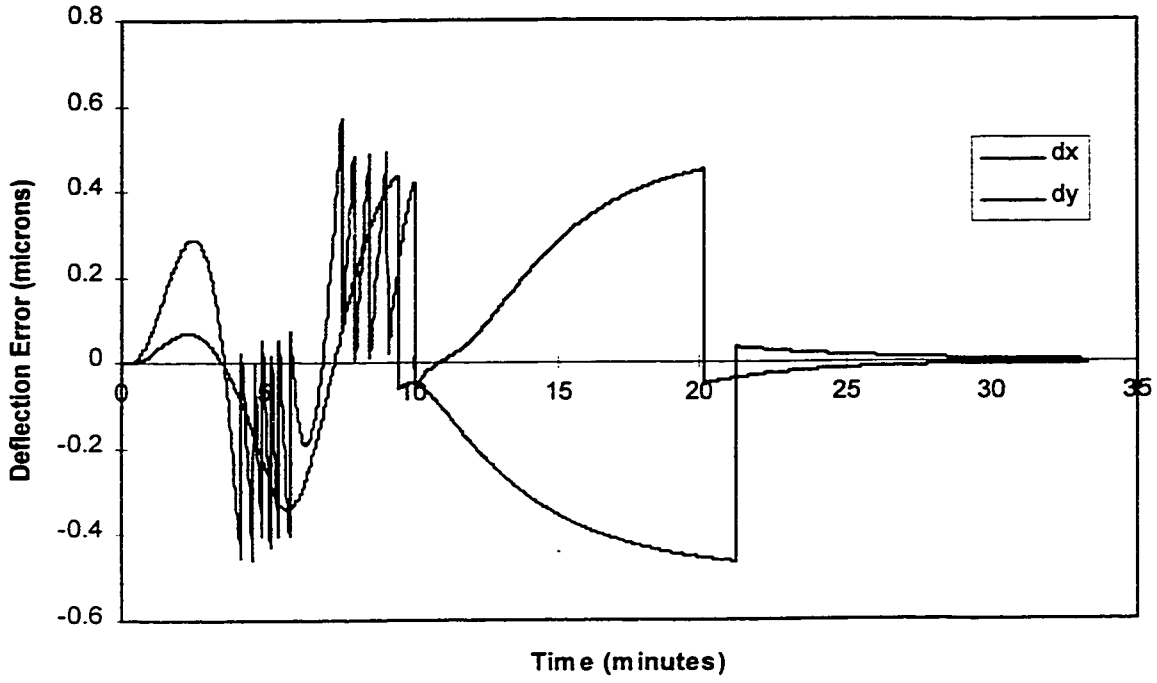

Figure 8.11: The Compensated Deflection Error

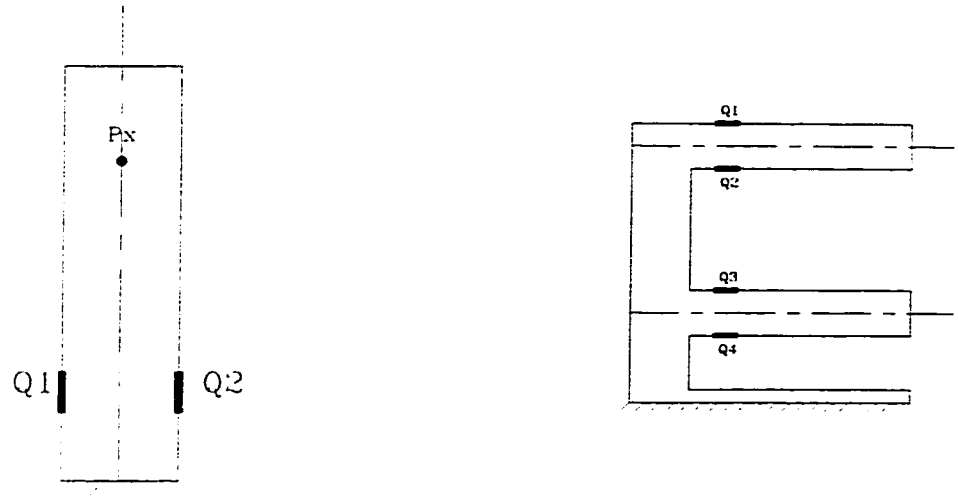

Figure 8.12: Schematic of (a) columnar structure, and (b) milling machine type structure

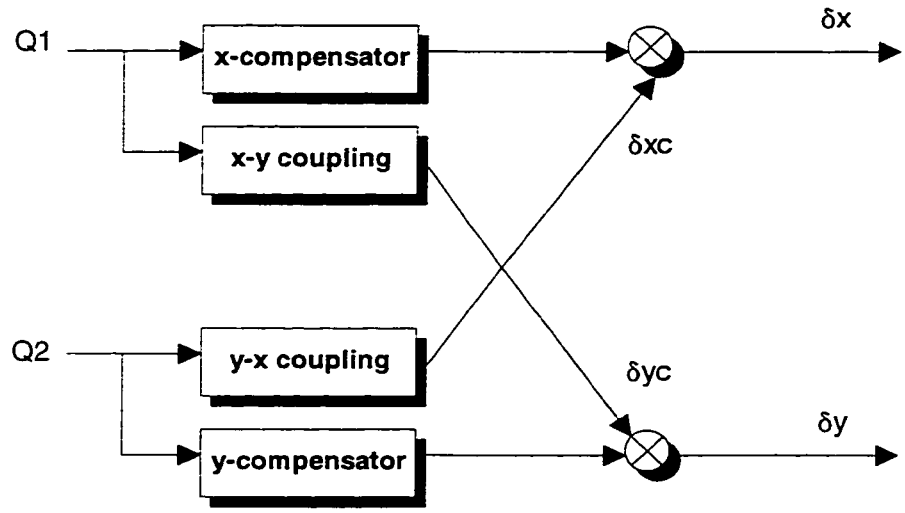

Figure 8.13: Block Diagram of Two-Axis Control System Illustrating the Effect of Coupling

system, and as a consequence for some geometries it may not be possible to control more than one axis at the same time.

Figure 8.13 shows a schematic example of a two-axis system with coupling. Assume for the moment that it is only the x-axis that is being controlled by heater Q1, and assume that for any desired deflection δ_x there is a corresponding steady-state value of Q1. Under these circumstances, the proper value of Q1 will achieve the desired δ_x, but will also produce a non-zero δ^c_y in the process. Now, if the y-axis must also be kept under control then the disturbance δ^c_y that was produced by Q1 must be compensated by the proper heat applied to Q2, which will in turn produce a disturbance deflection δ^c_x that must be compensated by Q1. This is an intuitive process only, but it illustrates how the coupling of the systems affects the heating values. If $\delta^c_x<\delta_x$ then there exists a combination of Q1 and Q2 which will produce the desired control on both axes, however in general the steady-state Q1 and Q2 values will be considerably larger than they would be for the case without coupling between the axes. If $\delta^c_x>\delta_x$ then there is no finite combination of Q1 and Q2 that will produce the desired position.

The above example shows that multi-axis heater compensation is geometry dependant, and is not suitable for all machine tool configurations. Furthermore, the transfer functions of the thermal deflection response have a very short bandwidth that results in slow tracking. The problems associated with heater actuation will be explained in greater detail in subsequent sections of this chapter, however it is worth stating at this point that heater actuation by itself is not recommended as a practical solution for the general case of multi-axis control. Heater actuation is best suited to supplement some other form of actuation, such as using NC position control on one or two axes, and then using heater compensation on the remaining axis or axes that do not have NC control.

In order to fully explore the potential and the limitations of heater actuation, the test cases that follow will employ two-axis position control using heating elements only. It must be pointed out that this is the most extreme case, and not necessarily the most suitable application for heat actuation elements.

8.5 Compensation Using Full-State Feedback on a Linear Physical Model

8.5.1 Control System Design Using the State Feedback Approach

Figure 8.14 shows a block diagram of the position control system using electric heater compensation and a full state feedback model. In figure 8.14, the estimated disturbance thermal deflection δ_d is estimated in the usual way from the inverse transfer function G(s) and the direct thermal deflection transfer function H(s). Figure 8.15 shows the state model portion of the control system, where δ_d is the disturbance deflection to be tracked by the control heaters and δ_e is the estimated controlled deflection. Figure 8.15 is a graphical representation of the state feedback system [105]:

$$\begin{aligned} \dot{x} &= Ax + Bu \\ \delta_e &= Cx \end{aligned} \tag{8.1}$$

where:

$$u = K(N_x \delta_d - x) + N_u \delta_d \tag{8.2}$$

The matrices A and B and C are defined by the thermal deflection transfer functions of the control heaters. The matrices N_x and N_u are defined by the equation [105]:

$$\begin{bmatrix} N_x \\ N_u \end{bmatrix} = \begin{bmatrix} A-I & B \\ C & 0 \end{bmatrix}^{-1} \begin{bmatrix} 0 \\ I \end{bmatrix} \tag{8.3}$$

The selection of feedback gain matrix K is used to manipulate the dynamics of the closed loop system. The advantage of the state-space formulation over the classical methods of cascade and feedback compensation is that it allows the poles of the closed loop system to be placed arbitrarily. This gives the designer more control over the dynamics of the closed loop system, however there are still significant limitations in the performance that can be achieved for a given

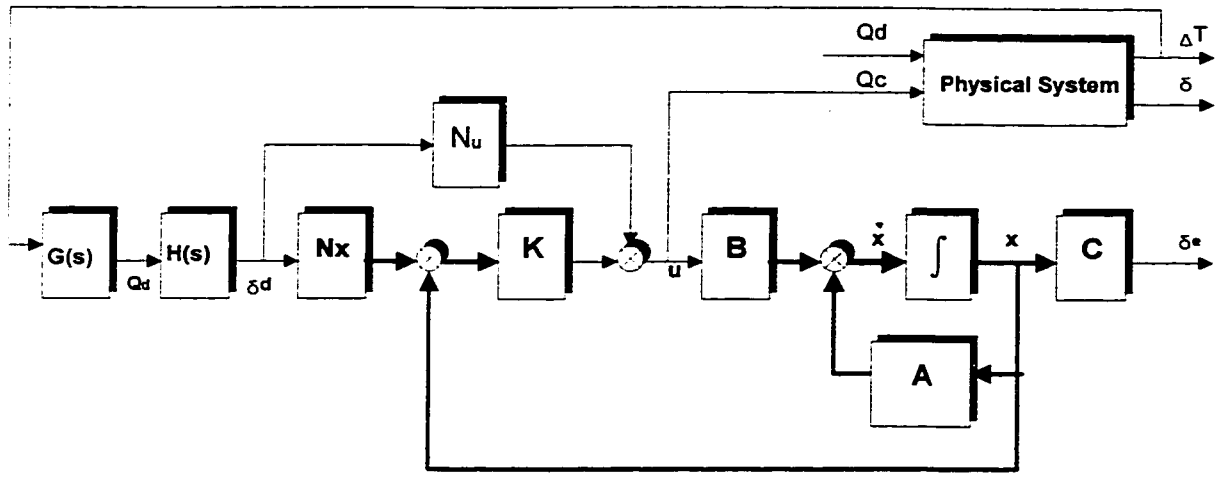

Figure 8.14: Schematic Block Diagram of Position Control System Using Electric Heater Compensation and a State Feedback Model

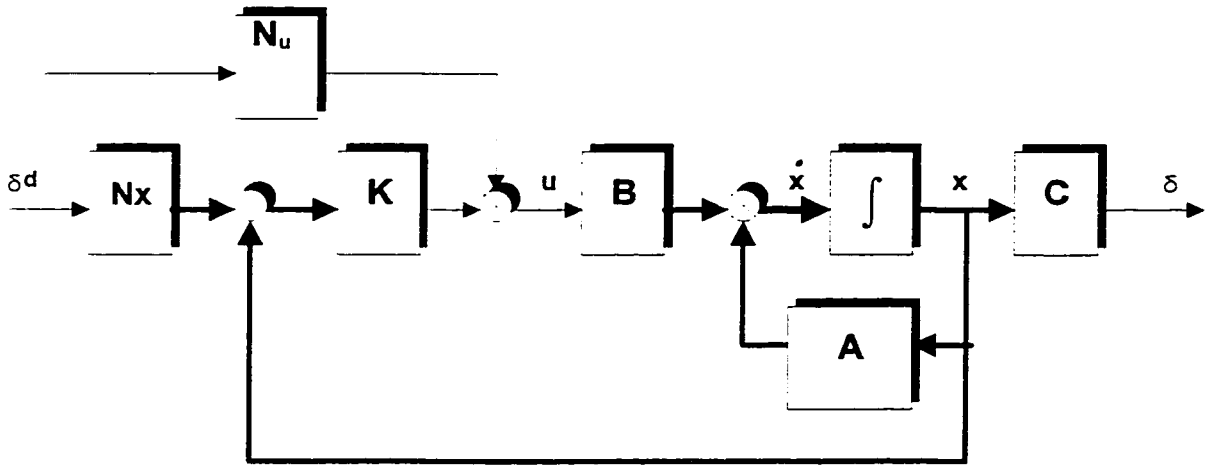

Figure 8.15: State Model Portion of Position Control System with Electric Heater Actuation

system. One important limitation for the designer is that state feedback cannot be used to influence the zeros of the closed loop system. From a physical standpoint this means that in some systems it is not possible to bring all of the states to zero in an arbitrarily short period of time without introducing an overshoot in the step response. In general the overshoot to a step input increases toward infinity as the largest time constant of the closed system approaches zero. Another important limitation is the saturation magnitude of the control actuator, which imposes practical limits on the speed of the response.

An important tool to aid in selecting closed loop pole locations is the theory of linear quadratic regulator (LQR) steady-state optimal control. The basis of optimal control is the minimization of a cost function:

$$\Upsilon = \int_0^\infty x^T Q_1 x + u^T Q_2 u \, dt \tag{8.4}$$

for a continuous system. In the case of the discrete system:

$$\begin{aligned} x_{(k+1)} &= \Phi x_{(k)} + \Gamma u_{(k)} \\ \delta_{e(k)} &= H x_{(k)} \end{aligned} \tag{8.5}$$

the discrete cost function is:

$$\Upsilon = \sum_{k=0}^{\infty} \left\{ x_{(k)}^T Q_1 x_{(k)} + u_{(k)}^T Q_2 u_{(k)} \right\} \tag{8.6}$$

The minimization of equation (8.6) is a constrained-minima problem which can be solved by the method of Lagrange multipliers [105]. The solution is obtained by the method of eigenvector decomposition of the system matrix, called the Hamiltonian matrix. The numerical solution for a given system can be obtained using control system software such as Matlab, CC, Matrix$_x$, or CTRL-C. In this thesis the Matlab software package will be used to obtain numerical solutions to the LQR problem.

The use of optimization methods in the development of the LQR design method is somewhat misleading since there is no single optimal solution. The 'optimal' solution that is determined by the LQR procedure depends on the weight matrices Q_1 and Q_2. The matrix Q_1 is the matrix of weights associated with each of the states of the system, and Q_2 is the matrix of weights associated with each of the inputs. The objective of the LQR procedure is to minimize the activity of the states when the system is subject to an initial condition, while at the same time minimizing the use of control effort. The relative weight that is given to the activity of each of the states and each control actuator is determined by the entries of the weight matrices. If Q_1 and Q_2 are diagonal matrices with only positive diagonal entries, then the cost function reduces to a sum of the square of each state and each control input, with the weight of each quadratic term given by the corresponding diagonal entry. It is this form that shall be used in the procedure that follows.

When selecting the weights for each state and control input it is important to consider the relative contribution of each state and control input. For example, suppose that there are two control inputs u_1 and u_2, and that the maximum allowable value of u_1 is 100 Newtons and the maximum allowable value of u_2 is 10 Nm. If equal weight is given to u_1 and u_2 then the optimal solution will tend to keep both inputs within the same range, which would either be too large for u_2 or else too narrow a range for u_1. The same is true for the states of the system, since some states might normally fluctuate in a large range while others are naturally contained within a narrow operating range. Bryson and Ho [106] suggest a procedure which ensures that the states enter the cost via the important outputs. According to this procedure the weight matrices are defined by:

$$Q_1 = H^T \overline{Q_1} H \tag{8.7}$$

and the diagonal entries of the Q_1 and Q_2 matrices are:

$$\begin{aligned} \overline{Q}1_{11} &= \frac{1}{m_1^2} \qquad & Q2_{11} &= \frac{1}{n_1^2} \\ \overline{Q}1_{22} &= \frac{1}{m_2^2} \qquad & Q2_{22} &= \frac{1}{n_2^2} \\ \overline{Q}1_{33} &= \frac{1}{m_3^2} \end{aligned} \tag{8.8}$$

where m_i is the maximum value for state x_i for a step input, and n_j is the maximum allowable value for input j. By following this procedure the weight that is allocated to a given state is the same as the weight that is allocated by the system output matrix H, and the weights are scaled according to the maximum amplitude of the state or input. In order to give a certain amount of flexibility in the design, two variable parameters are introduced into the procedure. The first variable is a constant ρ which defines the ratio between the weight allocated to the state error and the weight allocated to the use of control effort. This variable is introduced into equation (8.6), modifying it as follows:

$$\Upsilon = \sum_{k=0}^{\infty} \left\{ \rho x_{(k)}^T Q_1 x_{(k)} + u_{(k)}^T Q_2 u_{(k)} \right\} \tag{8.9}$$

The second variable is the constant α which is used to modify equation (8.5) as follows:

$$\begin{aligned} x_{(k+1)} &= \alpha \Phi x_{(k)} + \alpha \Gamma u_{(k)} \\ \delta_{e(k)} &= H x_{(k)} \end{aligned} \tag{8.10}$$

The effect of α is to apply 'pincers' around the discrete poles of the closed loop system, which has the effect of reducing the settling time at the expense of control effort [105]. It is by manipulating the variables α and ρ that the 'optimal' solution may be tailored to best satisfy the design requirements. For the designs and simulations that follow, the continuous system $[A_s]$, $[B_s]$, $[C_s]$, shall be transformed into its discrete equivalent $[\Phi_s]$, $[\Gamma_s]$, $[H_s]$, using a zero order sampling period of 0.7 seconds. Since the zero order sampling period is very much smaller than the time constants of the system, the practical difference between the continuous system and the discrete system is almost negligible.

8.5.2 Implementation of the LQR Optimal Solution

Figure 8.16 is a schematic diagram showing the proposed locations for the controlled heat sources. The deflection of the structure is measured as the difference between points a and b, shown in the figure, as explained in chapter 6. Heat source q1 is comprised of one 3x8 inch pad with a 330W heat capacity, and q2 is comprised of two symmetric 3x5 inch pads with a total of 165W heat capacity. The q2 heat pads are symmetric about the plane of the paper in figure 8.16. The heat source q1 primarily produces negative deflection along the y-axis by bending the edge of the overarm downwards, and q2 primarily produces negative deflection along the x-axis by causing the table to elongate in the x-direction. Figure 8.17 shows the calibrated deflection along the x-axis (dx) and the deflection along the y-axis (dy) for a step input of 330W to q1, which shall be non-dimensionalized to q1=0.72. Figure 8.18 shows the calibrated deflection along the X and Y axes for a step input of 165W to q2, which shall be non-dimensionalized to q2=0.72. The calibration was done using the fourth order linear model in equation (6.16). The transfer functions shall be designated by H_x^1, H_x^2, H_y^1, and H_y^2, where the superscript indicates either q1 or q2 and the subscript indicates the X or Y axis. The continuous state-space system shall be designated as $[A_s]$, $[B_s]$, and $[C_s]$. The figures show that q1 primarily causes negative deflection in X and q2 primarily causes deflection in Y, as expected. The figures also show the coupling between the axes since q1 produces a deflection in the y-direction and q2 produces a deflection in the x-direction. Since the coupled deflections are both negative and the disturbance step responses in X and Y are positive (see chapter 7) one might anticipate that this cross-coupling could improve the performance of the control system. The reasoning here is that when q1 is used to compensate for the positive disturbance in Y, the secondary deflection in X will tend to reduce the disturbance deflection in the x-direction, which is positive also.

By looking at various combinations of α and ρ, the best possible compromise was found to be α=0.7 and $\rho=10^{-11}$. Figure 8.19 shows the simulated closed loop x-axis step response, and figure 8.20 shows the simulated closed loop y-axis step response of the control system that is

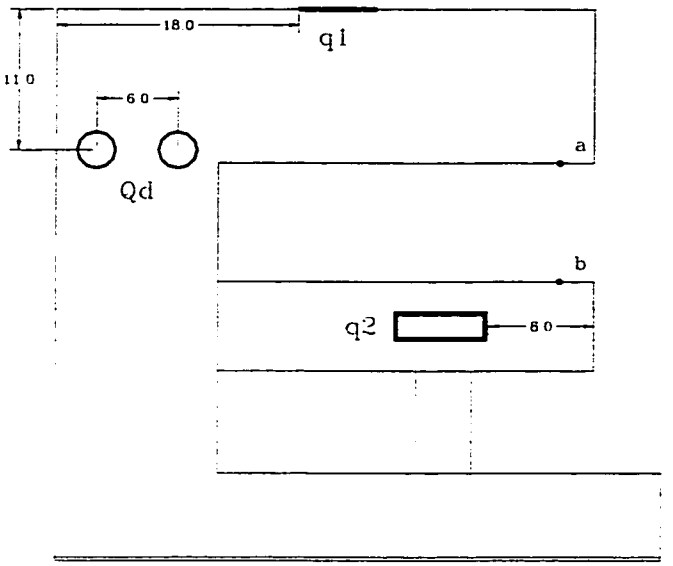

Figure 8.16: Schematic Diagram of Test Model Showing Locations of Heater Actuators

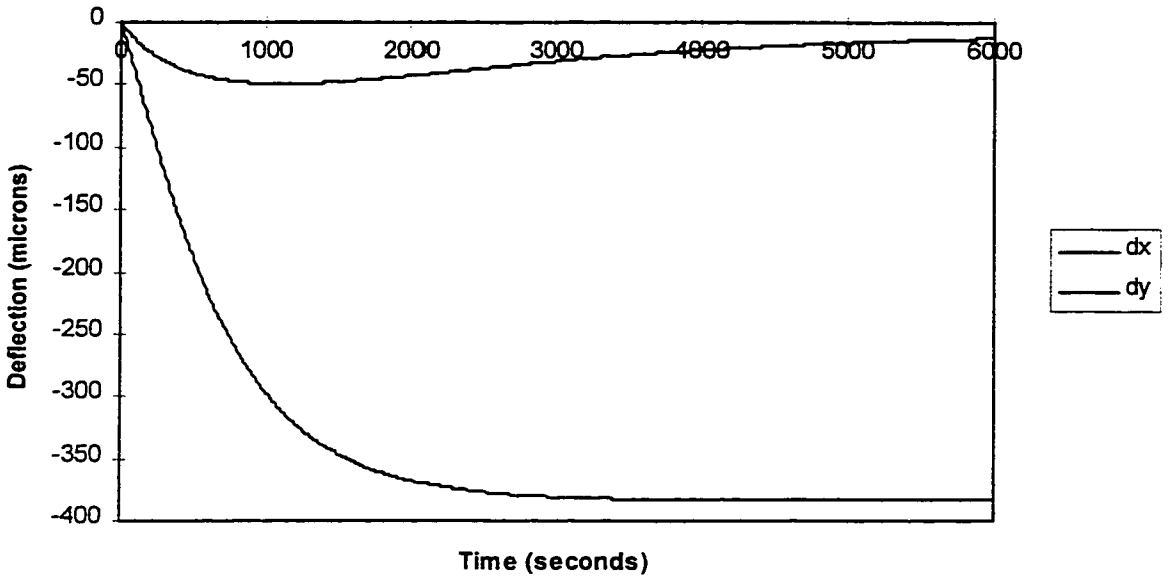

Figure 8.17: Calibrated Deflections in X andY for Unit Step Input to q1

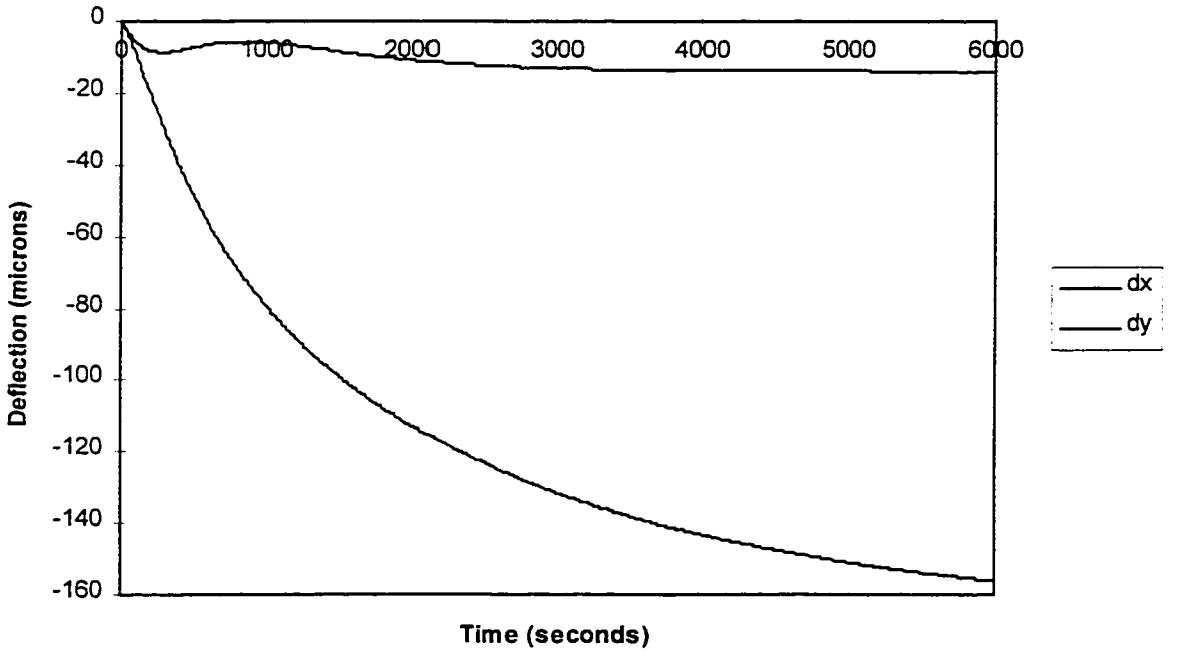

Figure 8.18: Calibrated Deflections in X and Y for Unit Step Input to q2

obtained from these values. The figures show how the feedback controller decouples the system by bringing the secondary deflections to zero in the steady-state. The obvious problem with these step responses is the time constant, which is estimated to be 30 minutes for the primary deflection from q1 and 17 minutes for the primary deflection from q2. The problem is that the time constants cannot be reduced any further without introducing an unacceptable overshoot in the step response. Figures 8.21 and 8.22 show the simulated step responses for q1 and q2 respectively for the feedback system designed with α=0.7 and $\rho=10^{-10}$. Figure 8.22 shows that the overshoot has increased from 20% to 130% while only reducing the time constant of the q1 response slightly. It has been established through trial and error that the system shown in figures 8.19 and 8.20 are about the best compromise between speed of response and overshoot that is possible for this type of controller. Figure 8.23 shows the response of the control system for a more realistic input, which is the simulated disturbance thermal deflection unit step response, shown in figures 6.21 and 6.22. It is clear from figure 8.23 that there is a considerable discrepancy between the desired control output and the actual control output. Figure 8.24 shows the difference between these two curves, which is the simulated error of the controlled system. The control system has reduced the thermal deflection error from a range of 0-250 microns to a range of -110 to 55 microns. It is clear from these simulated results that this type of control system is inadequate to achieve sufficient accuracy to meet the objectives of this thesis, and so a different type of control system will have to be explored.

The problem with the LQR approach that was just described is that the objective is to bring all of the states of the system to zero within as short a time as possible. Figure 8.25 shows the pole-zero map of the uncontrolled system transformed to continuous time, and figure 8.26 shows the pole zero map of the controlled system, also transformed to continuous time and designed with α=0.7 and $\rho=10^{-10}$. The figures show that the effect of the state feedback control is to move the dominant poles of the system away from the imaginary axis, reducing the settling time of the system. The figures also show that the poles are generally moving away from the

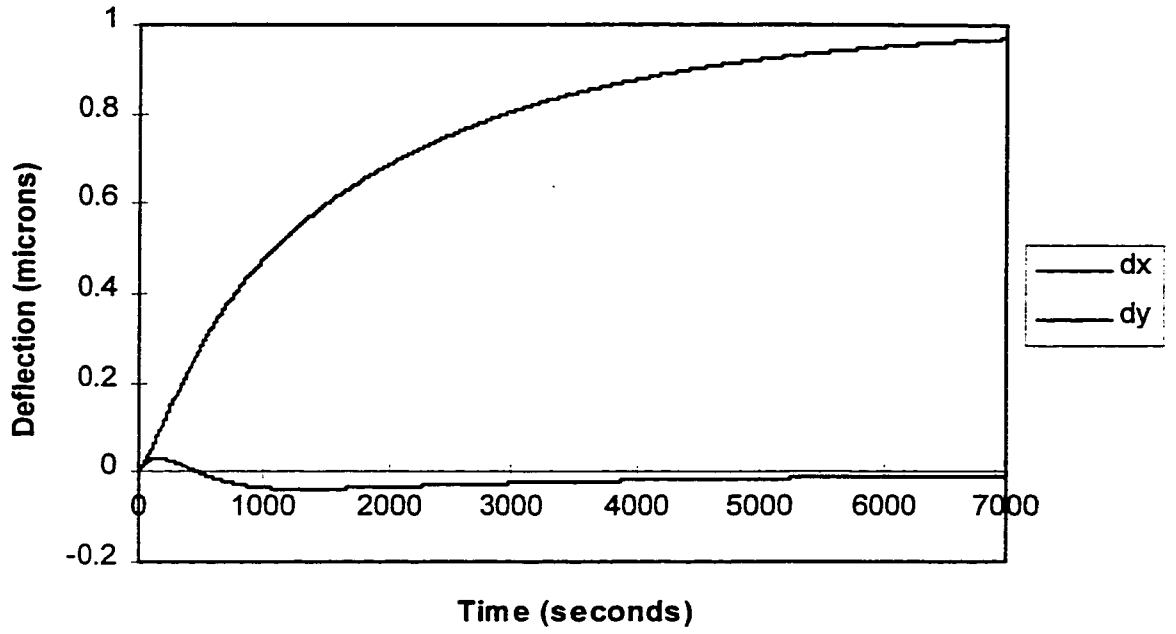

Figure 8.19: Simulated q1 Unit Step Response of LQR system, Parameter Case 1

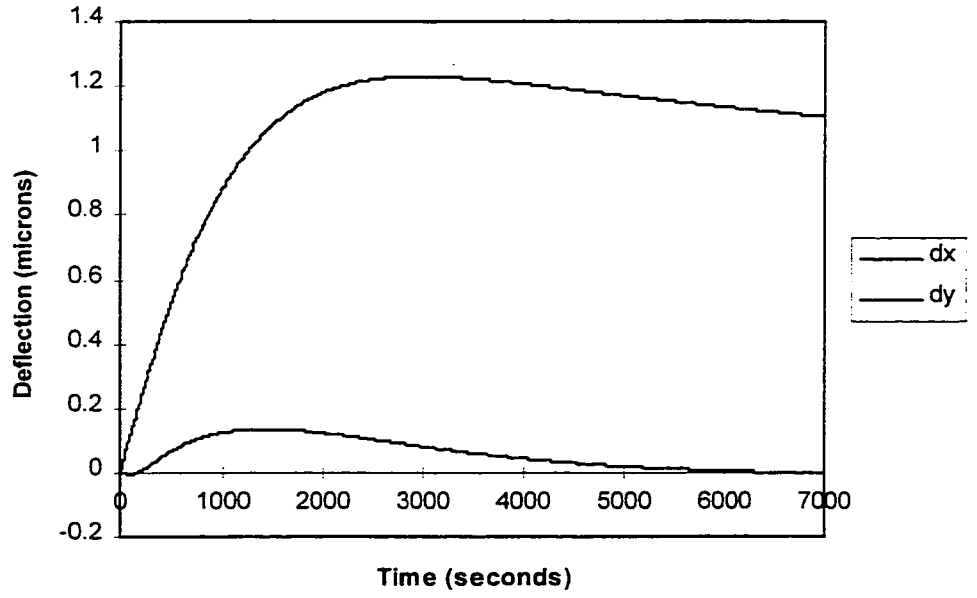

Figure 8.20: Simulated q2 Unit Step Response of LQR System, Parameter Case 1

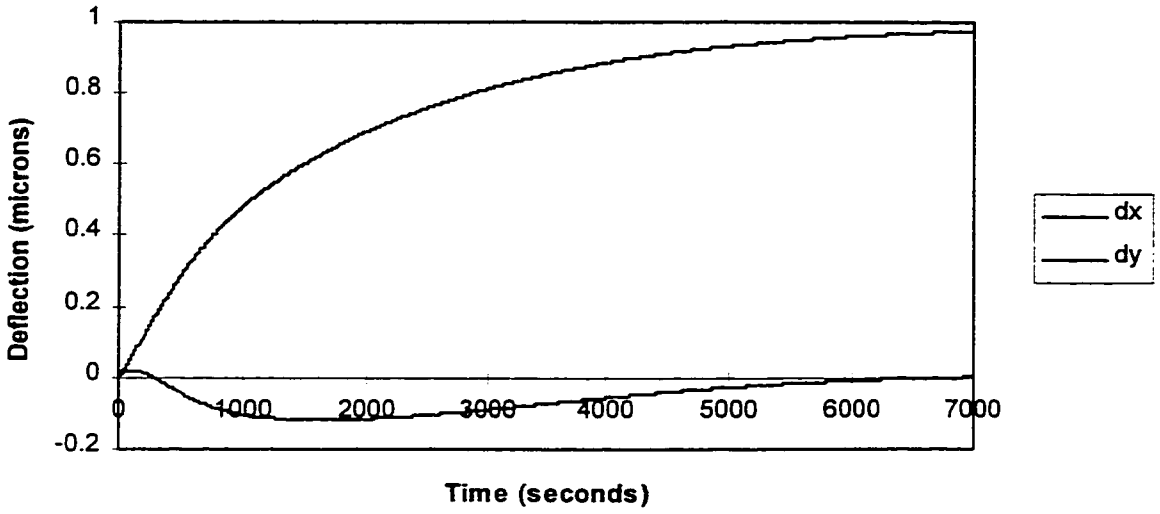

Figure 8.21: Simulated q1 Unit Step Response of LQR system, Parameter Case 2

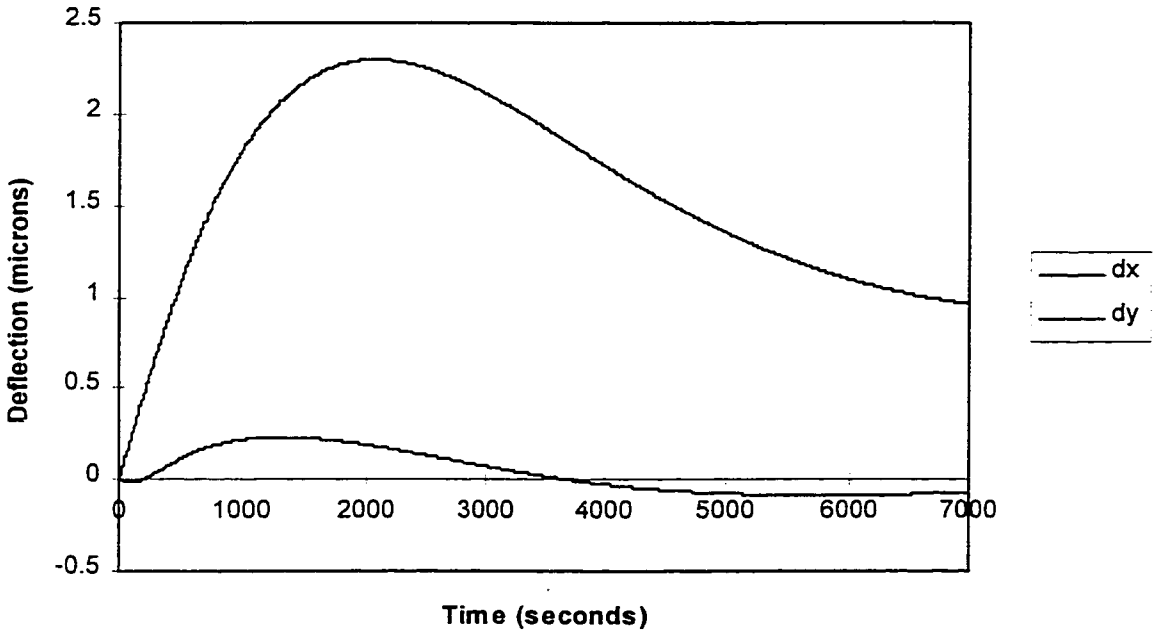

Figure 8.22: Simulated q2 Unit Step Response of LQR System, Parameter Case 2

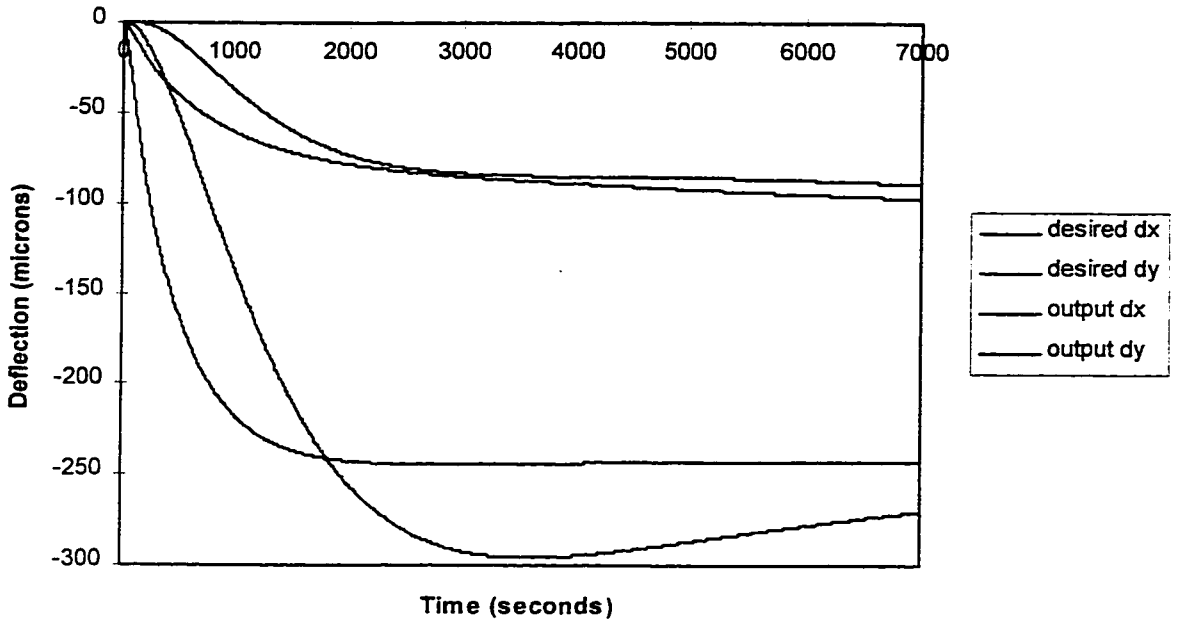

Figure 8.23: Simulated LQR Control System Response to Disturbance Unit Step Input Compared to Simulated Disturbance Step Input

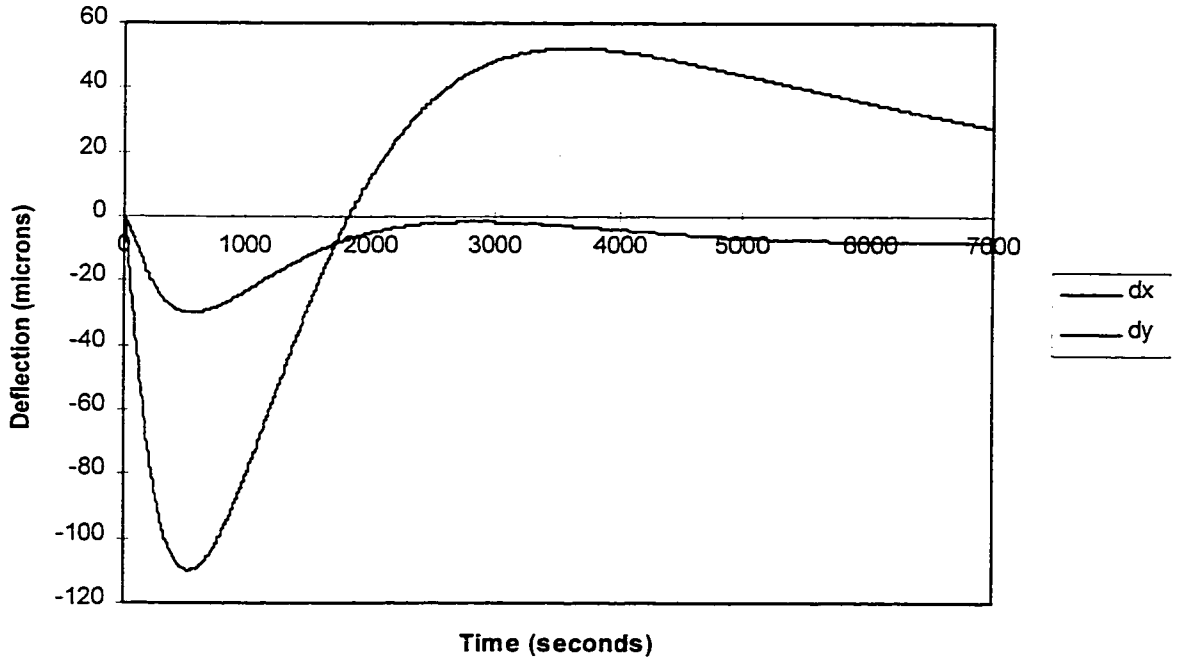

Figure 8.24: Simulated LQR Control System Tracking Error for Disturbance Unit Step Input

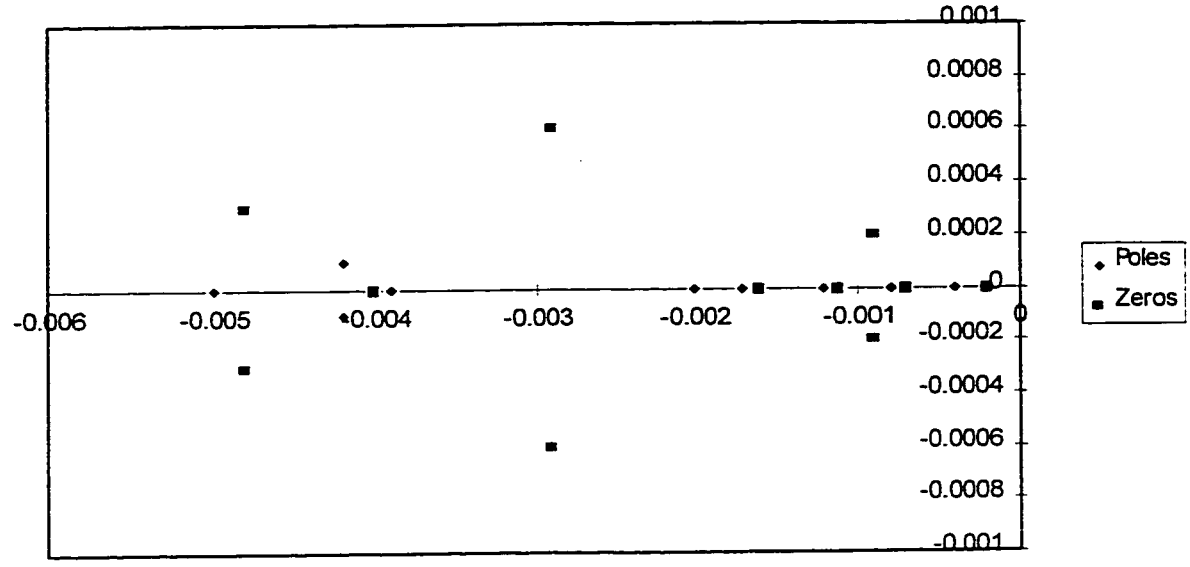

Figure 8.25: Pole-Zero Plot of Open Loop System

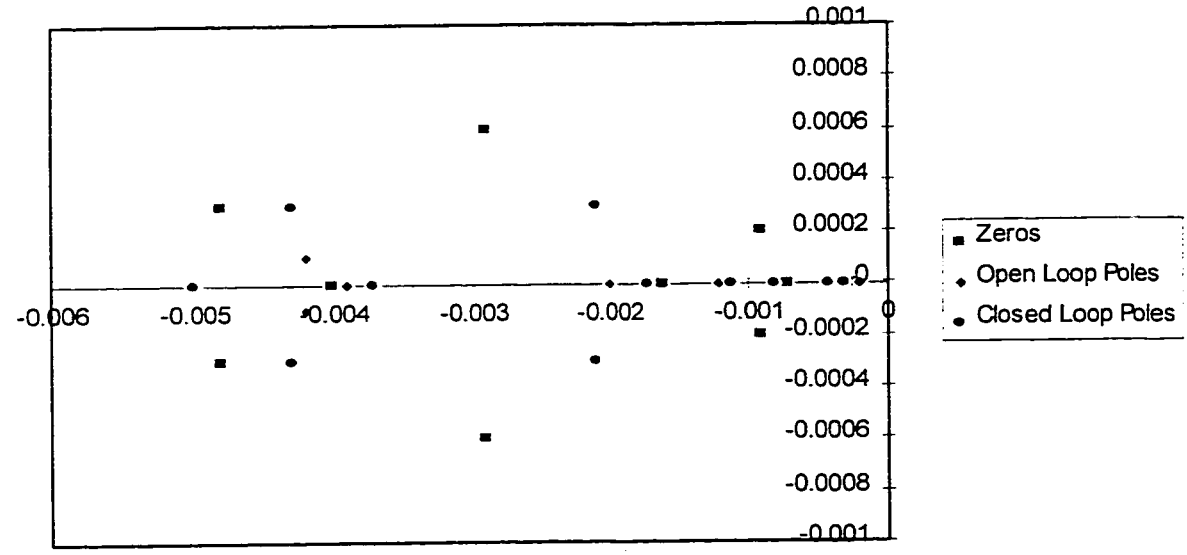

Figure 8.26: Pole-Zero Plot of Open Loop and Closed Loop Systems

zeros, which has the effect of increasing the amplitude response of each mode, and that is responsible for the overshoot shown in figure 8.22. The weakness of this approach is that it ignores the transmission zeros, which have a strong influence on the closed loop behaviour of the system.

8.6 Compensation Using a Feedforward Controller

8.6.1 The Robustness of the Control System

An alternative approach to feedback compensation is the use of a feedforward compensator. In contrast with the LQR approach just discussed, the objective of a feedforward controller is not to bring all of the states of the system to zero when subjected to an initial condition, rather the objective is to mask the activity of the states by preventing it from reaching the output. This is done by generating an actuation input that just balances the activity of the internal states at the output of the system. Unlike the LQR approach, the control effort produced by a feedforward controller does not necessarily become constant when the output of the system has reached the desired condition. That is, even after the output of the system apparently shows no activity, the control input may continue to show considerable activity as it acts to balance the continued activity of the internal states of the system [105].

The advantage of a feedforward controller is that it is possible to achieve perfect control of the output with the minimum control effort. The major disadvantage of a feedforward controller is that the controlled system is not as robust as it would be with a feedback controller, where robustness is defined as the ability of the controlled system to reject parameter variations of the open-loop system. From a mathematical perspective a feedforward compensator contains a zero corresponding each pole of the system and a pole corresponding to each zero of the system. If the poles and zeros of the system can be located with exact certainty then there will be perfect pole-zero cancellation and the dynamics of the system will be completely masked from the perspective of the output. However, if there is any mathematical discrepancy between

the actual system and the compensator then the masking will not be perfect and the dynamics of the system will appear at the output, although reduced by the compensator. Furthermore, because a feedforward compensator does not monitor the actual output it cannot compensate for external disturbances that could not be anticipated at the time of the design.

The reason why feedback control is normally preferred to feedforward control is because of the robustness of the closed-loop system, as explained above, where the robustness of the feedback system derives from the measurement of the system output [105]. It will now be shown that for the thermal deflection system shown in figure 8.14, feedback control does not offer any advantage over feedforward control, because the actual system output is not available for measurement. The system equations for the thermal control system with an estimator are as follows:

$$\begin{aligned} \dot{x} &= Ax + Bu \\ \delta_e &= Cx \\ u &= K(N_x \delta_d - x) + N_u \delta_d + L(\delta_a - \delta_e) \end{aligned} \tag{8.11}$$

where δ_a is the actual thermal deflection measured on the structure. It can be shown that equations (8.11) can be re-written in transfer function form as follows:

$$\delta_e = \left[C(sI + BK + BLC - A)^{-1} B (KN_x + N_u)\right]\delta_d + \left[C(sI + BK + BLC - A)^{-1} BL\right]\delta_a \tag{8.12}$$

and the control effort is given by:

$$u = \left[KN_x + N_u - (K + LC)\left((sI + BK + BLC - A)^{-1} B (KN_x + N_u)\right)\right]\delta_d + \left[L - (K + LC)(sI + BK + BLC - A)^{-1} BL\right]\delta_a \tag{8.13}$$

This transfer function is shown in block diagram form in figure 8.27, which is the conventional transfer function representation of a state feedback system with output measurement and state estimation. The state equations for the electric heat actuators, given by equations (8.1) and (8.2) differ from equations (8.11) in that there is no output measurement used for state estimation. This is explained in chapter 3, where the impracticality of real time measurement was discussed. The transfer function representation of equations (8.1) and (8.2) is as follows:

$$\delta_e = \left[C(sI + BK - A)^{-1} B\,(KN_x + N_u)\right]\delta_d \tag{8.14}$$

and the control effort is given by:

$$u = \left[I - K(sI + BK - A)^{-1} B\right]\,(KN_x + N_u)\delta_d \tag{8.15}$$

which is shown in block diagram form in figure 8.28. Figure 8.28 shows that the system equations given by equations (8.1) and (8.2) are feedforward in nature, even though the control system is formulated as having state feedback. The performance of the closed loop system is determined by the control matrix K. In a properly designed system the transfer function U(s) contains zeros which tend to cancel the poles of the open loop system, replacing the open loop dynamics with new dynamics chosen by the designer. This can be understood more easily by referring to the simple feedback system shown in figure 8.29, where the control effort is given by:

$$u = \frac{KD(s)}{D(s) + KN(s)} \tag{8.16}$$

If this control signal is used to control the actual system, as shown in figure 8.29, the effect is the cancellation of the system poles $D_a(s)$ with the estimated poles D(s), just as with a feedforward compensator. Considering the formulation of equation (8.14), even when the control system design is formulated as a state feedback system, the operation of the real time controller is ultimately reduced to pole-zero cancellation, and the effectiveness of the control is limited by the accuracy of the calibrated system model. Thus, the advantages of feedback control cannot be realized for this system, while the limitations of this type of design continue to affect the performance of the control system.

8.6.2 Designing the Feedforward Controller

Since the ultimate objective of a feedforward controller is to reshape the output system response to a given input, a better approach is implement pole-zero cancelation directly, without going through the feedback formulation. We begin by writing the control deflection in transfer function form as a sum of the deflection from each of two sources:

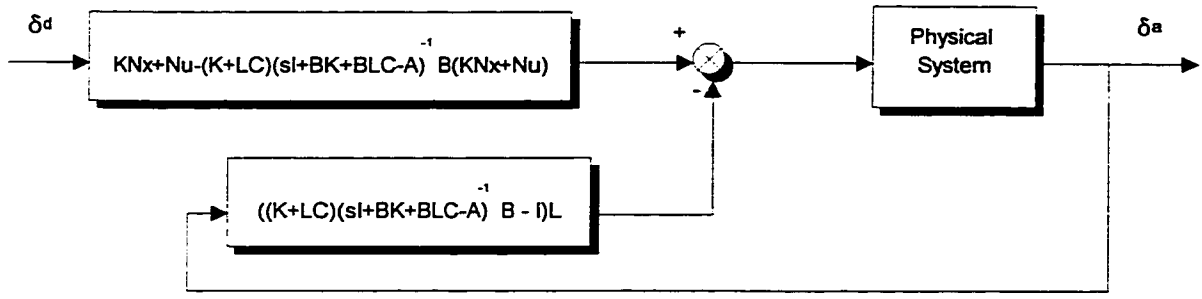

Figure 8.27: Feedback Block Diagram

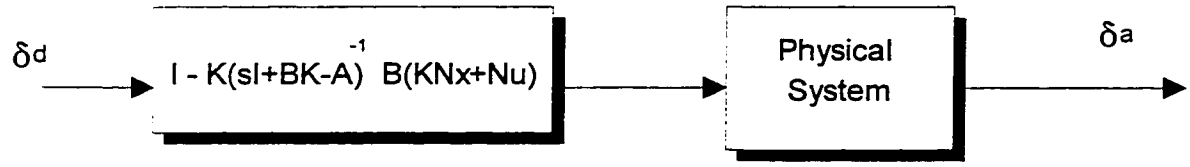

Figure 8.28: Feedforward Block Diagram

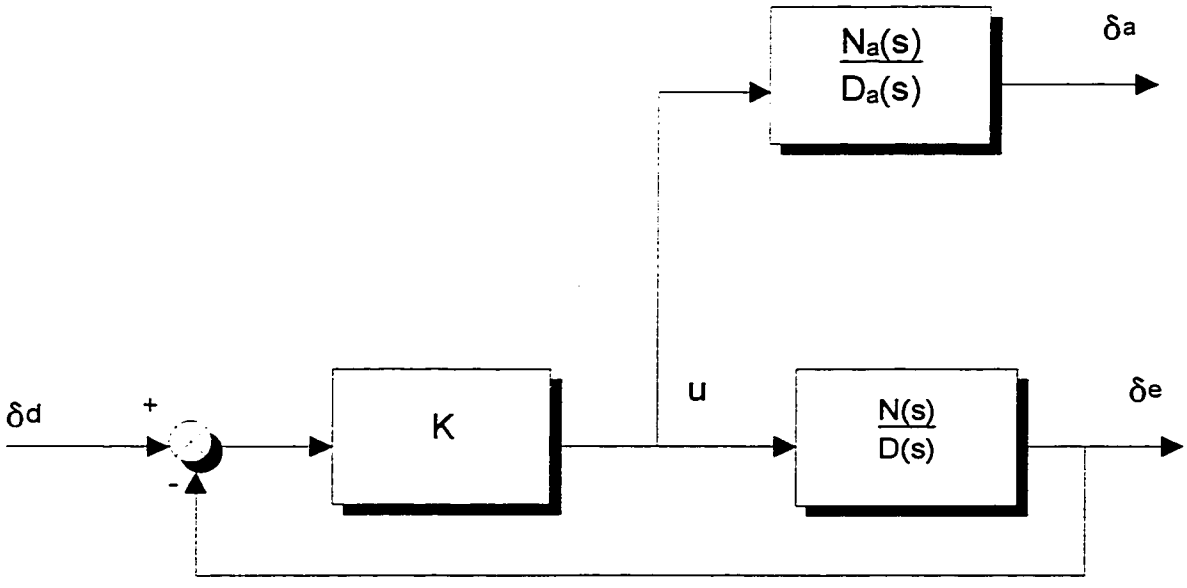

Figure 8.29: Block Diagram of Simple Feedback

$$\delta_x = H_x^1 q_1 + H_x^2 q_2$$
$$\delta_y = H_y^1 q_1 + H_y^2 q_2 \tag{8.17}$$

The X and Y deflections are equated to the disturbance deflection which is the desired deflection:

$$\begin{bmatrix} \delta_x^d(s) \\ \delta_y^d(s) \end{bmatrix} = \begin{bmatrix} H_x^1(s) & H_x^2(s) \\ H_y^1(s) & H_y^2(s) \end{bmatrix} \begin{bmatrix} q_1(s) \\ q_2(s) \end{bmatrix} \tag{8.18}$$

The next step is to solve for the matrix [q], which is the control effort that will exactly achieve the desired deflections:

$$\begin{bmatrix} q_1(s) \\ q_2(s) \end{bmatrix} = \begin{bmatrix} H_x^1(s) & H_x^2(s) \\ H_y^1(s) & H_y^2(s) \end{bmatrix}^{-1} \begin{bmatrix} \delta_x^d(s) \\ \delta_y^d(s) \end{bmatrix} \tag{8.19}$$

The desired deflections are related to the disturbance heat generation $Q_d(s)$ as follows:

$$\begin{bmatrix} q_1(s) \\ q_2(s) \end{bmatrix} = \begin{bmatrix} H_x^1(s) & H_x^2(s) \\ H_y^1(s) & H_y^2(s) \end{bmatrix}^{-1} \begin{bmatrix} H_x^d(s) \\ H_y^d(s) \end{bmatrix} [Q_d] \tag{8.20}$$

The system matrix is inverted to yield:

$$\begin{bmatrix} \dfrac{H_y^2(s)\, H_x^d(s)}{H_x^1(s)H_y^2(s) - H_y^1(s)H_x^2(s)} + \dfrac{-H_x^2(s)\, H_y^d(s)}{H_x^1(s)H_y^2(s) - H_y^1(s)H_x^2(s)} \\ \dfrac{-H_y^1(s)\, H_x^d(s)}{H_x^1(s)H_y^2(s) - H_y^1(s)H_x^2(s)} + \dfrac{H_x^1(s)\, H_y^d(s)}{H_x^1(s)H_y^2(s) - H_y^1(s)H_x^2(s)} \end{bmatrix} \tag{8.21}$$

This matrix was transformed into a 16x16 state-space system matrix by means of the MATLAB control toolbox, using the calibrated transfer functions H_x^1, H_y^1, H_x^2, and H_y^2, based on equation (6.16) shown in figures 8.17 and 8.18. The disturbance transfer functions H_x^d and H_y^d were calibrated in chapter 7, and given as equations (6.18) and (6.19). The continuous system shall be designated by $[A_{ff}]$, $[B_{ff}]$, $[C_{ff}]$, and the corresponding discrete system by $[\Phi_{ff}]$, $[\Gamma_{ff}]$, $[H_{ff}]$,

with zero order sampling period T=0.7 seconds. The input to this system is the disturbance heat generation [Q_d] and the output is the control heat generation [q]. When the control heat generation [q] is applied as input to the actuation system [A_s], [B_s], [C_s], the dynamics of the system should be cancelled and the output match the response to the deflection transfer functions H_x^d and H_y^d.

The performance of the feedforward controller is evaluated using a step input in disturbance heat generation Q_d=0.5. Figure 8.30 shows the simulated control effort response of equation (8.20), and figure 8.31 shows the simulated response of the system to this control effort. Figure 8.31 also shows the simulated step response of the disturbance deflection system. The difference between the curves in figure 8.31 is zero within the numerical resolution of the simulation software, which indicates perfect pole-zero cancellation, as expected for a simulation. However, figure 8.30 shows that the simulated heat generation of q1 is negative for approximately the first 100 seconds after the application of the step input, which is not achievable on the actual system since only positive heat generations possible. The explanation for the positive control heating is the large negative x-deflection coupling of the q1 heater, seen in figure 8.17. It is this negative coupled deflection that requires a positive output from q2 to compensate.

The performance of the system can be improved by adding an additional 25W heating pad to q1, as shown in figure 8.32. This heater receives power from the same power source as the larger q1 heating pad and so the two heaters are dependant, requiring no additional control hardware. The purpose of the smaller heating pad at the end of the overarm is to reduce the negative x-deflection coupling, as shown by the calibrated step responses of the modified system in figures 8.33 and 8.34. A comparison between figures 8.16 and 8.33 shows how the additional heating pad reduces the coupling almost to zero in the first 5 minutes following the step input. The simulated control effort for a step input to Q_d=0.5 is shown in figure 8.35 and the simulated system response to this input is shown in figure 8.36, along with the simulated step response of

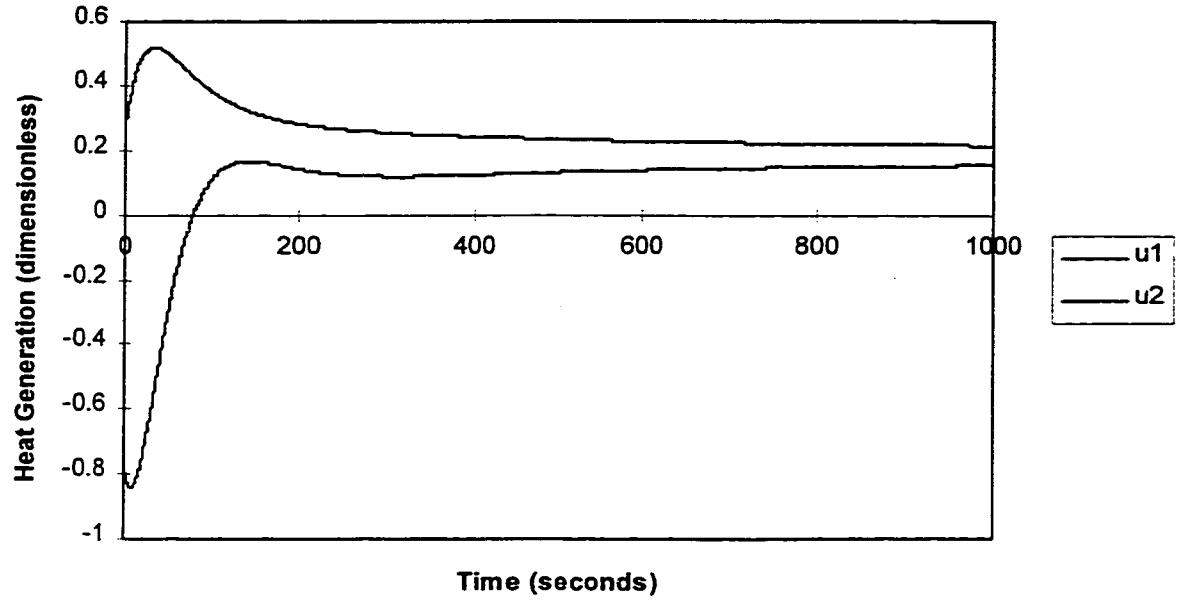

Figure 8.30: Control Effort for Feedworward Step Response (original system)

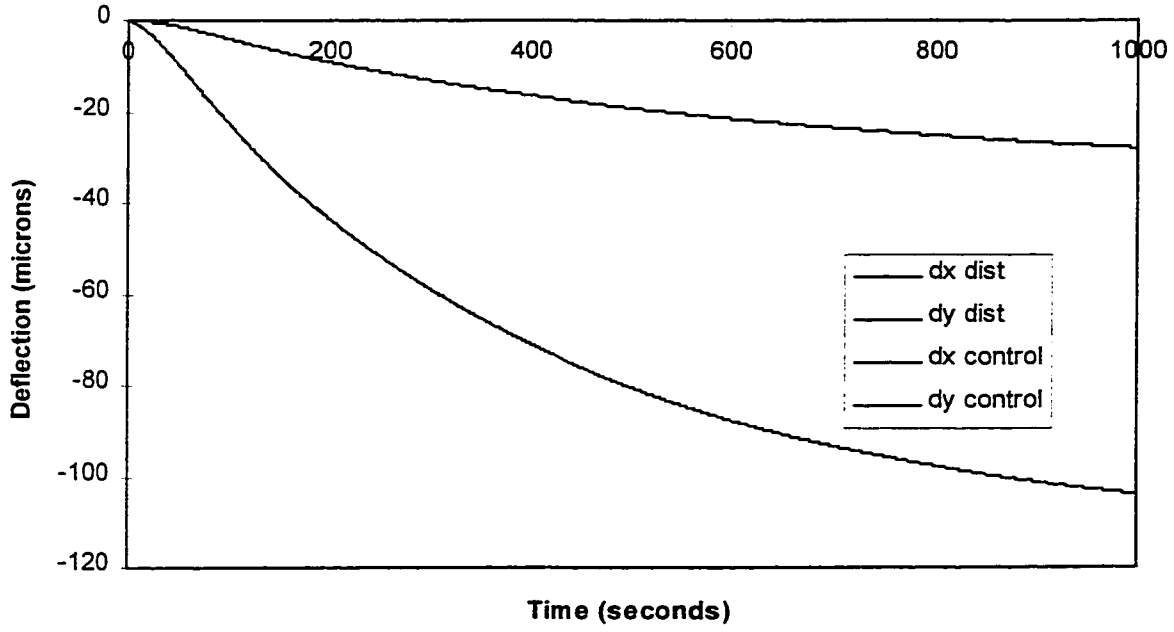

Figure 8.31: Feedforward Step Response (original system)

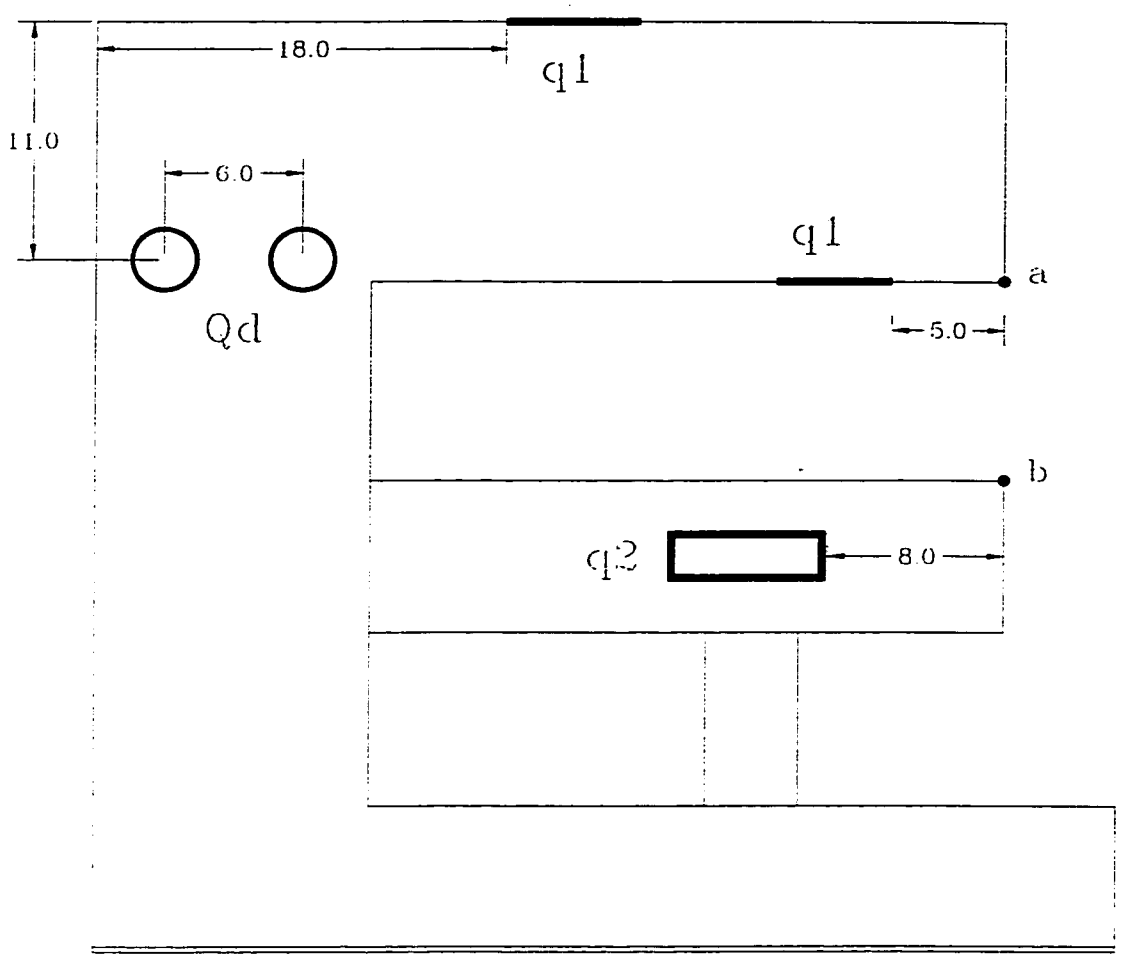

Figure 8.32: Heater Configuration of Modified System

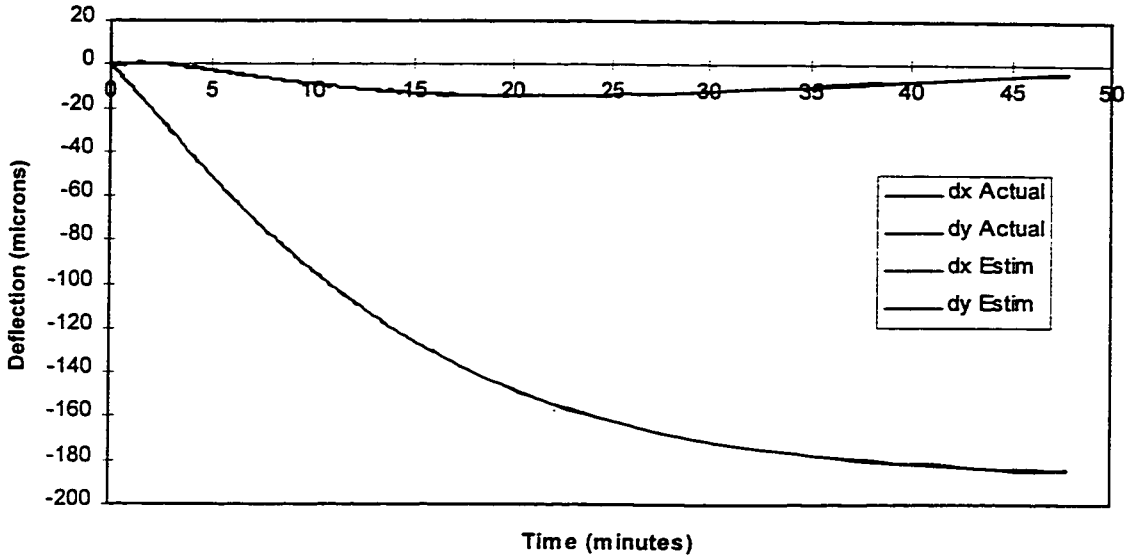

Figure 8.33: Calibrated and Actual System Step Response to q1 (modified System)

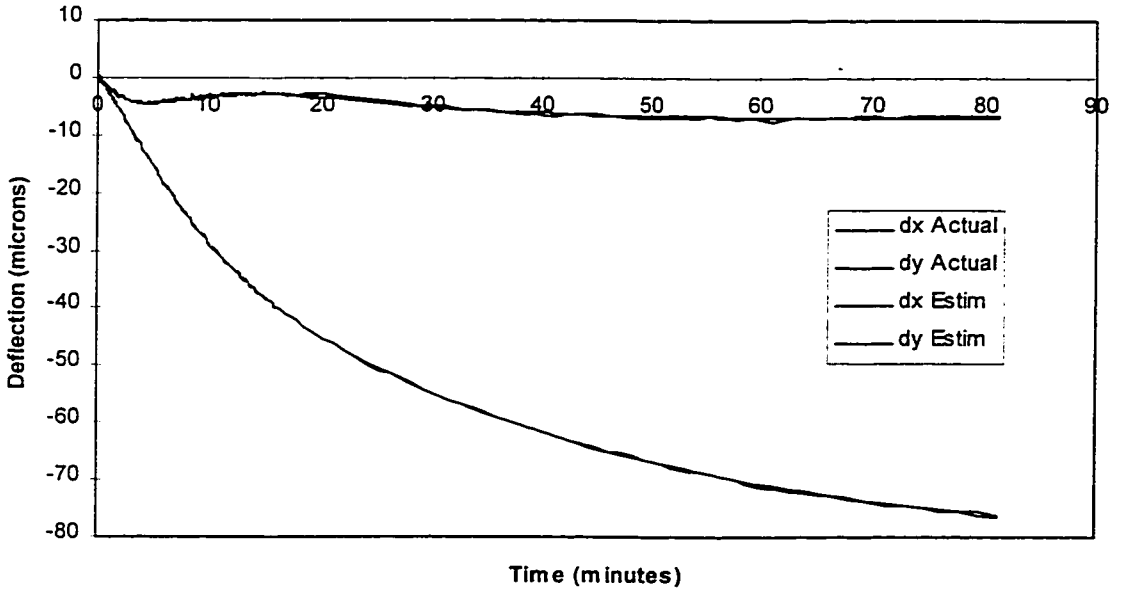

Figure 8.34: Calibrated and Actual Step Response to q2 (modified system)

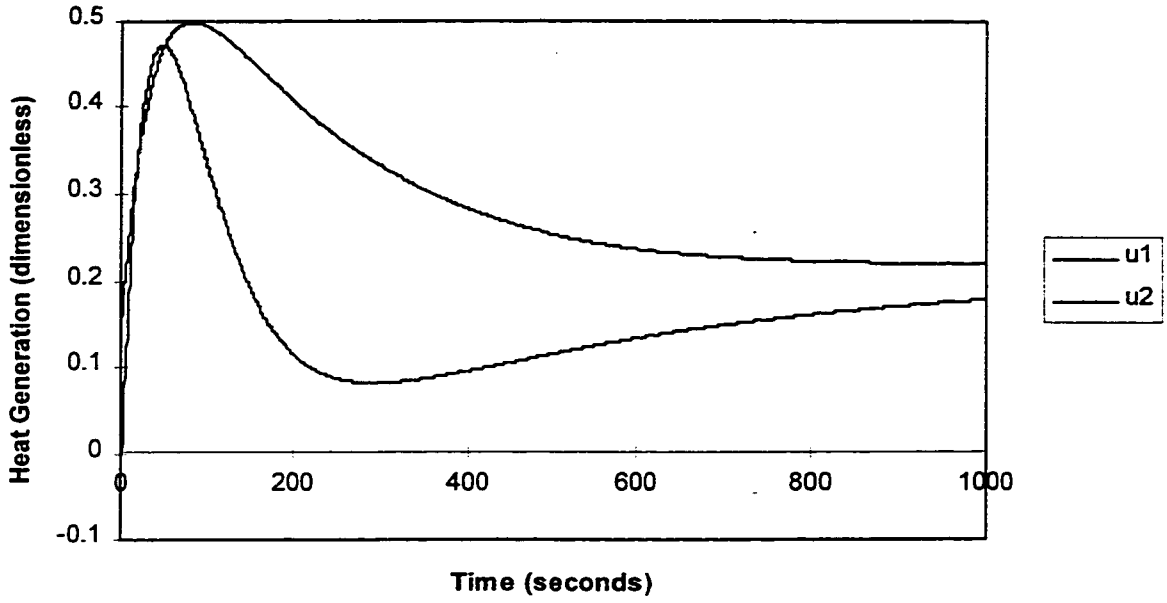

Figure 8.35: Control effort for feedforward (modified system)

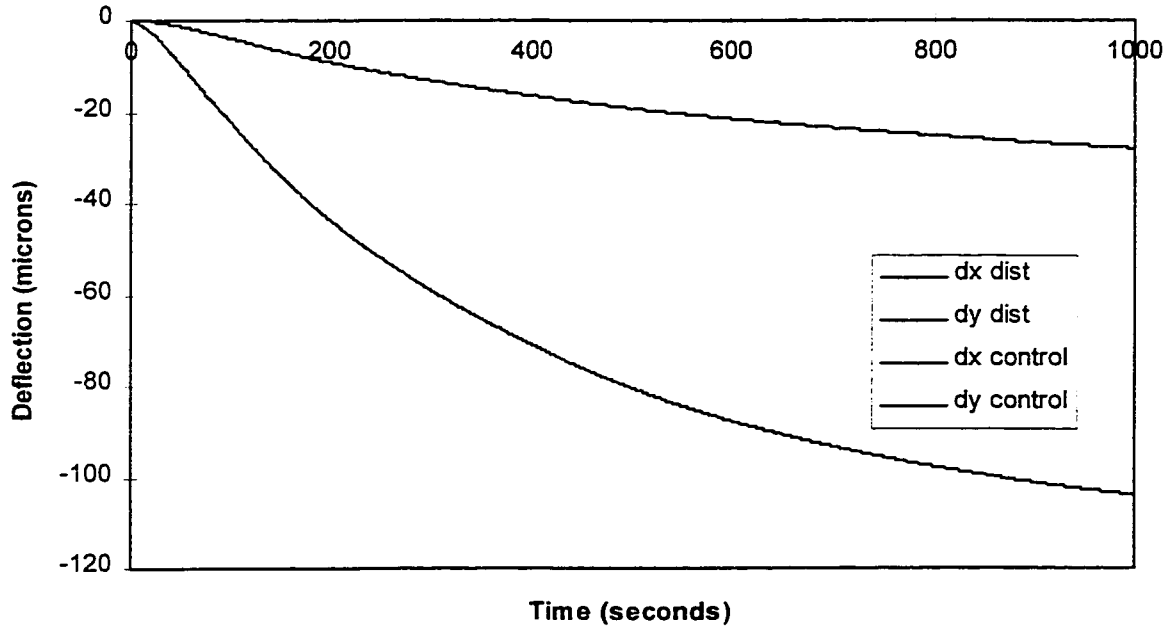

Figure 8.36: Step Response for Feedforward (modified system)

the disturbance system. As with the unmodified system, the difference between the two curves in figure 8.36 is zero, indicating perfect compensation by the feedforward controller. Figure 8.35 shows that the control effort which achieves this compensation is always positive, and is therefore physically realizable with positive heating elements.

A comparison between the results of the optimal LQR controller in section 8.3 with the feedforward controller in section 8.4 is striking. While the simulated tracking error of the LQR controller for a unit step disturbance input is contained within 60 to -110 microns (0 to -300 microns uncompensated), the simulated tracking error of the feedforward controller is zero within the numerical resolution of the simulation software for the same input. Furthermore, the feedforward control heating for this input is kept well within the operating range of the control heaters, so it is physically realizable by the heat source actuators. It must be remembered however, that these results were produced by simulation. The assumptions made by the simulation are as follows: 1) the calibrated control system model exactly matches the physical system, 2) the calibrated disturbance model exactly matches the physical system, 3) the input is a perfect unit step in heat generation at t=0 with no noise or fluctuation, 4) the control heating [q] that is requested by the controller is achieved perfectly by the heat source actuators. The first two of these assumptions are reasonable because of the accuracy of the modelling procedure, demonstrated in chapter 6. It is the fourth assumption that is not easily achievable in practice, particularly when there is high frequency input fluctuation.

Heat actuation error arises from three sources, which are transition error, saturation error, and steady-state error. Transition error occurs when the desired output changes abruptly, causing a deviation between the desired power output and the actual output. Saturation error is produced when the desired heating power is beyond the range of the heat actuator. In the present case this would correspond to a control effort outside of the range 0→1 for either q1 or q2 in non-dimensional units. Steady-state error is the constant error which is produced by a steady input,

and tends to vary with the magnitude of the input. The trouble with heat actuation error is that it is cumulative, and since there is no on-line deflection measurement to detect this error, a considerable error may accumulate even when the actual deviations are small. A practical control system which takes account of heat actuation error shall be developed in the next section.

8.7 The Features of the Real Time Thermal Deflection Control System

8.7.1 The Heat Actuation Control System

A Schematic block diagram of the feedforward control system is shown in figure 8.37, where the blocks that are enclosed by the dashed lines are hardware implemented systems and the other blocks are software implemented systems. The design of the feedforward system is based on a thermal deflection model that was calibrated for step heat inputs of various magnitudes. By using a step input for calibration, some of the dynamics of the heat actuation system, shown in figure 8.37, are concealed. The saturation error is concealed because the calibration step input is always within the range 0-1, and the transition error is concealed because the set power is constant. It is only the linear portion of the steady-state error that appears in the calibrated model, while the dynamics have been neglected. The problem now is that when operated in real time, high frequency components in the control inputs [u] may excite significant dynamics that were not anticipated by the calibrated model of the thermal deflection system.

One possible solution to this problem is to create an accurate model of the heat actuator system, along the same lines as the thermal deflection system model. This is unnecessary however, if an accurate measurement of the actual heating power is available. Figure 8.38 shows a block diagram of the hardware implemented heat actuation system that was used for this control system, which shall be referred to as the outer loop control system. The main components of the outer loop control system are the voltage controlled AC power supply and

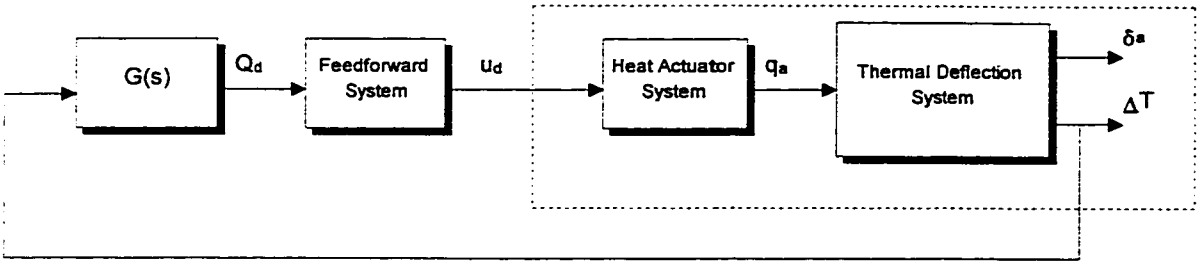

Figure 8.37: Schematic of Feedforward

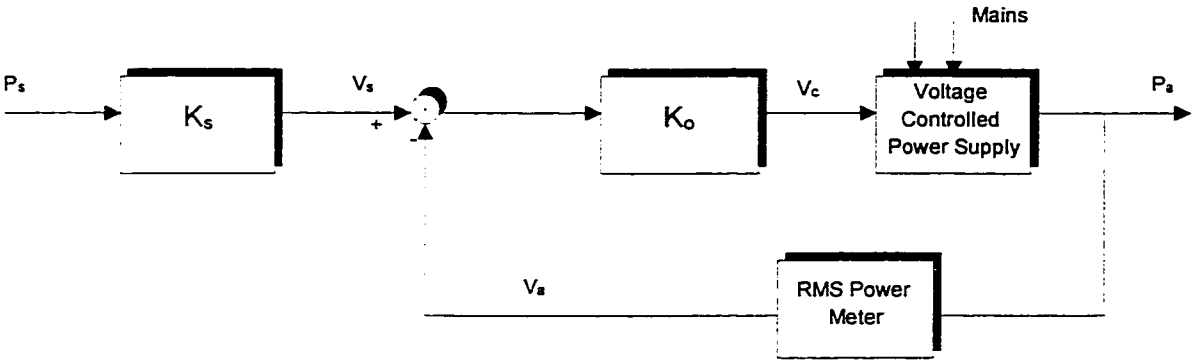

Figure 8.38: Schematic of Outer Loop Control System

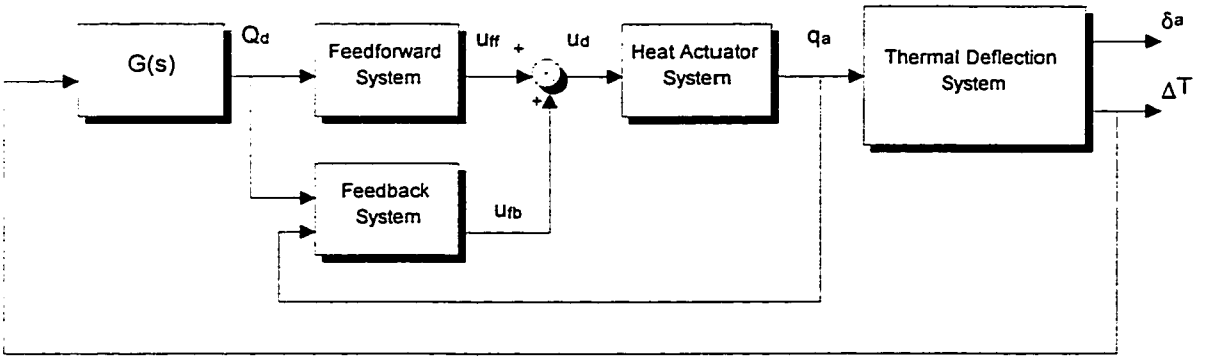

Figure 8.39: Schematic of Complete Control System

the RMS power meter. The control input is the desired power P_s, which is converted to a set voltage by a transformation equation K_s which is programmed into the computer controller. The output true RMS power P_a is converted to an analog voltage V_a by the power meter, which drives the voltage controlled power supply through a constant gain K_0, all of which is implemented through linear electronics devices.

The outer loop control system significantly improves the performance of the voltage controlled power supply by reducing the response time, reducing the inherent nonlinearity, and reducing the effect of temperature variations and external power supply fluctuations, which would otherwise affect the output of the voltage controlled power supply when used alone. The RMS power meter also provides a convenient measurement of the heating power actually delivered to the resistance heaters, which does not always correspond to the desired power P_s. All of the components in figure 8.38 are inexpensive and easy to implement. With a forward gain of approximately 50, the step response of the RMS power is underdamped with an overshoot of about 45% and a 5% settling time of about 2.0 seconds. There is also a steady-state limit cycle fluctuation of less than 2% of the maximum rated power with a period of about two seconds, which is caused by a deadband in the voltage controlled power supply. It is possible that the dynamics of the outer loop could be improved with the implementation of a hardware PID controller, however this is made unnecessary by of the data acquisition processor. An accurate estimate of the power delivered during one control cycle can be obtained by sampling the instantaneous power at a rate that is much faster that the inverse of the smallest time constant, which is 0.5 Hz for a time constant of 2.0 seconds. The measured power is sampled by the data acquisition processor at a rate of about 1.5 kHz, which is more than sufficient, and the averaged results are delivered to the computer controller as the average power delivered during the control cycle.

In addition to improving the accuracy of the heat actuation system, the configuration of figure 8.38 provides a convenient measurement of the heating power that is actually delivered to the resistance heaters. Thus, unlike the thermal deflection system, the dynamics of the heat actuators can be sensed and controlled in a true feedback configuration, which is shown by the schematic block diagram in figure 8.39. In order to understand the configuration in figure 8.39, consider the case where Q_d contains only low frequency components so that the dynamics of the heat actuation system are negligible. In this case the actual power delivered, q_a, will be equal to the power requested by the feedforward controller u_{ff}, and the control of δ_a will be as accurate as the estimate of Q_d and the thermal deflection model will allow, which is the ideal case for the feedforward controller. If, on the other hand, the dynamics of the heat actuators are excited by the input Q_d to produce either saturation error or transition error, then q_a will not be equal to the correct u_{ff}, and an actuation error will be created. As discussed above, actuation error tends to be cumulative, causing significant deflection error in a relatively short time. The purpose of the feedback control system shown in figure 8.39 is to sense the power actuation error and compensate for it. To complicate matters further, it may not always be possible to immediately compensate for power actuation errors, as for example when the actuator is already saturated at q=0 or q=1. The inputs to the feedback controller are selected as Q_d and q_a, however a scheme based on inputs u_{ff} and q_a would work just as well since Q_d and u_{ff} are mathematically related by the feedforward system $[\Phi_{ff}]$, $[\Gamma_{ff}]$, $[H_{ff}]$.

Figure 8.40 is a block diagram that shows how the feedback system in figure 8.39 is implemented. All of the elements of figure 8.40 are implemented through software in the computer controller, in parallel with the feedforward system. There are three principle processes in figure 8.40, identified by the dashed boxes and labelled Block 1 through Block 3. Since figure 8.40 shows the real time implementation of the system, the processes are designated as discrete systems. The inputs to the system are labelled as $Q_d(k)$ and $q_a(k)$ to indicate that they are sampled at discrete intervals and held constant during the interval, as already explained in

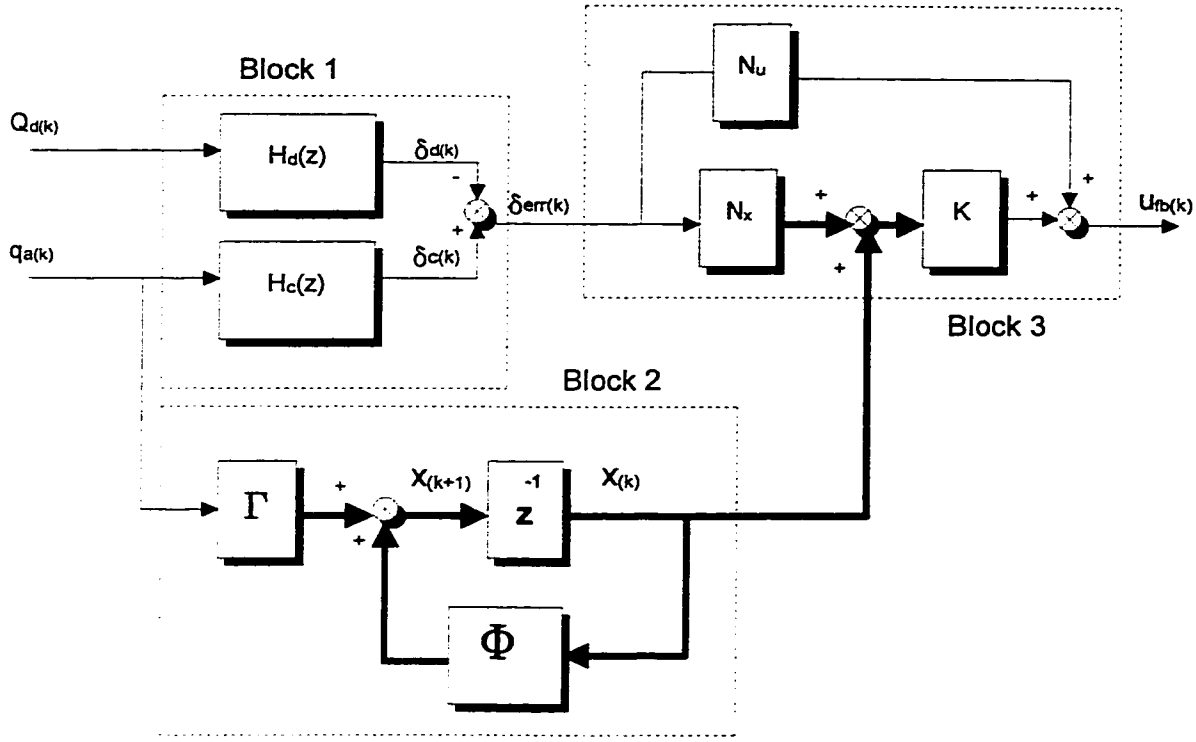

Figure 8.40: Block Diagram of Feedback Element

chapter 6. Block 1 is composed of two processes, $H_d(z)$ and $H_c(z)$, which are the discrete equivalents of the thermal deflection disturbance system $H_d(s)$ and the thermal deflection control actuator system $H_c(s)$, respectively. The discrete systems are defined by equation (6.34) and the calibrated system parameters, as was derived in section 6.11.2. We recall from the derivation of equation (6.34) that the hold interval is redefined for every iteration, accommodating a variable sample period, which is an important attribute that will be discussed again shortly. The output of $H_d(z)$ is the estimated deflection of the disturbance heater $\delta_d(k)$, and the output of $H_c(z)$ is the estimated deflection of the control heaters $\delta_c(k)$. The sum of $\delta_c(k)$ and the negative of $\delta_d(k)$ is the negative of the estimated net deflection of the structure, labelled $\delta_{err}(k)$ in figure 8.40. The variable $\delta_{err}(k)$ is the desired defection, or sometimes called the tracking deflection of the feedback system since it is the negative of the estimated total deflection of the structure. Block 3 in figure 8.40 determines the required output $u_{fb}(k)$ according to the state-space equation:

$$u_{fb}(k) = K\left(N_x\delta_{err}(k) - x(k)\right) + N_u\delta_{err}(k) \tag{8.22}$$

The matrix x(k) in equation (8.22) is a column vector of the current values of the states of the system. The states are generated by Block 2 in figure 8.40, which is a graphical representation of the equation:

$$x(k+1) = \Phi_s x(k) + \Gamma_s u(k) \tag{8.23}$$

The advantage of the discrete formulation is that states at each time kT can be found recursively by simple matrix multiplication, as shown in equation (8.23). A problem arises however, when the sample period T is not constant, since the matrices $[\Phi_s]$ and $[\Gamma_s]$ can only be calculated from the continuous system for a particular value of T. It will be shown that the sample period is not constant for this system, and so this problem will be dealt with in a subsequent section of this chapter.

8.7.2 The Design of the Feedback System Using Output Optimization

The feedback control system shown in figure 8.40 is designed by choosing the matrix K such that the closed loop system meets certain design specifications. It was shown in section 8.3 that the LQR design procedure proposed by Bryson and Ho produces a closed loop system with poor tracking of the input signal, as shown by the simulated response to a disturbance step input in figure 8.23. The problem with the design procedure in section 8.3 is that the transmission zeros of the system were ignored by the optimization. While this produces a control system which is robust, it misses the opportunity to mask the activity of the internal states behind the transmission zeros of the system. In order to make better use of the transmission zeros of the system a new procedure will be introduced in this section that is based on output optimization. The basis of this procedure is the minimization of the system outputs [δ] rather than the matrix of states [x]. Thus, the error equation (8.9) is modified as follows [105]:

$$\Upsilon = \sum_{k=0}^{\infty} \left\{ \rho\, \delta_{(k)}^{T} Q_1 \delta_{(k)} + u_{(k)}^{T} Q_2 u_{(k)} \right\} \tag{8.24}$$

where δ(k)=Hx(k). The minimization of equation (8.24) results in a modified Hamiltonian matrix that can be solved using the MATLAB Control Toolbox. The important difference between output minimization and state minimization is that with output minimization there is no weight given to the activity of any individual state of the system, it is only the combination of states reaching the output that is given weight in the minimization of equation (8.24). There are two main disadvantages to output minimization: 1) individual states may show considerable activity even though the output appears inactive, even becoming unstable if the system contains zeros in the right half of the imaginary plane, and 2) variations in the transmission zeros of the physical system can have significant consequences in terms of closed loop performance, meaning that the system is not as robust. The second of these two disadvantages is not relevant for the thermal deflection system in this thesis because it is, by its nature, an open loop system anyway. With respect to the first of these disadvantages, the nature of the system which is to be controlled is very important, and should be screened for positive real zeros before attempting

to apply the procedure. The form of the thermal deflection model in equation (6.16) is usually flexible enough to allow for than more than one calibrated solution if the zeros of the transfer function, given by equations (6.20) and (6.21) , contain any positive real parts.

The output optimized solution was obtained for the following values of the weight matrices:

$$Q_1 = \begin{bmatrix} 1.00 & 0 \\ 0 & 1.00 \end{bmatrix} \qquad Q_2 = \begin{bmatrix} 0.75 & 0 \\ 0 & 1.00 \end{bmatrix} \tag{8.25}$$

Figures 8.41 and 8.42 show the simulated unit step response of the discrete system for a step input to q1 and q2 respectively, and figures 8.43 and 8.44 show the simulated control effort for each of these step responses. The weight matrices were varied by a trial and error process until a good compromise between the speed of the step response and the use of control effort was achieved, as shown by figures 8.41-8.44. Figure 8.45 shows the simulated response of the feedback control system to the simulated thermal deflection disturbance step response Q_d=0.5, and figure 8.46 shows the resulting control effort. These figures show that output optimization produces results that are far superior to those for state optimization, even approaching the accuracy that was achieved by the feedforward controller in figures 8.35 and 8.36. The reason for this improvement in accuracy is the way that the optimization locates the poles of the closed loop system. Figure 8.47 shows the dominant poles and zeros of the continuous open loop system, and figure 8.48 shows how the dominant poles have been relocated by the optimized closed loop system. The closed loop poles have been moved on top of the system zeros, performing pole-zero cancellation in the same way as the feedforward controller. Since there is no state estimator for this system, the performance of the control system is dependant on the accurate identification of the transmission zeros by the calibrated system model. It is for this reason that considerable attention was given to the accurate modelling of the thermal deflection system in chapter 6.

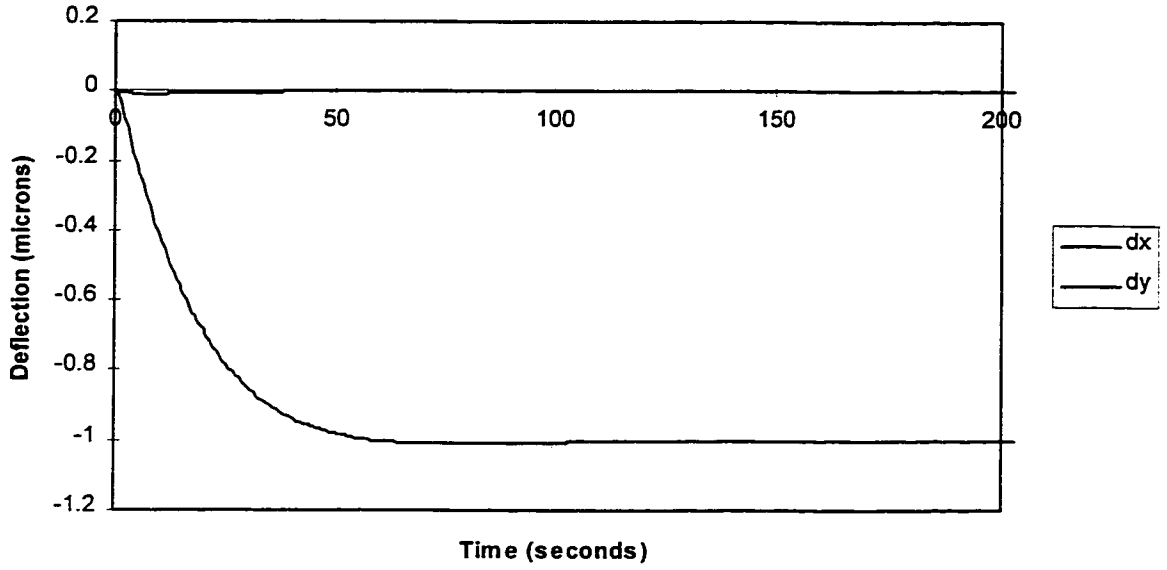

Figure 8.41: Regulator Step Response to q1

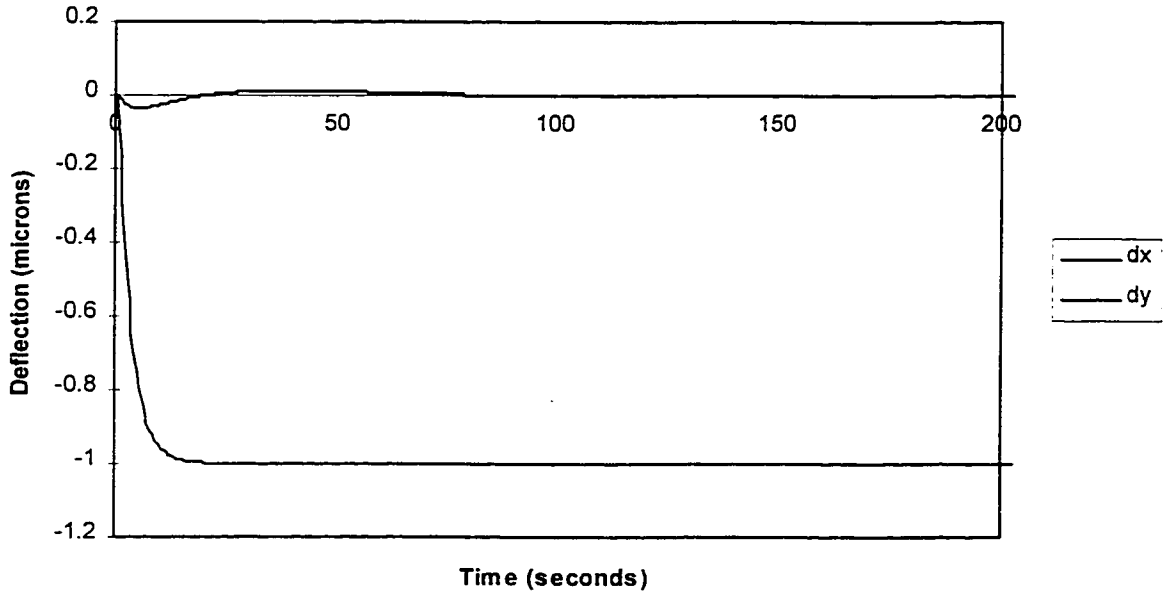

Figure 8.42: Regulator Step Response for q2

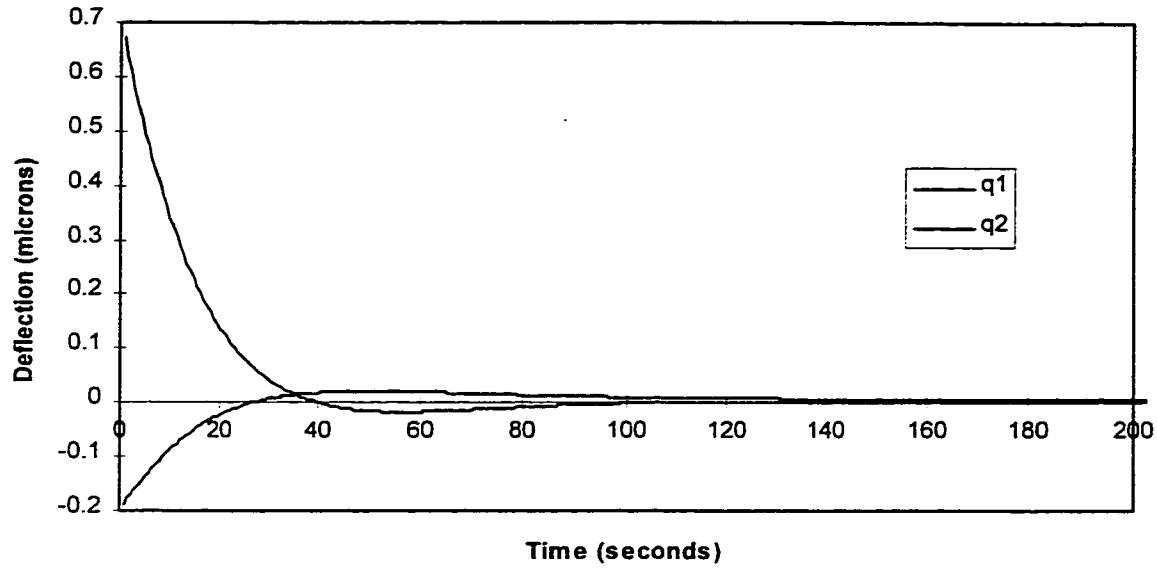

Figure 8.43: Control Effort for Step in x

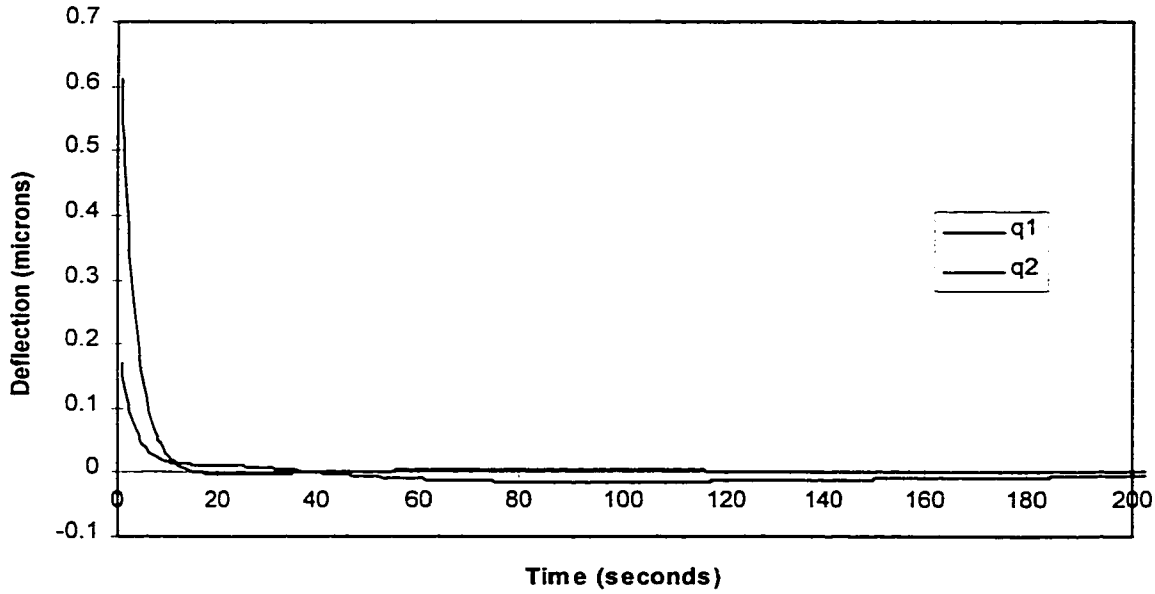

Figure 8.44: Control Effort for Step in y

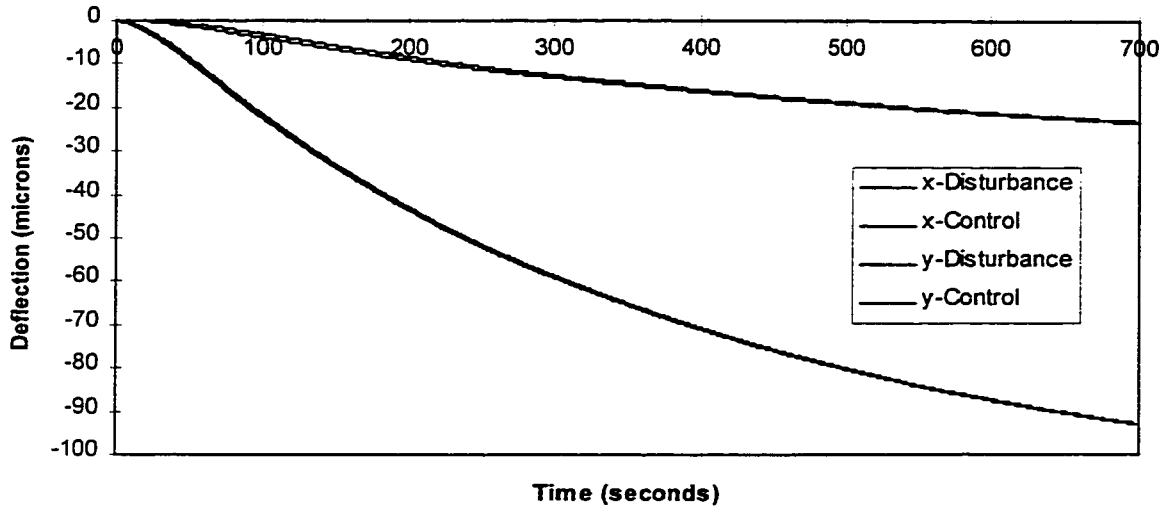

Figure 8.45: Response to Disturbance Step Input

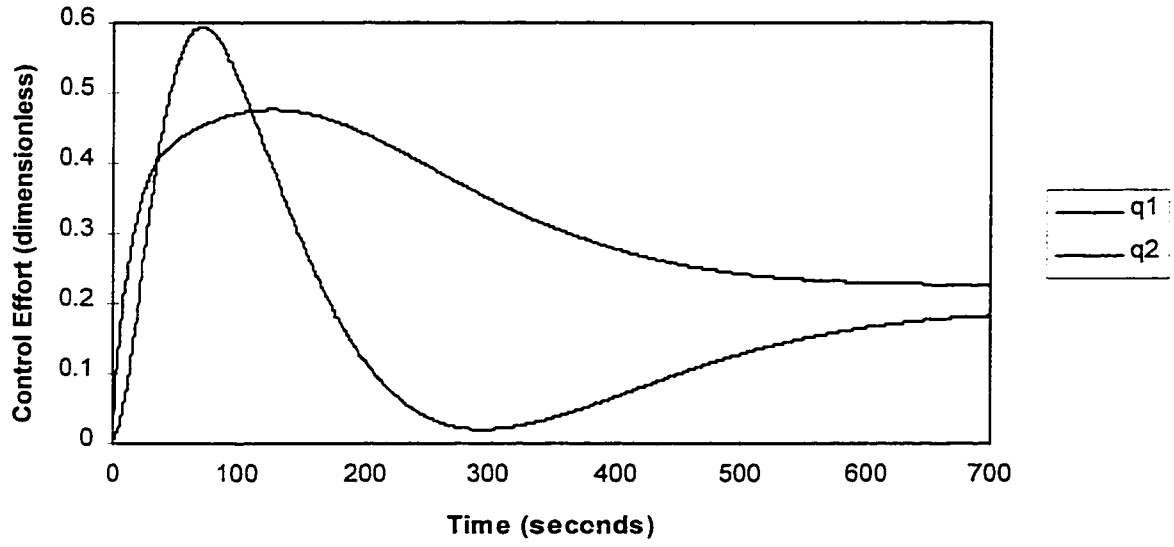

Figure 8.46: Control Effort for Disturbance Step Input

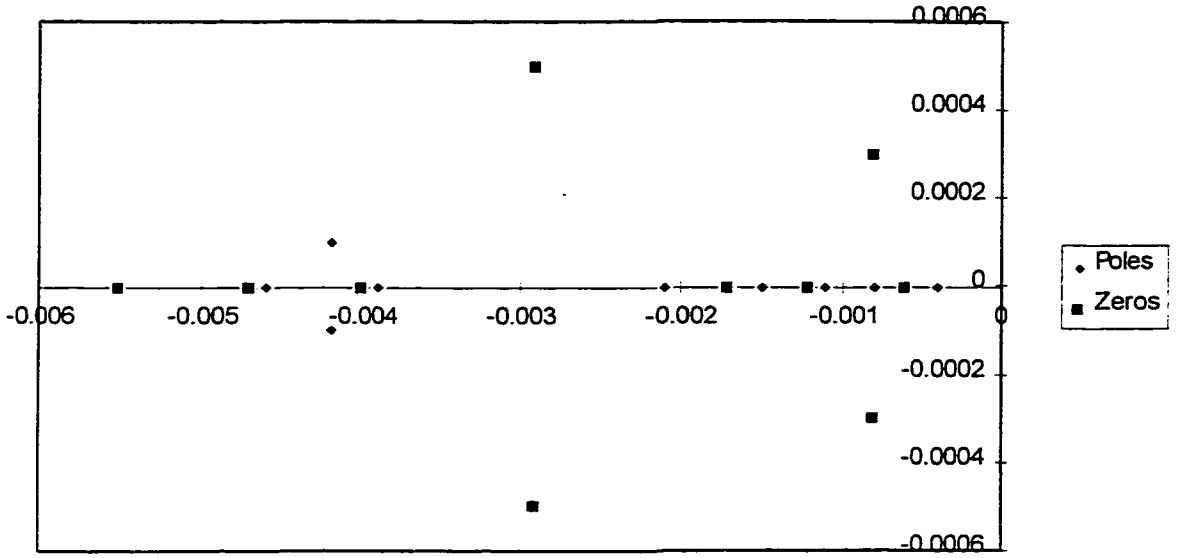

Figure 8.47: Pole-Zero Plot of Open Loop System

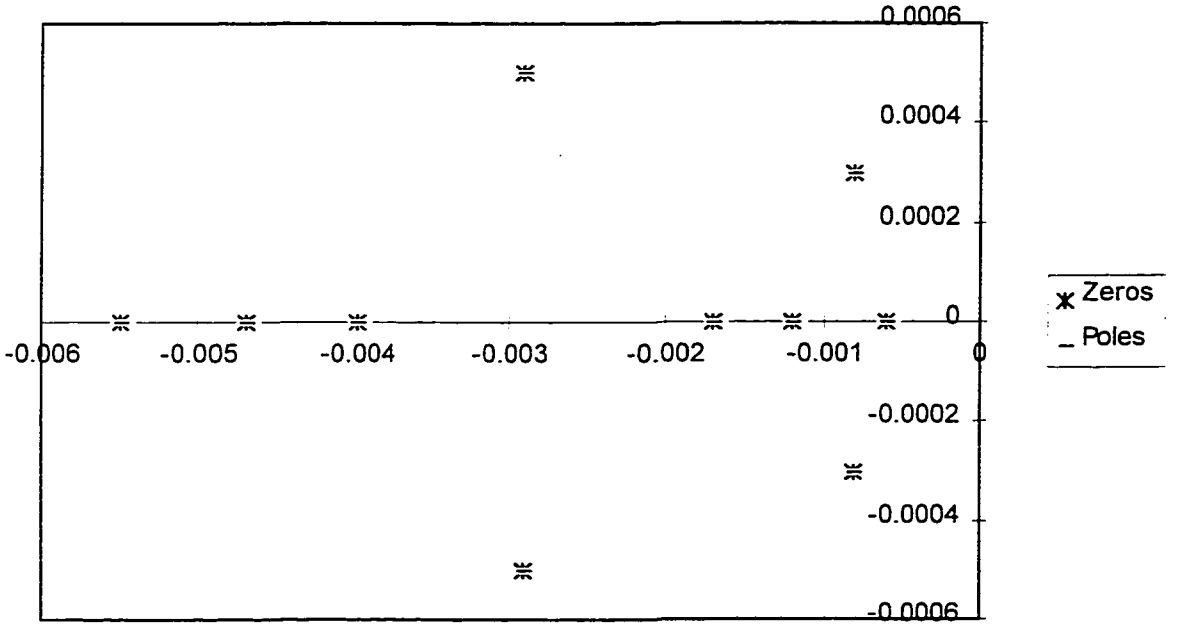

Figure 8.48: Pole-Zero Plot of Closed Loop System

8.7.3 Measurement Sampling and Real Time Processing

The control power output is sampled by the data acquisition processor in the same way as the measured temperature, as discussed in chapter 6. The data acquisition processor samples the measured variable at a much higher rate than the control cycle and then averages the values before sending the result to the computer controller. For the present system the sampling rate is above 1 kHz, and the period of the control cycle is governed by the collection of a fixed number of samples. Although the DAP 1200 data acquisition board has provision for an external trigger, so such triggering hardware has been implemented for these experiments. Thus, the control cycle time period is not exactly constant from one cycle to the next. Figure 8.49 shows a plot of the typical sampling period distribution for a real time experiment. Rather than implementing an external trigger to synchronize the control cycle to a fixed period which is larger than the largest possible period, the software shall be implemented to accommodate a variable cycle period. The inverse algorithm and the discrete transfer functions shown as Block 1 in figure 8.40 inherently accommodate a variable sample period. The discrete state constructor shown as Block 2 in figure 8.40 and the discrete feedforward controller shown in figure 8.39 must be defined for a fixed sampling period T. The discrete state space system [Φ], [Γ] is computed from the continuous state space system by the transformation equations [105]:

$$\Phi \approx I + \frac{AT}{2}\left(I + \frac{AT}{3}\left(\cdots \frac{AT}{N-1}\left(I + \frac{AT}{N}\right)\right) \cdots \right)$$

$$\Gamma = \Phi TB \tag{8.26}$$

In the case of the feedforward controller it is not worth the extra effort to transform the continuous system to the discrete system on-line. The feedforward controller is transformed off-line for an average sampling period T=0.6136 seconds and the discrete system is stored by the on-line program. The accuracy of the feedforward controller is not so critical because it is used only to approximate the control effort and there is a feedback controller working in parallel to correct the error. The accuracy of the state constructor shown in figure 8.40 is more critical because it is used to fine tune the control to within less than a couple of microns. Thus, the

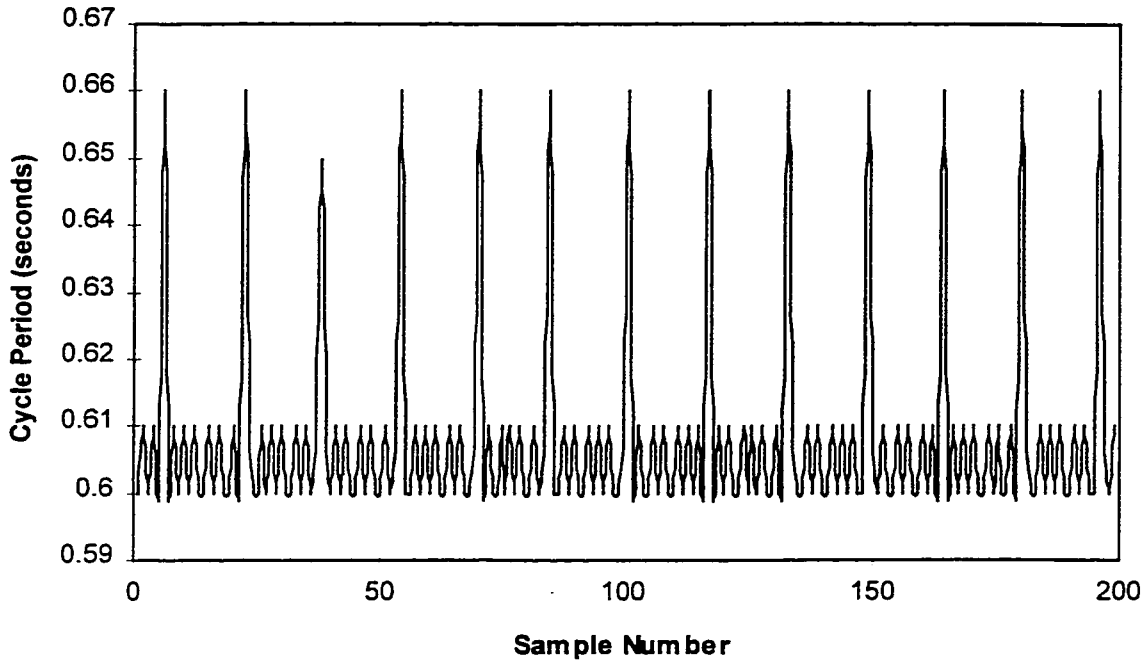

Figure 8.49: Cycle Period of Control System in Operation

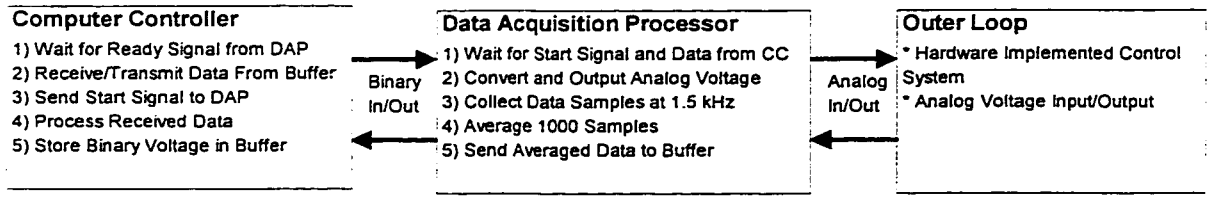

Figure 8.50: Schematic Block Diagram of System Architecture

discrete system matrices $[\Phi_{fb}]$, $[\Gamma_{fb}]$ shall be computed from the continuous system matrices $[A_{fb}]$, $[B_{fb}]$ by the controller in real time using equation (8.26).

8.7.4 The Complete Real Time Thermal Deflection Control System

The architecture of the complete thermal deflection control system is shown by the schematic block diagram in figure 8.50. The three system components are 1) the Controller Computer, 2) the Data Acquisition Processor board (DAP) which includes the ADC and DAC converters and buffers as well as the processor itself, and 3) the Outer Loop control system which is hardware implemented as shown in figure 8.38. The three components operate independently in parallel, with the interfacing between system components shown schematically in figure 8.50. There is an analog interface between the outer loop and the DAP and a digital interface between the Controller Computer and the DAP. The operations performed by each system component are summarized inside the blocks in figure 8.50. The controller computer and the DAP are synchronized by each one going into a wait state after fully executing one control cycle, beginning the next cycle when signalled by the other system component. In this way the period of the control cycle is the longer of the time required for the controller computer or the DAP to complete one control cycle.

A schematic block diagram of the of the operations performed by the controller computer is shown in figure 8.51, in summarized form. The first operation is the acquisition of data from the DAP. The second operation is the calculation of the estimated heat generation for the previous cycle by the method of a convolution integral, as was derived in chapter 5. The third process is the feedforward transfer function, which uses the discrete system matrices stored in memory. The fourth process is the calculation of the estimated deflection, using discrete transfer function models of the disturbance system and the control heater system, derived in section 6.11. The fifth process is the calculation of the correction control heat generation from the feedback system matrices. The feedback system matrices must first be computed from the matrices of the

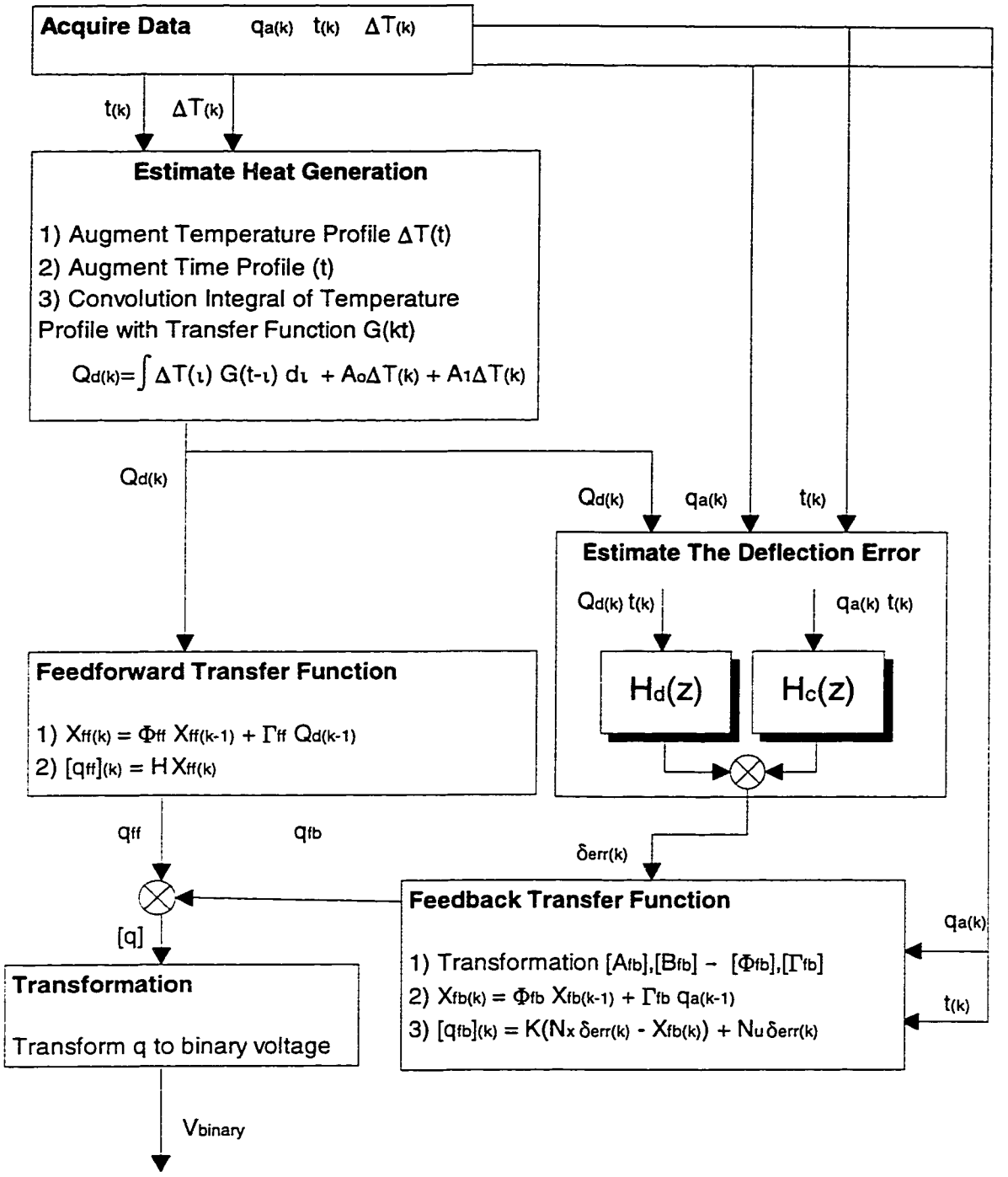

Figure 8.51: Schematic Block Diagram of Computer Controller Algorithm

continuous system, as shown in the figure. The final operation is the transformation of the control heat generation to a binary voltage using a calibrated look-up table and a linear interpolation program. In spite of the modularized representation of the system in figure 8.51, the program modules actually operate from common data base and share many important subroutines. Despite the fact that some modules in figure 8.51 are shown connected in parallel, the program executes sequentially, calculating the required variables in the sequence shown. It should be remembered that this flowchart shows only the basic operations performed by the controller computer in summarized form. Many of the details that have been discussed in this and previous chapters have been omitted for brevity.

8.8 Validation of the Thermal Deflection Control System using Electric Heater Actuation

8.8.1 The Validation Procedure

The performance of the control system will be tested by applying known inputs to the disturbance heater, while running the control system in real time. The actual deflection will be measured and recorded for comparison with the estimated deflection, and certain other system parameters will also be recorded for analysis. The input functions are chosen so as to be similar to the actual disturbance heat generation that would be expected for a real machine tool in an industrial environment, normally a series of step inputs of various magnitude and duration. The input functions are also chosen so as to expose the limitations of this type of control system.

8.8.2 Test Case 1: Single Step Input of Magnitude 0.5

The first case is a single step in heat generation from zero to 0.5, beginning at t=30 seconds. Figure 8.52 shows the measured temperature profiles for this test case, and figure 8.53 shows the temperature difference. Figure 8.54 shows the on-line estimate of the disturbance heat generation, labelled $Q_{d(k)}$ in figure 8.51. Figure 8.55 shows the estimated uncompensated thermal deflection of the structure for this input, where the estimate was produced on-line by the transfer function $H_d(z)$, shown in figure 8.51. Figure 8.56 shows the on-line estimate of the compensated

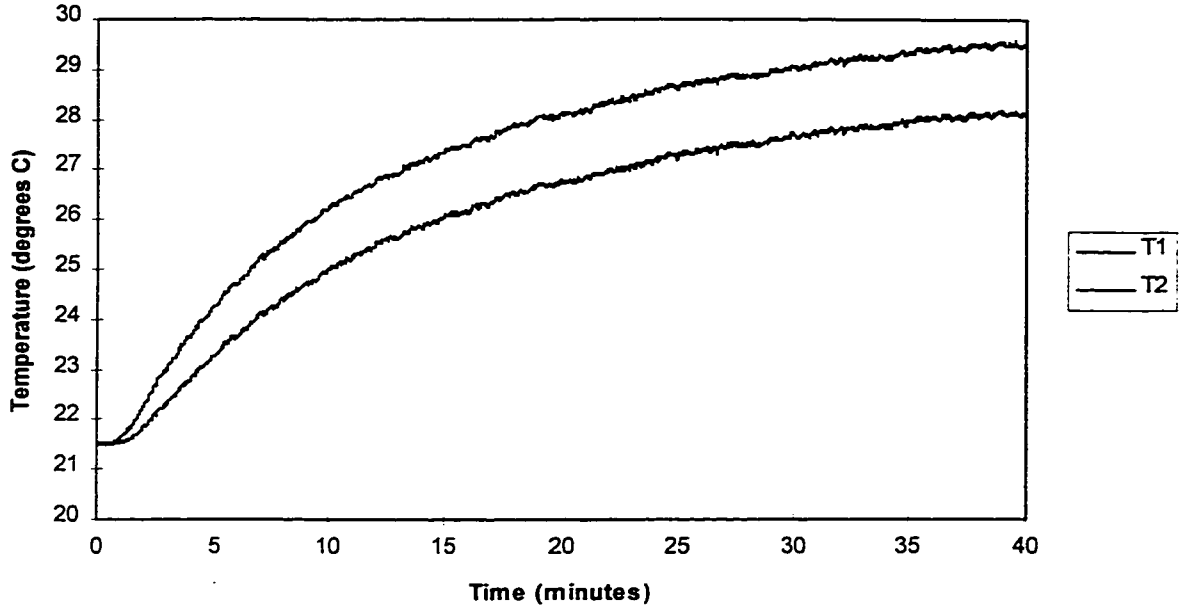

Figure 8.52: Temperature Profiles for Case 1: Step Input Magnitude Q=0.5

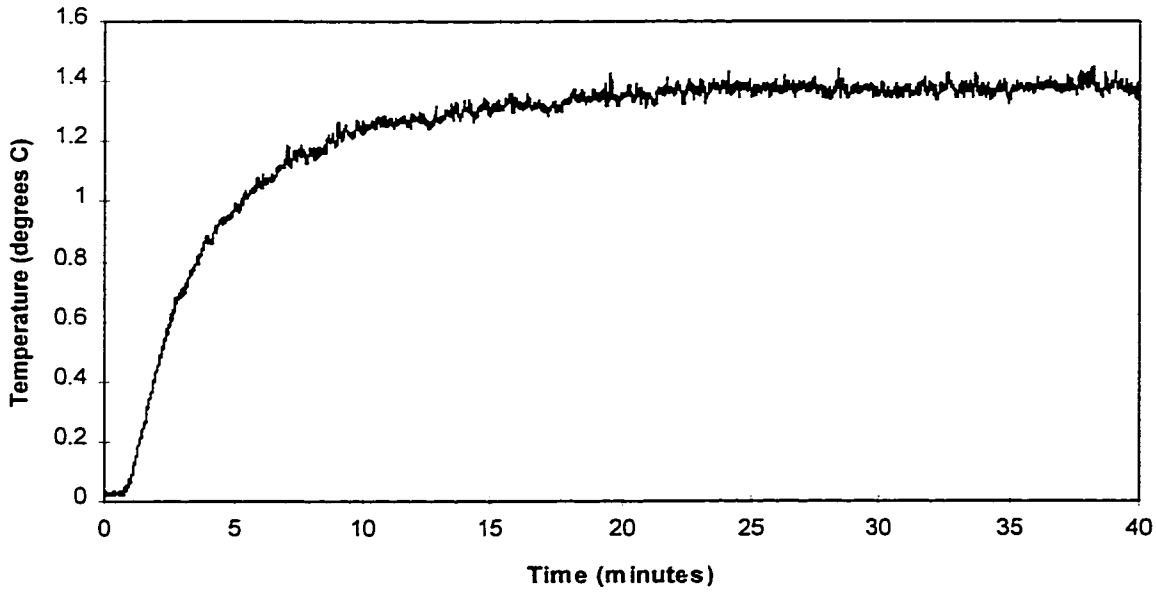

Figure 8.53: Temperature Difference Profiles for Case 1: Step Input Magnitude Q=0.5

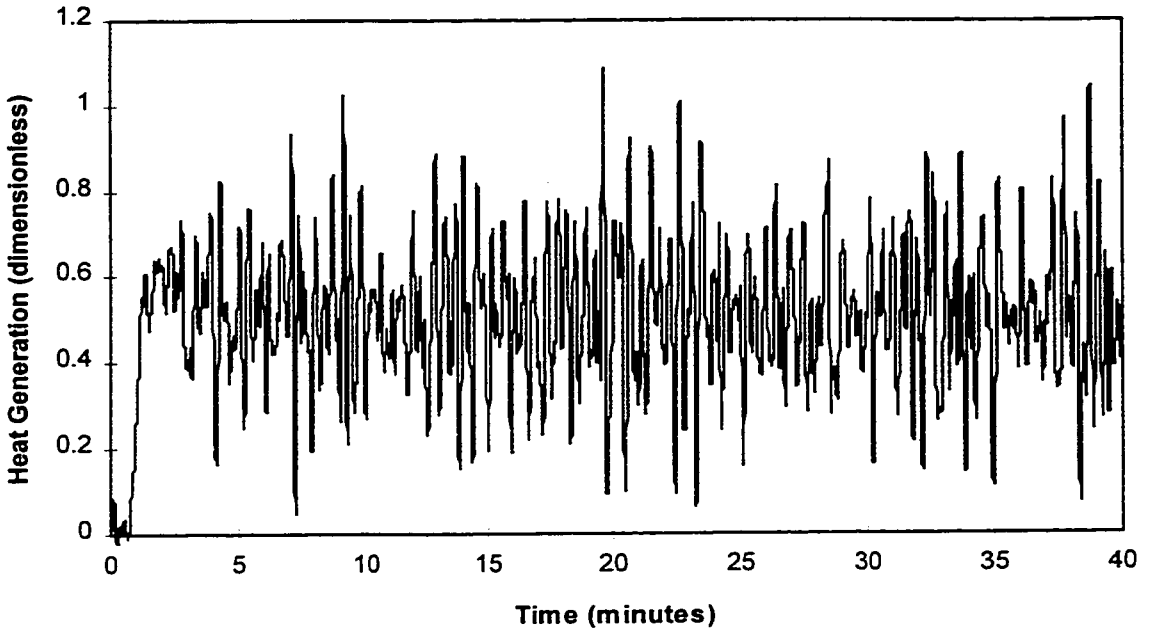

Figure 8.54: Estimated Heat Generation for Case 1: Step Input Magnitude Q=0.5

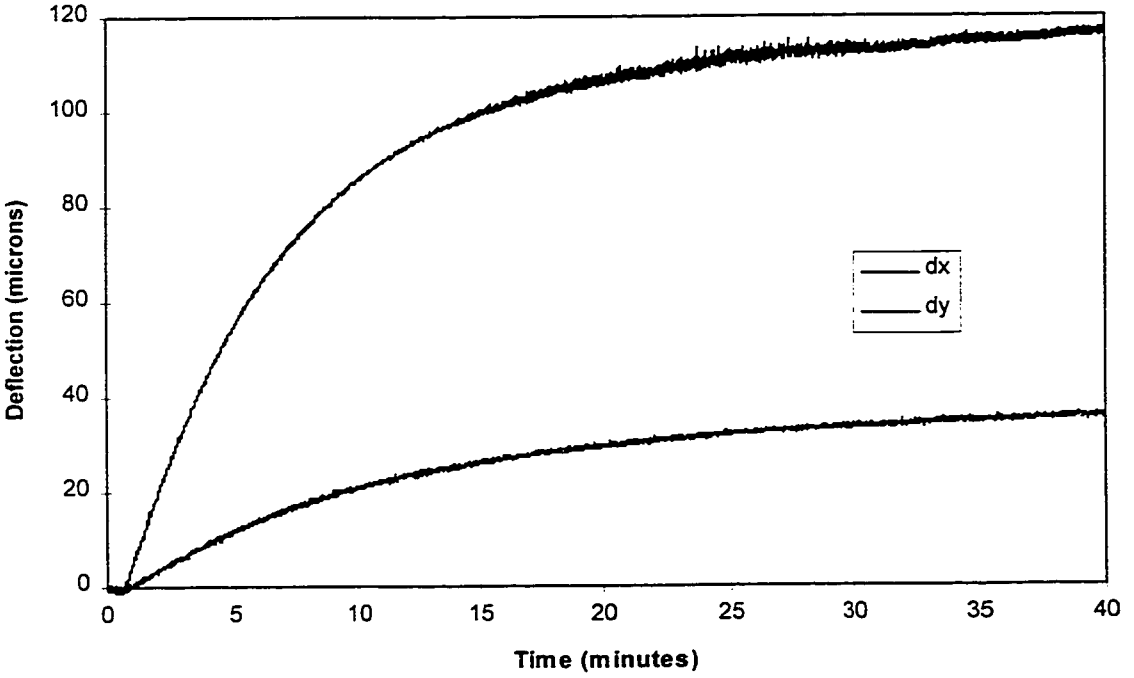

Figure 8.55: Estimated Uncompensated Deflection for Case 1: Step Input Magnitude Q=0.5

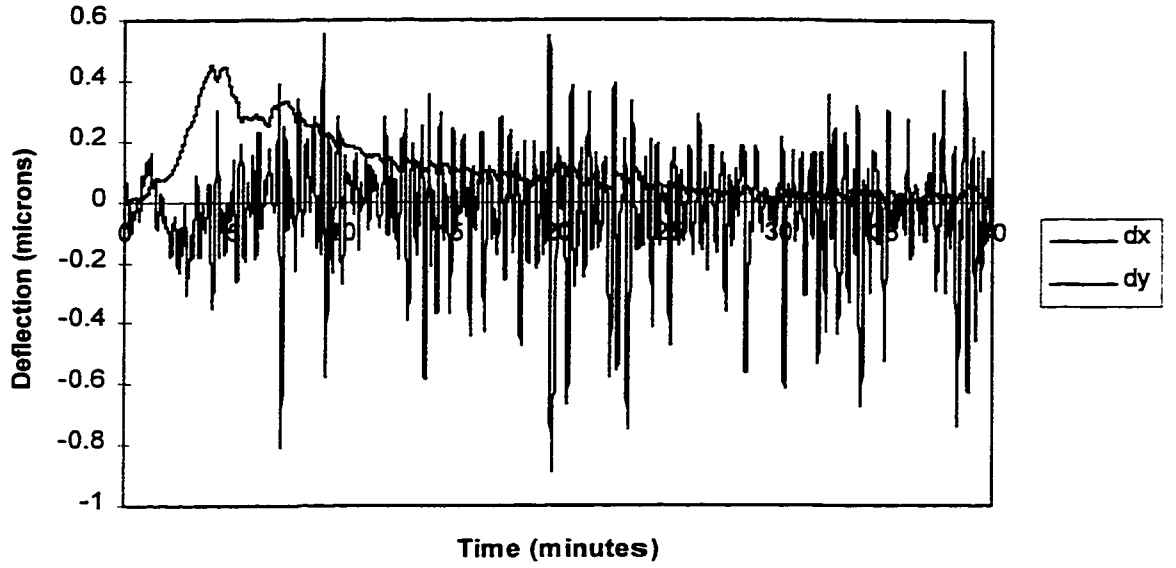

Figure 8.56: Estimated deflection Error for Case 1: Step Input Q=0.5

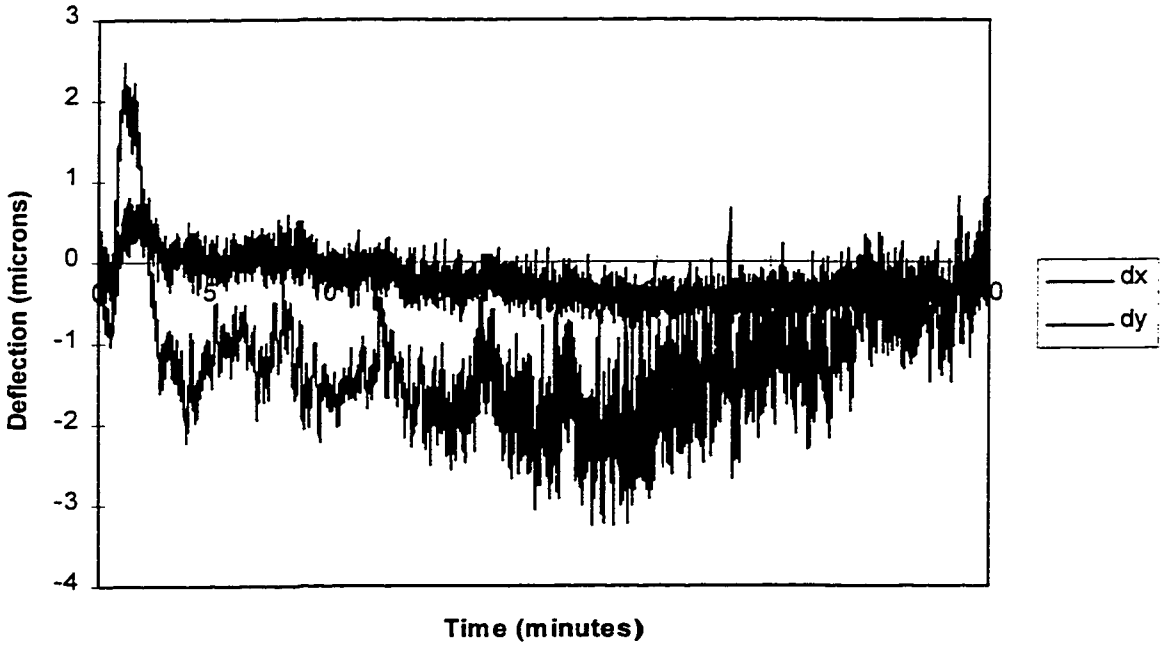

Figure 8.57: Actual Deflection Error for Case 1: Step Input Q=0.5

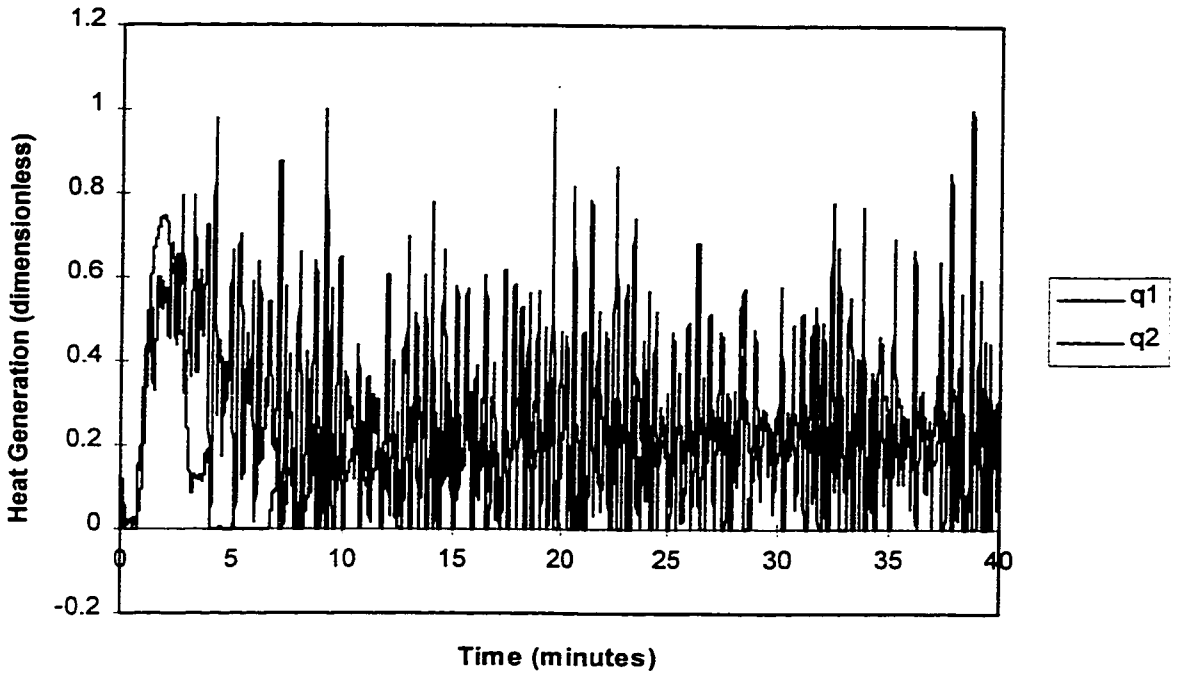

Figure 8.58: Actuator Heat Generation for Case 1: Step Input Q=0.5

thermal deflection error for this input, which is labelled $\delta_{err(k)}$ in figure 8.51, and figure 8.57 shows the actual deflection error for this input, obtained by the LVDT position measurement apparatus. A plot of the actuator heat generation is shown in figure 8.58.

A comparison of figures 8.55 and 8.57 shows that the estimated uncompensated thermal deflection of 119 microns has been reduced to an actual controlled deflection of +2.5 microns to -3.5 microns, for a total range of 6 microns, and a percent reduction of 95%. Figure 8.58 shows that the heat actuators do not suffer any upper bound saturation for this input, although there is considerable lower bound saturation.

8.8.2 Test Case 2: Single Step Input of Magnitude 1.0

Test case 2 is a single step in heat generation from zero to 1.0, beginning at t=30 seconds. Figure 8.59 shows the measured temperature difference profile for this test case. Figure 8.60 shows the on-line estimate of the disturbance heat generation, and Figure 8.61 shows the estimated uncompensated thermal deflection of the structure for this input, which reaches 243 microns in Y, and 84 microns in X. Figure 8.62 shows the actual and estimated controlled deflection of the structure, which is in the range of +7 to -2.5 microns in Y and within +3.5 and -1 in X, for a maximum total range of 8.5 microns. Figure 8.63 shows the actuator heat generation for this test input.

The figures show that the thermal deflection control system has reduced the net thermal deflection by 96% in Y and by 95% in X, a slight improvement over test case 1. The reason for the improvement in the percent reduction is partly due to the increased signal to noise ratio of the measured temperature difference for the larger input, shown in figure 8.59. Another reason for the improved percentage reduction is that the saturation of the actuation heaters is now approximately equal at the maximum and minimum cut-off values, shown in figure 8.63. However, in absolute terms the thermal deflection error has increased from 6 microns in case

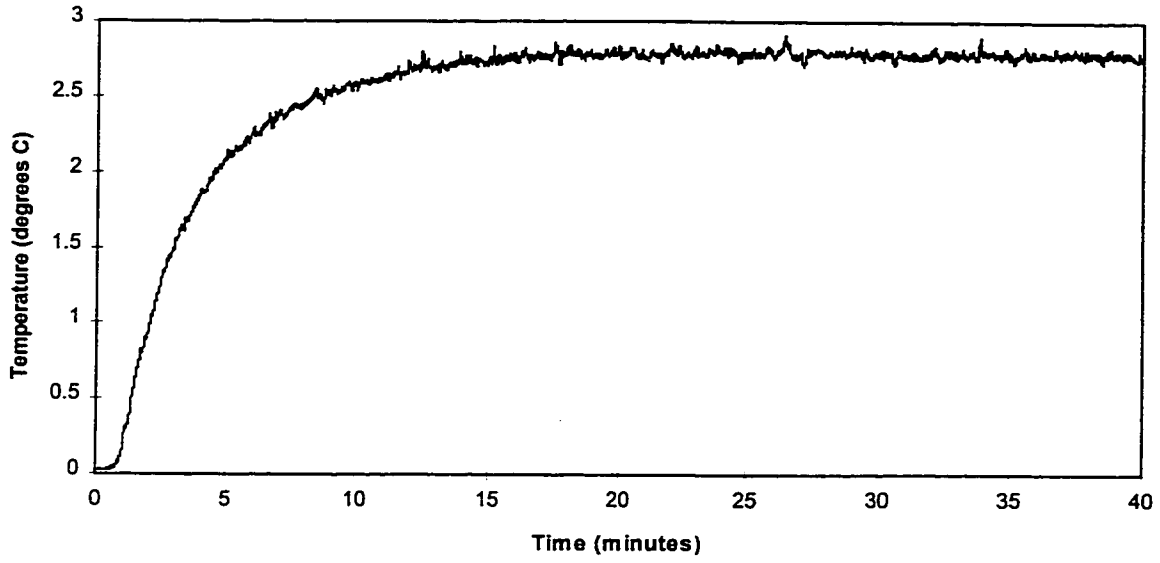

Figure 8.59: Temperature Difference for Case 2: Step Input Magnitude Q=1.0

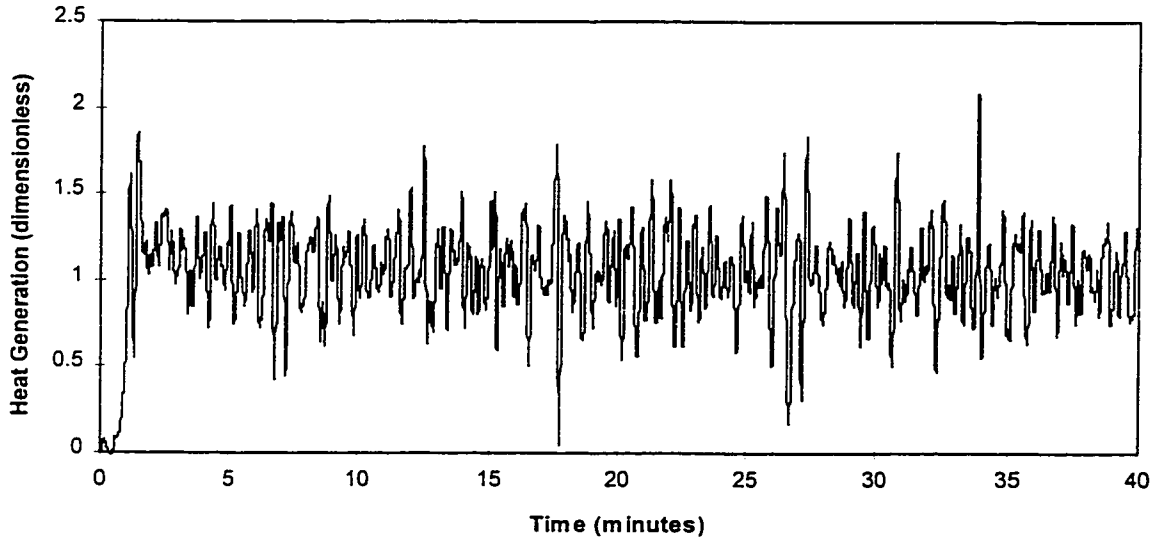

Figure 8.60: Estimated Heat Generation for Case 2: Step Input Magnitude Q=1.0

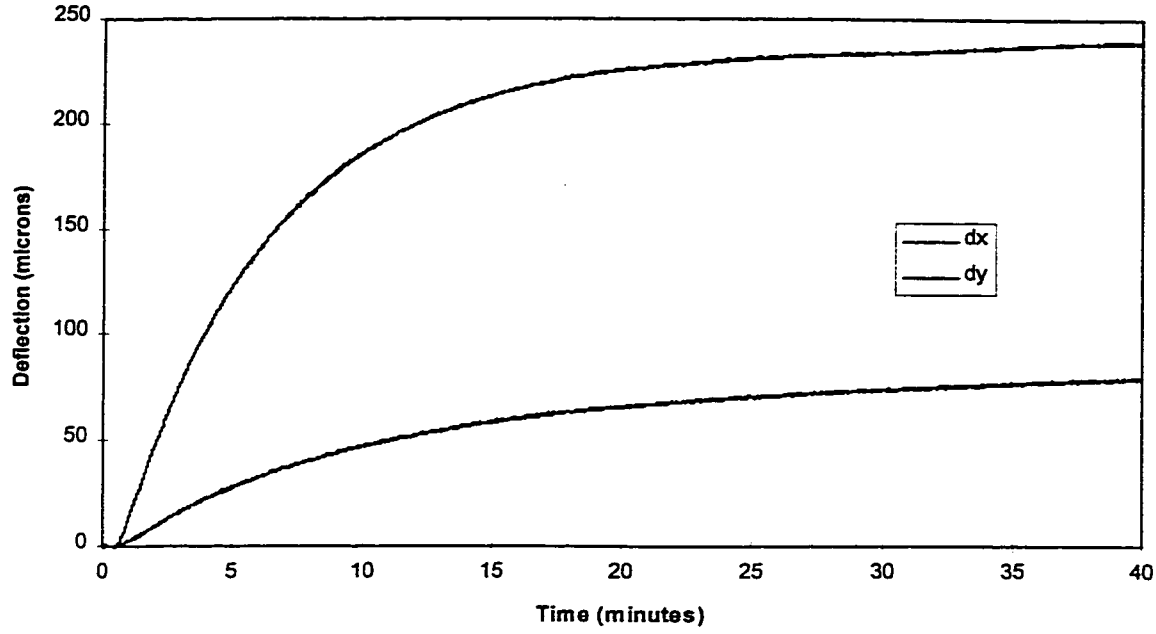

Figure 8.61: Uncompensated Deflection for Case 2: Step Input Magnitude Q=1.0

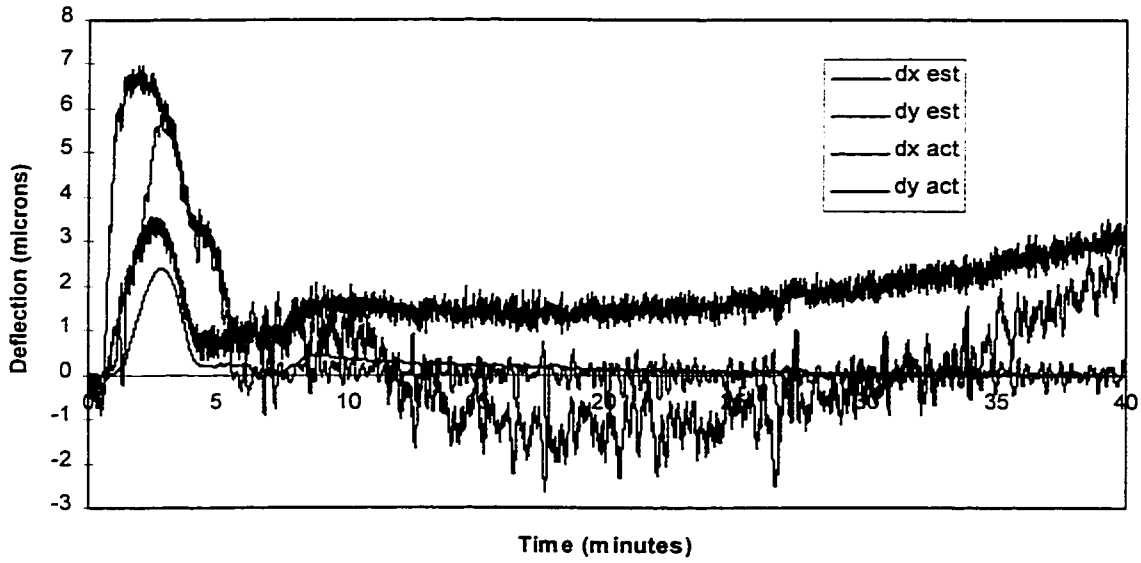

Figure 8.62: Actual and Estimated Controlled Deflection for Case 2: Step Input Q=1.0

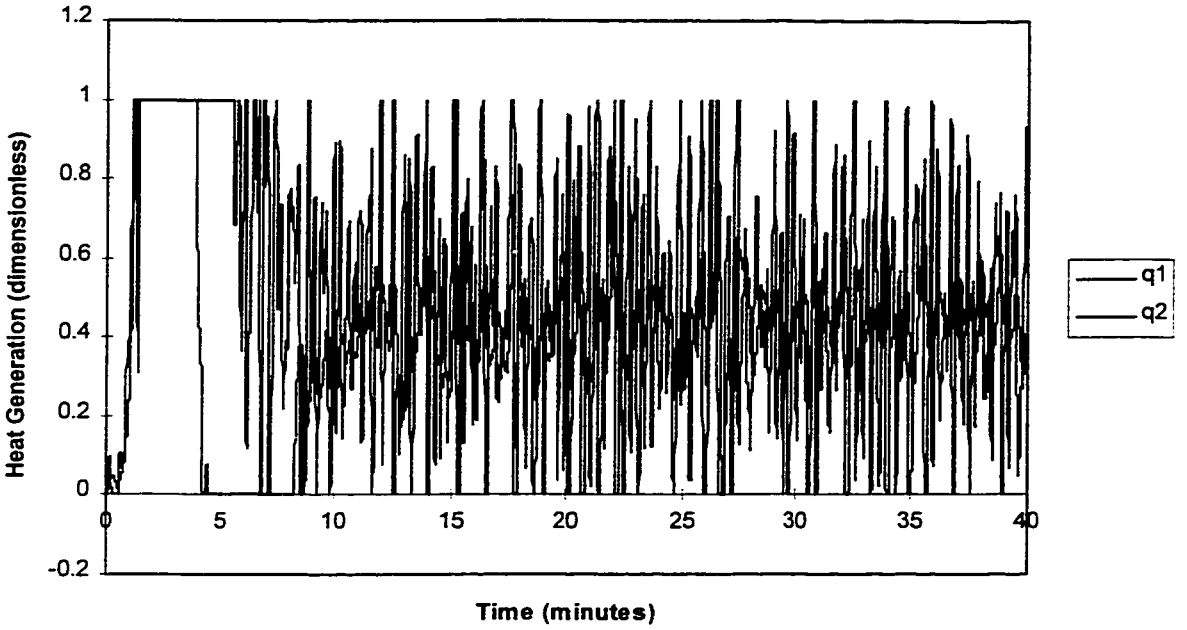

Figure 8.63: Actuator Heat Generation for Case 2: Step Input Magnitude 1.0

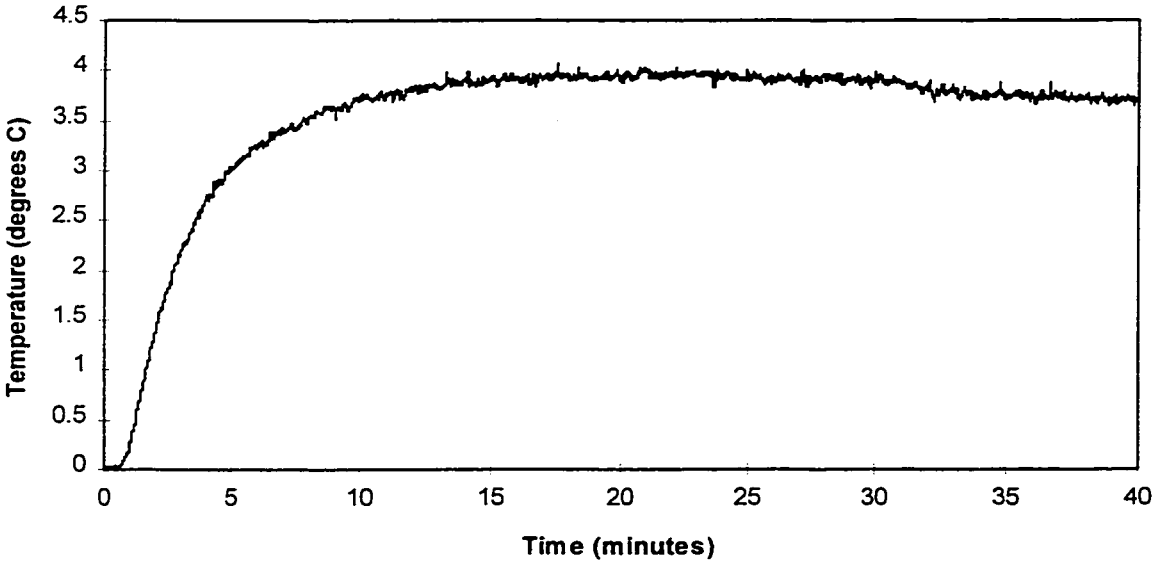

Figure 8.64: Temperature Difference for Case 3: Step Input Magnitude 1.5

1 to 9.5 microns in case 2. A large part of this absolute error is due to the initial saturation of the control heaters, which is evident by the large peak in the estimated controlled deflection in figure 8.62 which mirrors the actual deflection. This peak in estimated deflection indicates that the controller is aware of the deflection but is unable to compensate for it because the heaters are in a state of saturation, shown in figure 8.63.

8.8.2 Test Case 3: Single Step Input of Magnitude 1.5

Test case 3 is a single step disturbance of magnitude 1.5, applied at t=30 seconds. Figure 8.64 shows the temperature difference profile, figure 8.65 shows the estimated heat generation, and figure 8.66 shows the estimated uncompensated thermal deflection. Figure 8.67 shows the estimated and actual controlled deflection and figure 8.68 shows the actuator heat generation.

The purpose of this input is to show the limitations of the control system when subjected to too large of a disturbance input. Figure 8.67 shows that both the estimated and the actual thermal deflection reach an initial peak of 32 microns in Y before coming back slowly to within 7 microns error. The reason for this tracking error is the initial saturation of heater q1, lasting for nearly 15 minutes, as shown in figure 8.68. The result of this test case shows that the thermal deflection control system cannot be used to compensate for a step input of magnitude zero to 1.5. Furthermore, the steady-state error shows that an input this large produces significant saturation error, even in the steady-state. Thus, the conclusion is that the absolute heat generation cannot reach much beyond 1.0 for this system of compensation heaters. In general, any system of compensation heaters will have a maximum operating range for the disturbance heat source.

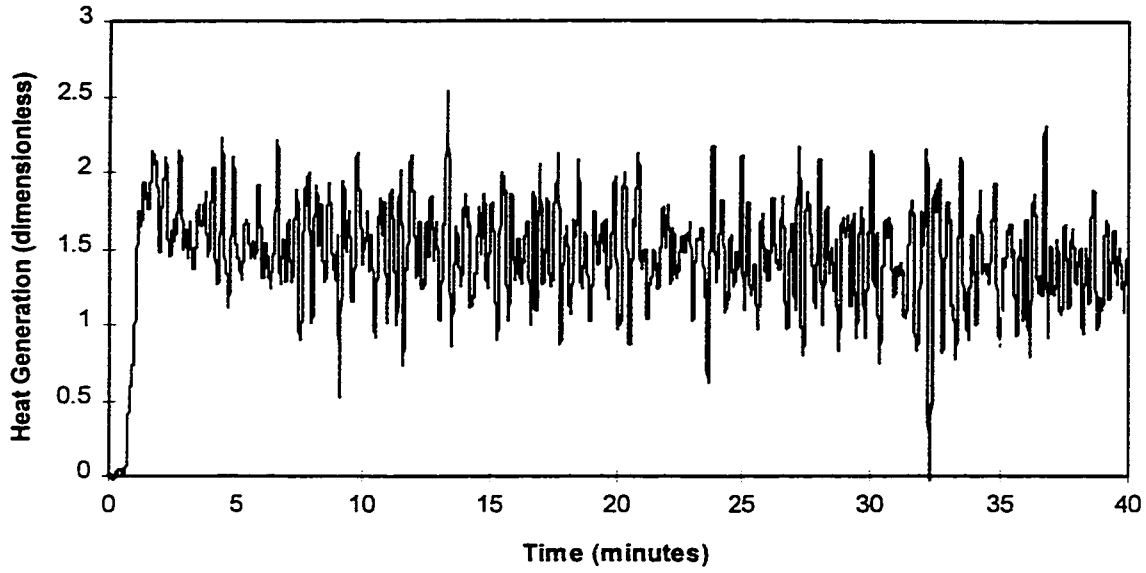

Figure 8.65: Estimated Heat Generation for Case 3: Step Input Magnitude 1.5

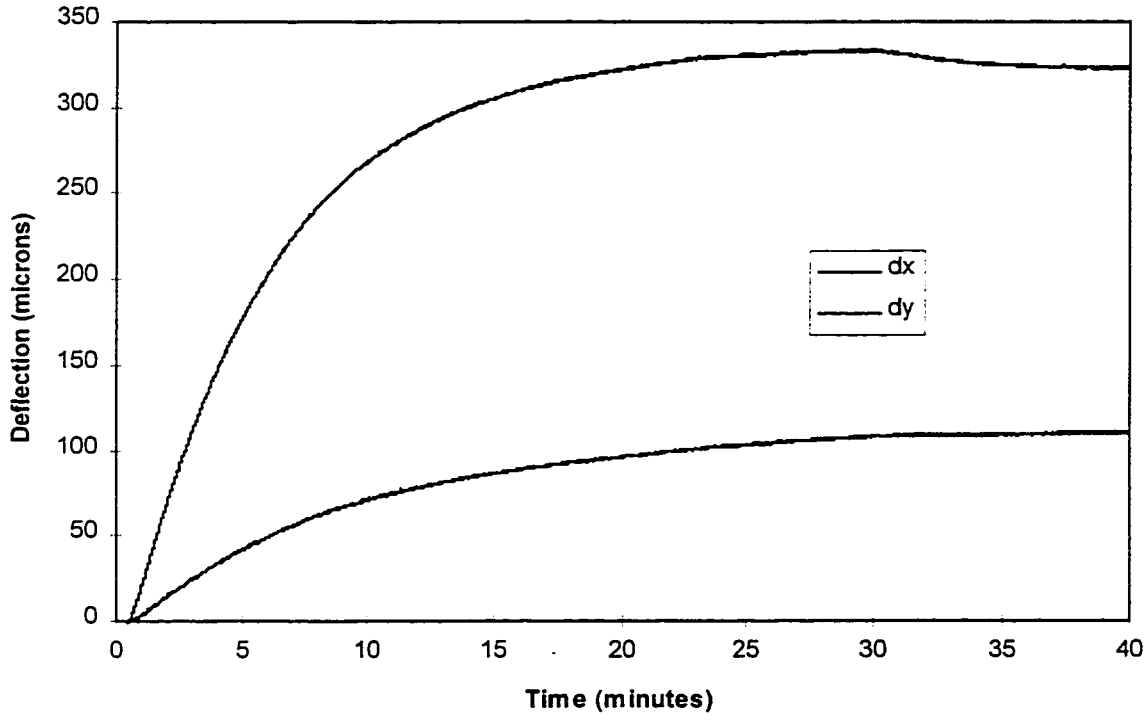

Figure 8.66: Estimated Uncontrolled Deflection for Case 3: Step Input Magnitude 1.5

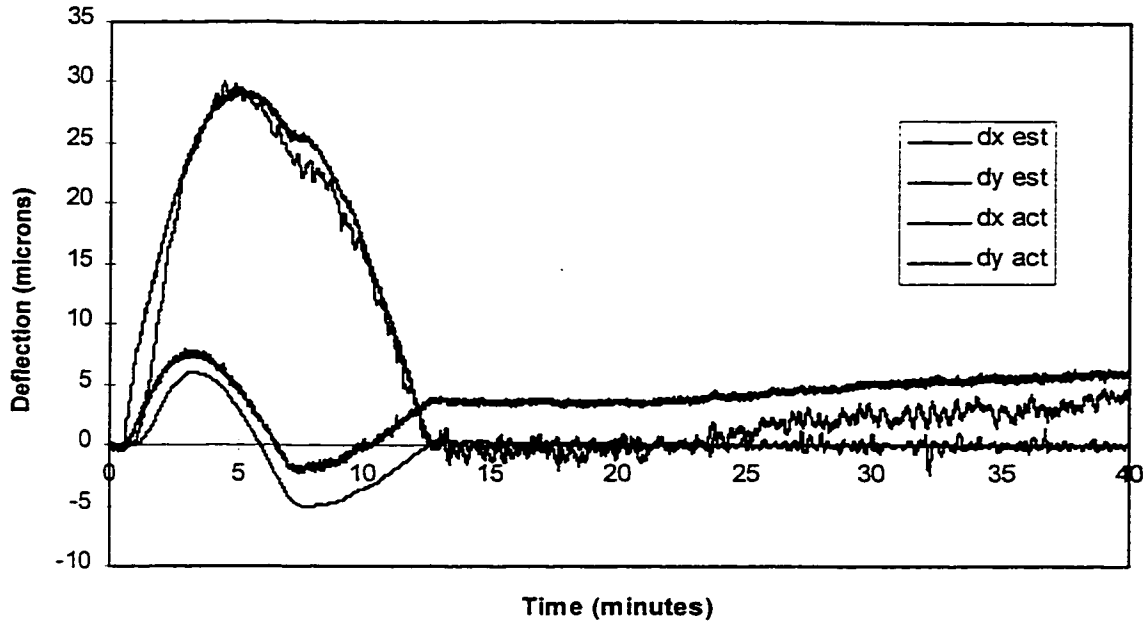

Figure 8.67: Estimated and Actual Controlled Deflection for Case 3: Step Input Q=1.5

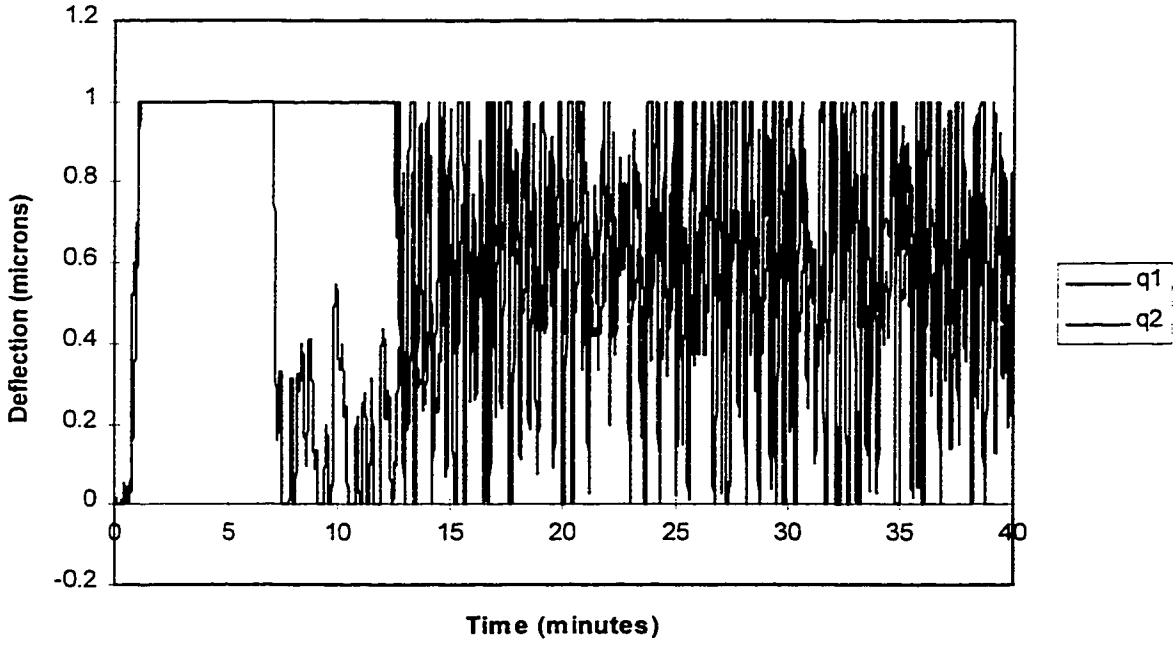

Figure 8.68: Actuator Heat Generation for Case 3: Step Input Magnitude Q=1.5

8.8.3 Discussion of the Test Case Results

The results show that the thermal deflection control system is capable of reducing the net thermal deflection of the structure by more than 93% for disturbance heat magnitudes up to Q_d=1.0, with a maximum deflection range of 9.5 microns. The two main sources of error are 1) errors in the estimation of the disturbance heat generation, and 2) actuation error as a result of control heater saturation. For a step input, most of the disturbance heat estimation error occurs in the first minute following the application of the step input, as shown in figures 8.54 and 8.60, which produces an initial peak in the net thermal deflection, shown in figures 8.57 and 8.62. The effect of actuator saturation error is to produce deflection error throughout the operation of the control system, although this error is accentuated by sudden changes in the demand for control heating, as shown in figures 8.57 and 8.62.

A simple way to improve machining accuracy when using this control system is to wait five minutes after an abrupt change in the operating conditions of the machine before using the machine to cut metal. For test case 2, with an input magnitude Q_d=1.0, this would reduce the absolute deflection error range from 9.5 microns to 4 microns. Although this simple solution would be effective for heat inputs that are related to the speed of the motor or the spindle, it could not be used effectively for heat inputs that are related to the cutting forces.

A more effective method of improving the accuracy of this system is to locate the measured temperature points closer to the heat source. Although this tends to increase the signal to noise ratio of the measurement, it also reduces the initial temperature delay to a step input, which has the effect of reducing the delay in the estimation of the disturbance heat generation, as discussed in chapter 5. As already discussed, the distance of the measured temperatures from the disturbance source used for the above experiments is at the extreme outer end of what would be expected for the heat sources on a real machine tool. In the next sections, the performance

of the system will be investigated for measured temperature points that are closer to the heat source.

8.8.4 Test Case 4: Unit Step Response of System with Intermediate Temperature Nodes

Figure 8.69 shows the locations of the intermediate temperature measurement pair, labelled pair 2, which are 1.7 centimetres and 3.7 centimetres form the outer edge of the disturbance heat source. Figure 8.70 shows the measured temperature difference for a disturbance step input Q_d=0.5, along with the calibrated generalized thermal model and the regularization term. Figure 8.71 shows the first five minutes of the measured and calibrated temperature profiles, showing the initial regularization more closely. Figure 8.72 shows the actual thermal deflection of the structure corresponding to the above input, along with the calibrated model. Both the temperature and the thermal deflection calibrations were done using a subset of the total data series, using a higher density of points for the initial part of the curve and the lowest density near the steady-state. Only the temperature and deflection samples that were actually used in the calibration are shown in figures 8.71 and 8.72.

The input for test case 4 is a heat generation step from zero to 0.5, which produces the temperature difference of node pair 2 shown in figure 8.73. Figure 8.74 shows the estimated uncontrolled deflection, which reaches 104 microns in Y and 32 microns in X. Figure 8.75 shows the actual and estimated net thermal deflection error, and figure 8.76 shows the estimated disturbance heat generation.

A comparison of figures 8.57 and 8.75 shows that node 2 pair has improved the performance of the control system over node pair 1 by reducing the initial peak in actual thermal deflection from about 2.5 microns to about 2.0 microns. This improvement is due to a reduction in the initial delay in the estimated thermal deflection, as expected by locating the measured temperature nodes closer to the heat source. The system using node pair 2 also has a 0.5 micron

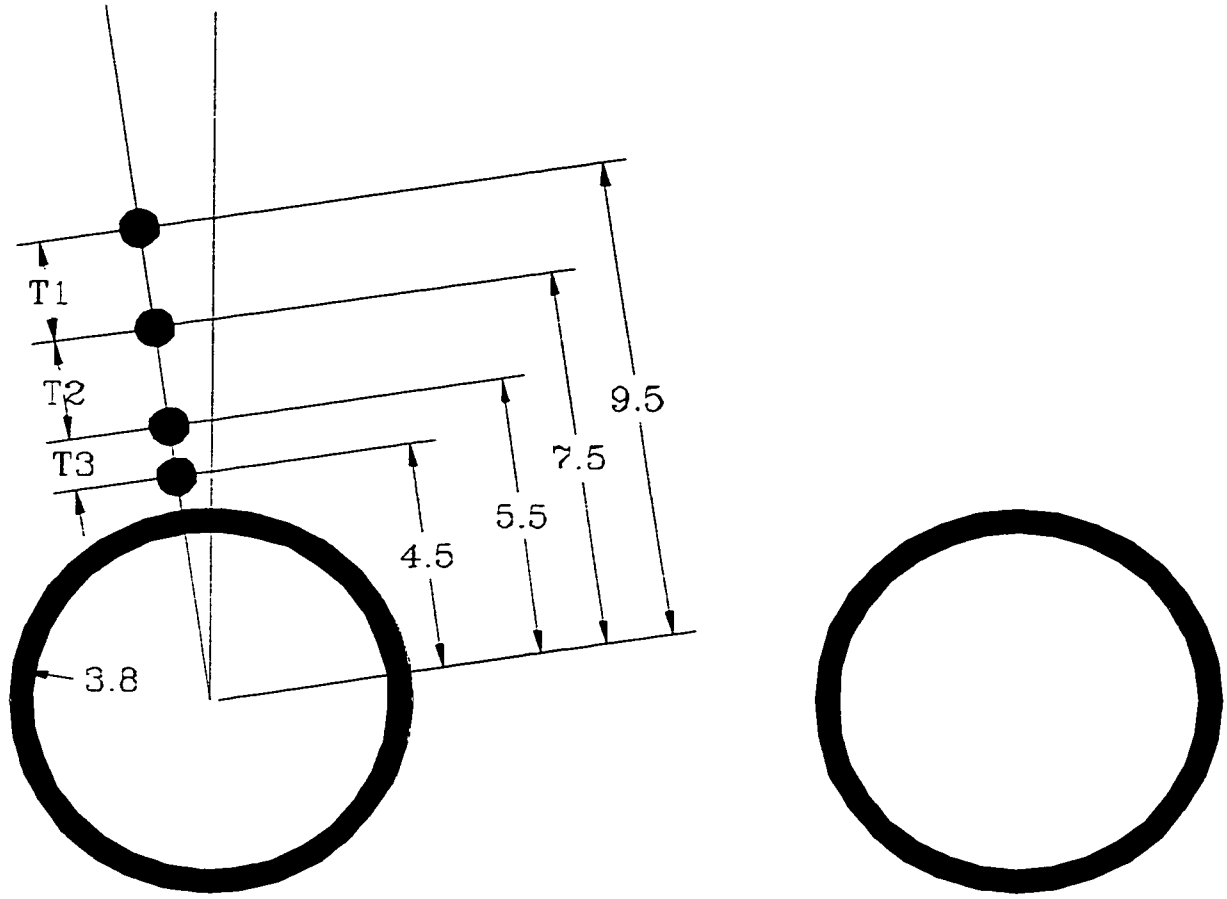

Figure 8.69: Position of Temperature Measured Points (Dimensions in Centimeters)

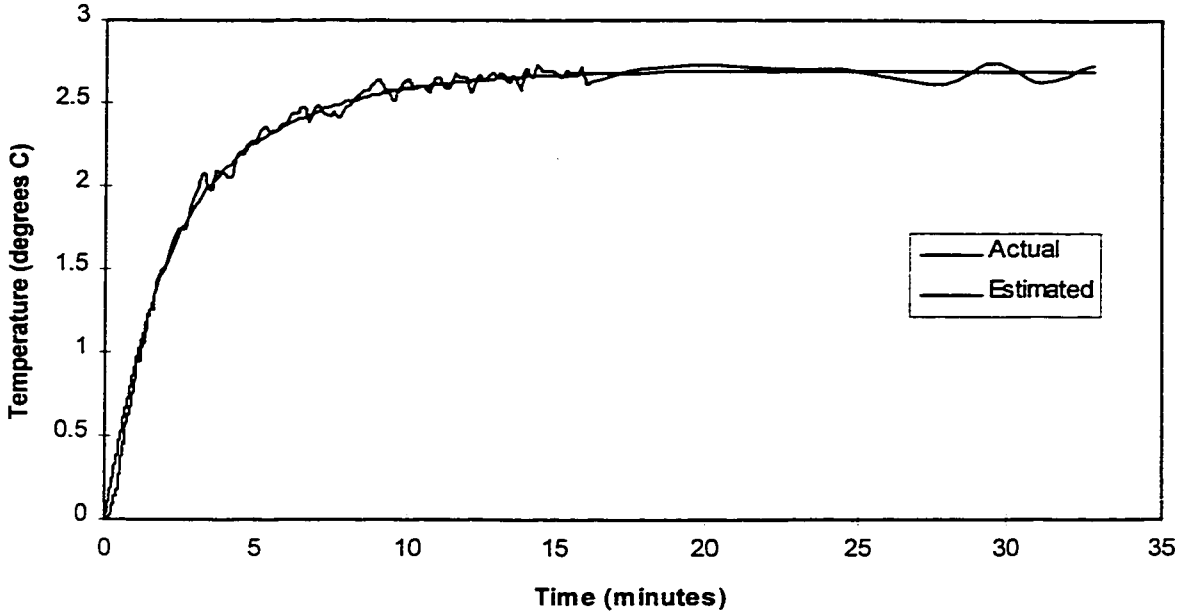

Figure 8.70: Actual and Calibrated Temperature Difference for Pair 2 Including Regularization

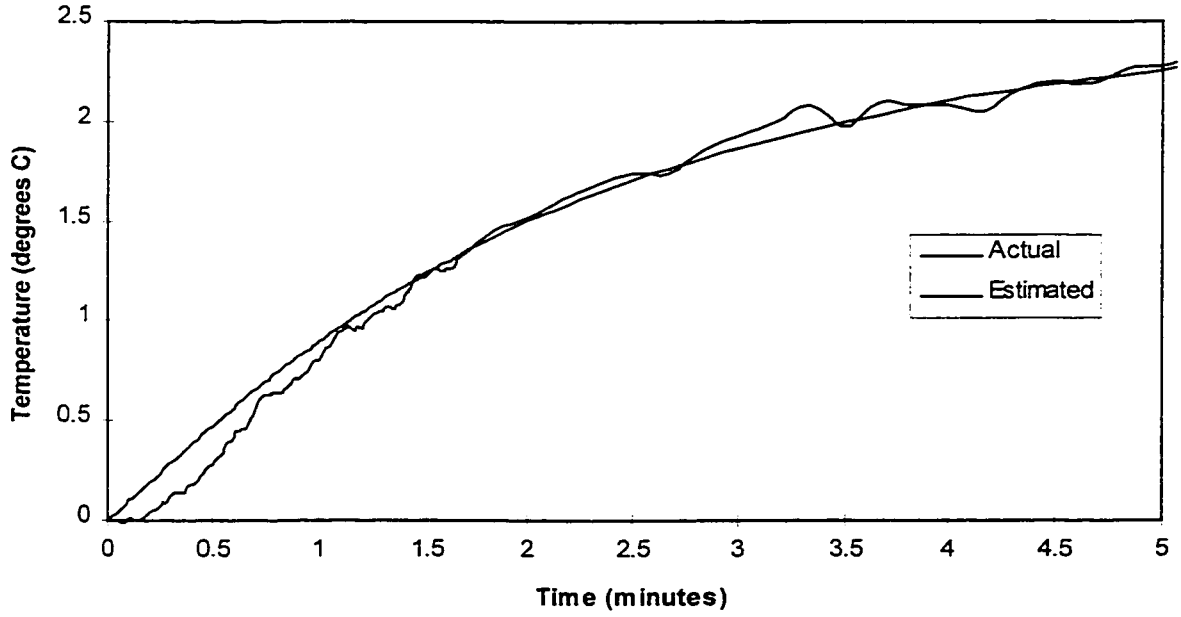

Figure 8.71: Actual and Calibrated Temperature Difference for Pair 2 Including Regularization (first 5 minutes)

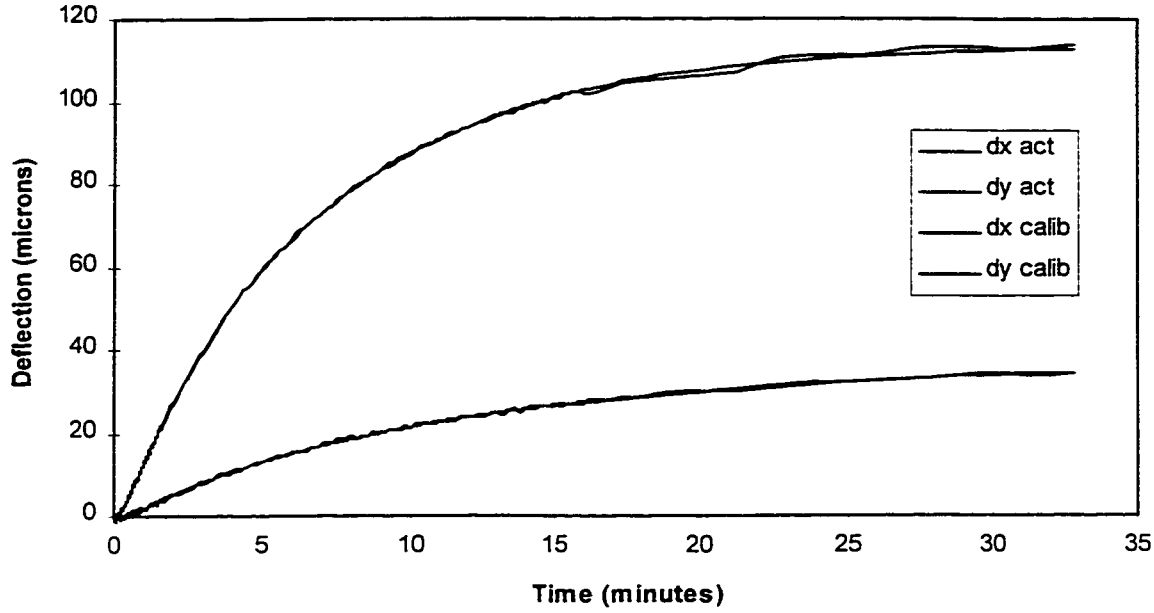

Figure 8.72: Actual and Calibrated Thermal Deflection for Calibration of Pair 2

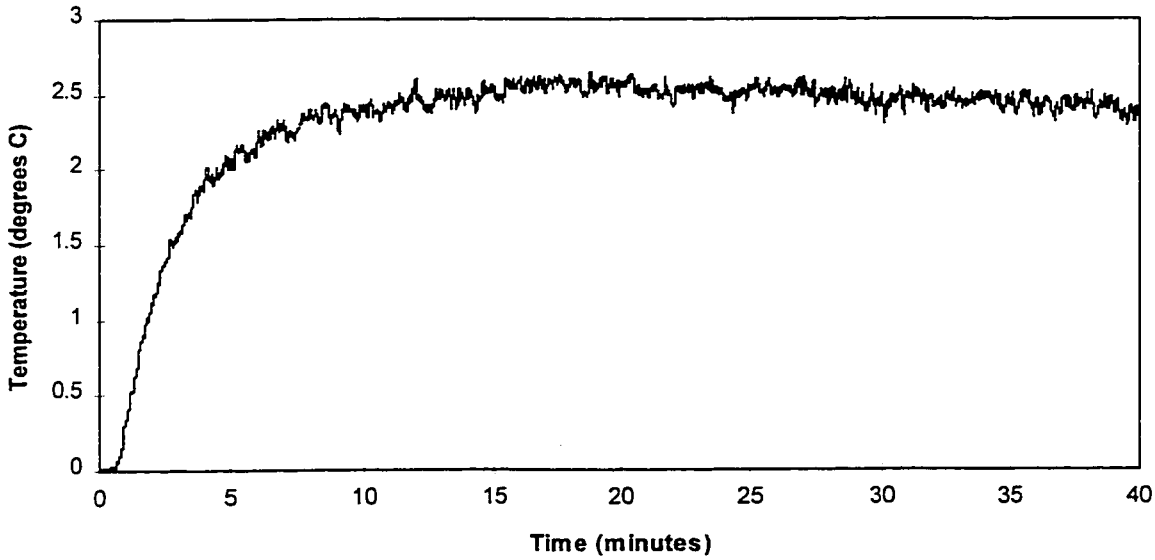

Figure 8.73: Temperature Difference for Case 4: Step Input Magnitude Q=0.5

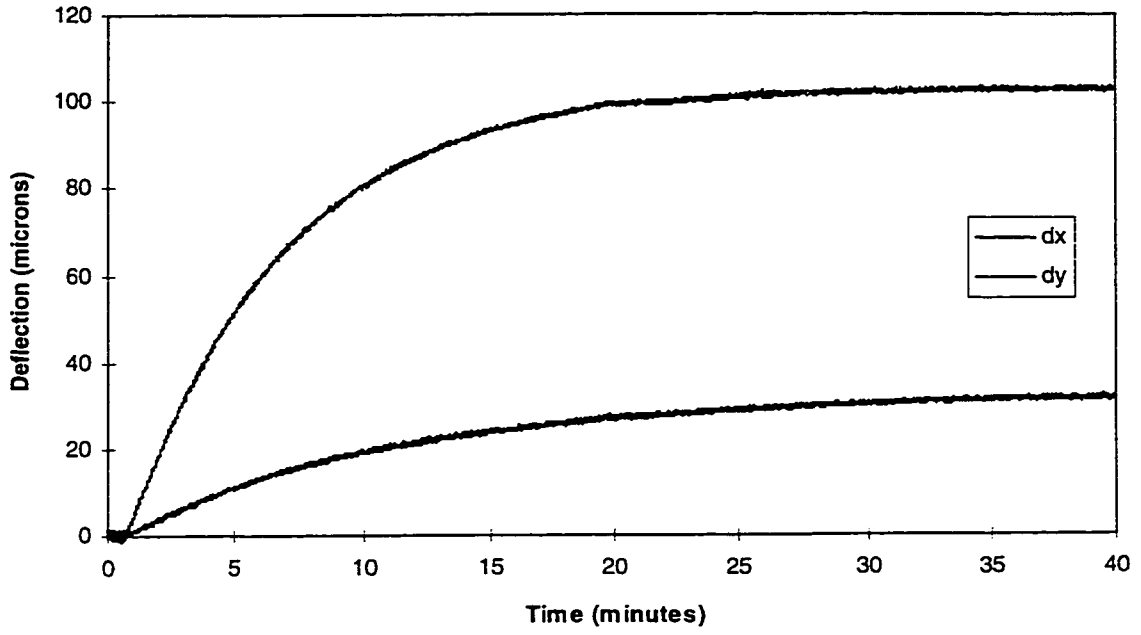

Figure 8.74: Estimated Uncontrolled Deflection for Case 4: Step Input Magnitude Q=0.5

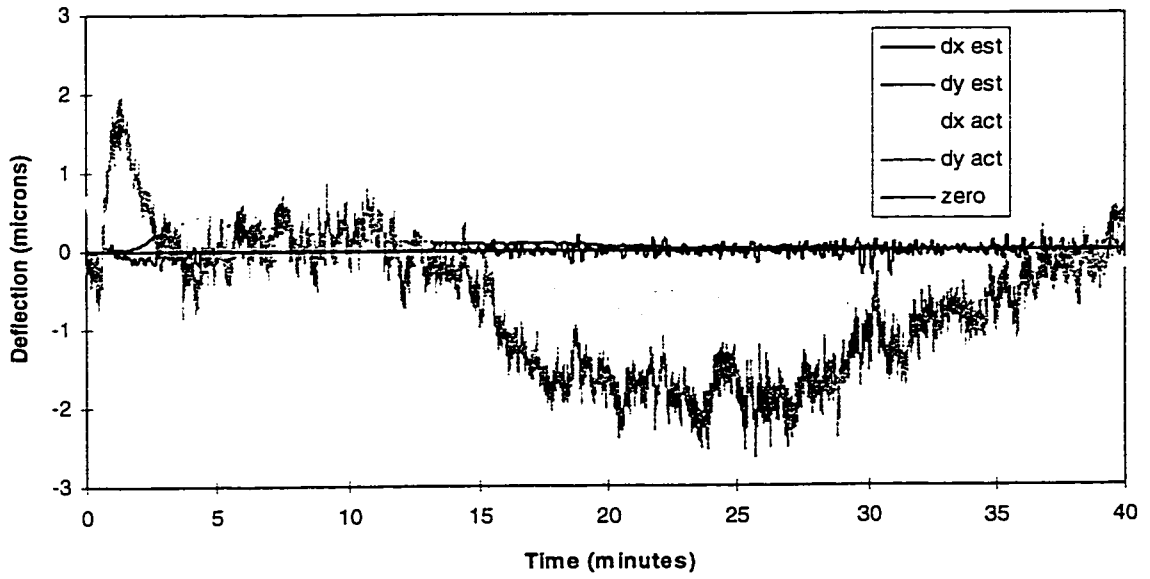

Figure 8.75: Estimated and Actual Controlled deflection for Case 4: Step Input Q=0.5

lower maximum error between 10 and 30 minutes, which is probably due to random variations and possibly a more accurate thermal deflection calibration.

8.8.5 Test Case 5: Unit Step Response of System with Close Temperature Nodes

Figure 8.69 shows the locations of the inner most temperature measurement pair, labelled pair 3, which are 0.7 centimetres and 1.7 centimetres form the outer edge of the disturbance heat source. Figure 8.77 shows the measured temperature difference for a disturbance step input Q_d=0.5, along with the calibrated generalized thermal model and the regularization term. Figure 8.78 shows the first five minutes of the measured and calibrated temperature profiles, showing the initial regularization more closely. The calibrated thermal deflection model is shown in figure 8.72. Since the temperature data for the calibrations of node pairs 2 and 3 were both collected for the same input, the thermal deflection model is common to both.

The input for test case 5 is also a heat generation step from zero to 0.5, which produces the temperature difference of node pair 3 shown in figure 8.79. Figure 8.80 shows the estimated uncontrolled deflection, which reaches 106 microns in Y and 35 microns in X. Figure 8.76 shows the estimated disturbance heat generation, and figure 8.75 shows the actual and estimated net thermal deflection error.

A comparison of figures 8.54, 8.76 and 8.81 shows how the signal to noise ratio of the estimated heat generation varies with the position of the measured nodes. As the measured nodes are moved closer to the source the signal to noise ratio of the measured temperature difference is increased but the singularities of the convolution transfer function are reduced. As a result of these conflicting effects, the signal to noise of the ratio of the estimated heat generation is reduced slightly from node pair 1 to node pair 2, however it increases considerably from node pair 1 to node pair 3. A comparison of figures 8.57 and 8.82 shows that node 3 pair has improved the performance of the control system over node pair 1 by reducing the initial

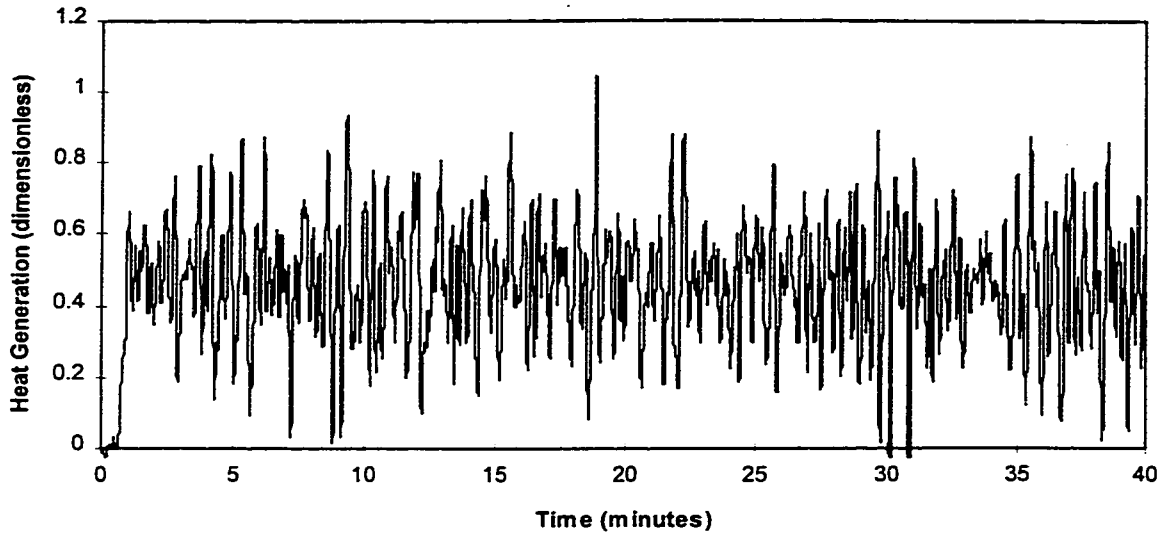

Figure 8.76: Estimated Heat Generation for Case 4: Step Input Magnitude Q=0.5

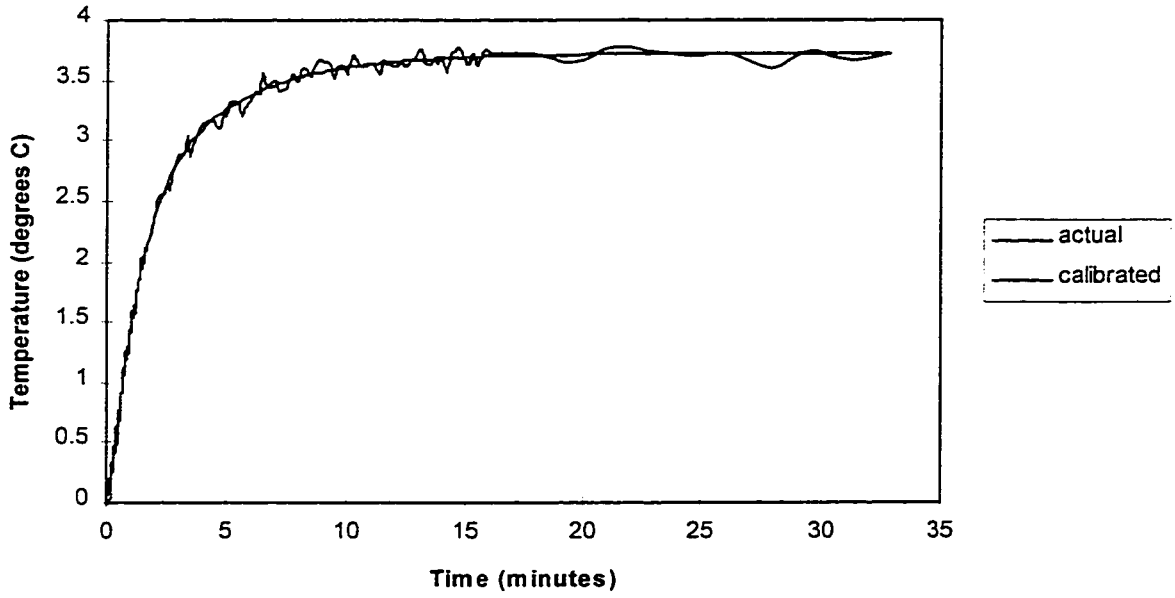

Figure 8.77: Actual and Calibrated Temperature Difference for Node Pair 3 Including Regularization

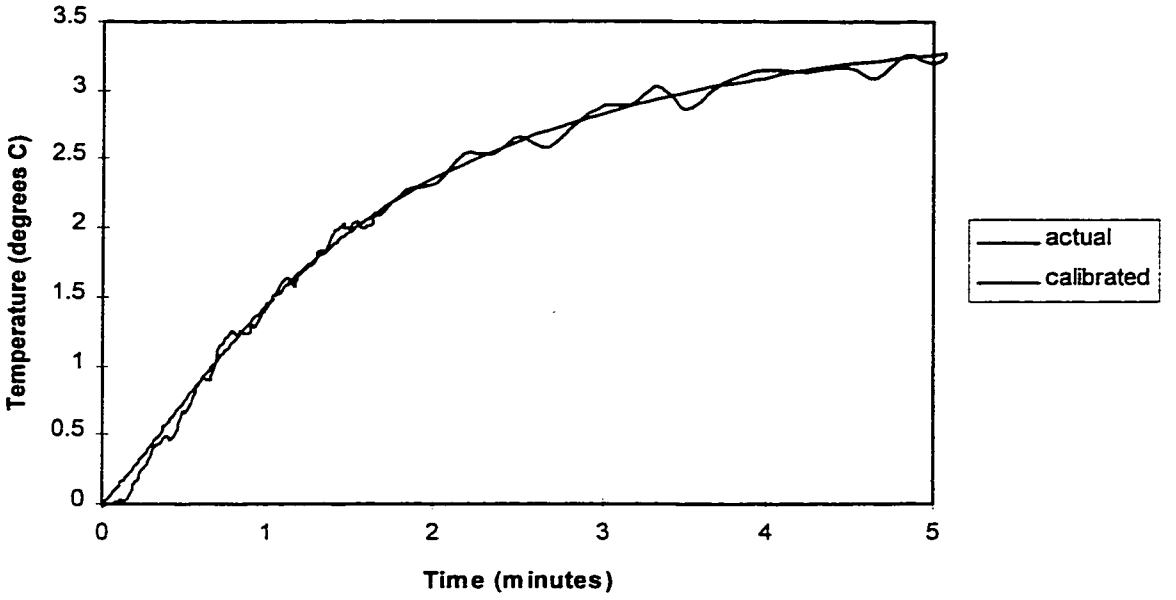

Figure 8.78: Actual and Calibrated Temperature Difference for Pair 3 Including Regularization (first 5 minutes)

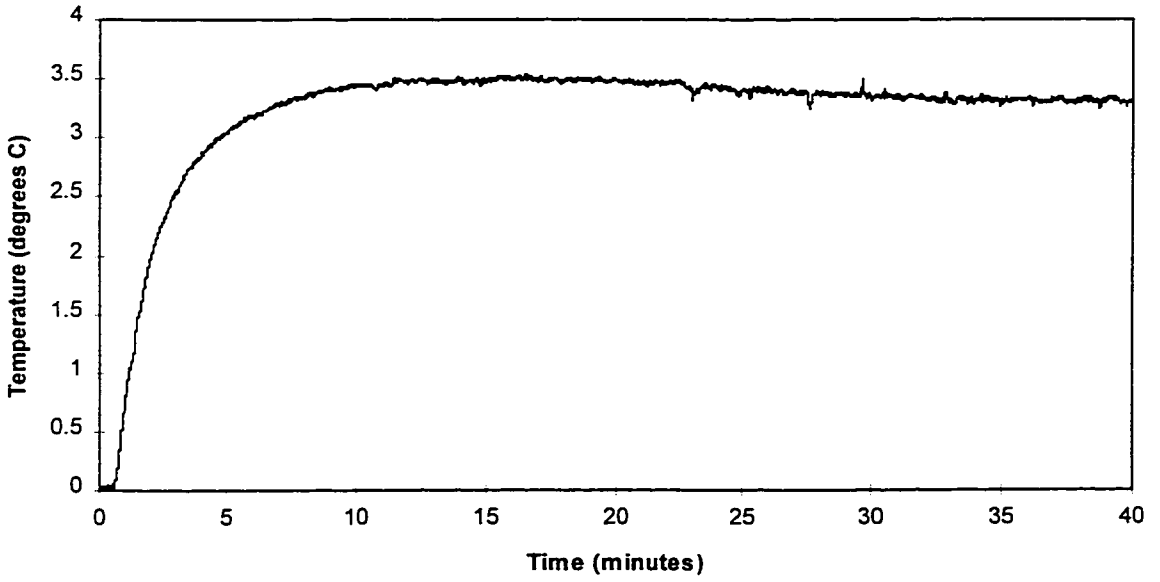

Figure 8.79: Temperature Difference for Case 5: Step Input Magnitude Q=0.5

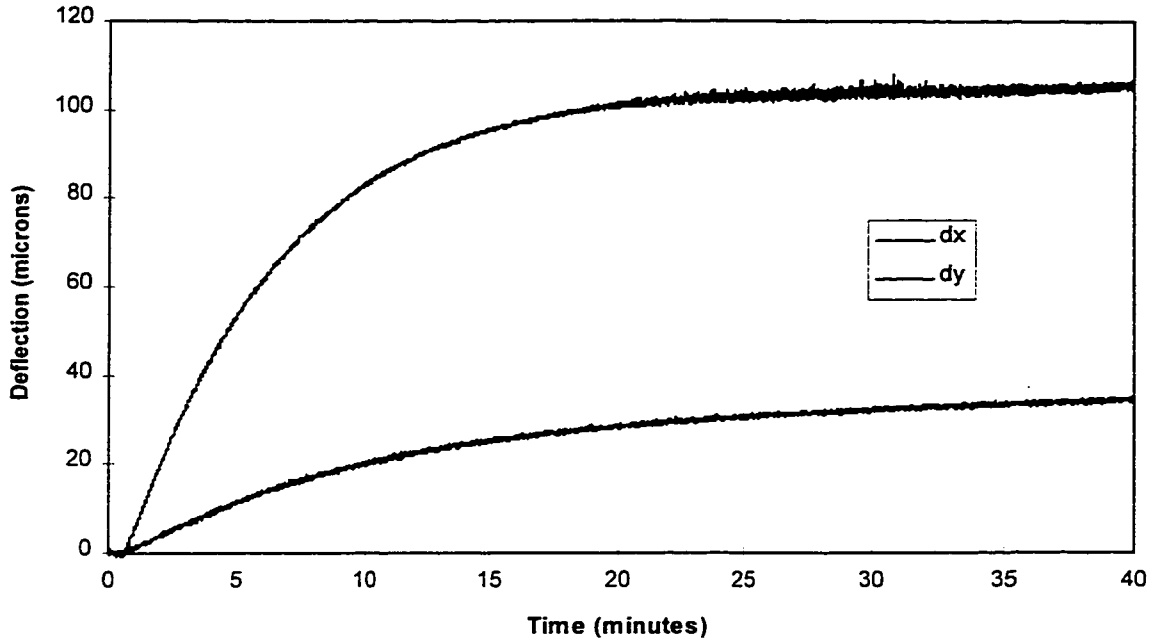

Figure 8.80: Estimated Thermal Deflection for Case 5: Step Input Magnitude Q=0.5

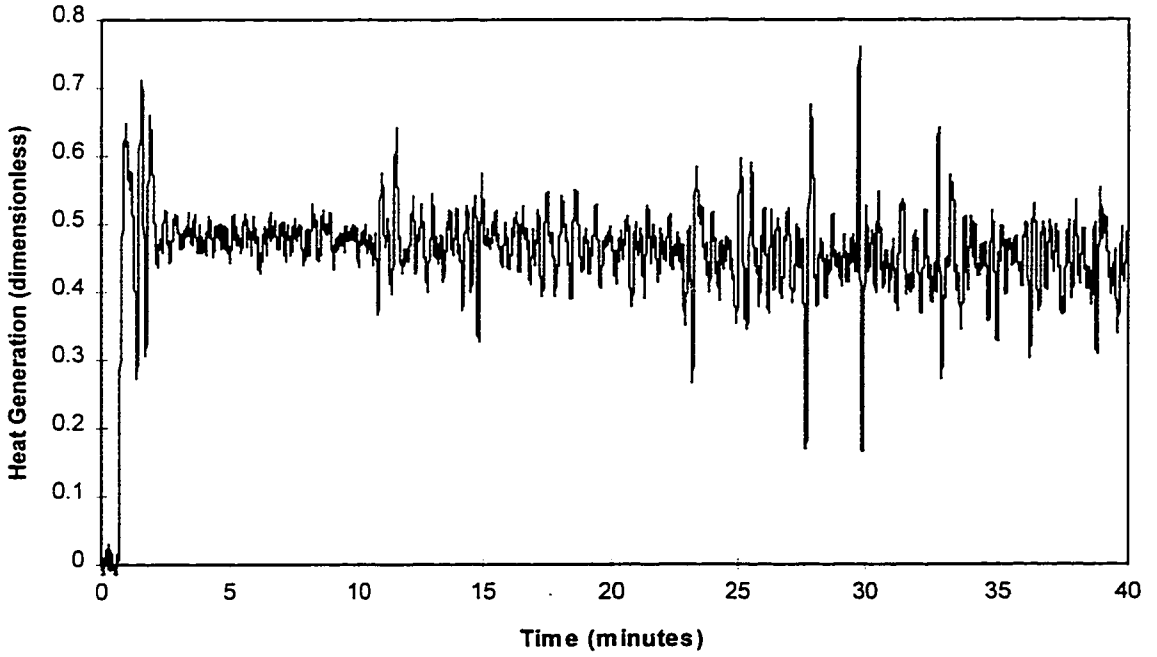

Figure 8.81: Estimated Heat Generation for Case 5: Step Input Magnitude Q=0.5

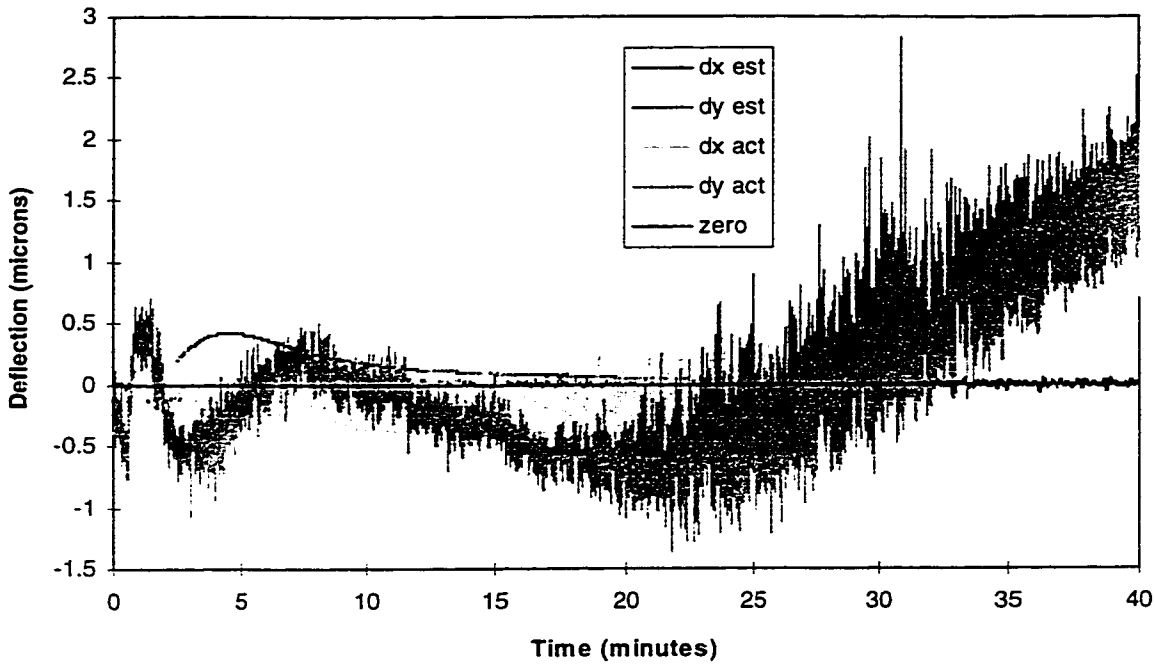

Figure 8.82: Estimated and Actual Controlled Deflection for Case 5: Step Input Q=0.5

peak in actual thermal deflection from about 2.5 microns to about 0.7 microns. The total error range of the system using node pair 3 is about 4 microns, compared with 9.5 microns for the system using node pair 1.

8.8.6 Test Case 6: Response of System to Arbitrary Input with Measurement Pair 1

The final test case that will be used for verification of the thermal deflection control system is an arbitrary input consisting of short steps and ramps of disturbance heat input. The input is applied manually over a period of 30 minutes, simulating the sort of duty cycle that would typically be expected from a real machine tool in operation. For the purpose of comparison with the other results, the measured temperature pair T1, shown in figure 8.69, will be used as the measured input for the IHCP solver.

Figure 8.83 shows the measured temperature difference corresponding to this heat input, and figure 8.84 shows the estimated heat generation. The magnitude of the heat generation covers the full usable range of the disturbance input, noticeably exceeding the maximum allowable Q_d between t=5 and t=10 minutes. Figure 8.85 shows the estimated uncompensated thermal deflection corresponding to this input, which rises to a maximum of 168 microns on the y-axis and 43 microns on the x-axis at about t=10 minutes. Figure 8.86 shows the actual controlled deflection, which is contained within a range of 13 microns, a reduction of 92%. As can be seen from the control heat generation plots in figure 8.87, the distinct peaks in the controlled deflection error correspond to the periods of actuator saturation in figure 8.87. The range of the controlled deflection error is somewhat larger than for the pure step cases because of the effect of cooling down the machine after t=5 minutes, which tends to saturate the controller around zero. The configuration of the heaters was chosen to maximize compensation for positive disturbance heat inputs by generating negative control deflection. The only way to produce positive control deflections is by shutting the controlled sources off and allowing the structure to cool down. This situation could be improved by adding additional control heaters

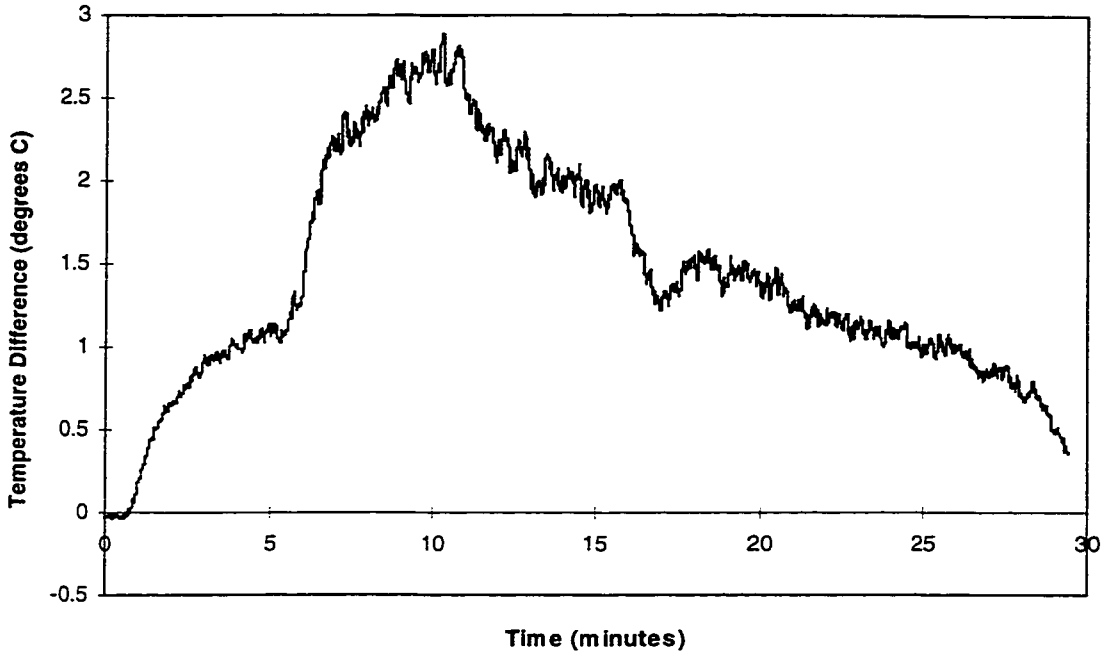

Figure 8.83: Measured Temperature Difference for Case 6: Node Pair 1, Arbitrary Input

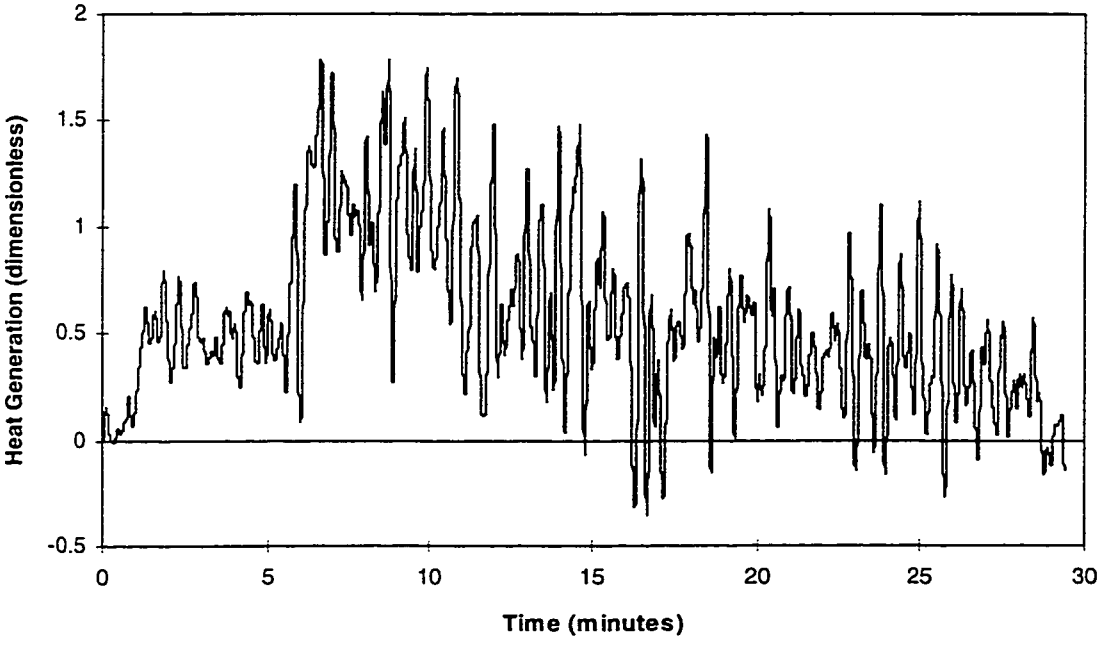

Figure 8.84: Estimated Heat Generation for Case 6: Node Pair 1, Arbitrary Input

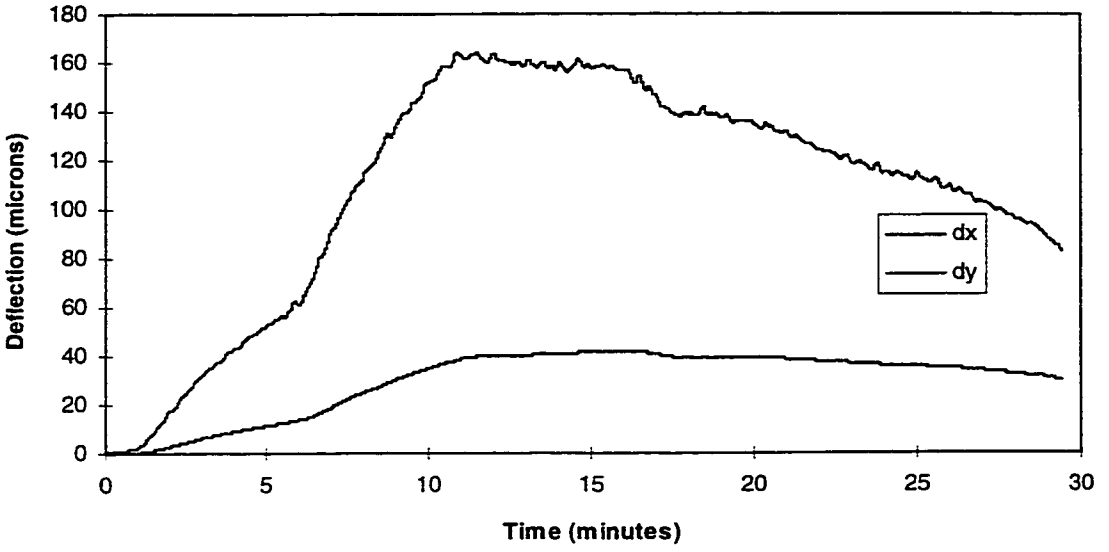

Figure 8.85: Uncompensated Deflection for Case 6: Node Pair 1, Arbitrary Input

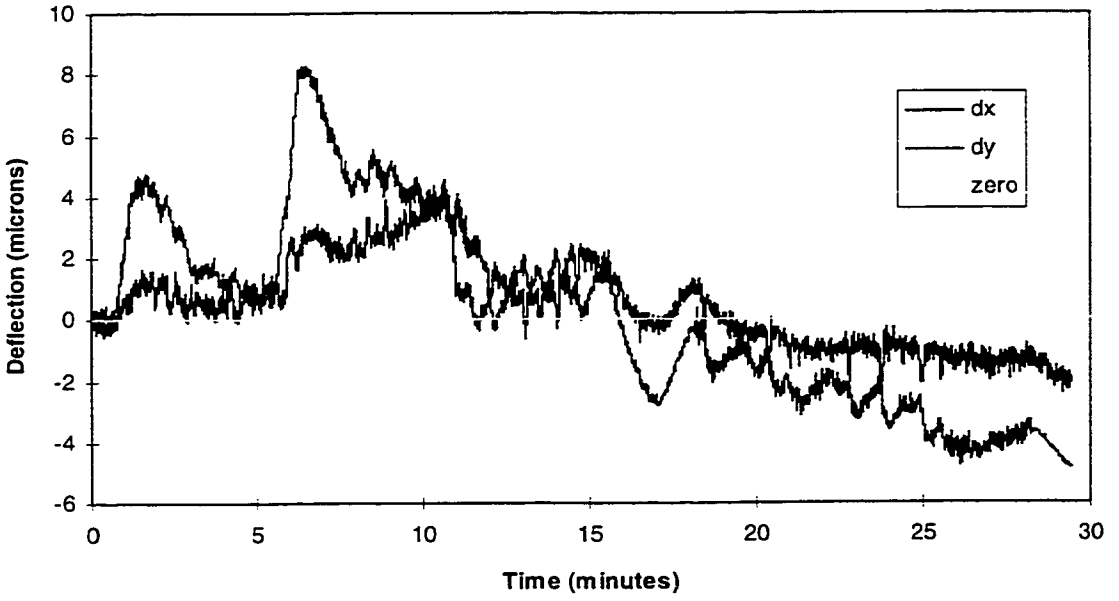

Figure 8.86: Actual Controlled Deflection for Case 6: Node Pair 1, Arbitrary Input

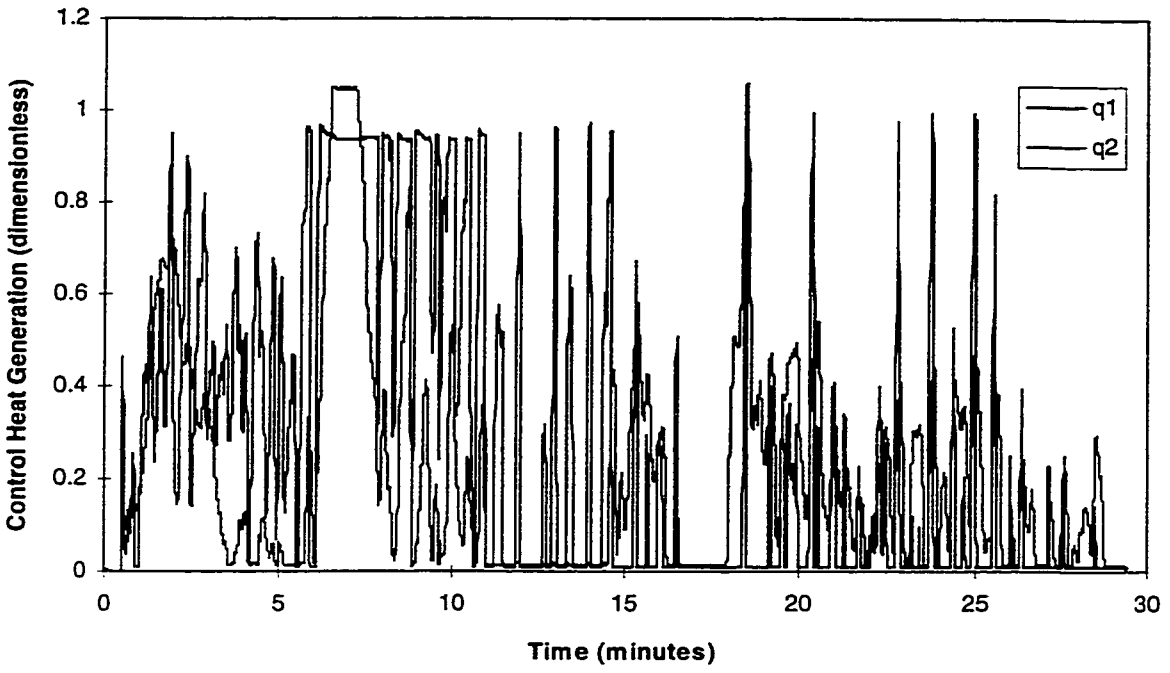

Figure 8.87: Actuator Heat Generation for Case 6: Node Pair 1, Arbitrary Input

which produce primarily negative control deflection. In general, two control heaters are required to produce controlled positive and negative deflection for one axis, a total of six for three axis. The use of such a large number of controlled heaters would probably not be practical however, and unnecessary since heater actuation would normally be used in combination with an NC position controller on some of the axes.

CHAPTER 9: CONCLUSIONS AND RECOMMENDATIONS FOR FUTURE WORK

9.1 Conclusions

A review of the research into the problem of modelling and control of the thermal deformation of machine tools has led to the identification of voids in the present state of knowledge and the key elements required to develop a generic multi-variable closed loop control system. Because of the recent availability of powerful computer facilities and sophisticated calibration software such as neural network design tools, the trend has been to devote less time to mathematical modelling for real time variable estimation. However, the computer modelling approach has not proven to be successful for accurately estimating thermal deflection in a real time environment because of the complexity of the estimation problem.

The performance of the identification process was significantly improved in this thesis by incorporating powerful mathematical tools with the numerical calibration procedures that have been used by other researchers. The approach recognizes the need for real time estimation of the heat inputs and for the thermal deformation of the machine tool structure. The concept of "generalized modelling" is used for the estimation of the heat inputs, which combines mathematical modelling with empirical calibration, and is based on the existence of a mathematical similarity between the real process and a simplified model. The mathematical form of the generalized models which were developed in this thesis is closely related to the mathematical behaviour of the real system, particularly in the delayed nature of the temperature response to a heat input. The form of the model allows for the identification of heat inputs even where the measured temperatures are located far from the source, and noise is present in the measured signal.

The real time solution to the generalized model is based on the convolution integral approach using the generalized inverse thermal transfer function $G^{-1}(s)$. The singularity

functions in $G^{-1}(s)$ are identified and an analytical solution of its inverse Laplace transformation was derived. This allows for the computation of the convolution integral and the inverse Laplace transformation of $G^{-1}(s)$ numerically. The form of the solution changes the ill-posed nature of the inverse heat conduction problem, and allows for regularization to control the instability. Due to the generalized nature of the formulation, this method can readily be applied to any class of machine tools without any further developments by the end user.

An important aspect of the estimation problem which has never been fully investigated is the nonlinear effect of the contact joint interaction problem. The finite-element models that have been developed in this thesis demonstrate that this phenomenon exists for some classes of machine tools, and the effect can be considerable. The generalized modelling procedure has been used successfully to simulate the mathematical form of the contact interface, and to generate a model of the joint induced nonlinearity which can accurately estimate the nonlinear deviation of the thermal deflection in real time. Because of the mathematical foundation of the model, it has been shown to accurately predict the nonlinear deviation resulting from thermal inputs outside of the range of calibration, and even external mechanical inputs for which no calibrated data was available.

The multi-variable thermal deflection control system which was developed in this thesis incorporates a real-time inverse heat conduction algorithm to identify the time variation of the heat generation sources, a real-time dynamic model of the thermal deformation of the structure, and an adaptive model of the contact joints to correct for the nonlinear joint interaction phenomenon. The combination of these dynamic models has been shown to predict the actual thermal deflection in a finite-element and a physical machine structure to within ±4 microns. The knowledge of the system dynamics which is provided by these models is the basis for the multivariable optimization of the thermal deflection control system, and the thermal deflection which is predicted by this procedure in real-time is used as simulated feedback signal to the

controller. Two mechanisms have been investigated for micro-positioning the cutting tool for compensation, the first being an NC position control system, and the second is an array of resistance heaters positioned strategically on the machine structure. Since there is a significant time delay between the actuation of the electric heaters and the resulting control deformation, and since actuation for control on one axis produces undesired deflection along other axes, an optimized control strategy is essential for maximizing the operational performance of the closed loop system.

Verification tests were conducted on two models of a machine structure. The first is a physical model incorporating all of the measurement and power actuation hardware that will be required on a real machine tool. The second model is a three-dimensional finite-element model of a machine tool structure, which is designed to simulate the effect of significant joint nonlinearity, as would be encountered on a relatively massive machine structure. The results confirmed the accuracy and inherent stability of the IHCP solver and the control system for the measurement and power actuation hardware that was used. The regularized inverse thermal transfer function minimizes the propagation of random temperature measurement errors, so that the accuracy of the estimated thermal displacement is excellent. The results confirmed that the objectives of the proposed control system for maintaining residual errors $< 10\ \mu m$ and control cycle < 1 second were met.

9.2 Recommendations for Future Work

The next step for the future development of the method is for verification on a real machine tool in operation. The major challenge to implementing the procedure on a real machine tool will be the identification of the major heat sources and running them independently for calibration. The thermal imaging camera has been shown to be highly effective at identifying the principal heat sources for the structures in this thesis. A possible method of verification testing would be to produce precision parts with and without the thermal deflection control

system. An analysis of the machining accuracy could be obtained by an analysis of the accuracy of the machined parts. In order to test the adaptive model for estimating contact joint nonlinearity on a real machine tool it will be necessary to find a machine tool that exhibits significant nonlinear behaviour. It might be necessary to test a number of machine tools before a suitably nonlinear response is found. It would be interesting to study the feasibility of using heat sinks as well as heat sources to increase the flexibility of the control system. Heat sinks could be provided by miniature heat pipes or thermo-electric cooling units.

The method could also be extended to variable geometry machine tools by incorporating adaptive parameter variation of the thermal deformation models. The measured input for this proposed system would be the linear position of the table, or another variable geometry element. The parameters of the models would be modified according to the position of the geometrical element, perhaps using a neural network based adaptive strategy.

REFERENCES

1. Dehaes, J., Kruth, J., and Vanherck, P., "K. U. Leuven Research on Thermal Compensation of Five Axis Milling Machine", CIRP conf. on Thermal Behaviour, Intelligent Diagnostics and Supervising of Machining Systems, edited by J. Jedrzejewski, Poland, 1996, pp.125-137.

2. Chiappulini, R., Giannotti, L., and Galbersanini, "On-Line Correction via Software of Thermal Errors in Numerically Controlled Machine Tools", presented at the Scientific Committee 'M' of 41th CIRP General Assembly, August, 1991.

3. Attia, H. "Thermal deformation of Machine Tools and its Effects on Machining Accuracy", Lecture Notes, Mechanical Engineering Department, Concordia University.

4. Sata, T., Takeuchi, Y., Sato, N., and Okubo, N., "Analysis of Thermal Deformation of Machine Tool Structure and its Application," Proc. 14th Int. MTDR Conference, Macmillan Press, 1973, pp. 275-280.

5. Hatamura, Y., Nagao, T., Mitsuishi, M., Kato, K., Taguchi, S., Okumura, T., Nakagawa, G, and Sugishita, H., "Development of an Intelligent Machining Centre Incorporating Active Compensation for Thermal Distortion", Annals of the CIRP, Vol. 42/1, 1993, pp. 549-552.

6. Fraser, S., Attia, M.H., and Osman, M.O.M., "Modelling, Identification and Control of Thermal Deformation of Machine Tool Structures: Part II- Concept of Generalized Transfer Functions", submitted for publication in the Trans. ASME, J. Engrg. Industry.

7. Spur, G., and Fischer, H., "Untersuchung des Thermischen Verhaltens der Tischgruppe einer Grosswerkzeugmaschine", Annals of the CIRP, Vol. 16, 1968, pp. 75-83.

8. Weck, M., Schuze, O., Michels, F., and Bonse, R., "Optimization of Machine Tools Performance and Accuracy", ASME Symposium on Intelligent Machine Tool Systems, Int. Mech. Engrg. Congress and Exposition, November, 1994, pp.895-908.

9. Moriwaki, T., Horiuchi, A., and Okuda, K., "Effect of Cutting Heat on Machining Accuracy in Ultra Precision Diamond Turning", Annals of the CIRP Vol 39, Jan 1990.

10. Spur, G. and Fischer, H., "Thermal Behaviour of Machine Tools," Proc. 10th Int. MTDR Conference, McMillian Press, 1969, pp. 147-160.

11. Lowen, E., "Air Shower Thermal Stability", proc. SME Prec. Machining Workshop, Williamsburg, Va., (1978).

12. Attia, M.H., "Modelling of Thermal Deformation of Machine Tool Structures: Design and Control Issues", Invited Keynote Paper, Proc. Int. Symposium on Manufacturing and Materials Processing, Int. Centre of Heat and Mass Transfer, Dubrovnik, Yugoslavia, August, 1990.

13. Hemingray, C.P., "Some Aspects of the Accuracy Evaluation of Machine Tools", Proc. 14th Int. MTDR Conference, MacMillan Press, 1973, pp.281-284.

14. Bryan, J., "International Status of Thermal Error Research (1990)", Annals of the CIRP, Vol. 39, Feb. 1990.

15. Mottu, A., "Guidages et paliers de machinesoutils. Industrielle Org. 29 (1960).

16. Spur, G., Konstruktive Gestaltung und Automatisierung der Werkzeugmaschine", Industrie-Anzeiger, 90 Jg, Nr. 67 v.20, 1968.

17. Okushima, K., Kakino, Y., Kondo, K., and Kikuchi, T., "An Optimum Design of Machine Tools for Thermal Deformations", Bull. Japan Soc. Of Prec. Engg., Vol 7, No. 2, 1973.

18. Bryan, J.B., and McLure, E.R., "Thermal Stability-Key to NC Accuracy", Proc. &th Annual Meeting, Numerical Control Society, pp.119-126.

19. Spur, G., Hoffman, E., Paluncic, Z., Benzinger, and Nyomen, H., "Thermal Behaviour Optimization of Machine Tools", Annals of the CIRP, 37 (1988) 1, pp.401-405.

20. Yoshida, Y., and Honda, F., "Thermal Deformation of a Vertical Milling Machine, Part II", Proc. 8th Int. MTDR Conference, MacMillan Press, 1967, pp.83-96.

21. Trapet, E., and Walede, F., "Co Ordinate Measuring Machines in the Production Line: Influence of Temperature and Measuring Uncertainties", IV Congress Intl. Metrologia Industrial, Zaragosa, Nov. 1989.

22. Bryan, J., Donaldson, R., McLure, E., and Clouser, R., "A Practical Solution to the Thermal Stability Problem in Machine Tools", S.M.E. MR72-138 UCRL 73577 (1972).

23. Donaldson, R., and Patterson, S., "Design and Construction of a Large Vertical Axis Diamond Turning Machine", SPIE 27th ann. Tech. Symp. (1983).

24. McKeown, P.A., Weck, M., and Bonse, R., "Reduction and Compensation of Thermal Errors in Machine Tools", Annals of the CIRP, Vol. 44/2, 1995.

25. Tonshoff, H.K. and Wulfsberg, J.P., "Developments in Diagnosis of Thermal Induced Displacements in Machine Tools", Symposium on Grinding Fundamentals and Applications, ASME-WAM, San Francisco, Dec. 1989, pp. 281-295.

26. Mou, J., Donmez, M.A., and Cetinkunt, S., "An Adaptive Error Correction Method Using Feature-Based Analysis Techniques for Machine Performance Improvement, Part 2: Experimental Verification", Trans ASME, J. Engrg. for Ind., Vol. 117, 1995, pp. 591-600.

27. Ferreira, P.M., and Liu, C.R., "A Method for Estimating and Compensating Quasistatic Errors of Machine Tools", Trans ASME, J Engrg. for Ind., Vol. 1993, Feb., 1993, pp. 149-159.

28. Ni, J., and Wu, S.M., "An On-line Measurement Technique for Machine Volumetric Error Compensation", Trans ASME, J Engrg. for Industry, Vol. 1993, Feb., 1993, pp. 85-92.

29. Chen, J.S., Yuan, J.X., Ni, J., and Wu, S.M., "Real-time Compensation for Time-Variant Volumetric Errors on a Machining Center, Trans ASME, J. Engineering for Industry, Vol. 115, November, 1993, pp. 472-479.

30. Sata, T., Takeuchi, Y., Sakamoto, M., and Weck, M., "Improvement of Working Accuracy on NC Lathe by Compensation for the Thermal Expansion of Tool", Annals of the CIRP, Vol 30, No 1, 1981, pp. 445-449.

31. Sata, T., Takeuchi, Y., and Okubo, N., "Control of the Thermal Deformation of a Machine Tool", Proc., 16th Int. MTDR Conference, McMillan Press, 1975, pp. 203-208.

32. Mou, J., and Liu, C.R., "An Adaptive Methodology for Machine Tool Error Correction", J. Engineering for Industry, Vol. 117, August, 1995, pp.389-399.

33. Balsamo, A., Marques, S., and Sartori, S., "A Method for Thermal Deformation Correction of CMMs", Annals of the CIRP, Vol. 39/1/1990, pp.557-560.

34. Ichimiya, R., "Compensation for Thermal Deformation of Milling Machine", Proc. Conf. Numerical Methods in Machine Tool Design, Wroclaw, Poland, 1980, pp. 39-49.

35. Spur, G., and Heisel, U., "Automatic Compensation of Thermal Disturbances in Machine Tools," Proceeding of the 3rd International Conference on Production Engineering, Kyoto, 1977.

36. Duffie, N.A., and Malmberg, S.J., "Error Diagnosis and Compensation Using Kinematic Model and Position Error Data", Annals of the CIRP, Vol. 36/1, 1987, pp. 355-358.

37. Ichimiya, R., Yokoyama, K., and Watanabe, Y., "Experimental Study on Thermal Deformation of Machine Tool", Research Report No. 25, Faculty of Engineering, Niigata University, 1976.

38. Jedrzejewski, J., "Kompansation thermischer Verlagerungen einer Drehmaschine", Werkstatt und Betrieb, 118, 2, 1985, pp. 85-87.

39. Schellekens, P., Soons, J., Spann, H., Look, V., Trapet, E., Dooms, J., De Ruiter, H., and Maisch, M., "Development of Methods for the numerical Correlation of Machine Tools", Report to the Commission of the European Communities, EUR 15377 EN 1-191, 1993.

40. Mou, J., Donmez, M.A., and Cetinkunt, S., "An Adaptive Error Correction Method Using Feature-Based Analysis Techniques for Machine Performance Improvement, Part 1: Theory Derivation", J. Engrg. for Industry, Vol. 117, November, 1995, pp.584-590.

41. Aronson, R., "Machine Tool 101: Part 7, Machine Tools of the Future, Manufacturing Engineering, July 1994, pp. 39-45.

42. Veldhuis, S.C., and Elbestawi, M.A., "A Strategy for the Compensation of Errors in Five-Axis Machining", Annals of the CIRP, 1995.

43. Moriwaki, T., and Zhao, C., "Neural Network Approach to identify Thermal Deformation of Machining Center", Human Aspects in Computer Integrated Manufacturing, edited by G.J. Olling and F. Kimura, Elsevier Science Publishers B.V. (North-Holland), 1992, pp. 685-697.

44. Chen, J.S., Yuan, J.X., Ni, J., and Wu, S.M., "Thermal Error Modelling for Volumetric Error Compensation", Sensors and Signal Processing for Manufacturing, ASME /PED-Vol. 55, 1992, pp. 113-125.

45. Moriwaki, T., "Thermal Deformation and Its On-Line Compensation of Hydraulically Supported Precision Spindle", Annals of the CIRP, Vol. 37, n 1, 1988, pp. 393-396.

46. Sata, T., Takeuchi, Y., and Okubo, N., "Control of the Thermal Deformation of a Machine Tool", Proc., 16th Int. MTDR Conference, McMillan Press, 1975, pp. 203-208.

47. Fraser, S., Attia, M.H., and Osman, M.O.M., "Modelling, Identification and Control of Thermal Deformation of Machine Tool Structures: Part I- Concept of Generalized Modelling", submitted for publication in the Trans. ASME, J. Engrg. Industry.

48. Fraser, S., Attia, M.H., and Osman, M.O.M., "Modelling, Identification and Control of Thermal Deformation of Machine Tool Structures: Part III- Real Time Identification of Heat Input to the Structure", submitted for publication in the Trans. ASME, J. Engrg. Industry.

49. Beck, J.V., Blackwell, B., and St. Clair, C.R., "Inverse Heat Conduction: Ill-posed Problems", Wiley-Interscience Publication, New York, 1985.

50. Hensel, E., "Inverse Problems for Multi-dimensional Parabolic Partial Differential Equations", Applied Mechanics Reviews, ASME, Vol. 41, No. 6, June 1988, pp. 263-269.

51. Stolz, G., "Numerical Solutions to an Inverse Problem of Heat Conduction for Simple Shapes", Trans. ASME, J. Heat Transfer, Vol. 82, 1960, pp. 20-26.

52. Bass, B.R., "Application of the Finite element Method to the Nonlinear Inverse Heat Conduction Problem Using Beck's Second Method", Trans. ASME, J. Engrg for Industry, Vol. 102, 1980, pp. 168-176.

53. Lesnic, D., Elliott, L., and Ingham, D.B., "Application of the Boundary Element Method to Inverse Heat Conduction Problems", Int. J. Heat Mass Transfer, Vol. 39, 1996, pp. 1503-1517.

54. Vogel, J., Sara, L., and Krejci, L., "A Simple Inverse Heat Conduction Method with Optimization", Int J. Heat Mass Transfer, Vol. 36, No. 17, 1993, pp. 4215-4220.

55. Beck, J.V., "Surface Heat Flux Determinations Using an Integral Method", Nucl. Eng. Design, Vol. 7, 1968, pp. 170-187.

56. Raynaud, M., and Bransier, J., "A New Finite Difference Method for Nonlinear Inverse Heat Conduction Problem", Num Heat Transfer, Vol. 9, No. 1, 1986, pp. 27-42.

57. Flach, G.P., and Ozisik, "An Adaptive Inverse Heat Conduction Method with Automatic Control", Trans. ASME, J Heat Transfer, Vol. 114, 1992, pp. 5-13.

58. Miller, K., "Least Square Methods for Ill-Posed Problems With a Prescribed Bound", SIAM J. Math. Anal., Vol. 1, No. 1, Feb, 1970, pp. 52-74.

59. Tikhanov, A.N., and Arsenin, V.Y., "Solutions of Ill-Posed Problems", V.H. Winston & Sons, Washington DC (1977).

60. Alifanov, O.M., and Artyukhin, F.A., "Regularized Numerical Solution of Non-Linear Inverse Heat Conduction Problem", J. Eng Phy 29, 934-938, 1975.

61. Alifanov, O.M., Artyukhin, E.A., and Rumyantsev, S.V., "Extreme Methods for Solving Ill-Posed Problems with Applications to Inverse Heat Transfer", Begell House, New York, 1995.

62. Murio, D.A., "The Mollification Method and Numerical Solution of Ill-Posed Problems", Wiley, New York, 1993.

63. Beck, J.V., and Murio, D.A., "Combined Function Specification-Regularization Procedure for Solution of Inverse Heat Conduction Problem", Inst Aeronautics and Astronautics, AIAA-84-0491, 1984.

64. Murio, D.A., "On the Characterization of the Solution of the IHCP", ASME Winter Annual Meeting. 1985, Paper No. 85-WA/HT-41.

65. Raymond, M., and Beck, J.V., "Methodology for Comparison of Inverse Heat Conduction Methods", Trans. ASME, J. Heat Transfer, Vol. 110, Feb 1988, pp. 30-37.

66. Raynaud, M., and Bransier, J., "Experimental Validation of a New Space Marching FD Algorithm for the Inverse Heat Conduction Problem", Proc. 8th Int Heat Transfer Conference, San Francisco, Ca, 1986, pp. 603-608.

67. Hills, R.G., and Mulholland, G.P., "The Accuracy and Resolving Power of One-dimensional Inverse Transient Heat Conduction Theory as Applied to Discrete and Inaccurate Measurements", Int J Heat Mass Transfer, Vol. 22, 1979, pp. 1221-1229.

68. Imber, M., "Temperature Extrapolation Mechanism for Two-dimensional Heat Flow", AIAA J., Vol. 12, No. 8, 1974, pp. 1089-1093.

69. Dumek, V., Druckmueller, M., Raudensky, M., and Woodbury, K.A., "Novel Approach to IHCP: Neural Networks and Expert Systems", Proc. ASME Conf on Inverse Problems in Engineering, 1993, pp. 275-282.

70. Haji-Sheikh, A., and Buckingham, F.P., "Multidimensional Inverse Heat Conduction Using the Monte Carlo Method", Trans ASME, J Heat Transfer, Feb. 1993, vol. 115, pp. 26-33.

71. Beck, J.V., "Comparison of the Iterative Regularization and function Specification Algorithms for the Inverse Heat Conduction Problem", Proc. ASME Conf on Inverse Problems in

Engineering, 1993, pp. 23-30.

72. Orlande, H.R.B., and Ozisik, M.N., "Determination of the Reaction Function in a Reaction-Diffusion Parabolic Problem", Proc. ASME Conf on Inverse Problems in Engineering, 1993, pp. 117-124.

73. Whitmore, R.A., "Harmony of Instrumentation for Accurate Temperature Measurement", Hy-Cal Engineering TR-391, 12105 Los Nietos Road, Santa Fe Springs, California, 90670.

74. O'Brien, B., Miller, S., "Thermocouples, RTDs can Boost Temperature Measurement Accuracy", Industrial Research and Development, Nov. 1983, pp.98-100.

75. Conley, R., Ravitz, S.F., and Kendall, W.B., "Device for the precise Measurement of Small Temperature Changes", The Review of Scientific Instruments, Vol. 35, No. 6, June, 1964, pp.729-732.

76. Calverd, A.M., "A Very Low Power AC Bridge for High Resolution Remote Resistance Thermometry", J. Phys. E.:Sci, Instrum., Vol. 15, 1982.

77. Omega Catalog

78. Takeuchi, Y., Sakamoto, M., and Imura, K., "Development of Integrated Turning System with Predictive Compensatory Function for Machining Errors", Annals of the CIRP, Vol 34, No 1, 1985, pp. 519-523.

79. Fraser, S., Attia, M.H., and Osman, M.O.M., "Modelling, Identification and Control of Thermal Deformation of Machine Tool Structures: Part IV-A Multi-Variable Closed-Loop Control System", submitted for publication in the Trans. ASME, J. Engrg. Industry

80. Ichimiya, R., "Compensation for Thermal Deformation of Milling Machine", Proc. Conf. Numerical Methods in Machine Tool Design, Wroclaw, Poland, 1980, pp. 39-49.

81. Kudryavtsev, Y.V., "Unsteady-State Heat Transfer", Iliffe Books Ltd., London, 1996.

82. Luikov, A.V., "Analytical Heat Diffusion Theory", Academic Press, New York, 1968.

83. Fraser, S.F., "Modelling and Control of Thermal Deformation in Machine Tool Structures", Masters Thesis, 1993.

84. ALGOR Process Reference Manual, Algor Interactive Systems, Inc., Pittsburgh, PA.

85. Attia, M.H., and Kops, L., "Nonlinear Thermoelastic Behaviour of Structural Joints-Solution to a Missing Link for Prediction of Thermal Deformation of Machine Tools", ASME Journal of Engineering for Industry, Vol. 101, 1979.

86. Attia, M.H., and Kops, L., "Importance of Contact Pressure Distribution on Heat Transfer in Structural Joints of Machine Tools", ASME Journal of Engineering for Industry, Vol. 102, 1980, pp. 159-167.

87. Masuko, M., Ito, Y., and Fujimoto, "Behaviour of the Horizontal Stiffness and the Micro-Sliding on the Bolted Joint Under the Normal Pre-Load", 12th int. Machine Tool Design and Research Conference 1973, pp.81-88.

88. Ito, Y., and Masuko, M., "Experimental Study on the Optimum Interface Pressure on a Bolted Joint Considering the Damping Capacity", 12th Intl. Machine Tool Design and Research Conference, 1973, pp.97-105.

89. Attia, M.H., and Kops, L., "Effect of Fretting on Thermal deformation of a Machine Structure", ASME Journal of Engineering for Industry, Vol. 113, 1991, pp.425-433.

90. Levina, Z.M, "Research on Static Stiffness of Joints of Machine Tools", Proc. 8th Int. Machine Tool Design and Research Conference, 1967, pp.737-758.

91. Ostrovskii, V.I., "The Influence of Machining Methods on Slide Way Contact Stiffness", Machines and Tooling, Vol. 36, No. 1, 1965, pp.17-19.

92. Kirsovana, V.N., "The Shear Compliance of Flat Joints", Machines and Tooling, Vol. 38, No. 7, 1967, pp.30-34.

93. Back, N., Burdekin, M., and Cowley, A., "Review of the Research on Fixed and Sliding Joints", 13th Int Machine Tool Design and Research Conference, 1972, pp. 87-97.

94. Tsukada, T., and Anno, Y., "An Analysis of the Deformations of Contacting Rough Surfaces - 3rd Report: Introduction of a New Contact Theory of Rough Surfaces", Bulletin of the Journal of Japanese Society of Mechanical Engineers JSME, Vol. 15, No. 86, 1972, pp.996-1003.

95. Tsukada, T., and Anno, Y., "An Analysis of the Elastic and Plastic Deformations of Mechanical Surfaces in Contact - 2nd Report: Comparison Between Calculated and experimental Results on the Deformations of Rough Surfaces in Contact ", Bulletin of the Journal of Japanese Society of Mechanical Engineers JSME, Vol. 17, No. 105, 1974, pp.385-392.

96. Back, N., Burdekin, M., and Cowley, A., "Analysis of Machine Tool Joints by the Finite-Element Method" 14th Intl. Machine Tool Design and Research Conference, 1973, pp. 529-537.

97. Clausing, A.M., and Chao, T.B., "Thermal Contact Resistance in a Vacuum Environment", J. Heat Transfer, Vol. 87, 1965, pp.243-252.

98. Yovanovitch, M.M., "Thermal Contact Correlations", Spacecraft Radiative Transfer and Temperature Control, T.E. Horton (ed.), Vol. 83 of Progress in Astronautics and Aeronautics, 1982.

99. Schankula, M.H., Patterson, D.W., and Yovanovich, M.M., "The Effect of Oxide Films on the Thermal Resistance Between Contacting Zirconium Alloys", Materials in Nuclear Energy, Proc. Of the Conference of the American Society for Metals, Huntsville Ontario, Canada, Sept. 1982.

100. Mikic, B., "Thermal Constriction Resistance due to Non-Uniform Surface Conditions", Intl. J. Heat Mass Transfer, Vol. 13, 1970, pp.1497-1500.

101. Yovanovich, M.M., DeVaal, J., and Hegazy, A.H., "A Statistical Model to Predict Thermal Gap Conductance Between Conforming Rough Surfaces", AIAA Paper 82-0888, AIAA/ASME 3rd Joint Thermophysics, Fluids, Plasms, and Heat Transfer Conference, Louis, Missouri, 1982.

102. Turyk, P.J., and Yovanovich, M.M., "Modified Effective Conductivity Models for Basic Cells of Simple Cubic Packed Beds", Heat Transfer in Porous Media and Particulate Flows, L.S. Yao et al. (Ed.)- HTD Vol. 46, 1985.

103. Crump, K.S., "Numerical Inversion of Laplace Transforms Using a Fourier Series Approximation", Journal of the Association for Computing Machinery, Vol. 23, No. 1, Jan. 1976, pp. 89-95.

104. REFERENCE FROM MHA

105. Franklin, G.F., Powell, J.D., Workman, M.L., *Digital Control of Dynamic Systems*, 2nd ed., Addison-Wesely:1990.

106. Bryson, A.E., and Ho, Y.C., *Applied Optimal Control*, Halsted Press, Washington, D.C., 1975.